Search for Gravitinos in R-Parity violating Supersymmetry at HERA

Dissertation
zur Erlangung des Doktorgrades
des Fachbereichs Physik
der Universität Hamburg

vorgelegt von

Claus Horn

aus Mönchengladbach

Hamburg
2006

Gutachter der Dissertation:	Prof. Dr. P. Schleper Prof. Dr. C. Hagner
Gutachter der Disputation:	Prof. Dr. R. Klanner Prof. Dr. J. Mnich
Datum der Disputation:	27.07.2006
Vorsitzender des Prüfungsausschusses:	Prof. Dr. A. Lichtenstein
Vorsitzender des Promotionsausschusses:	Prof. Dr. G. Huber
MIN-Dekan:	Prof. Dr. A. Frühwald

Abstract

In this thesis a search for gravitinos in R_P-violating supersymmetry is presented using data recorded with the ZEUS detector in the years 1996 to 2005, corresponding to an integrated luminosity of $300\,\mathrm{pb}^{-1}$. Collisions are recorded from e^-p and e^+p scattering at center-of-mass energies of 300 GeV and 318 GeV, using unpolarised as well as polarised lepton beams.

Gravitinos are naturally expected in Gauge Mediated Supersymmetry Breaking (GMSB) models where the gravitino is the lightest supersymmetric particle. At HERA gravitinos may result from the GMSB decay of neutralinos ($\tilde{\chi}^0 \to \gamma\tilde{G}$) produced in t-channel slepton exchange processes ($eq \to q'\tilde{\chi}$) *via* an R_P-violating ($\not{R}_P$) Yukawa coupling λ'_{ijk}. It was assumed that only one of the $\not{R}_P$ couplings λ'_{111}, λ'_{121}, λ'_{112} or λ'_{113} is different from zero at a time. To extend the investigated GMSB parameter space, also the two dominant R_P-violating decay channels ($\tilde{\chi} \to e^{\pm}qq$ and $\tilde{\chi} \to \nu qq$) were taken into account. For the signal-to-background optimisation a dynamic discriminant method was developed.

The data was observed to be well described by the expected Standard Model processes and no evidence for the production of supersymmetric particles was found. Limits were calculated for the masses of the left-handed selectron and the lightest neutralino and the variation of these limits was investigated in the entire GMSB parameter space. For some parameter regions, selectron masses of up to 360 GeV and neutralino masses of up to 190 GeV can be excluded at 95% CL. Similar mass limits were found to hold for large regions of GMSB parameter space.

Zusammenfassung

Diese Arbeit präsentiert die Suche nach Gravitinos in R-Paritäts-verletzender Supersymmetrie mit dem ZEUS Detektor am Teilchenbeschleuniger HERA. Die untersuchten Daten, mit einer integrierten Luminosität von $300\,\mathrm{pb}^{-1}$, bestehen aus Elektron-Proton Streureaktionen bei Schwerpunktsenergien von 300 GeV und 318 GeV, aufgenommen in den Jahren 1996 bis 2005.

Gravitinos werden erwartet in Modellen der Übertragung der Supersymmetriebrechung durch Eichwechselwirkung (GMSB Modell), in denen das Gravitino das leichteste supersymmetrische Teilchen ist. Bei HERA können Gravitinos aus Zerfällen von Neutralinos ($\tilde{\chi}^0 \to \gamma\tilde{G}$) entstehen, die durch t-Kanal Austauch von Sleptonen ($eq \to q'\tilde{\chi}$), mittels einer R-Paritäts verletzenden ($\not{R}_P$) Yukawa Kopplung λ'_{ijk}, erzeugt werden. Es wurde angenommen, dass nur eine der vier Kopplungen λ'_{111}, λ'_{121}, λ'_{112} oder λ'_{113} eine Stärke ungleich Null hat. Um den untersuchten GMSB Parameterraum zu erweitern, wurden auch die beiden R-Paritäts verletzenden Zerfallskanäle ($\tilde{\chi} \to e^{\pm}qq$ und $\tilde{\chi} \to \nu qq$) untersucht. Zur Optimierung des Signal zu Untergrund Verhältnisses wurde eine dynamische Diskriminanten Methoden entwickelt.

Die Daten stimmen gut mit den Standardmodell Erwartungen überein, und kein Hinweis auf supersymmetrische Teilchen wurde gefunden. Ausschlussgrenzen für die Masse des linkshändigen Selektrons und des leichtesten Neutralinos wurden berechnet und ihre Variation im gesammten noch nicht ausgeschlossenen GMSB Parameterraum wurde untersucht. In einigen Parameterbereichen können Selektronmassen bis zu 360 GeV und Neutralinomassen bis zu 190 GeV mit 95% Sicherheit (95% CL.) ausgeschlossen werden. Ähnliche Grenzen gelten in grossen Bereichen des GMSB Parameterraumes.

Contents

Abstract iii
Contents v
List of Figures ix
List of Tables xv
List of Symbols xvii

1 Introduction **1**

2 Theory **5**
2.1 Standard Model 5
2.2 Deep Inelastic Scattering (DIS) 11
2.3 Shortcomings of the Standard Model 14
2.4 Supersymmetry (SUSY) 17
2.4.1 Theoretical Framework 21
2.4.2 Minimal Supersymmetric Standard Model (MSSM) 23
2.4.3 Broken Supersymmetry 29
2.4.4 Gauge Mediated Supersymmetry Breaking (GMSB) 31
2.4.5 R-Parity 36
2.4.6 Sparticle Decay 38

3 SUSY at HERA **41**
3.1 Basic HERA Topologies 41
3.2 SUSY-flow Graphs 43
3.3 Abstract Notation 44
3.4 Fundamental Vertices 44
3.5 Abstract Diagrams 45
3.6 SUSY Processes at HERA 54
3.6.1 Signatures 55

3.6.2 Conclusion 57

4 Signal Processes and GMSB Phenomenology 59

4.1 Signal Processes 59

4.1.1 Signal Topologies and Possible SM Background 62

4.1.2 Search Strategy and Analysis Structure 66

4.2 Effect of GMSB Parameters 67

4.2.1 Influence of Process Parameters on Observables 69

4.2.2 Influence of GMSB Parameters on Process Parameters . . . 71

4.3 Limits of GMSB Parameter Space 78

4.3.1 Standard Parameters 78

5 HERA and ZEUS 81

5.1 HERA Accelerator 81

5.1.1 Polarisation Measurement 86

5.2 ZEUS Experiment 87

5.2.1 Central Tracking Detector (CTD) 90

5.2.2 Micro Vertex Detector (MVD) 92

5.2.3 Calorimeter (CAL) 93

5.2.4 Trigger and Data Acquisition System (DAQ) 95

5.2.5 Luminosity Measurement 97

6 Event Reconstruction 101

6.1 Kinematic Variables 101

6.1.1 Electron Method 102

6.1.2 Jacquet-Blondel Method 102

6.1.3 Double Angle Method 103

6.2 Track and Vertex Reconstruction 104

6.3 Calorimetric Variables 104

6.4 Electron Identification 106

6.4.1 Photon Identification 107

6.5 Energy Flow Objects 109

6.6 Jet Reconstruction 111

6.6.1 Jet Finding Algorithm 112

6.7 Additional Event Variables 112

7 Monte Carlo Simulation **115**
7.1 Hard Process . . . 115
7.2 Higher Order and Non-Perturbative Effects . . . 116
7.2.1 QCD Radiation . . . 116
7.2.2 Fragmentation and Hadronisation . . . 117
7.3 Simulation of Background . . . 117
7.4 Simulation of Signal . . . 118
7.5 Detector Simulation . . . 119

8 Discriminant Method **121**
8.1 Introduction . . . 121
8.2 Dynamic Discriminant Method . . . 123

9 Event Selection **129**
9.1 Data Set . . . 129
9.2 Generator Studies . . . 130
9.3 Selection of Electron Sample . . . 134
9.4 Control Selection for Gravitino Channel . . . 136
9.4.1 Selection of HERA II Data . . . 141
9.5 Studies of Photon Properties . . . 142
9.6 Final Selection for Gravitino Channel . . . 146
9.6.1 Selection of HERA II Data . . . 148
9.7 Cut Performance Studies . . . 149
9.8 Effect of Slepton Mass on Selection Efficiency . . . 151
9.9 Signal-to-Background Optimisation . . . 153
9.10 R_P-violating Decay Channels . . . 157
9.10.1 R_P-violating Decay Channel with Electron Final State . . . 157
9.10.2 R_P-violating Decay Channel with Neutrino Final State . . . 158

10 Limit Calculation **163**
10.1 Systematic Uncertainties . . . 163
10.2 Confidence Level Calculation . . . 166
10.3 Limits on Model Parameters . . . 167

11 Results **175**
11.1 Limits on Sparticle Masses . . . 175
11.1.1 Limit for Standard Parameters . . . 176

11.1.2 Influence of Strength of R_P-violating Coupling 177
11.1.3 Limit for Different λ'_{ijk} Couplings 177
11.2 Limit Dependence on GMSB Parameters 178
11.2.1 Influence of Messenger Scale, $\mathbf{tan}\beta$ and $\mathbf{sign}(\mu)$ 179
11.2.2 Influence of Number of Messenger Fields 180
11.2.3 Influence of SUSY Breaking Scale 181

12 Conclusions and Outlook **185**
12.1 Summary 185
12.2 Prospects at HERA 186
12.3 Prospects at LHC and ILC 187

A List of SUSY Production Diagrams at HERA **189**

B Trigger Definitions **193**

C Generated MC Samples **197**

D Analysis Framework **201**

E Implementation of Discriminant Method **205**

F Publication Plots **207**

Bibliography **213**

Acknowledgements **222**

List of Figures

2.1 Basic fermion vertices of the SM 10
2.2 Basic boson vertices of the SM 11
2.3 Diagram of electron proton scattering 11
2.4 Differential cross section for NC and CC DIS 13
2.5 Parton density functions 14
2.6 First order loop corrections to the Higgs mass 15
2.7 Electroweak fit to the Higgs mass. 16
2.8 Running of the gauge couplings, with and without supersymmetry 19
2.9 Solution of the hierarchy problem 20
2.10 Basic sfermion vertices of the MSSM 27
2.11 Basic gaugino vertices of the MSSM 27
2.12 Schematic illustration of hidden sector models 30
2.13 Evolution of sparticle masses as function of energy scale. 31
2.14 Generation of sfermion and gaugino masses in GMSB 34
2.15 Dominant decay channels for the lightest neutralino 39
2.16 Dominant decay channels for the lightest chargino 39
2.17 Dominant decay channels for sleptons 39

3.1 Classification scheme for SUSY diagrams 41
3.2 Basic HERA topologies 42
3.3 SUSY-flow graphs of type F for the R_P-conserving case 43
3.4 Fundamental vertices of the MSSM 45
3.5 $\not{R}_P$ vertices in abstract notation 46
3.6 Diagrams of type A 47
3.7 SUSY-flow graphs of type B 48
3.8 Abstract diagrams of type B 48
3.9 R_P-conserving diagrams of type C. 49

3.10 SUSY-flow graphs of type C with $\not{R}_P$ vertices 49
3.11 R_P-violating diagrams of type C 50
3.12 R_P-conserving diagrams of type D and E 51
3.13 R_P-violating diagrams of type D and E 51
3.14 R_P-violating diagrams of type D 52
3.15 R_P-violating diagrams of type E 52
3.16 R_P-conserving diagrams of type F. 53
3.17 R_P-violating diagrams of type F with one $\not{R}_P$ vertex 53
3.18 R_P-violating diagrams of type F with two $\not{R}_P$ vertices 54

4.1 Signal Processes 60
4.2 Number of expected events for different $\not{R}_P$ couplings 63
4.3 Event display of a generated MC event for the gravitino channel . 64
4.4 Event display of a generated MC event for the RPV channel with electron in the final state 65
4.5 Comparison of signal and background topologies 66
4.6 Overview of analysis structure 67
4.7 Influence of GMSB parameters on signal processes 68
4.8 Production cross section 70
4.9 Branching ratio for the GMSB decay of the lightest neutralino for different values of $\sqrt{F}$ 72
4.10 Influence of $\sqrt{F}$ and strength of λ'_{ijk} coupling on the branching ratio 73
4.11 Branching ratios for decays of $\tilde{\chi}_1^+$ and $\tilde{\chi}_2^0$ 74
4.12 Number of expected events for the three lightest gauginos at $\sqrt{F} =$ 230 GeV 75
4.13 Number of expected events for the three lightest gauginos at $\sqrt{F} =$ 3300 GeV 76
4.14 Dalitz-like neutralino composition plot 77
4.15 Parameter region where $\tilde{\tau}_1^{\pm}$ is the NLSP 77

5.1 Aerial view of DESY laboratory in Hamburg, Germany 82
5.2 Schematic view of HERA and the pre-accelerator system 83
5.3 Integrated luminosities delivered by HERA and gated by ZEUS 1994 – 2000 85
5.4 Integrated luminosities delivered by HERA and gated by ZEUS 2002 – 2005 86

5.5 Polarisation at HERA II 87
5.6 ZEUS coordinate system 88
5.7 ZEUS detector cross section along beam axis 89
5.8 ZEUS detector cross section perpendicular to beam axis 90
5.9 Cross section of a CTD octant 91
5.10 MVD schematic layout 93
5.11 Schematic view of ZEUS CAL 95
5.12 Schematic view of CAL towers and an FCAL module 96
5.13 Overview of ZEUS trigger and data acquisition system 98
5.14 Schematic view of ZEUS LUMI monitor system 99

6.1 Electron finder efficiencies for EM and SIRA5 108
6.2 Energy resolution for CTD and CAL 109
6.3 Schematic representation of an EFO 110

8.1 One dimensional cut example 122
8.2 Box size factor distribution 125
8.3 Discriminant distributions for different N_{min} values 126

9.1 Photon distributions at generator level 131
9.2 Correlation of photon energy and theta 132
9.3 $Q_{\tilde{l}}^2$ and $E_{\tilde{\chi}}$ for different slepton and gaugino masses 133
9.4 Effect of different slepton masses on η_γ and $p_{T,\gamma}$ 133
9.5 Gravitino distributions at generator level 134
9.6 Control distributions for electron sample 135
9.7 Distributions of electron variables for electron sample 136
9.8 Control distributions for gravitino channel (HERA I), set one . . . 137
9.9 Control distributions for gravitino channel (HERA I), set two . . . 138
9.10 Control distributions for gravitino channel (HERA I), set three . . 139
9.11 Control distributions for the gravitino channel (HERA II), set one 141
9.12 Control distributions for the gravitino channel (HERA II), set two 142
9.13 EM probability distribution 143
9.14 DCA distribution 144
9.15 Photon cone energy fraction 145
9.16 Photon variables for gravitino channel after final selection (HERA I) 146
9.17 Discriminant variables for gravitino channel after final selection (HERA I) 147

9.18 Photon variables for gravitino channel after final selection (HERA II) 148
9.19 Discriminant variables for gravitino channel after final selection (HERA II) . . . 149
9.20 Exclusive cut effect for different neutralino masses . . . 151
9.21 Total signal selection efficiency . . . 152
9.22 Effect of slepton mass on selection efficiency . . . 153
9.23 Purity against efficiency after cuts on the discriminant for different sets of discriminant variables . . . 154
9.24 Discriminant distribution for gravitino channel . . . 155
9.25 Efficiency and purity for gravitino channel as a function of discriminant cut . . . 156
9.26 Control distributions for R_P-violating channel with electron final state . . . 157
9.27 Discriminant distribution for R_P-violating channel with electron final state . . . 159
9.28 Control distributions for R_P-violating channel with neutrino final state . . . 160
9.29 Discriminant distribution for R_P-violating channel with neutrino final state . . . 161

10.1 Standard analysis cycle . . . 168
10.2 Relations between process parameters . . . 170
10.3 Improved analysis cycle for one particle and one decay channel . . . 171
10.4 Analysis cycle for m particles and n decay channels . . . 172

11.1 Mass limits for different strength of λ'_{111} coupling . . . 176
11.2 Mass limit for different λ'-couplings . . . 178
11.3 Mass limit dependence on messenger scale and $sign(\mu)$ for $tan\beta = 2$ 179
11.4 Mass limit dependence on messenger scale and $sign(\mu)$ for $tan\beta = 50$ 180
11.5 Mass limits for different number of messenger fields . . . 181
11.6 Mass limit dependence on SUSY breaking scale . . . 182

D.1 Example class for the variable SELQ2 . . . 202
D.2 Class structure of analysis framework . . . 204

F.1 Discriminant distribution . . . 208
F.2 Discriminant distribution . . . 209

F.3 Efficiency and purity as a function of discriminant cut 210
F.4 Limits for varying strength of R_P-violating coupling 210
F.5 Mass limit dependence on messenger scale and $sign(\mu)$ for $tan\beta = 2$ 211
F.6 Mass limit dependence on messenger scale and $sign(\mu)$ for $tan\beta = 50$211
F.7 Mass limits for different number of messenger fields 212

List of Tables

2.1 Fundamental fermions of the Standard Model 6
2.2 Fundamental Bosons of the Standard Model 7
2.3 Supermultiplets of the MSSM 25
2.4 Chiral supermultiplets of the MSSM. 25
2.5 Vectorial supermultiplets of the MSSM. 26
2.6 Particle content of the MSSM. 28
2.7 Free parameters of the GMSB 32
2.8 Overview of GMSB scenarios 35
2.9 NLSP decay scenarios in GMSB 36

3.1 Definition of abstract SUSY symbols 44
3.2 SUSY production processes without squarks at HERA 55
3.3 Interesting SUSY signatures at HERA 56

4.1 Gaugino production processes for different λ' couplings 61
4.2 Example cross sections for different λ' couplings 62
4.3 Background contributions from different SM processes 65
4.4 Overview of neutralino decay channels 71
4.5 Allowed regions of GMSB parameters 79

5.1 HERA parameters for different running periods 84
5.2 MVD design parameters 92
5.3 CAL parts with angular ranges and dimensions of the cells. 96

6.1 Energy correction factors for the CAL 105

7.1 Generator programs 118

9.1 Data set 130

9.2 Effect of different track cuts 144
9.3 Cut performance studies 150
9.4 Number of observed and expected events in the gravitino channel . 152
9.5 Number of observed and expected events in the R_P-violating decay channels 161

10.1 Considered systematic uncertainties 165

11.1 Special scenarios 179

A.1 List of SUSY production diagrams at HERA 189

C.1 PhP MC samples 197
C.2 Generated signal MC samples 198
C.3 CC DIS MC samples 199
C.4 NC DIS MC samples 200

List of Symbols

The whole point of this sentence is to make clear
what the whole point of this sentence is.

Douglas R. Hofstadter (Metamagicum)

θ^m	Parameter of a theoretical model
θ^p	Parameter of the physical process
E_T	Total transverse energy in the calorimeter
$P_{T,miss}$	Scalar sum of transverse momentum in the calorimeter
ϕ	Polar angle in the ZEUS coordinate system
θ	Azimuthal angle in the ZEUS coordinate system
η	Pseudorapidity: $\eta = -ln\, tan(\frac{\theta}{2})$
b	Particle with integer spin (boson)
f	Particle with half integer spin (fermion)
q	Any strongly interacting SM fermion (quark)
l	Any not strongly interacting SM fermion (lepton)
ν	Any only weakly interacting SM fermion (neutrino)
$e^{\pm}$	Electron or positron
p	Proton
γ	Photon
H	Higgs boson
$\tilde{G}$	Gravitino, superpartner of the graviton
$\tilde{\chi}$	Any gaugino (superpartner of neutral SM bosons)
$\tilde{\chi}_1^0$	Lightest neutralino (neutral gaugino)
$\tilde{e}_L$	Left-handed selectron (superpartner of left-handed electron or positron)

λ'	Yukawa coupling
G_N	Newton's gravitational constant
M_{Pl}	Planck mass (10^{19} GeV)
Q^2	Momentum transfer between lepton and quark
x	Fraction of proton momentum carried by the interacting quark
y	Inelasticity
μ	Higgsino mass parameter
$tan\beta$	Ratio of the vacuum expectation values of the two MSSM Higgs doublets
$\sqrt{F}$	Scale at which SUSY is broken in the hidden sector
Λ	Sparticle mass scale in the visible sector
M	Messenger mass scale
N	Number of messenger fields

Chapter 1

Introduction

Who wants to go the way needs to find the way and then go it.

Zen-Kôan

On the way to a concise understanding of the fundamental laws governing the world of the elementary building blocks of our universe, it is well plausible, that we stand at the edge of discovering the last symmetry of space and time: Supersymmetry.

The extraordinary success of the Standard Model (SM) of elementary particle physics can not conceal the facts arising from both, theoretical considerations and experimental evidence, that it does not provide a complete description of all physical observations.

The most promising candidate for a theory beyond the SM is supersymmetry [1, 2] (SUSY), which extends the Poincaré group of spacetime symmetries by introducing a symmetry between fermions and bosons. In this way it provides solutions to some of the most severe theoretical and experimental problems of particle physics. In predicting a new heavier superpartner for each SM particle, with masses expected to lie within the reach of today's particle accelerators, it constitutes an obvious target for experimental investigations.

This thesis gives a complete list of the most promising channels for the production of supersymmetric particles (sparticles) at the HERA electron-proton accelerator, taking into account also R-parity violating vertices which are contained in the most general supersymmetric Lagrangian. Event signatures are derived by considering the decays of the produced particles according to the couplings and mass spectra for the MSSM and the GMSB model.

While previous searches were mostly performed in the framework of the Minimal Supersymmetric Standard Model (MSSM), in recent years the interest in more predictive models has grown, which provide a description of the supersymmetry breaking mechanism. A natural candidate for such a model is the Gauge Mediated Supersymmetry Breaking (GMSB) model. Since in the GMSB the gravitino is the lightest supersymmetric particle (LSP), it predicts distinct experimental signatures.

Anomalous events with a signature of a photon, a muon and missing energy have been observed by the CDF collaboration [3] which may be explained in the R_P-violating GMSB model *via* smuon production and the subsequent decay $\tilde{\mu} \rightarrow \mu\tilde{\chi}_1^0 \rightarrow \mu\tilde{G}\gamma$.

Due to its unique initial state, HERA provides an ideal place for the investigation of R-parity violating couplings λ'. Previous analyses investigated resonant squark production in the s-channel and derived high λ'-dependent squark mass limits [4, 5, 6]. If squarks are heavier than sleptons, processes where the initial electron and a quark from the proton exchange a slepton in the t-channel become important leading to the production of gauginos. Their decays has been studied in the MSSM [7] for which a control analysis was performed in the course of this thesis. Since R_P is assumed to be violated in the production process the dominant decay channels proceed through a $\not{R}_P$ coupling leading to multiple jets and either an electron or a neutrino in the final state.

The topic of this thesis is to study the decays of gauginos in the GMSB model. In addition to the R_P-violating decay channels also the neutralino decay into a gravitino has been investigated which is the dominant decay channels in most of the GMSB parameter space.

This thesis presents several innovations: A classification scheme for SUSY processes (Chapter 3); a dynamic discriminant calculation method (Chapter 8); a way to calculate limits for n particles decaying into m different decay channels (Chapter 10); the representation of sparticle mixing in a kind-of Dalitz plot (Chapter 4); and a generic framework for ntuple-based data analyses (App. D). The following gives a short overview of the different chapters.

In the first chapter the theoretical models which are used to describe elementary particles are summarized, starting with the standard model, putting special emphasis to the open questions, most of which provide motivations for supersymmetric extensions of the SM. Models for supersymmetry are then presented,

especially the MSSM and GMSB models.

A list of all possible sparticle production processes at HERA with a potentially high-enough cross section is derived in Chapter 3. Then, the signal processes are described together with studies of the GMSB parameter space (Chapter 4).

In Chapter 5 the experimental setup is described, the HERA accelerator and the ZEUS detector, with special emphasis on the components relevant for the presented analysis. Chapter 6 describes how physical objects, such as jets and photons, are measured.

The following two chapters introduce Monte Carlo methods (Chapter 7) and how they can be used to optimise the signal-to-background ratio in a full multidimensional description of the physical problem (Chapter 8).

After all necessary tools have been collected, in Chapter 9 the event selection criteria are described in detail, separately for HERA I and HERA II data. Then the procedures for limit calculation are explained (Chapter 10) and finally, in Chapter 11, the derived limits for the GMSB parameter space are presented.

In the end the analysis is summarised and an outlook on the prospects for a potential discovery of supersymmetry at HERA and at the future colliders LHC and ILC is given (Chapter 12).

Chapter 2

Theory

Alles sollte so einfach wie möglich gemacht werden,
aber nicht einfacher.[1]

Albert Einstein

In this chapter the theoretical concepts which motivate the following analyses are presented, starting with an introduction to the Standard Model which is a consolidation of the current understanding of the world of elementary particles. On this basis, the different processes of lepton-proton scattering are described, as investigated at HERA. Finally, supersymmetric extensions of the Standard Model are presented, especially the MSSM and GMSB models.

2.1 Standard Model

The Standard Model (SM) of elementary particle physics describes electromagnetic, weak and strong interactions over an energy range from a few eV to 1 TeV with very high accuracy. The only other known fundamental force of nature, gravity, is not included since it can not be described with the same theoretical tools and its effects in particle interactions lie way below the experimentally accessible accuracy, becoming of comparable strength only at energies of the order of the Planck mass ($M_{Pl} = \sqrt{\frac{\hbar c}{G_N}} \simeq 10^{19}$ GeV, where G_N is Newton's constant[2]).

All mater particles in the SM are fermions (particles with half integer spin), whereas the interactions are described via the exchange of bosons (integer spin

[1] Everything should be made as easy as possible, but not easier.

[2] In this thesis natural units are used, where $c = \hbar = 1$.

TABLE 2.1: Fundamental Fermions of the Standard Model. Listed are only the values for the left handed components. Q_{el} is the electric charge in units of the positron charge e^+, I_3 is the third component of the weak isospin and Y is the hypercharge. They are connected by the Gell-Mann-Nishijima relation: $Q_{el} = I_3 + \frac{1}{2}Y$ [8].

Particles				Q_{el}	I_3	Y
Quarks	$\begin{pmatrix} u \\ d \end{pmatrix}$	$\begin{pmatrix} c \\ s \end{pmatrix}$	$\begin{pmatrix} t \\ b \end{pmatrix}$	2/3 -1/3	1/2 -1/2	1/3 1/3
Leptons	$\begin{pmatrix} \nu_e \\ e \end{pmatrix}$	$\begin{pmatrix} \nu_\mu \\ \mu \end{pmatrix}$	$\begin{pmatrix} \nu_\tau \\ \tau \end{pmatrix}$	0 -1	1/2 -1/2	-1 -1

particles). Fermions are classified, according to whether they participate in strong interactions or not, into quarks and leptons (see Tab. 2.1). While quarks take part in all three interaction of the SM, a subgroup of the leptons, the neutrinos, interact only weakly, which makes them difficult to detect. Due to this fact it has been established only lately that they are, like all the other fermions, massive particles and the details of their properties are still under investigation[3].

All fermions appear in three generations of particles with the same quantum numbers but different masses. Each family consists of left-handed doublets and right-handed singlets with respect to the weak interaction. The masses show a huge variation for the three generations, *e.g.* the masses of the electron, muon and tau are 0.511 MeV, 106 MeV and 1780 MeV, respectively. In hadrons, the predominant part of the mass results from interaction energy of the strong force. The rest mass of the u and d quarks, *e.g.* are known to lie between $1 - 5$ MeV and $3 - 9$ MeV, respectively, compared to a proton[4] mass of 938 MeV. In the quark sector, the mass difference between the three generations is even more dramatic with a top quark mass of 172.5 ± 2.3 GeV [10]. For each particle a corresponding anti-particle exists with the same mass but opposite electric and color charge. While the eight gluons, communicating the strong interaction, are irreducible representations of the $SU(3)_C$ group of color charge, the photon and the Z^0 and $W^\pm$ bosons emerge

[3]Neutrino mass limits can be derived from oscillation experiments. The Super-Kamiokande experiment measured, for instance, atmospheric muon neutinos converting into tau neutrinos and derived a mass difference of $1.9 \cdot 10^{-3}\,\mathrm{eV}^2 < \Delta m^2 < 3.0 \cdot 10^{-3}\,\mathrm{eV}^2$ at 90% CL [9].

[4]The proton is composed of two u and one d quark which interact mainly by gluon exchange.

TABLE 2.2: Fundamental Bosons of the Standard Model (see *e.g.* [11, 12, 13]).

Interaction	Gauge Boson	Q_{el}	Spin	Mass	Strength
Electromagnetic	γ	0	1	0	1/137
Weak	Z^0	0	1	91.2 GeV	1/30
	$W^{\pm}$	± 1	1	80.4 GeV	
Strong	$8 \times g$	0	1	0	$0.1 - 1$
Gravity	G	0	2	0	10^{-38}
Higgs Potential	H	0	0	> 114.7 GeV	$\propto m$

from $SU(2)_L \times U(1)_Y$ after electroweak symmetry breaking (the SM gauge bosons are listed in Tab. 2.2).

The theoretical framework for the description of these interactions is quantum field theory (for an introduction see *e.g.* [14, 15, 16, 17, 18]), where the fields $\phi(x)$ are linear superpositions of operators $a^\dagger(p)$ and $a(p)$ which respectively create and annihilate particles of momentum p. The $\phi(x)$ obey equations of motion (the Euler-Lagrange equations) that are derived from a Lagrangian $\mathcal{L}$ via Hamilton's variational principle[5]

$$\delta \int \mathcal{L}(t) dt = 0 \,. \tag{2.1}$$

In the case of the most simple Lorentz invariant Lagrangian for the fermion field ψ

$$\mathcal{L}_{\text{kin}} = i\psi^* \gamma^\mu \partial_\mu \psi \tag{2.2}$$

the application of the principle of least action (Eq. (2.1)) leads to the Dirac equation[6]

$$(i\partial\!\!\!/ - m)\psi(x) = 0 \,, \tag{2.3}$$

which describes the kinematic properties of a massive fermion field. To incorporate interactions between different fields an interaction term $\mathcal{L}_{\text{int}}$ is added to the free Lagrangian:

$$\mathcal{L} = \mathcal{L}_{\text{kin}} + \mathcal{L}_{\text{int}} \tag{2.4}$$

The interactions can be derived by requiring the Lagrangian to be invariant under *local gauge transformations* (locality here means that the transformation may differ

[5] $\mathcal{L}$ is fixed besides the possible addition of a total derivative $\mathcal{L} \to \mathcal{L}' = \mathcal{L} + \partial_\mu K^\mu$ which leaves the equations of motion unchanged.

[6] Here γ^μ are the four-dimensional *gamma*-matrizes see *e.g.* [19], and $\partial\!\!\!/ = \gamma^\mu \partial_\mu$.

from point to point in space and time):

$$|\psi\rangle \rightarrow |\psi'\rangle = U|\psi\rangle \tag{2.5}$$

where U is either a phase space factor ($U = e^{-iq\theta}$) for Abelian transformations or a unitary matrix in the general case:

$$U(\theta) = e^{-i\theta^i J_i} \tag{2.6}$$

with *generators* J_i which fulfill *Lie* algebras:

$$[J_i, J_k] = i\epsilon_{ikl} J_l \tag{2.7}$$

where the structure constants ϵ_{ikl} are *e.g.* given by the elements of the totally antisymmetric *levi-cevita* tensor in case the matrices U are representations of SU(2). When making this transformation local (*i.e.* U depending on x) one observes that the terms including spacetime derivatives ∂_μ require new vector fields V_μ^j to be introduced in order to be covariant under transformations $U(x)$. Since they always appear together, covariant Lagrangians can (only) be constructed by making the replacement:

$$i\partial_\mu \rightarrow iD_\mu = i\partial_\mu - g\sum_j V_\mu^j \tag{2.8}$$

The D_μ are called *covariant derivatives* and the V_μ^j are the gauge bosons corresponding to the symmetry imposed by $U(x)$. All observed interactions of the SM can be derived by requiring the Lagrangian to be invariant under the full gauge group of the SM, the

$$SU(3)_C \times SU(2)_L \times U(1)_Y \tag{2.9}$$

symmetry group, where $SU(3)_C$ is the non-Abelian symmetry group of strong interactions, $SU(2)_L$ is the non-Abelian weak isospin group, associated to gauge fields W^i ($i = 1, 2, 3$), and $U(1)_Y$ is the Abelian hypercharge group associated with the gauge field B. The subscript "L" refers to the fact, that only left handed fermions (and right handed anti-fermions) take part in the weak interactions, "C" denotes the strong color charge and "Y" the hypercharge.

Electromagnetic and weak interaction are collectively described in the Glashow-Salam-Weinberg theory [20, 21, 22][7] with the Lagrangian:

$$\mathcal{L}_{EW} = -\frac{1}{4}W^a_{\mu\nu}W^{a\mu\nu} - \frac{1}{4}B_{\mu\nu}B^{\mu\nu} + \sum_\psi \bar{\psi} i\gamma^\mu D_\mu \psi \tag{2.10}$$

[7] Nobel prize 1979.

Here the first two terms describe the kinematics and self-interactions of the gauge fields. The W^3 and B gauge bosons mix to form the physical fields of the Z^0 boson and the photon[8]:

$$\begin{pmatrix} Z_\mu \\ A_\mu \end{pmatrix} = \begin{pmatrix} \cos\,\theta_W & \sin\,\theta_W \\ -\sin\,\theta_W & \cos\,\theta_W \end{pmatrix} \begin{pmatrix} W_\mu^3 \\ B_\mu \end{pmatrix} \tag{2.11}$$

and

$$W_\mu^\pm = \frac{1}{\sqrt{2}}(W_\mu^1 \mp i W_\mu^2)\,, \tag{2.12}$$

where θ_W is the Weinberg angle ($\theta_W = \arctan(g^{'}/g)$, g and g' are the coupling constants of the W_μ^3 and B_μ fields, respectively). After rotating the Lagrangian into the basis of the physical fields the different interactions get visible:

$$\begin{aligned} \mathcal{L}_{EW} = & \sum_\psi \bar{\psi} i\gamma^\mu \partial_\mu \psi - e \sum_\psi Q_\psi \bar{\psi}\gamma^\mu \psi A_\mu \\ & - \frac{g^2}{2cos\,\theta_W} \sum_\psi \bar{\psi}\gamma^\mu (g_V - g_A\gamma_5)\psi Z_\mu \\ & - \frac{g^2}{\sqrt{2}} \sum_\psi \bar{\psi}_L \gamma^\mu (\sigma_+ W_\mu^+ + \sigma_- W_\mu^-)\psi_L \end{aligned} \tag{2.13}$$

The terms describe: free fermions, electromagnetic interactions, weak neutral current interactions and weak charged current interactions.

A consequence of the principle of local gauge invariance is that all gauge fields have to be massless (terms of the form $m\psi_L^* \psi_R$ are not gauge invariant), which is obviously not the case for the gauge bosons of the weak interaction (see Tab. 2.2). This problem is solved by the *Higgs mechanism* [23, 24] which postulates the existence of a complex scalar field doublet with a non-zero vacuum expectation value[9]. In this way electroweak symmetry is spontaneously[10] broken and a new boson, the Higgs boson H, emerges. Whereas the $W^\pm$ and Z^0 bosons acquire their masses through the interaction with the H boson, fermion masses are added via Yukawa coupling terms. The Higgs boson is the only particle in the SM which has not been discovered yet.

[8] W and B can not be the physical fields since they couple to the neutrino, which is not the case for the photon (as the neutrino is neutral).

[9] Its success is based on t'Hooft's prove that the theory constructed in this way is renormalizable. (Nobel prize 1999)

[10] *i.e.* the potential is chosen so that it is invariant under $SU(2)_L \times U(1)_Y$ but the ground state is not.

For the quarks electroweak eigenstates and mass eigenstates are not equal and interactions of the $W^{\pm}$ bosons can cause transitions between generations (these are flavor changing charged currents, FCCC). The mixing is described by the Cabibbo-Kobayashi-Maskawa (CKM) matrix which is the source of CP-violation in the SM. Since neutrinos are now known to have non-zero masses a similar mixing also occurs in the lepton sector. The measurement of the mixing angles is an interesting field of current research.

The strong interaction can be described with the same formalism as shown for electroweak interactions above [25, 26]. However, the self-interactions between gluons lead to confinement and asymptotic freedom through anti-screening effects (the strength of the coupling constant increases with distance).As a consequence, perturbation theory is not applicable anymore for large distances. The strong charge comes in three types (called colors), each quark carrying one color charge. Since $SU(3)_C$ is a non-Abelian group the gluons themselves carry color and anti-color. Consequently there are eight different gauge bosons of the strong interaction (the gluons). Quarks are not observed as free particles but are confined in colorless packages of two quarks (mesons) or three quarks (baryons).

The interactions of the SM can be illustrated perturbatively by *Feynman diagrams* and the matrix elements (phase-space independent part of transition amplitudes) calculated by Feynman calculus. In order to give a condensed overview of all SM reactions they can be represented in a generic way with the help of *basic vertices* as shown in Figures 2.1 and 2.2. These diagrams can be read in both

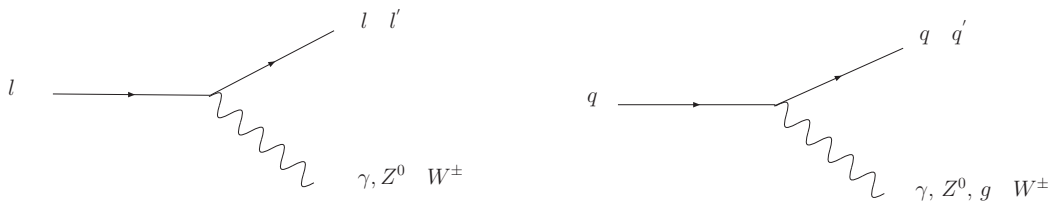

FIGURE 2.1: Basic fermion vertices of the SM. Here, l represents any lepton of all three families. Similarly, q stands for any quark.

directions corresponding to emission or absorption in Fig. 2.1 and creation or annihilation in Fig. 2.2. If for a given particle at the upper right line different particles are possible at the lower right line, they are separated by a comma. Different sets of particles at the two lines are separated by a larger space.

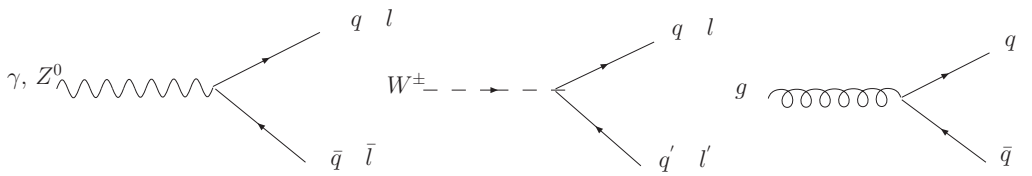

FIGURE 2.2: Basic boson vertices of the SM. Here, l represents any lepton of all three families. Similarly, q stands for any quark. The interactions of the Higgs boson are not shown, as well as the pure bosonic vertices of the SM (ggg, $gggg$, $Z^0W^-W^+$, γW^-W^+, $Z^0Z^0W^-W^+$, $\gamma\gamma W^-W^+$, $W^-W^+W^-W^+$ and $W^-W^+Z^0\gamma$).

2.2 Deep Inelastic Scattering (DIS)

At the electron-proton collider HERA the inner structure of the proton is investigated in electroweak and strong interactions. For this purpose the lepton (electron or positron), which is believed to be a point-like particle without spatial extension, is used as a probe. The achieved resolution is determined by the momentum transfer Q^2 between the lepton and a quark inside the proton via $\lambda \approx \hbar c/\sqrt{Q^2}$. HERA data cover a Q^2 region up to $40000\,\mathrm{GeV}^2$ corresponding to resolved distances of 10^{-18} m which is 1/1000 of the proton radius. The basic process is depicted in Figure 2.3. Depending on the nature of the virtual vector boson exchanged between the lepton ($e^{\pm}$) and the proton (p) the following processes are distinguished:

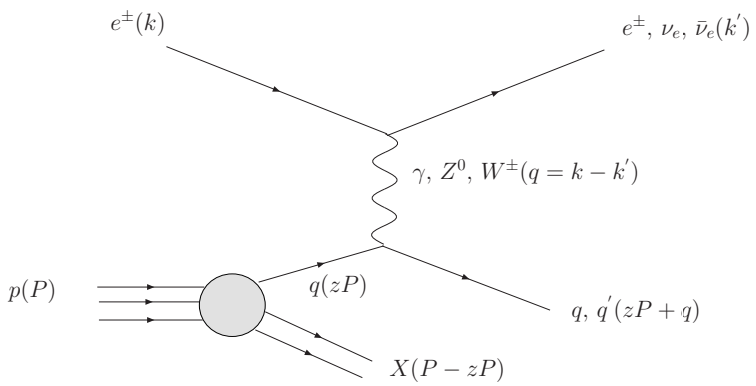

FIGURE 2.3: Diagram illustrating the lowest order processes in deep inelastic scattering between an electron or positron and a proton. The four-vectors of the particles are given in parenthesis.

- **Neutral Current (NC) processes:**
  In these events the exchanged boson is a γ or Z^0 so that the electron stays unchanged. Consequently, these events are characterized by an electron and one or more jets. Missing energy can only be the result of mismeasurement. At HERA a subcategory are the **Photoproduction (PhP) processes** which possess so low values of Q^2 ($\ll 1\,\mathrm{GeV}^2$) that the scattered electron is not observed in the main detector but escapes through the beam pipe. So called "soft" processes, where the photon is (quasi) real and no high transverse momentum particles are produced, represent the dominant type of interaction with a cross section of around $150\,\mu b$.

- **Charged Current (CC) processes:**
  When the exchanged boson is a charged $W^{\pm}$ boson the initial electron gets converted into a neutrino. Since these particles remain undetected CC events are characterized by large values of missing energy.

The kinematics of these processes can be described most conveniently by introducing Lorentz invariant products of four-vectors, which are assigned to the corresponding particles as denoted in Figure 2.3.

$$s = (k+P)^2 \tag{2.14}$$

$$Q^2 = -q^2 = (k-k')^2 \tag{2.15}$$

where $\sqrt{s}$ is the maximal available center of mass energy, and Q^2 is the four-momentum transfered from the proton to the lepton which determines the virtuality of the exchanged boson. The fact that the momentum comming from the proton side is *a priori* unknown is accounted for by the two *Bjorken* variables x and y:

$$x = \frac{Q^2}{2\,P\,q} \tag{2.16}$$

$$y = \frac{q\,P}{k\,P} \tag{2.17}$$

where x is the fraction of the proton momentum carried by the interacting quark and y is the so called inelasticity which is the fraction of energy transfered from the electron to the hadronic system, measured in the proton rest frame. Due to momentum conservation only three of these four variables are independent and a simple relation between them can be derived by neglecting the mass terms:

$$Q^2 = sxy \tag{2.18}$$

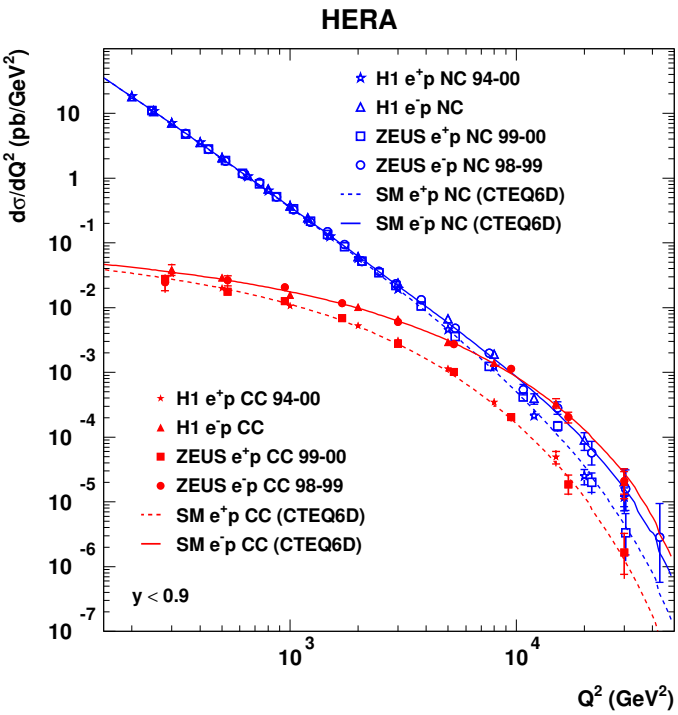

FIGURE 2.4: Differential cross section for NC and CC DIS as a function of Q^2 measured by H1 and ZEUS.

Since $\sqrt{s}$ is fixed at HERA, all measured quantities can be given as a function of two of the remaining variables, commonly x and Q^2. With typical values of y in the range $0.005 < y < 1$ the above relation show that the accessible x values vary between $10^{-5} \lesssim x \lesssim 10^{-3}$ for $Q^2 \approx 1\,\mathrm{GeV}^2$ and between $10^{-2} \lesssim x \lesssim 1$ for $Q^2 \approx 10^3\,\mathrm{GeV}^2$. Another useful variable is

$$W = (q + P)^2 \tag{2.19}$$

which represents the invariant mass of the recoiling hadronic system and can be interpreted as the center of mass energy of the boson-proton system.

The term Deep Inelastic Scattering (DIS) refers to processes with $Q^2 \gg 1\,\mathrm{GeV}^2$ and $W \gg m_p$ where the proton is destroyed. For these processes the cross section is in good approximation independent of Q^2 (at a fixed x value)[11] while it falls rapidly for "soft" processes where the proton stays intact. A detailed introduction to DIS can be found elsewhere [27].

[11] This behaviour was predicted by Bjorken and is therefore called *Bjorken scaling*.

The cross sections for NC and CC DIS are shown in Figure 2.4. A suppression of CC events is visible at low Q^2 which results from the additional mass term in the propagator for massive particle exchange: $\sigma^{CC} \propto \frac{m_W^4}{(Q^2+m_W^2)^2}$, compared to: $\sigma^{NC} \propto \frac{1}{Q^2}$ for the photon propagator. An additional difference is observed between e^-p and e^+p processes which results from the difference in u and d quark densities in the proton (see Figure 2.5). Since Q^2 and x are positively correlated and the sea quark fraction (which is u-d symmetric) decreases toward higher x the difference in u and d densities increases with Q^2.

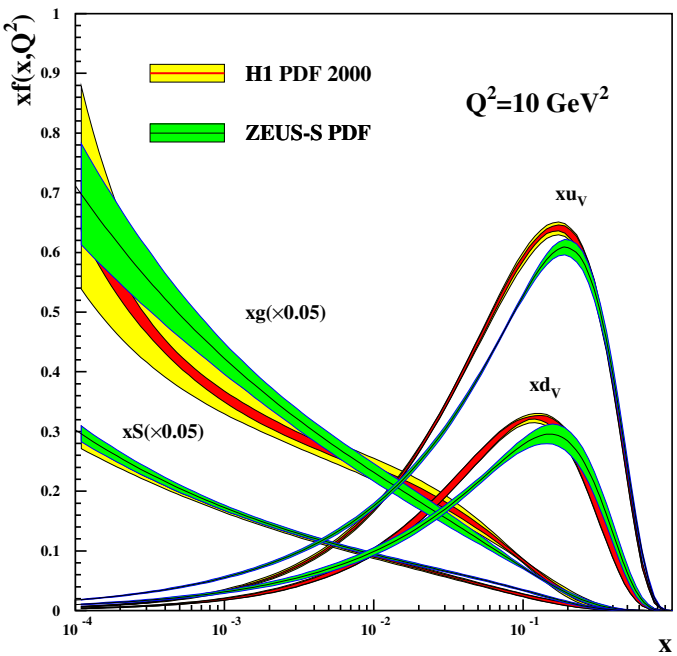

FIGURE 2.5: Parton density functions for varying x as extracted from NLO QCD fits at $Q^2 = 10\,\mathrm{GeV}^2$ by H1 and ZEUS. Shown are the distributions for u and d valence quarks and for s quarks (as an example for sea quark distributions) and also for gluons.

2.3 Shortcomings of the Standard Model

Despite its success in describing the vast majority of the observed phenomenology of elementary particles with high accuracy, the SM suffers from a number of unsolved problems some of which are listed in the following:

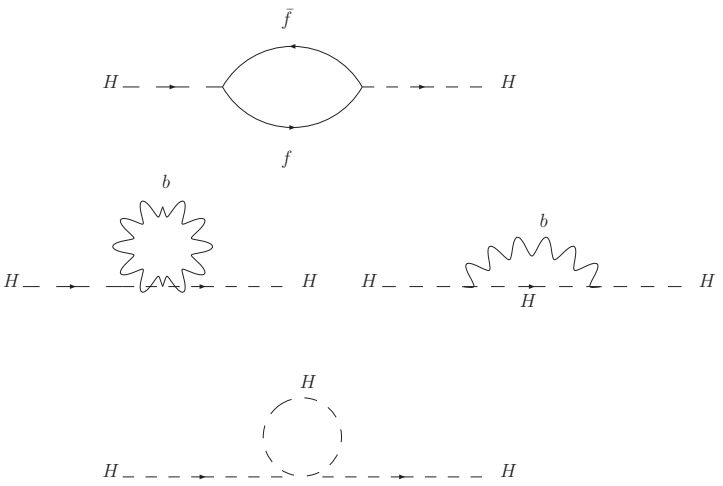

FIGURE 2.6: First order loop corrections to the Higgs mass. Fermion-antifermion production and anhilation (top), boson loops (middle) and Higgs self interaction (bottom).

- **No unification of forces**
  It is generally believed that the SM is only a low-energy approximation of a more fundamental theory. Such a theory should unify all interactions of the SM, with the couplings reaching the same value at a higher energy scale (the GUT[12] scale), which is not the case in the SM. Furthermore, gravity can not be included in the SM as quantum field theories of gravity are known to be non-renormalizable.

- **Hierarchy problem**
  The introduction of the Higgs boson explains the origin of mass in the SM but also poses a new problem, as the loop diagrams depicted in Figure 2.6 introduce quadratically divergent terms which lead to unnaturally large corrections to the Higgs mass. The first order contributions from fermion, boson and Higgs (self interaction) loops are:

$$\Delta m^2_{H,\text{fermion}} \sim -\frac{\lambda^2}{16\pi^2}\Lambda^2_{UV} \tag{2.20}$$

$$\Delta m^2_{H,\text{boson}} \sim \frac{\lambda^2}{16\pi^2}\Lambda^2_{UV} \tag{2.21}$$

$$\Delta m^2_{H,\text{Higgs}} \sim \frac{\lambda^2_H}{16\pi^2}\Lambda^2_{UV} \tag{2.22}$$

[12]The term GUT stands for Grand Unified Theory.

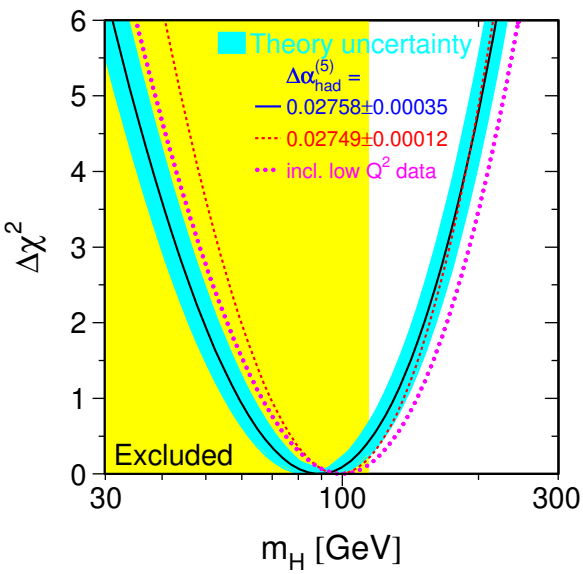

FIGURE 2.7: Global fit of electroweak data as a function of the SM Higgs mass [30]. The dashed line includes a newer value of the top mass. Obviously a light Higgs is favoured within the SM.

where Λ_{UV} is the energy scale at which new physics sets in. With Λ_{UV} of the order of M_{Pl} these corrections turns out to be 30 orders of magnitude larger than the physical Higgs mass[13]. A cancellation of all correction terms is possible but requires a tuning of λ with an accuracy of 17 orders of magnitude! This is known as the *fine tuning problem*. Moreover, different fine tuning is needed for each order of perturbation theory.

Since all SM fermions acquire their masses through interactions with the Higgs boson, m_H defines the scale of the SM. On the other hand, the measured quantities of the SM, which are sensitive to the logarithm of the Higgs mass through radiative corrections, can be used to constrain the mass of the Higgs within the SM (see Fig. 2.7). However, if new particles exist with masses at a scale Λ_{UV} (*e.g.* the Planck scale), the natural scale for m_H would be also Λ_{UV} and the reason for the existence of two different scales remains

[13] An upper limit for the Higgs mass can be deduced from elastic W^+W^- scattering: $m_H <$ 1 TeV [28, 29]

a mystery. This is the *naturalness* or *hierarchy problem*.

- **Cosmological problems**
  The particle content of the SM can not explain the amount of *dark matter* observed in the universe[14]. (Contributions from neutrinos, known as hot dark matter, are much too small [31].) In order to be dark, candidates must have no electromagnetic charge, thus be only weakly interacting massive particles (WIMPs) and they must have a very long lifetime (cold dark matter).

  Also the observed asymmetry between matter and antimatter in the universe can not be explained, since the CP-violating processes possible within the SM (through the CKM mechanism) which could have lead to this discrepancy during the early evolution of the universe are not sufficiently strong.

- **Fundamental parameters**
  The SM contains 25 parameters (masses, mixing angles (also in the lepton sector) and coupling constants) to which the speed of light c, Planck's constant h and the gravitational constant G_N, have to be added for a full description of elementary particles and their interactions. In order to reduce the number of free parameters, more fundamental theories are expected to predict relations between the different gauge couplings and fermion masses. Examples of still open questions in this respect are:

  – What determines the number of quark and lepton generations?

  – Why do electron and proton have the same absolute value of charge?

2.4 Supersymmetry (SUSY)

Symmetries play an essential role in the understanding of all physical processes. The fundamental power of this concept is demonstrated by *Noether's theorem*, according to which a conserved quantity can be deduced from each symmetry. (For instance, the invariance under a change in the phase of the wave-function[15] leads to charge conservation.) In the past, symmetry considerations have lead to the postulation of new particles which were subsequently discovered. The most

[14] The amount of dark matter can be interfered by comparing the visible matter distribution with calculations of rotational curves of galaxies.

[15] Also the fields have to be transformed accordingly.

prominent example of which is perhaps the extension of non-relativistic quantum electrodynamics by Lorentz invariance which lead to the discovery of antimatter[16].

In the realm of elementary particles two different types of symmetries exist. On the one hand internal symmetries, which relate different particles in particle spaces (like gauge symmetries, or *e.g.* the $SU(3)_C$ in QCD) and on the other hand the fundamental symmetries of spacetime itself which altogether form the *Poincaré* symmetry group[17]. According to the *Haag-Lopuszanski-Sohnius* (HLS) theorem [32], supersymmetry is the only possible extension of the Poincaré group (see discussion below).

The SUSY generator Q and its conjugate $Q^\dagger$ transform fermions f into bosons b and *vice versa*:

$$Q|f\rangle \propto |b\rangle \qquad\qquad Q^\dagger|b\rangle \propto |f\rangle \tag{2.23}$$

where the particle and its superpartner have the same quantum numbers except for the spin which differs by $\frac{1}{2}$. Since, in the SM, matter particles are described by fermions and forces by bosons, a symmetry between fermions and bosons leads to a unified description of matter and forces. In trying to apply these relations to particles within the SM one observes that no suitable particle pairs can be found[18]. Therefore, a new superpartner is postulated for each SM particle and the non-observation of these sparticles is explained with their higher masses, *i.e.* SUSY has to be a broken symmetry.

An argument which makes SUSY theoretically appealing is provided by the *non-renormalization theorem* [33], according to which the superpotential (see below) does not receive any renormalization to any order in perturbation theory. Furthermore, SUSY models offer a possible way to cure most of the shortcomings of the SM listed in Section 2.3:

- **Unification of forces**
  Supersymmetry enables the unification of the SM gauge couplings at high energies. The evolution of the coupling constants from an energy Q to an energy μ is described by the renormalization group equations (RGEs):

$$\frac{d\tilde{\alpha}_i^2}{dt} = b_i\tilde{\alpha}_i^2, \quad \tilde{\alpha}_i^2 = \frac{\alpha_i}{4\pi}, \quad t = ln(Q^2/\mu^2) \tag{2.24}$$

[16]Dirac postulated the positron in 1930, it was first observed in 1932 by Anderson.

[17]The Poincaré group consists of translations in space and time, Lorentz boosts and rotations in spacetime.

[18]The only candidates would be the Higgs and the neutrino, but this assumption does not lead to a satisfactory theory.

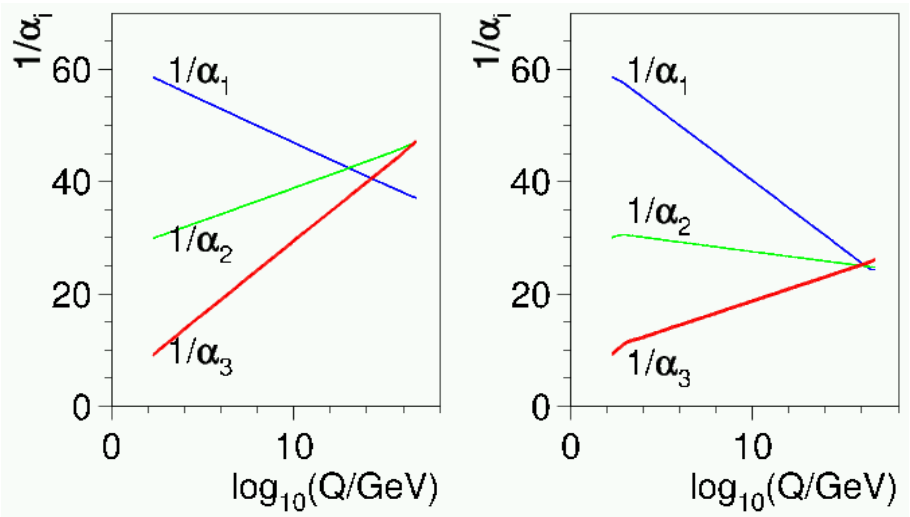

FIGURE 2.8: Running of the gauge couplings, before (left) and after (right) the introduction of supersymmetry, as describes by the RGEs.The change in slope at the energy scale Λ is caused by the contributions from SUSY particles.

where the slope b_i of the running lines is given by the masses of the particles which are accessible at this particular energy. By introducing the postulated SUSY particles near to the electroweak scale the slopes are changed just by the right amount to yield a unification of the couplings at energies of about 10^{16} GeV (for SUSY breaking scales of the order of 1 TeV). This unification depends only weakly on the sparticle spectrum.

Popular candidates to unite gravity with the other forces in a quantised way are *string theories*. Both bosonic and fermionic strings seem to be necessary for this purpose, so that SUSY is a naturally assumed ingredient of string theories[19].

- **Solution of the Hierarchy problem**
  In the presence of supersymmetry the above mentioned quadratically divergent contributions to the Higgs mass from particles and their superpartners cancel out (see Fig. 2.9) and thus ensure a stable Higgs mass. The crucial point is that bosons and fermions of the same supermultiplet couple with

[19]Indeed, it was within the framework of string theories were the idea of supersymmetry was born [34].

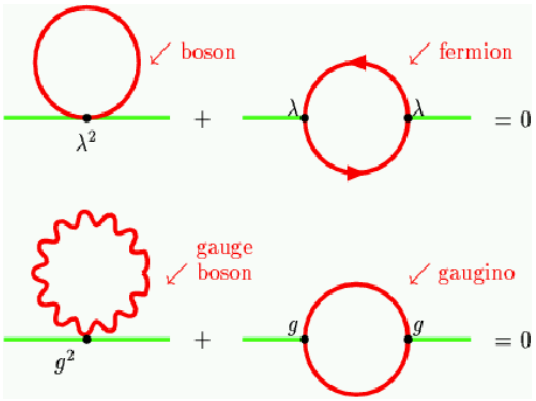

FIGURE 2.9: Cancellation of contributions from particles and there superpartners to the Higgs mass.

the same strength λ^2, but opposite sign. This cancellation mechanism works to all orders in perturbation theory[20] (a consequence of the nonrenormalization theorem[21]), which explains the stability and *naturalness* of the weak scale compared to M_{GUT} and M_{Pl}. However, the cancellation is only exact for unbroken supersymmetry. If supersymmetry is broken one can define a SUSY breaking scale Λ as:

$$\Lambda^2 := \Sigma_{bosons} m^2 - \Sigma_{fermions} m^2 \tag{2.25}$$

In which case the correction to the Higgs mass is simply given by:

$$\Delta m_H^2 \propto \lambda^2 \Lambda \tag{2.26}$$

The naturalness assumption normally made in this context is that the corrections to the Higgs mass should not be much bigger than the Higgs mass itself ($\Delta m_H^2 \lesssim m_H^2$). Thus, the current upper limit on the Higgs mass $m_H \leq 114.7\,\text{GeV}$ [35] translates into an upper limit for Λ. For $\lambda \approx 0.1$ one obtains $\Lambda \lesssim 1\,\text{TeV}$, *i.e.* the masses of the superpartners should not be much higher than about 1 TeV [36].

[20] A similar mechanism is known from QED where the radiative corrections to the photon mass are zero in any order of perturbation theory.

[21] This theorem can be proven with the help of *supergraphs* with super-Feynman rules in superspace (see below).

- **Candidates for dark matter and new sources of CP violation**
  The neutral[22] LSP of SUSY models represents an ideal candidate for dark matter. The most famous example is the neutralino in R_P-conserving[23] MSSM (or the mSUGRA model[24]). Another possibility is the gravitino in GMSB and gaugino mediated supersymmetry breaking models [37, 38] (see Section 2.4.4). Similar to the CKM mixing in the SM, flavour mixing can occur in the squark sector described by the super-CKM matrix, which introduces large possible sources of CP violation (the same holds for the lepton/slepton sectors).

2.4.1 Theoretical Framework

In addition to the tensor algebras of Eq. (2.7) which are known from classical mechanics, in relativistic Quantum Mechanics also *spinors* make their appearance. According to their statistical properties, tensors are bosons and spinors are fermions. Here, the theorem of Coleman and Mandula comes into play, who showed that: *"In a theory with non-trivial scattering in more than 1+1 dimensions, the only possible conserved quantities that transform as tensors under the Lorentz group are the generators of the Poincaré group and scalar quantum numbers."* [39] Thus, no further bosonic generators can be added to the Poincaré group (except as a trivial direct product, like for internal symmetries) and the only possible way to extend it is to combine both bosonic and fermionic generators in the same algebra[25] (this is the HLS theorem).

The basic structure of the supersymmetric algebra can be derived in a toy model from the basic properties of bosons and fermions as summarized in Eq. (2.27) and Eq. (2.28), respectively:

$$\begin{array}{l} b^+|n\rangle \sim |n+1\rangle \\ b^-|n\rangle \sim |n-1\rangle \end{array} \quad \Rightarrow \quad \begin{array}{c} [b^-, b^+] = 1 \\ [b^-, b^-] = [b^+, b^+] = 0 \end{array} \tag{2.27}$$

Where the number inside the *ket* vector gives the number of particles in the same quantum state. Contrary to bosons, fermions are subject to the Pauli exclusion

[22] The LSP is necessarily neutral in R_P-conserving models, since otherwise its relic density left over from the Big Bang would have already been discovered.

[23] see Sect. 2.4.5

[24] see Sect. 2.4.3

[25] Mathematicians call this type of algebra a *graded* Lie algebra.

principle:

$$\begin{array}{ll} f^+|0\rangle = |1\rangle & f^+|1\rangle = 0 \\ f^-|0\rangle = 0 & f^-|1\rangle = |0\rangle \end{array} \quad \Rightarrow \quad \begin{array}{c} \{f^-, f^+\} = 1 \\ \{f^-, f^-\} = \{f^+, f^+\} = 0 \end{array} \tag{2.28}$$

Thus, the algebraic properties are already fixed by the definitions on the left hand sides: Bosons fulfill commutator relations whereas fermions fulfill anticommutator relations. When taking into account that the total energy is proportional to the number of particles $H \sim b^+b^- + f^+f^-$, and that the SUSY operator which converts a boson into a fermion has to be $Q \sim f^+b^-$ (and $Q^\dagger \sim b^+f^-$) it is easy to compute that:

$$[H, Q] = 0 \tag{2.29}$$

$$\{Q, Q^\dagger\} = H \tag{2.30}$$

From Eq. (2.29) already two important properties of supersymmetric theories are visible:

1. The supercharge Q is a conserved quantity (as it commutes with the Hamiltonian).

2. The described system has an equal number of bosonic and fermionic states which are degenerate in energy[26].

This result can be generalized by adding also the other components of the energy-momentum operator:

$$\{Q, Q^\dagger\} = P_\mu \tag{2.31}$$

$$\{Q, Q\} = \{Q^\dagger, Q^\dagger\} = 0 \tag{2.32}$$

$$[P^\mu, Q] = [P^\mu, Q^\dagger] = 0 \tag{2.33}$$

This is the famous $N = 1$ SUSY algebra (N gives the number of different SUSY operators Q). N is constrained by the maximal spins described within the considered theory by $N \leq 4S$. Extended SUSY models, with $N \geq 2$, possess additional types of supermultiplets which are difficult to reconcile with the known particles of the SM. Hence, only models with $N = 1$ are typically considered in models of experimental relevance.

[26] Equation (2.30) has more profound implications as discussed below.

Another theoretically appealing aspect of supersymmetry which is obvious from Eq. (2.31) is the close connection of SUSY and the structure of spacetime: Since the P_μ are defined in spacetime, supersymmetry must necessarily be a spacetime symmetry. Furthermore, making SUSY local (Q depending on x) entails local spacetime translations ($P_\mu(x)$). This means, a theory where SUSY is local must incorporate gravity (since the postulate of invariance under local coordinate transformations is the starting point of Einsteins theory of general relativity). Such theories are therefore called supergravity (SUGRA).

Computations in $N = 1$ supersymmetry can be conveniently performed in *superspace*, which is the space where equations are manifestly covariant under SUSY transformations (playing a similar role as Minkovski space for Lorentz transformations). In order to achieve this, two anti-commuting *Grassman* coordinates θ and $\bar{\theta}$ are added to the ordinary space-time coordinates, which fulfill:

$$\{\theta_i, \theta_j\} = 0 \qquad \Leftrightarrow \qquad \theta_i\theta_j = -\theta_j\theta_i \quad \text{and} \quad \theta_i^2 = 0 \tag{2.34}$$

This obviously has some advantages, since all Taylor expansions in θ and $\bar{\theta}$ are finite[27]. The fields defined on superspace are called *superfields*. Expansion in the new coordinates shows that they have the general form:

$$\Phi(x, \theta, \bar{\theta}) = \phi(x) + \theta\psi(x) + \bar{\theta}\psi(x) + \theta\bar{\theta}F(x) \tag{2.35}$$

Where the auxiliary field F has no physical meaning since it transforms as a total derivative under SUSY transfromations[28] (thus giving zero contribution to the action). The fields ϕ and ψ are the bosonic and fermionic component fields of Φ:

$$[\Phi, \Phi] = 0 \qquad \Rightarrow \qquad [\phi, \phi] = 0 \quad \text{and} \quad \{\psi, \psi\} = 0 \tag{2.36}$$

Hence, bosonic and fermionic field are incorporated in a symmetric way.

2.4.2 Minimal Supersymmetric Standard Model (MSSM)

As the name suggests the MSSM is the model with the minimal number of SUSY particles which can be added to the SM in order to give a supersymmetric and

[27] Anti-commuting numbers provide a useful mathematical tool for many problems, similar as complex numbers.

[28] In superspace SUSY transformations are induced by $Q = \frac{\partial}{\partial\theta} - i\sigma^\mu\bar{\theta}\partial_\mu$.

gauge invariant theory. The MSSM Lagrangian in component fields has the form[29]:

$$\begin{aligned}\mathcal{L}_{SUSY} &= -D^\mu\phi^* D_\mu\phi - i\bar{\psi}\bar{\sigma}^\mu D_\mu\psi - \frac{1}{4}F^a_{\mu\nu}F^{a\mu\nu} - \lambda^{a\dagger}\bar{\sigma}^\mu D_\mu\lambda^a \\ &\quad -\frac{1}{2}W^i W_i^* + \frac{1}{2}g_a^2(\phi^* T^a\phi)^2 - \frac{1}{2}(W^{ij}\psi_i\psi_j + W^{ij*}\psi^{i\dagger}\psi^{j\dagger})\end{aligned} \tag{2.37}$$

where the first two terms describe the kinetics of the scalar fields ϕ and the fermion fields ψ, with D_μ being the covariant derivative for these fields. The next two terms describe the interactions of the gauge and gaugino fields. Here F is the field-strength tensor for strong and electroweak interactions. The interactions between gauge bosons and gauginos λ^a are included in the covariant derivative. The next line consists of the potential terms for the scalars and the fermions including all interactions and mass terms. In addition R_P-violating interactions (see Section 2.4.5) and soft SUSY breaking terms can be added (see below).

All particles connected by Q are placed together in one *supermultiplet*. These are the irreducible representations of the SUSY algebra of Eq. (2.31)[30]. Different types of supermultiplets can be distinguished by imposing special conditions on the general superfield of Eq. (2.35). The three types that hold the particles of the MSSM (and the only ones that exist for $N = 1$) are listed in Table 2.3. The supermultiplets differ in the value of helicity which is 1/2 in the chiral case (with spin 0 and 1/2) and 1 in the vectorial (spin 1/2 and 1) case. If gravity is to be included, an additional supermultiplet with spins 2 and 3/2 for the graviton and the gravitino is needed. All particles within one supermultiplet have the same charge, weak isospin and color which follows from the fact that Q commutes with the generators of the corresponding gauge transformations.

The SM fermions (f_L and f_R), together with their bosonic SUSY partners ($\tilde{f}_L$ and $\tilde{f}_R$) form chiral supermultiplets[31] as listed in Table 2.4. In general $\tilde{f}_L$ and $\tilde{f}_R$ are not mass-eigenstates, but they mix with a strength proportional to m_f. The mass-eigenstates of the third generation squarks and sleptons, where the mixing is

[29]The sigma matrices are defined as $\sigma^\mu = (I, \sigma^p)$, $\bar{\sigma}^\mu = (I, -\sigma^p)$, where σ^p $(p = 1, 2, 3)$ are the Pauli spin matrices.

[30]SUSY partners of known particles are denoted by placing a tilde over the corresponding particle. Their names are constructed by either putting an "s" in front of the particle name, in the case of fermionic particles, or appending "-ino" for bosons.

[31]It would also be possible to place them into vectorial supermultiplets, but require the postulation of new vector fields (*i.e.* gauge groups).

TABLE 2.3: Supermultiplets of the MSSM. ϕ is a complex scalar field, ψ and λ are fermion fields and A^μ is a vector field. D is the covariant derivative in superspace.

Supermultiplet	Symbol	Spin	Particles
Chiral ($D\Phi = 0$)	$\Phi = \begin{pmatrix} \psi \\ \phi \end{pmatrix}$	$1/2$ 0	$\begin{pmatrix} \text{fermion} \\ \text{sfermion} \end{pmatrix}, \begin{pmatrix} \text{higgsino} \\ \text{higgs} \end{pmatrix}$
Vector ($V = V^\dagger$)	$V = \begin{pmatrix} A^\mu \\ \lambda \end{pmatrix}$	1 $1/2$	$\begin{pmatrix} \text{gauge boson} \\ \text{gaugino} \end{pmatrix}$
Gravity	$\Psi = \begin{pmatrix} e \\ G \end{pmatrix}$	2 $3/2$	$\begin{pmatrix} \text{graviton} \\ \text{gravitino} \end{pmatrix}$

large, are denoted by $\tilde{f}_1$ and $\tilde{f}_2$[32] for the lighter and heavier state, respectively[33]. Finally, one should notice, that the "L" and "R" subscripts of sfermions do not refer to their own helicity (they are scalars) but to the one of their SM partners.

TABLE 2.4: Chiral supermultiplets of the MSSM. The first five supermultiplets exist in three versions corresponding to the three generations. The Higgs fields are labeled with a subscript indicating whether they couple to u-type or d-type quarks.

Chiral supermultiplet Φ	Spinor ψ (spin 1/2)	Scalar ϕ (spin 0)
Q	(u_L, d_L)	$(\tilde{u}_L, \tilde{d}_L)$
$\bar{U}$	$u_R^\dagger$	$\tilde{u}_R^*$
$\bar{D}$	$d_R^\dagger$	$\tilde{d}_R^*$
L	(ν_L, e_L)	$(\tilde{\nu}_L, \tilde{e}_L)$
$\bar{E}$	$e_R^\dagger$	$\tilde{e}_R^*$
H_u	$(\tilde{H}_u^+, \tilde{H}_u^0)$	(H_u^+, H_u^0)
H_d	$(\tilde{H}_d^0, \tilde{H}_d^-)$	(H_d^0, H_d^-)

In supersymmetric theories at least two Higgs doublets (placed in two chiral supermultiplets) are required which can be understood phenomenologically from the fact that after spontaneous electroweak symmetry breaking (EWSB) both $W^\pm$

[32] $m^2_{\tilde{l}_{1,2}} = \frac{1}{2}\left(m^2_{\tilde{l}_L} + m^2_{\tilde{l}_R} \mp \sqrt{(m^2_{\tilde{l}_L} - m^2_{\tilde{l}_R})^2 + 4a_l^2 m_l^2}\right)$, where the a_l is positivly correlated with $tan\beta$

[33] Also intergenerational mixing is possible, leading to FCNCs.

bosons must have a SUSY partner[34]. The primary set of superpartners of neutral SM bosons ($\tilde{W}^0$, $\tilde{B}$, $\tilde{H}_u^0$, $\tilde{H}_d^0$) is rotated by EWSB into ($\tilde{\gamma}$, $\tilde{Z}^0$, $\tilde{H}$, $\tilde{H}'$) according to:

$$\tilde{\gamma} = \sin\theta_W \tilde{W}^0 + \cos\theta_W \tilde{B} \quad (2.38)$$

$$\tilde{Z} = \cos\theta_W \tilde{W}^0 - \sin\theta_W \tilde{B} \quad (2.39)$$

$$\tilde{H} = \sin\beta \tilde{H}_u^0 - \cos\beta \tilde{H}_d^0 \quad (2.40)$$

$$\tilde{H'} = \cos\beta \tilde{H}_u^0 + \sin\beta \tilde{H}_d^0 \quad (2.41)$$

The properties of the Higgs sector are determined by the Higgs potential, which is made up of quadratic mass terms and quartic interaction terms where the only free parameters are $\tan\beta$ and m_A.

The vectorial supermultiplets hold the SM gauge bosons and their superpartners as listed in Table 2.5. The fields are given at high energies, the winos and

TABLE 2.5: Vectorial supermultiplets of the MSSM before electroweak symmetry breaking.

Vectorial supermultiplet V	Vector A^μ (spin 1)	Spinor λ (spin 1/2)
V	B^0	$\tilde{B}^0$
V^i, $i = 1, 2, 3$	$W^\pm, W^0$	$\tilde{W}^\pm$, $\tilde{W}^0$
V^a, $a = 1..8$	g^a	$\tilde{g}^a$

binos correspond to unbroken $SU(2) \times U(1)$. At low energies both SM particles and sparticles acquire mass through the supersymmetric version of the Higgs mechanism. The Goldstone boson produced by the symmetry breaking mechanism (called goldstino) is identified with the longitudinal component of the gravitino.

In the unconstrained version the free parameters of R_P-conserving MSSM are:

- the three gaugino masses M_1, M_2 and M_3;
- the Higgs mixing mass parameter μ;
- the ratio of the vacuum expectation values of the two neutral Higgs fields, $\tan\beta$;
- the squark and slepton masses and their mixing angles and
- the pseudo-scalar Higgs mass m_A.

[34] A theoretical argument is that theories with only one Higgs doublet are not renormalizable.

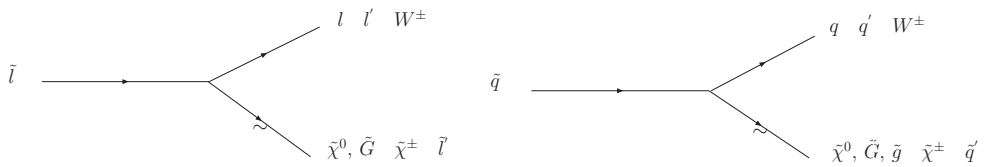

FIGURE 2.10: Basic SUSY vertices of the MSSM. Shown are the possible interactions for sfermions. $\tilde{l}$ represents any slepton of all three families. Similarly, $\tilde{q}$ stands for any squark.

Similar as it was done for the SM fermions and bosons (in Fig. 2.1 and Fig. 2.2) also the interactions of their MSSM superpartners can be summarized in a generic way, as shown in Figure 2.10 and Figure 2.11[35] (these vertices will be used in Chapter 3). Also here interactions of the Higgs sector have been omitted.

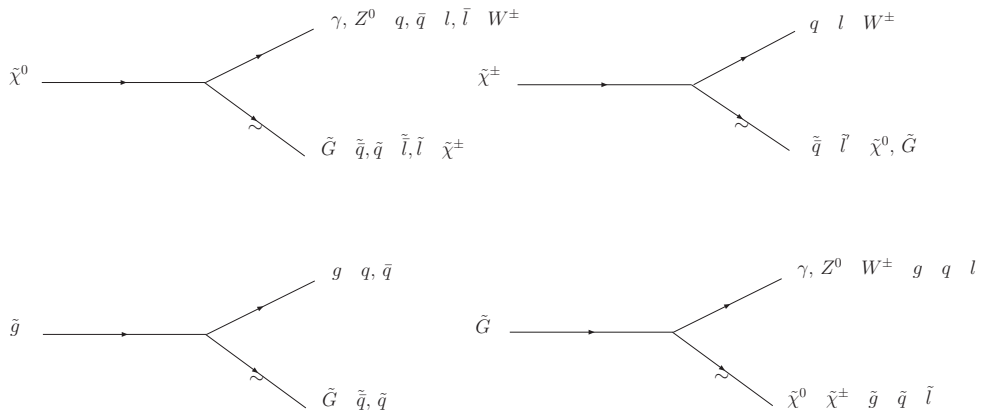

FIGURE 2.11: Basic SUSY vertices of the MSSM. Shown are the possible diagrams starting with a gaugino or gravitino. $\tilde{l}$ represents any lepton of all three families. Similarly, $\tilde{q}$ stands for any quark.

The mass eigenstates of the gaugino sector are the four neutralinos ($\tilde{\chi}^0_{1,2,3,4}$, ordered by their masses, $\tilde{\chi}^0_1$ being the lightest) and four charginos ($\tilde{\chi}^{\pm}_{1,2}$, similarly ordered) which are mixings of the gauginos with the same quantum numbers[36] (neutral Higgsinos + zino + photino → neutralinos ; charged higgsinos + winos →

[35] If no subscript is given $\tilde{\chi}^0$ denotes any of the $\tilde{\chi}^0_{1234}$ and the same notation is used for $\tilde{\chi}^{\pm}$.

[36] The in general possible mixing of sfermions with the same quantum numbers are strongly restricted by constraints on FCNCs and CP violation.

charginos). The neutralino mass-mixing matrix depends on M_1, M_2, μ and $\tan\beta$:

$$\begin{pmatrix} \tilde{\chi}_1^0 \\ \tilde{\chi}_2^0 \\ \tilde{\chi}_3^0 \\ \tilde{\chi}_4^0 \end{pmatrix} = \begin{pmatrix} M_1\cos\theta_W & -M_1\sin\theta_W & m_Z\sin\theta_W & 0 \\ M_2\sin\theta_W & M_2\cos\theta_W & -m_Z\cos\theta_W & 0 \\ 0 & m_Z\cos\beta & -\mu\sin\beta & -\mu\cos\beta \\ 0 & -m_Z\sin\beta & \mu\cos\beta & -\mu\sin\beta \end{pmatrix} \begin{pmatrix} \tilde{\gamma} \\ \tilde{Z}^0 \\ \tilde{H} \\ \tilde{H}' \end{pmatrix} \tag{2.42}$$

One observes that the photino is only contained in the two lightest neutralinos. If $M_1, M_2 \gg m_Z$ the same becomes true for the zino. For $|\mu| \gg m_Z$ the two heavier neutralinos become purely higgsino-like[37]. The chargino mass-mixing is independent of M_1:

$$\begin{pmatrix} \tilde{\chi}_1^\pm \\ \tilde{\chi}_2^\pm \end{pmatrix} = \begin{pmatrix} M_2 & \sqrt{2}\sin\beta\, m_W \\ \sqrt{2}\cos\beta\, m_W & \mu \end{pmatrix} \begin{pmatrix} \tilde{W}^\pm \\ \tilde{H}^\pm \end{pmatrix} \tag{2.43}$$

For large M_2 the lightest chargino becomes wino dominated, while the higgsino component of the heavier chargino increases with $|\mu|$. The particles of the MSSM are summarized in Table 2.6.

TABLE 2.6: Particle content of the MSSM (after electroweak symmetry breaking). The sparticles are named: squarks, sleptons, neutralinos and charginos, gluinos and gravitino.

SM particles	Spin	Superpartners	Spin
q_L, q_R	1/2	$\tilde{q}_L$,$\tilde{q}_R$	0
l_L , l_R	1/2	$\tilde{l}_L$,$\tilde{l}_R$	0
γ, Z^0, $W^\pm$	1	$\tilde{\chi}_i^0$ (i=1..4), $\tilde{\chi}_j^\pm$ (j=1,2)	1/2
h^0, H^0, A^0, $H^\pm$	0		
g	1	$\tilde{g}$	1/2
G	2	$\tilde{G}$	3/2

It should be stressed here that in the MSSM no new interactions are introduced, but the sparticles interact via the known gauge interactions of the SM with the same couplings g, g' and g_s, *i.e.* gauginos and sfermions couple to the same particles as their SM superpartners. As a consequence their production cross sections at high energies are comparable to the cross section of SM particles. However, despite all

[37] Since $\tilde{B}^0 = \cos\theta_W\,\tilde{\gamma} - \sin\theta_W\,\tilde{Z}^0$ the lightest neutralino becomes a pure bino for $M_1, M_2, |\mu| \gg m_Z$.

its nice features the general MSSM also has some problems. In the MSSM, SUSY breaking is produced by introducing all possible *soft SUSY breaking* terms[38]. This leads to 106 new free parameters (plus 25 from the SM gives 131 for the MSSM) and spoils the original predictivety of the SUSY model. Furthermore, at a generic parameter point the most general MSSM is not consistent with phenomenological observations, mainly because:

- the separate lepton numbers L_e, L_μ and L_τ are not conserved;
- large sources of CP-violation are introduced;
- FCNC's are allowed.

The number of free parameters can be reduced considerably by the assumption that, at some high-energy scale, all gaugino and sfermion masses acquire the same values (*e.g.* $m_{1/2}$ and m_0 in mSUGRA models (see below)). The low-energy MSSM parameters are then determined by the renormalization group equations. Instead of introducing the SUSY breaking terms "by hand" more recent SUSY models describe the details of the SUSY breaking mechanism (*i.e.* the origin of these terms). In this way phenomenologically predictive models with only a few free parameters can be constructed which are commonly called *constrained* MSSMs (cMSSM).

2.4.3 Broken Supersymmetry

If SUSY was unbroken superpartners would be degenerate in mass, which is in disagreement with observation. Indeed, it is the description of the breaking mechanism which specifies the sparticle mass spectrum. The simplest symmetry breaking mechanism is spontaneous symmetry breaking (*i.e.* the ground state is not invariant under the symmetry of the system $Q|0\rangle \neq 0$) the way it is used in electroweak theory to give mass to the $W^\pm$ and Z^0 bosons. Unfortunately, this possibility is already excluded by experiment as a result of the *supertrace theorem* [40], which is a sum rule imposing constraints on combined sums of particle and sparticle masses. The most stringent example is the requirement $m_{\tilde{d}}^2 + m_{\tilde{s}}^2 + m_{\tilde{b}}^2 < (7\,\mathrm{GeV})^2$ which is obviously contradictory to experimental evidence.

A way to circumvent this problem are so called *hidden sector models*, in which, in addition to the "visible" sector of the SM particles and their SUSY partners a

[38] These terms are called "soft" since they are required to be gauge invariant and not to reintroduce the hierarchy problem (through quadratically divergent terms).

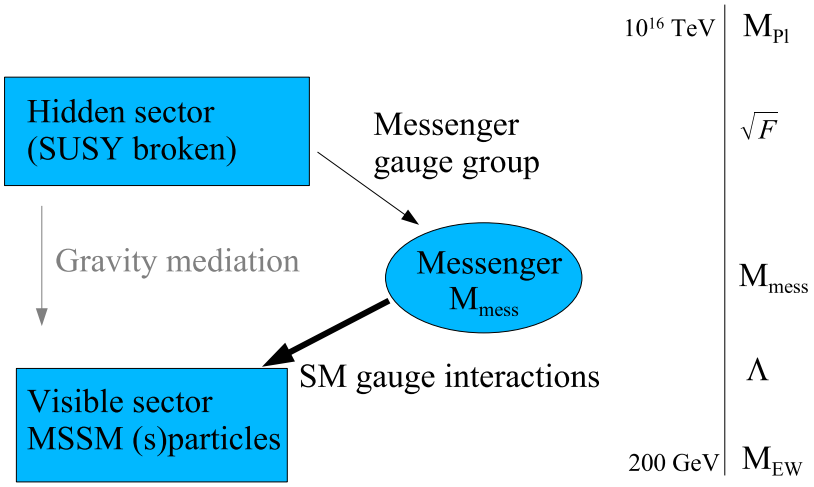

FIGURE 2.12: Schematic illustration of hidden sector models with the corresponding energy scales of the GMSB model (see next section).

"hidden" sector is introduced, which consists of particles that do not couple directly to sparticles in the visible sector nor take part in the SM gauge interactions (see Figure 2.12). SUSY breaking first occurs spontaneously in the hidden sector, at an energy scale $\sqrt{F}$, and is then communicated to the visible sector. In this way the soft SUSY breaking terms are produced indirectly by the interactions between the different sectors[39]. The natural candidate for such an interaction is gravity, since the particles of both sectors participate in this interaction anyway[40] (so called supergravity models, SUGRA). These interactions are, however, suppressed by an inverse power of the Planck mass, so that $\sqrt{F}$ needs to be of the order of M_{Pl} if the soft SUSY breaking terms are to become strong enough to provide sparticle masses above $\sim 200\,\text{GeV}$. As a result, FCNC's are introduced via RGE evolution of the soft terms (which are flavor mixing) from the Planck scale down to the electroweak scale[41]. In the minimal version of these models (mSUGRA) the

[39]Details of the hidden sector are of phenomenological interest only where large scales are involved, as in models of the evolution of the early universe.

[40]The interaction terms appear automatically when requiring the Lagrangian to be locally supersymmetric.

[41]Experimental limits on FCNCs are tight, *e.g.* $\Gamma(K^+ \to \pi^+\nu\bar{\nu})/\Gamma(K^+ \to all) = 1.6^{+1.8}_{-0.8} \times 10^{-10}$ [41] in agreement with the SM expectation from W^+W^- exchange $(0.4\,\text{to}\,1.2) \times 10^{-10}$.

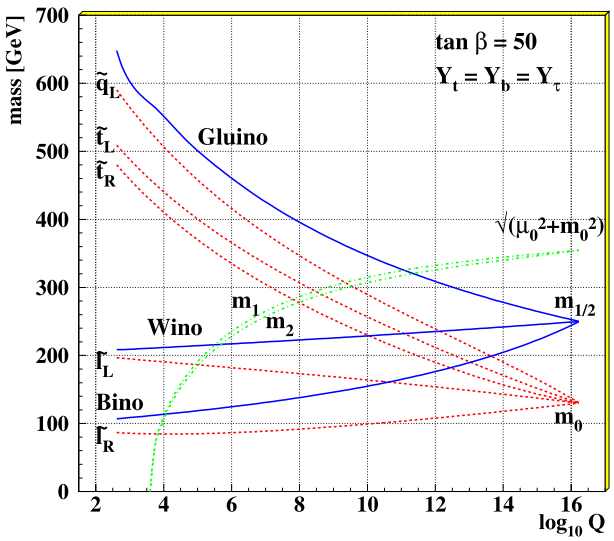

FIGURE 2.13: Evolution of sparticle masses and radiative production of electroweak symmetry breaking driven by the RGEs.

gravitino is very heavy ($O(1\,\text{TeV})$). An interesting feature of the mSUGRA model is that the breaking of electroweak symmetry can be *explained* through the running of the Higgs mass parameter μ, which is driven negative by the RGEs (Eq. (2.24)), and does not have to be imposed spontaneously. The situation is illustrated in Figure 2.13. Two other often considered models for SUSY breaking are *anomaly-mediated* SUSY breaking (AMSB) and *gaugino-mediated* SUSY breaking which both postulate the existence of higher dimensions. The roles of the hidden and visible sectors are then taken by two different branes (lower-dimensional manifolds existing in a higher dimensional spacetime) which communicate through the bulk (the higher dimensional space between the branes) by some messenger fields.

2.4.4 Gauge Mediated Supersymmetry Breaking (GMSB)

The GMSB model [42] is a hidden sector model with the additional introduction of a *messenger sector*[42] (see Fig. 2.12) consisting of particles (messengers) interacting with the visible sector *via* the SM gauge interactions (this is the easiest possible assumption) and at the same time with the hidden sector via some new interactions

[42] The introduction of these extra particles will of course change the values of the gauge couplings at the GUT scale. However, their unification remains unaffected.

TABLE 2.7: Free parameters of the GMSB model.

Symbol	Meaning
$\sqrt{F}$	The scale at which supersymmetry is broken in the hidden sector.
M	Sets the mass scale of the messenger particles: $m_{mess} = M\sqrt{1 \pm \Lambda/M}$.
Λ	The mass scale at which SUSY breaking is communicated to the visible sector.
N	Number of SU(5)[43]multiplets that make up the messenger sector.
$tan(\beta)$	Ratio of vacuum expectation values of the two Higgs doublets.
$sign(\mu)$	$\mu/\|\mu\|$, where μ is the higgsino mass parameter.

(produced by the messenger gauge group), for which the particles from the visible sector are neutral. Consequently the model has three characteristic mass scales. They fulfill the condition:

$$\Lambda < M < F \tag{2.44}$$

All parameters of the model are listed in Table 2.7. The phenomenologically most important of these parameters is Λ since it determines all low energy scalar and gaugino masses through loop-effects. For sparticle masses of order 1 TeV it must be ~ 100 TeV.

Although direct gravitational interactions between the hidden and the visible sector are still present, they become negligible compared to the gauge interactions with the messenger particles for $\sqrt{F} \ll M_{Pl}$. Since gauge interactions are much stronger than gravity, M is relatively low and the amount of RGE running of the soft SUSY breaking terms is much smaller than in the mSUGRA model. This effectively solves the problem of FCNC's which is persistent in the MSSM and mSUGRA models.

From dimensional analysis it follows that for the soft SUSY breaking terms:

$$m_{soft} \sim \frac{F}{M} \tag{2.45}$$

Therefore, low values of M require also a low lying SUSY breaking scale $\sqrt{F}$,

[43]Although SU(5) can not serve as a GUT theory since it does not allow to incorporate right handed neutrinos, it is the smallest group which contains the total gauge sector of the SM.

which determines the mass of the gravitino, through:

$$m_{\tilde{G}} = \frac{F}{\sqrt{3}M_{Pl}} \simeq 2.5 \times \left(\frac{\sqrt{F}}{100\,\mathrm{TeV}}\right)^2 \mathrm{eV} \tag{2.46}$$

Solving the SUSY flavor problem therefore requires a light gravitino. Since the gravitino emerges from the Super-Higgs mechanism, in contrast to its superpartner, the graviton, it takes also part in non-gravitational interactions and couples, for instance, to the photon, so that decay rates to it are high. Following Equation (2.46) the gravitino mass lies in the range of $4 \times 10^{-5}\,\mathrm{eV} < m_{\tilde{G}} < 1\,\mathrm{MeV}$ for $0.233 < \sqrt{F} < 63 \times 10^3\,\mathrm{TeV}$. Indeed, in the not jet excluded region of GMSB parameter space, the gravitino $\tilde{G}$ is always the LSP. Consequently, the next-to-lightest sparticle (NLSP) plays a crucial role in the phenomenology of sparticle production and decay. It decays into its SM superpartner and a gravitino. In the GMSB parameter region where $m_{\tilde{G}} \sim$ keV the gravitino can be a candidate for dark matter, even in R_P-violating scenarios[44] [43, 44].

Requiring the contribution of gravity mediated effects to be less than 0.1% leads to an upper bound of $M < \sqrt{n} \times 10^{14}\,\mathrm{GeV}$ [45]. This bound can be further lowered when taking into account the lower mass limit for the lightest chargino (of 103 GeV [46, 47]) to $M \lesssim O(10^8)\,\mathrm{GeV}$ and

$$1 < M/\Lambda < O(10^4)\,. \tag{2.47}$$

The *minimal* GMSB model, which shall be studied here, is based on the simplest potentially realistic assumption for the messenger sector (to be a representation of SU(5)). In this case, the rather low limit of the messenger scale restricts the maximal number of messenger fields to:

$$N \leq 5 \tag{2.48}$$

Similar to the mSUGRA model, electroweak symmetry is assumed to be broken radiatively (see Sect. 2.4.3) in the GMSB model, which leaves two free parameters for the Higgs sector: $\tan\beta$ and the sign(μ). Values of $\tan\beta > 50$ are theoretically forbidden. Due to the RGEs the squared sfermion masses depend only logarithmically on M/Λ.

[44] It has to be distinguished whether R_P is violated in the baryon sector ($\not{B}$) or in the lepton sector ($\not{L}$). In the first case the gravitino is stable as long as it is lighter than the lightest quark. In the second case the given masses result in a lifetime $\tau_{\tilde{G}} > t_{\mathrm{Universe}}$

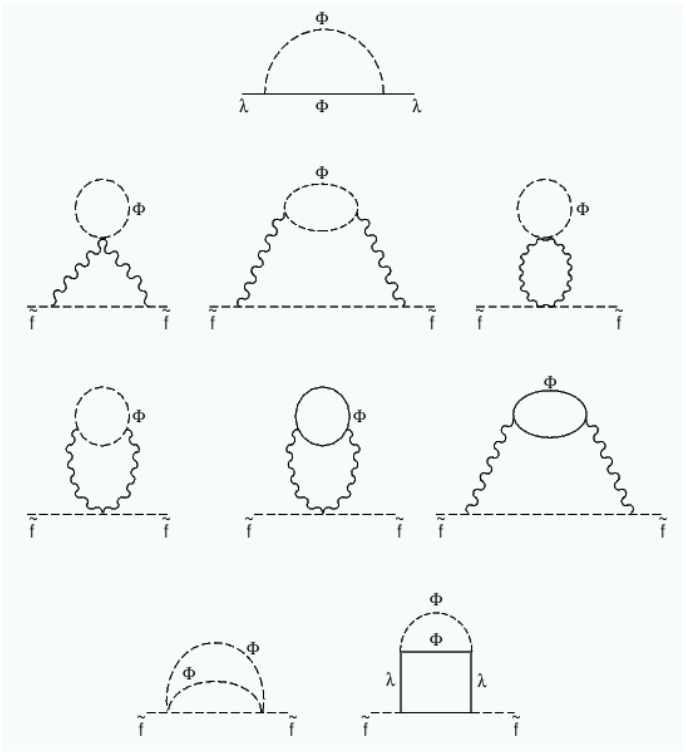

FIGURE 2.14: Feynman diagrams for the generation of gaugino (λ) and sfermion ($\tilde{f}$) masses in GMSB. The scalar and fermionic components of the messenger fields (Φ) are denoted by dashed and solid lines, respectively. SM gauge bosons are depicted as wavy lines.

The transmission of SUSY breaking to the particles of the MSSM *via* virtual exchange of messenger particles is shown in Figure 2.14 for both gauginos and sfermions. The gaugino masses resulting from one-loop diagrams are given by:

$$m_i \propto \frac{N}{4\pi}\alpha_i(M)\Lambda \tag{2.49}$$

where α_i are the coupling constants of the gauge group i at the GUT scale. From the two-loop diagrams follow the masses of the scalars, which do not receive corrections at one-loop order:

$$m^2_{scalar} \propto 2N\Lambda^2 \left[k_3 \left(\frac{\alpha_3(M)}{4\pi}\right)^2 + k_2 \left(\frac{\alpha_2(M)}{4\pi}\right)^2 + \frac{3}{5}\left(\frac{Y}{2}\right)^2 \left(\frac{\alpha_1(M)}{4\pi}\right)^2 \right] \tag{2.50}$$

where k_3 is zero for color singlets and k_2 is zero for weak singlets. Therefore,

TABLE 2.8: Overview of GMSB scenarios. Only R_P-conserving decays are considered.

Scenario	Typical Parameters	Decay
$\tilde{\chi}_1^0$ NLSP	small N, large M, small $tan\,\beta$	$\gamma\tilde{G}$
$\tilde{\tau}_1^\pm$ NLSP	large N, small M, large $tan\,\beta$	$\tau^\pm\tilde{G}$
$\tilde{e}_R^\pm$, $\tilde{\mu}_R^\pm$, $\tilde{\tau}_1^\pm$ co-NLSP	medium N, medium M, small $tan\,\beta$	$e^\pm\tilde{G}$, $\mu^\pm\tilde{G}$, $\tau^\pm\tilde{G}$
$\tilde{\chi}_1^0$, $\tilde{\tau}_1^\pm$ co-NLSP	medium N, medium M, large $tan\,\beta$	$\gamma\tilde{G}$, $\tau^\pm\tilde{G}$

squarks are heavier than sleptons. The masses at the EW scale have an additional factor $\ln(M)$ resulting from the RGEs (see Eq. (2.24)). Since the supersymmetry breaking mechanism is supposed to be flavor blind, all sparticles from different generations with the same quantum numbers are degenerate in mass at the GUT scale.

Depending on the nature of the NLSP three versions of GMSB models can be distinguished, as listed in Table 2.8. In the easiest scenario, of $N = 1$, the neutralino is the NLSP in most of the parameter space. However, if the sfermion mixing becomes strong, *i.e.* for high values of tan β (see footnote on page 25), due to the high tau mass the lightest stau becomes the NLSP (see also Fig. 4.15). This scenario becomes dominant for higher values of N, since the comparison of Equations (2.49) and (2.50) shows that

$$m_{\tilde{\chi}_1^0}/m_{\tilde{\tau}_1} \sim \sqrt{N} \tag{2.51}$$

A special case is the *slepton co-NLSP* scenario where $\tilde{\tau}_1$, $\tilde{e}_R$ and $\tilde{\mu}_R$ are almost mass degenerate and all decay directly into the LSP. Finally, also a neutralino-slepton co-NLSP scenario is possible.

The mean decay length is given by $L = \gamma\beta c\tau$. For the neutralino NLSP in GMSB scenarios one has:

$$c\tau_{\tilde{\chi}_1^0} \simeq \frac{1}{100}\left(\frac{\sqrt{F}}{100\,\mathrm{TeV}}\right)^4\left(\frac{m_{\tilde{\chi}_1^0}}{100\,\mathrm{GeV}}\right)^{-5} \tag{2.52}$$

According to this, one has to distinguish for collider experiments whether the NLSP decays inside or outside the detector (see Table 2.9). If also R_P-violating decay channels are present, the lifetime will be reduced. Therefore, for the parameter region investigated in this thesis always the first case applies.

The requirement of EW symmetry breaking can be achieved in the GMSB model only for large values of $|\mu|$. As a consequence, the lightest neutralino (and

TABLE 2.9: NLSP decay scenarios in GMSB. For the NLSP decaying inside the detector it would be further possible to distinguish events coming from the nominal vertex, events with a displaced vertex and events with a kinked track (for slepton NLSP).

NLSP	Characteristic	Signature
$\tilde{\chi}_1^0$	$\tilde{\chi}_1^0$ quasi stable	Missing energy
$\tilde{\chi}_1^0$	$\tilde{\chi}_1^0$ decays inside detector	Isolated photon + Missing energy
$\tilde{l}^{\pm}$	$\tilde{l}^{\pm}$ quasi stable	Unknown charged particle
$\tilde{l}^{\pm}$	$\tilde{l}^{\pm}$ decays inside detector	Isolated leptons + Missing energy

chargino) is mostly photinolike (see also Fig. 4.14), while the heavier versions have to be mainly higgsinos. Furthermore, the large $|\mu|$ enhances the $\tilde{\tau}_L - \tilde{\tau}_R$ mixing which is the reason why the lightest stau, $\tilde{\tau}_1$, is often the NLSP (for high tan β).

2.4.5 R-Parity

Once supersymmetry is introduced the possibilities of constructing Lagrangians are largely reduced. This theoretical unambiguousness[45] is an important reason for the popularity of supersymmetric theories. In the MSSM the only freedom lies in the choice of a superpotential W which can contain only bilinear or trilinear combinations of scalar and chiral supermultiplets in order to be renormalizable. This is where R-parity (R_P) comes into play, which is a multiplicative discrete symmetry defined as[46]:

$$R_P = (-1)^{3B+L+2S} \tag{2.53}$$

where S is the spin of the particle. As a result SM particles have $R_P = 1$ while sparticles have $R_P = -1$. R_P-conserving (RPC) vertices contain an even number of sparticle lines, *i.e.* sparticles always appear or disappear in pairs in all production or decay processes. Consequently, the lightest supersymmetric particle (LSP) is stable and therefore a natural candidate for dark matter.

In its most general form the superpotential contains the following R_P-

[45] In fact, the unbroken MSSM has one free parameter less than the SM.

[46] Another definition which is often found in the literature is $R_P = (-1)^{3(B-L)+2S}$. It is obviously identical to the one given in the text since it differs only by a factor $(-1)^{4L} = 1$.

violating[47] (RPV) terms [48, 49]

$$W_{\not R_P} = \lambda_{ijk} L_i L_j \bar{E}_k + \lambda^{'}_{ijk} L_i Q_j \bar{D}_k + \lambda^{''}_{ijk} \bar{U}_i \bar{D}_j \bar{D}_k + \mu_{nm} L_n H_m + h.c. \qquad (2.54)$$

where the λ's and μ's are Yukawa couplings and the superfields contain both the particle fields and their superpartner fields. The ijk denote family indices. The λ_{ijk} are antisymmetric under the exchange of i and j, and the $\lambda^{''}_{ijk}$ are antisymmetric under $i \leftrightarrow k$, so that in total 90 new free parameters are introduced in this way. The term $\mu_{nm} L_n H_m$ is the R_P-violating generalization of the R_P-conserving Higgsino mass parameter μ. The abstract superspace notation of Equation (2.54) can be expanded into component fields. For instance, the $\lambda^{'}$ terms read:

$$\begin{aligned} W_{\lambda'} \;=\; & \lambda^{'}_{ijk} (\tilde{\nu}_i d_{jL} \bar{d}_{kR} + \nu_i \tilde{d}_{jL} \bar{d}_{kR} + \bar{\nu}_i d_{jL} \tilde{d}^{*}_{kR} \\ & - \tilde{e}_{iL} u_{jL} \bar{d}_{kR} - e_{iL} \tilde{u}_{jL} \bar{d}_{kR} - \bar{e}_{iL} u_{jL} \tilde{d}^{*}_{kR}) + h.c. \end{aligned} \qquad (2.55)$$

Non-zero values of λ, $\lambda^{'}$ and μ violate total lepton number conservation and $\lambda^{''}$ violates the conservation of total baryon number. These types of violations are expected in theories at the GUT scale since L and B conservation can not be deduced from a gauge symmetry and they appear only accidentally in the SM. The simultaneous existence of $\lambda^{'}_{11k}$ and $\lambda^{''}_{11k}$ would lead to prompt proton decay $p \rightarrow e^{+}\pi^{0}$ *via* $u\,d \rightarrow \bar{\tilde{d}}_{R,k} \rightarrow \bar{u}\,e^{+}$. However, the stability of the proton is not an argument against RPV models since its decay requires both lepton and baryon number non-conservation at the same time (via (λ or $\lambda^{'}$) and $\lambda^{''}$, respectively). From the lower limit of the proton lifetime $\tau_p > 10^{32}$ years [50] an upper limit on the product of all possible $\lambda^{'}$ and $\lambda^{''}$ couplings can be deduced [51, 52]:

$$\lambda^{'} \lambda^{''} < 10^{-7} \qquad (2.56)$$

for squark masses of $O(TeV)$. Another argument against R_P-violation might be the preservation of coupling unification observed in RPC MSSM. However, it turns out that this restriction results only in some rather loose bounds on some of the $\lambda^{''}$ couplings [53, 54, 55].

On the other hand, R_P-violating SUSY provides a framework to describe non-zero neutrino masses via self energy loops of the neutrinos[48]. For instance, a $b\bar{\tilde{b}}$ loop

[47] The non-conservation of R_P for these terms can be seen as follows: The product of all $(-1)^{2S}$ terms for all fields at a vertex gives $+1$ due to angular momentum conservation and the factor $(-1)^{3(B-L)}$ equals -1 for squark and slepton supermultiplets. Consequently, the product of R_P for all fields is not $+1$, *i.e.* R_P is violated.

[48] It is also possible to construct SUSY theories with neutrino masses generated at the tree level.

would contribute to the mass of the electron neutrino and the upper mass limit of $m_{\nu_e} < 0.2\,\text{eV}$ from neutrinoless double β-decay experiments results in an upper limit for the Yukawa couplings $\lambda'_{133} < 1.7 \times 10^{-4}$ [56] and $\lambda'_{122} < 4.2 \times 10^{-3}$. The non-observation of neutrinoless double β-decays can also be used to restrict λ'_{111} as a function of squark mass [57]. Finally, experiments looking for atomic parity violation (APV) and charged current universality (CCU) have set limits on many of the Yukawa couplings assuming $m_{\tilde{q}} = 100\,\text{GeV}$. A common aspect of all these experiments is that they are sensitive to new physics through loop corrections from virtual sparticles, *i.e.* the cross section includes squark propagators $\sigma_{\text{lim}} \propto \lambda''^2/m_{\tilde{q}}^2$ (also λ' is possible). Therefore, these bounds on the Yukwa couplings depend like $\lambda'_{\text{lim}} \propto m_{\tilde{q}}$ on the squark masses. It should be stressed that in contrast to this, no squark propagator is involved in the processes investigated in this thesis (see the signal process in Sect. 4.1), thus λ' couplings can be large. Since the bounds on products of Yukawa couplings are generally observed to be much more severe than the products of the individual upper bounds [58, 59] , it is usually assumed that one Yukawa coupling is dominant (after EW symmetry breaking).

2.4.6 Sparticle Decay

The choice of the SUSY breaking mechanism determines the main aspects of the sparticle mass spectrum. Additionally, the free parameters of the model lead to possible variations of the masses and couplings. For a given set of parameters the possible decay channels are then fixed.

Since in R_P-conserving models all decay channels finally end with the LSP, its nature is especially important and results in characteristic decay signatures. It behaves similar to a neutrino since it interacts with SM particles only via sparticle exchange with masses similar to the W boson. Therefore, the prominent signature of R_P-conserving models is missing energy.

On the other hand, the existence of R_P-violating interactions opens up additional decay channels competing with the R_P-conserving ones. They lead to multilepton or multijet signatures (see Figs. (2.15), (2.16) and (2.17)). When heavy sparticles with long decay chains are produced (as in the case of LHC) the $\not{E}_T$ signature will also be visible in the case of R_P-violating interactions since an increasing number of neutrinos are produced on average in longer decay chains.

The lightest neutralino decays dominantly into the gravitino only if it is the NLSP. In the stau NLSP and slepton co-NLSP scenarios it would decay like $\tilde{\chi}_1^0 \to l^{\pm}\tilde{l}^{\mp} \to l^{\pm}l^{\mp}\tilde{G}$ leading to a different signature.

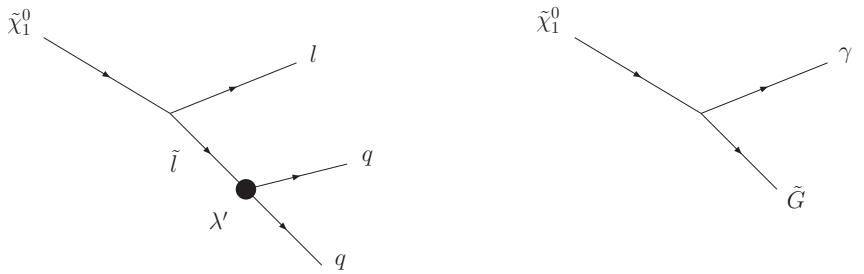

FIGURE 2.15: Dominant decay channels of the lightest neutralino. In R_P-conserving scenarios the neutralino is typically the stabel LSP. In the case of R_P-violation it decays into a lepton and two jets (left). Another (not shown) possibility would be the decay into two leptons and one jet via a virtual squark, which is surpressed for high squark masses. In the GMSB model with a light gravitino, the neutralino decays dominantly into the LSP (right).

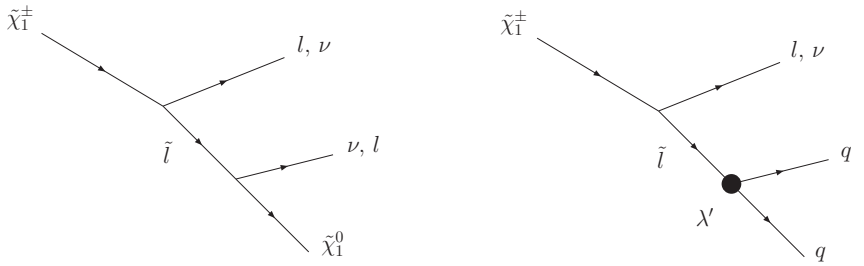

FIGURE 2.16: Dominant decay channels of the lightest chargino. For R_P-conserving scenarios (left) (also the decay into a neutralino and a $W^\pm$ is possible) and R_P-violating scenarios (right). The resulting neutralino might subsequently decay (if not the LSP), as shown in Fig. 2.15.

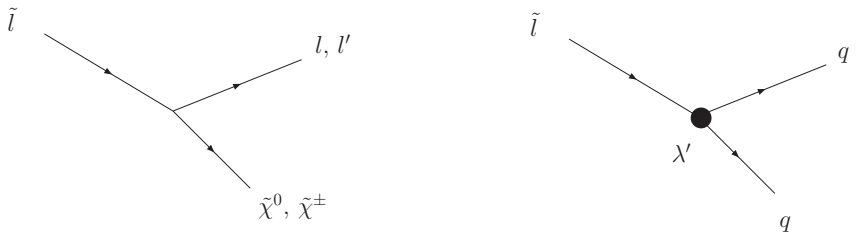

FIGURE 2.17: Dominant decay channels of sleptons. For R_P-conserving scenarios (left) and R_P-violating scenarios (right).

Chapter 3

SUSY at HERA

This chapter gives an overview of all possible SUSY processes with up to three final state (s)particles, that might be observed at HERA. For a systematic ordering of all diagrams an abstract notation is applied and the diagrams are classified according to their topology and whether they include R_P-violating vertices or not. The approach used is illustrated in Figure 3.1, which also gives an overview of the organization of this chapter. The first four sections describe the different ingredients needed for the derivation of all possible abstract diagrams in Section 3.5. Finally, the most promising SUSY processes at HERA are summarized in Section 3.6.

3.1 Basic HERA Topologies

The first important classification step is to distinguish different topological classes *i.e.* diagrams which can not be transformed into each other by topological operations.

For HERA six different graphs with up to three outgoing particles exist as

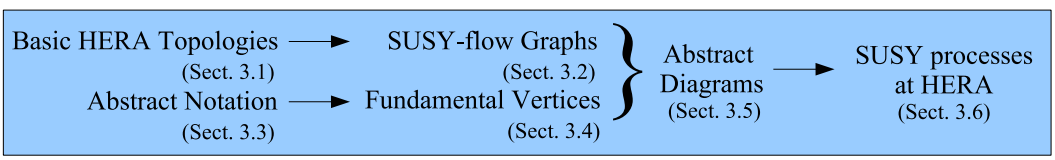

FIGURE 3.1: Overview of the approach applied for the derivation of interesting SUSY diagrams at HERA. The corresponding sections are given in parenthesis.

shown in Figure 3.2. In these graphs the lines can, in general, represent both bosonic and fermionic particles. However, diagrams with outgoing photons, gluons or Z^0 bosons will be neglected as they represent only radiative corrections to lower order diagrams (and thus have lower cross sections). Thus, only additional $W^{\pm}$ bosons are taken into account since they change the flavour content.

The number of outgoing particles was limited to three since adding an additional particle line to a diagram with three outgoing particles introduces an extra propagator term and a coupling in the matrix element.The resulting cross sections are too low to be observable at HERA with the available luminosity.

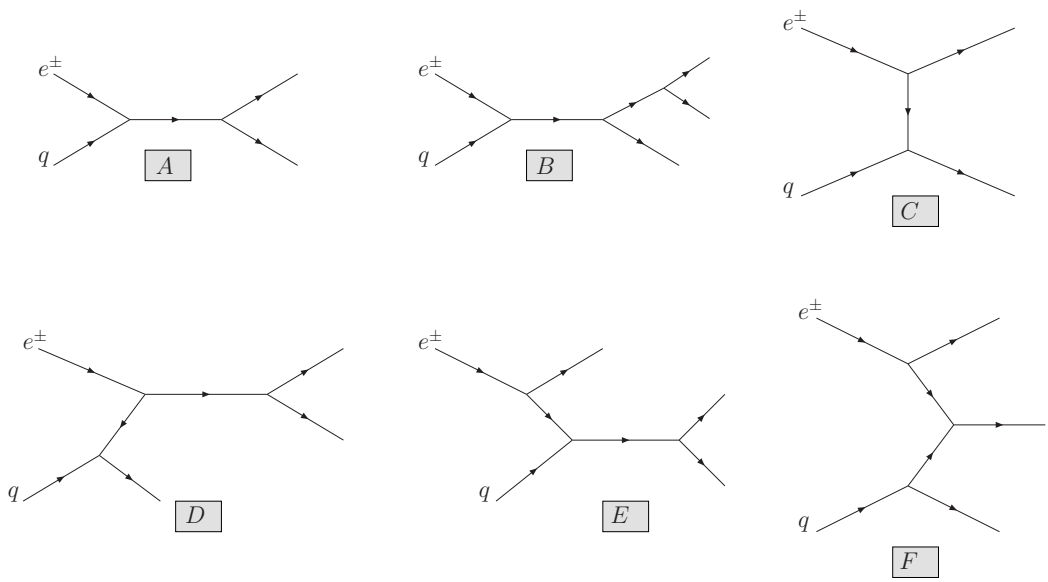

FIGURE 3.2: All basic HERA topologies with up to three outgoing particles.

The particle emitted from the proton can be a quark, a gluon or a photon. Gluons coming from the proton are disfavoured due to the low gluon density in the proton at large x. Direct photon radiation from the proton is even less probable (replacing α_s by α in the cross section). Therefore, in the following only diagrams with a quark from the proton are considered. However, they implicitly include also the direct gluon/photon radiation diagrams with two final state (s)particles when the lower incoming and outgoing quark lines are identified with the whole proton (this is possible, in the case of gluon radiation, only for the diagrams of type F and in the case of photon radiation for diagrams of type D and F).

If the initial state is fixed to be either an electron or positron on the one side and a quark from the proton on the other, no s-channel processes (type A) are possible within the SM but lowest order processes proceed via t-channel diagrams of type C. However, when allowing for R_P-violating interactions also topologies of type A can be exploited, as will be discussed in Section 3.5. The topologies of type D and E can be interpreted, on the one hand, as an initial state correction to the s-channel diagrams of type A or, on the other hand, as a final state correction to the t-channel diagrams of type C. u-channel processes are not discussed since they do not lead to new final states and can be easily derived from the given diagrams.

3.2 SUSY-flow Graphs

In the following, diagrams will be further classified by marking the particle lines which belong to a sparticle by a "$\sim$". The resulting diagrams will be called *SUSY-flow graphs*. It is instructive to consider R_P-conserving and R_P-violating diagrams separately which lead to different SUSY-flow graphs. In the case of R_P-conservation, all SUSY-flow graphs can be obtained by starting at an outgoing line and going through the graph, while marking each passed line with a "$\sim$", until another outgoing line is reached. In this way, each vertex will have either two or none adjacent sparticle lines. Therefore, R_P-conserving diagrams include always connected C-formed groups of sparticle lines. As an example, Figure 3.3 shows the three SUSY-flow graphs which can be derived for topologies of type F when R_P is conserved.

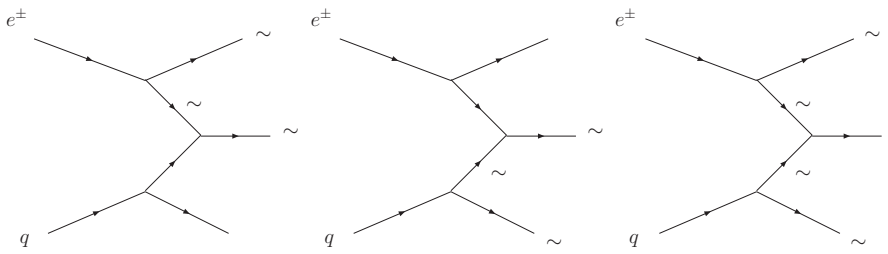

FIGURE 3.3: SUSY-flow graphs of type F for the R_P-conserving case.

In the following, graphs including two or more SUSY propagators (like the right graph in Figure 3.3) are not considered since their cross section can be expected to be small. Thus, the two R_P-conserving SUSY-flow graphs of type F have two

outgoing sparticle lines and one SUSY propagator. For R_P-violating diagrams the consequence is that three-sparticle-vertices will be neglected and only $\not{R}_P$ vertices with one sparticle will be considered. Thus, in diagrams with only one $\not{R}_P$ vertex the sparticle has to be an outgoing particle.

3.3 Abstract Notation

In order to be able to give a concise account of all possible SUSY diagrams an abstract notation is used in this chapter as defined in Table 3.1. In combining processes which always occur simultaneously into one representation, it enables a compact description of the physical alternatives.

TABLE 3.1: Definition of abstract SUSY symbols as used in this chapter. Deviating from common notation, l ($\tilde{l}$) represents not only charged leptons (sleptons) but also neutrinos (sneutrinos). The same generalization naturally leads to a common symbol for neutalinos and charginos.

Symbol	l	q	$\tilde{l}$	$\tilde{q}$	Γ	$\tilde{\chi}$
Particles	lepton	quark	slepton	squark	γ, Z^0, $W^\pm$	$\tilde{\chi}^0_{1,2,3,4}$, $\tilde{\chi}^\pm_{1,2}$, $\tilde{G}$

The labeling of particle lines with these symbols means that at least one diagram exists for all possible corresponding particles at each line, but not all combinations of adjacent particles are possible. However, the possible combinations can be read of quite simply by considering the conservation of the according quantum numbers at each vertex. Following the same logic, the symbol l *e.g.* can represent different leptons in the same diagram, so that the $W^\pm e\nu_e$ vertex is represented by Γll.

3.4 Fundamental Vertices

With the help of this notation, the basic vertices of particles and sparticles given in Section 2.1 and Section 2.4.2 can be combined to the five abstract vertices of Figure 3.4. They considerably facilitate the construction of all possible diagrams for a given SUSY-flow graph.

Since their cross sections are too small, some of the possible diagrams are discarded from the beginning by making the following restrictions:

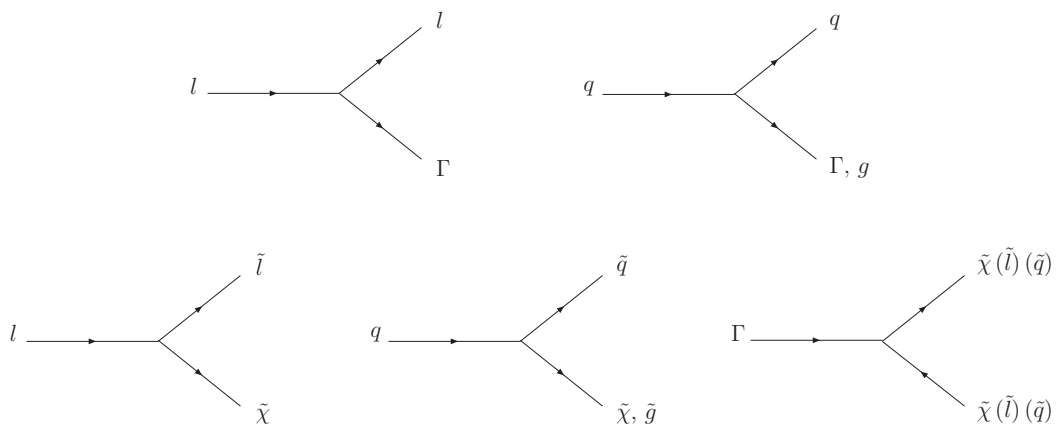

FIGURE 3.4: Fundamental vertices of the MSSM.

- interactions of the Higgs boson are not taken into account;
- pure bosonic vertices are neglected.

Within these restrictions, however, the vertices of Figure 3.4 describe all possible interaction of R_P-conserving MSSM.

In order to be able to investigate also R_P-violating scenarios the Yukawa terms of Equation (2.54) have to be converted to abstract notation. The resulting four R_P-violating vertices are shown in Figure 3.5, ordered in three columns according to whether they represent Yukawa couplings λ, $\lambda^{'}$ or $\lambda^{''}$, respectively. Following the argument given above, only vertices with one sparticle line are considered. Because of charge and color conservation, they are not symmetric under a $l \leftrightarrow q$ exchange, in particular no $\tilde{q} \rightarrow ll$ and $\tilde{l} \rightarrow lq$ vertices exist.

Similar to the R_P-conserving case, not all combinations of adjacent particles corresponding to the abstract symbols are possible at a given vertex but the restrictions of Equation (2.54) have to be taken into account.

3.5 Abstract Diagrams

Now that all necessary concepts have been introduced, the vertices included in the SUSY-flow graphs of types A - F can be identified with the fundamental vertices of Figures 3.4 and 3.5 to derive all possible *abstract diagrams* (*i.e.* diagrams where the particle lines are denoted with abstract notation).

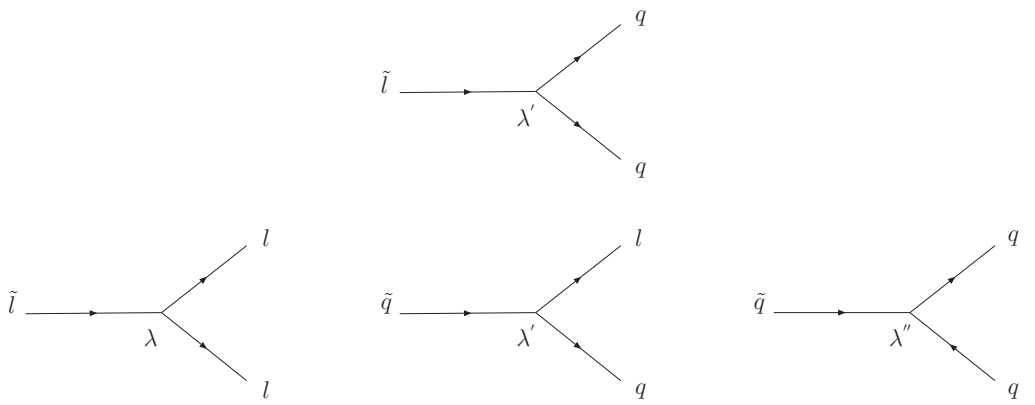

FIGURE 3.5: $\not{R}_P$ vertices in abstract notation.

Due to the abstract notation and the pre-ordering of possible diagrams this procedure is fast and clear. In most cases, only one or two alternative (s)particles can be assigned to a given particle line, which allows to denote all applicable alternatives for one diagram in a concise way. On the other hand, although the resulting abstract diagrams still represent a lot of different Feynman diagrams it is easy to identify the interesting ones.

For an efficient evaluation of the possible diagrams, it is advisable to start at a vertex with an incoming particle and proceed toward the other incoming particle vertex.

Restrictions made

Several restrictions are made during the following evaluation of interesting SUSY diagrams in order to reduce the number of abstract diagrams that need to be considered. For better clarity, they are summarised here:

- Diagrams with more than three (s)particles produced on-shell are neglected since their cross section is expected to be small;
- outgoing γ, g and Z^0 bosons are not discussed as they only represent higher order radiative corrections;
- for processes with a direct gluon emitted from the proton, diagrams with three outgoing (s)particles are discarded due to the low gluon density in the proton at large x;

- interactions of Higgs bosons are not considered since the Higgs mass limit is about a factor two higher than general sparticle limits in RPV scenarios;
- pure bosonic SM vertices are neglected since they lead to small cross sections;
- u-channel processes are not stated separately.

Furthermore:

- Diagrams including more than one SUSY propagator are discarded;
- diagrams consisting of three $\not{R}_P$ vertices are not all shown explicitly;
- diagrams with an additional outgoing $W^{\pm}$ bosons are not primary interesting candidates for SUSY production.

Diagrams of type A

Diagram A is the *leptoquark* channel which in the framework of SUSY proceeds via the R_P-violating Yukawa coupling λ'_{ijk} (vertex from Figure 3.5). Thus, the only possibility for the s-channel particle is a squark. Depending on whether the second vertex is R_P-conserving or not, two cases can be distinguished as shown in Figure 3.6. In the R_P-conserving case, two of the vertices of Figure 3.4 can

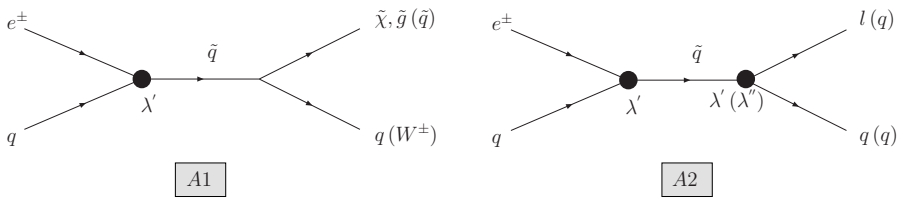

FIGURE 3.6: Possible diagrams of type A. Alternatives are given in parenthesis.

be applied (see Fig. 3.6), one of which describes the radiation of a $W^{\pm}$ boson or gaugino production, and the other leading to a final state of, *e.g.* one jet and a $\tilde{\chi}_1^0$.

If R_P is violated also at the second vertex, a final state with only SM particles results in a contact interaction like signature. Again, the two alternatives can be read off from the fundamental vertices of Figure 3.5. For the first alternative, with a λ' coupling also at the second vertex, the process leads to NC or CC like events depending on whether the outgoing lepton is an electron or neutrino, respectively. However, the cross section will decrease rapidly with decreasing λ' (where $\sigma \sim \lambda'^2$

for on-shell produced squarks with $m_{\tilde{q}} < \sqrt{\hat{s}}$ and $\sigma \sim \lambda^{'4}$ for virtual squarks with $m_{\tilde{q}} > \sqrt{\hat{s}}$.). The other alternative of having $\lambda^{'}$ and $\lambda^{''}$ simultaneously is disfavored since stringent limits exist on the product $\lambda^{'}\lambda^{''}$ [51].

Diagrams of type B

These diagrams present a higher order correction to the type A diagrams. Adding an additional vertex at one of the outgoing particle lines allows to draw seven different SUSY-flow graphs of type B.

In all cases a consistent assignment with (s)particles is possible. The less interesting ones can already be separated at the SUSY-flow graph level (see Figure 3.7). While the first two can be interpreted as type A diagrams with the additional radiation of an $W^{\pm}$ boson, the last two include two SUSY propagators and are thus ignored.

The remaining three SUSY-flow graphs lead to abstract diagrams as shown in Figure 3.8. Now, also sleptons can be produced, which was not possible with diagrams of type A. The final state of 2jets $+ \tilde{l}$ from the right diagram includes a combination of $\lambda^{'}$ and λ'' vertices. An interesting channel is jet $+ l + \tilde{l}$. With

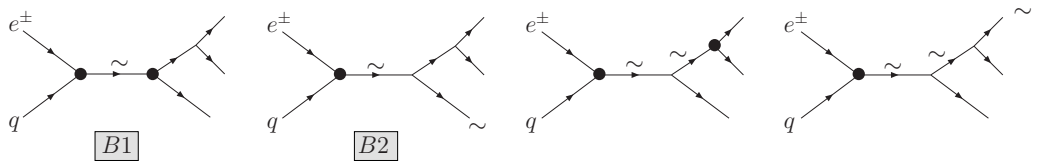

FIGURE 3.7: SUSY-flow graphs of type B which are not primary interesting. $B1$ and $B2$ emerge from $A2$ and $A1$ in higher order. The two right diagrams are neglected as they include two SUSY propagators.

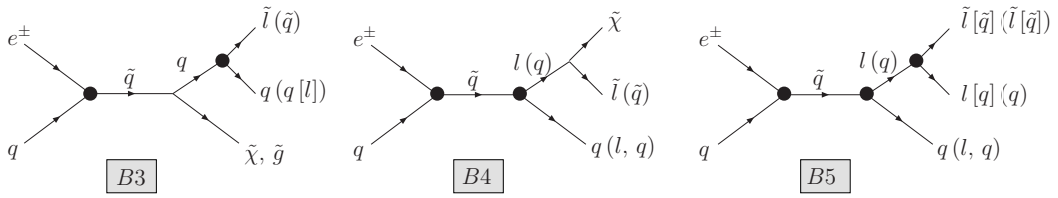

FIGURE 3.8: Abstract diagrams of type B. R_P-violating vertices are marked with a dot. Alternatives are given in parenthesis.

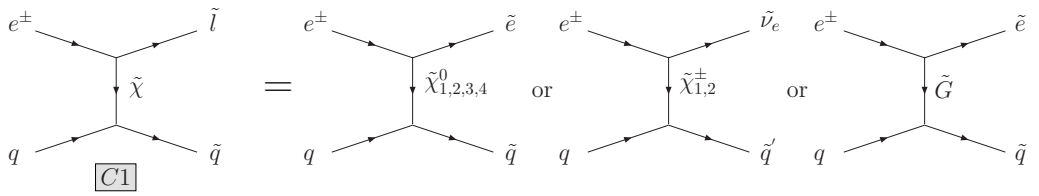

FIGURE 3.9: R_P-conserving diagrams of type C. Shown is the diagram in abstract notation on the left and the Feynman diagrams it represents on the right.

three R_P-violating vertices the last diagram has a cross section which goes with the sixth power of a product of Yukawa coefficients. Such diagrams will not be considered in the following.

Diagrams of type C

These are t-channel processes where one particle is exchanged between the lepton and a quark from the proton, consequently consisting of two vertices. For diagrams of type C only one R_P-conserving SUSY-flow diagram exists, as shown in Fig. 3.9.

By consulting the list of fundamental MSSM vertices given above (Fig. 3.4), one sees that the only sparticles coupling both to a lepton and a quark are $\tilde{\chi} = \tilde{\chi}^0_{1,2,3,4}$, $\tilde{\chi}^{\pm}_{1,2}$, $\tilde{G}$. After specifying the exchanged sparticle, the outgoing sparticles

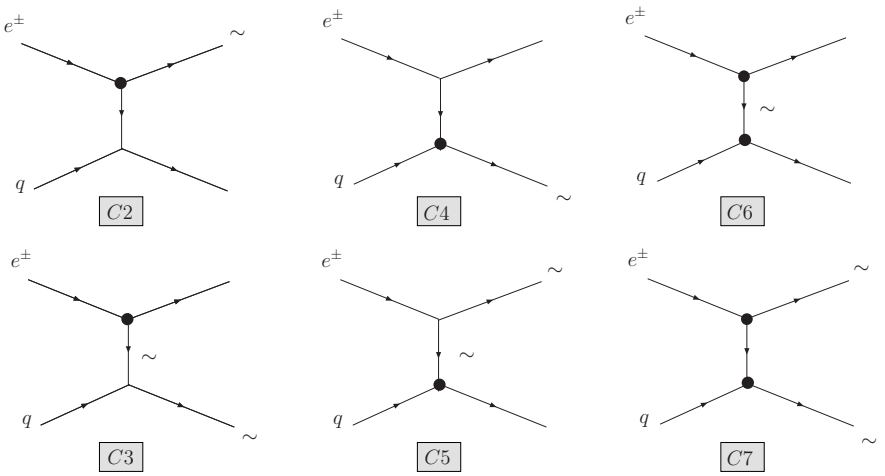

FIGURE 3.10: SUSY-flow graphs of type C with $\not{R}_P$ vertices (marked with a dot).

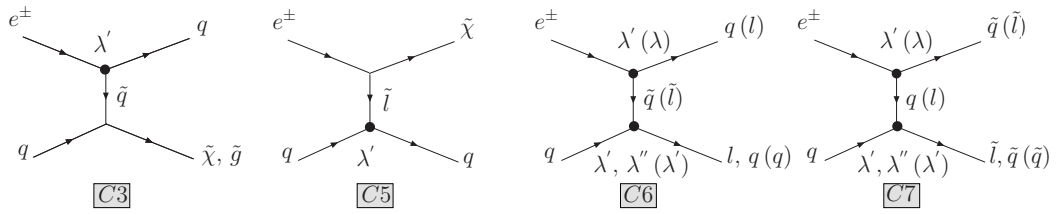

FIGURE 3.11: Possible R_P-violating diagrams of type C. In the last two diagrams a second alternative is given in parenthesis. R_P-violating vertices are marked with a dot.

are fixed (see Fig. 2.11), resulting in the three possible Feynman diagrams denoted in Figure 3.9.

When allowing for R_P-violating interactions, additional diagrams have to be taken into account. The possible SUSY-flow diagrams are shown in Figure 3.10. Because of the incoming particles the upper vertex can be only λ or $\lambda^{'}$ and the lower one $\lambda^{'}$ or $\lambda^{''}$ so that the exchanged particle can only be a (s)lepton or a (s)quark. The upper two diagrams of the first two columns ($C2$ and $C4$), where this particle is a SM particle, can only be interpreted as the radiation of a $W^{\pm}$ boson (since the exchanged particle has to be a fermion) in addition to a type A diagram, leading to the final state $W^{\pm}\tilde{q}$. The remaining four diagrams, on the other hand, are interesting (see Figure 3.11). Diagram $C3$ leads via squark exchange to $\tilde{\chi}^0$, $\tilde{\chi}^{\pm}$, $\tilde{g}$ or $\tilde{G}$ production together with a quark in the final sate. The reversed process is slepton exchange in $C5$, again with a final quark and $\tilde{\chi}^0$, $\tilde{\chi}^{\pm}$ or $\tilde{G}$ production. With only SM particles in the final state, diagram $C6$ can produce either NC or CC like events via a squark exchange and two $\lambda^{'}$ Yukawa couplings with an electron or a neutrino in the final state, thus interfering with diagrams of type $A2$. The reverse diagram $C7$ is the easiest way to produce two sfermions; it has one SM propagator and two $\not{R}_P$ vertices.

Diagrams of type D and E

To derive the diagrams of type D and E, it is useful to start from the type C diagrams discussed above.

In case of R_P-conservation, however, the diagram from Figure 3.9 leads to a type D/E diagram but it would include two SUSY propagators. New R_P-conserving diagrams emerge which have only SM propagators, as shown in Figure 3.12. Similar diagrams emerge when only the new vertex is R_P-violating (see

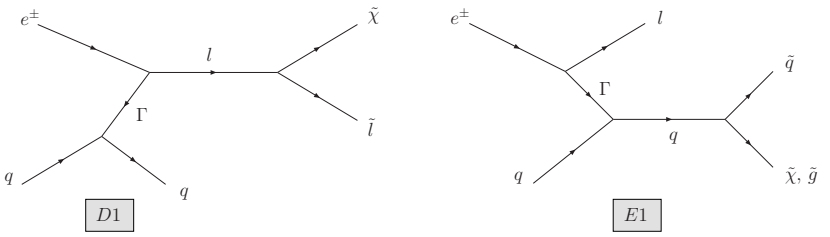

FIGURE 3.12: R_P-conserving diagrams of type D (left) and E (right).

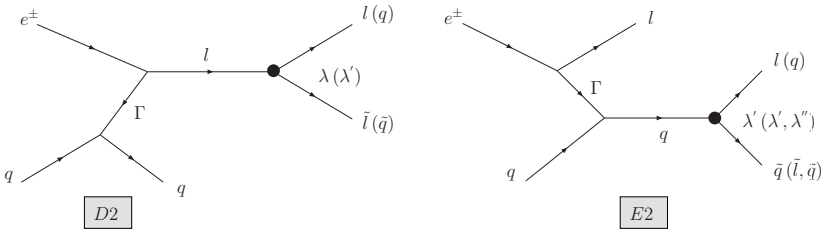

FIGURE 3.13: R_P-violating diagrams of type D (left) and E (right).

Fig. 3.13).

The other R_P-violating diagrams can be obtained from the four diagrams of type C (Fig. 3.10) by adding an additional vertex to the upper (lower) outgoing particle line, for diagrams of type D (E), respectively. Figures 3.14 and 3.15 show the resulting diagrams. Diagrams $D5$ and $E3$ are excluded since they include two SUSY propagators. In addition, two diagrams with three R_P-violating vertices exist, but are discarded as noted above. The diagrams which result from the $C7$ diagram are not shown separately, since they are identical to $D6/E6$ but with an inverted[1] tilde sign on the (s)fermions. They will be called $D7/E7$. Also the $C2$ and $C4$ diagrams can receive an additional vertex at the squark line as listed for the type A diagrams. The resulting diagrams are thus the same as $A1$ and $A2$ with an additional outgoing $W^{\pm}$ boson, called $D7$, $D8$ and $E7$, $E8$. More diagrams with outgoing $W^{\pm}$ bosons can be constructed from the diagrams of Figure 3.14 by replacing the outgoing $\tilde{\chi}$ line by a $W^{\pm}$ line. Starting from the $D3$ diagram either the lower $\tilde{\chi}$ line can be replaced (the resulting diagram will be labeled $D8$) or the upper one ($D9$) or both ($D10$). For $D4$ and $D6$ there is only one possibility (called $D11$ and $D12$). Similarly, there are diagrams $E8$ to $E12$.

[1]This inversion turns particle lines into sparticle lines and *vice versa*.

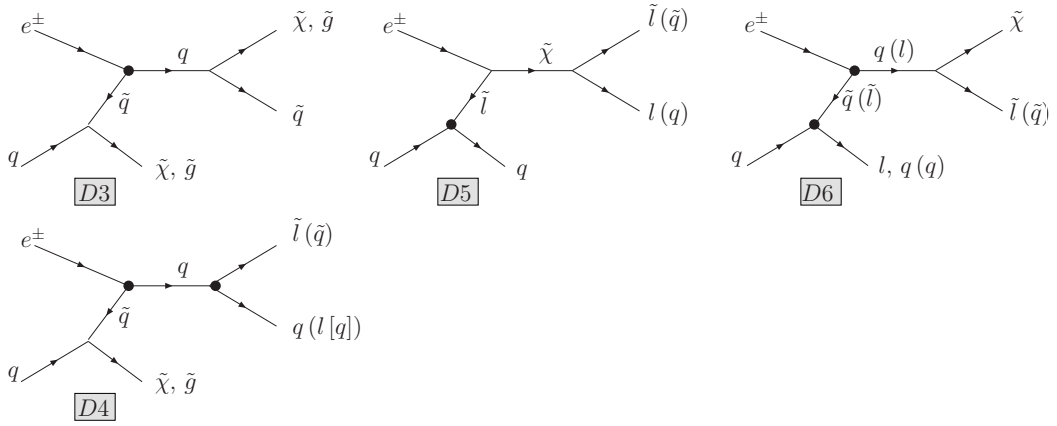

FIGURE 3.14: R_P-violating diagrams of type D. The three columns correspond to the first three cases of Figure 3.10, while the upper (lower) row contains the case of an R_P-conserving (-violating) extra vertex. The diagrams $D7/E7$ (not shown) are identical to $D6/E6$ with an inverted tilde sign. R_P-violating vertices are marked with a dot.

Diagrams of type F

The diagrams of type F possess one propagator more than the A and C type diagrams. Consequently, tighter restrictions have to be made so that the cross-section can still be expected to be sufficiently high.

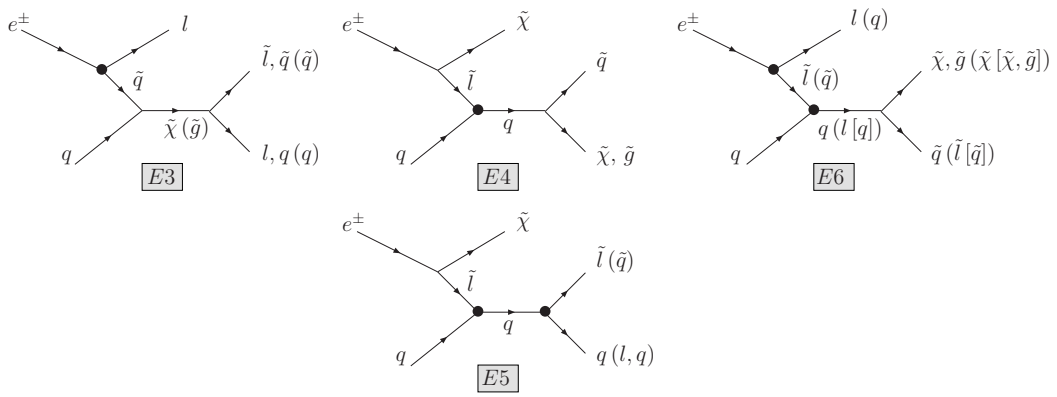

FIGURE 3.15: R_P-violating diagrams of type E. The three columns correspond to the first three cases of Figure 3.10, while the upper (lower) row contains the case of an R_P-conserving (-violating) extra vertex. R_P-violating vertices are marked with a dot.

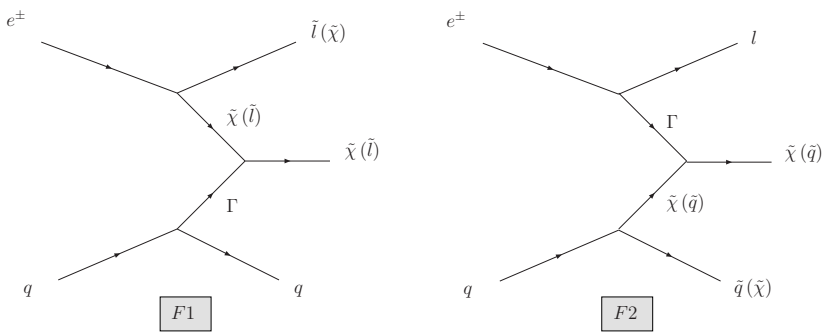

FIGURE 3.16: R_P-conserving diagrams of type F.

The three SUSY-flow diagrams for the R_P-conserving case were already shown in Figure 3.3. For the two cases with only one SUSY propagator the abstract diagrams are shown in Figure 3.16.

Both $F1$ diagrams have the same final state of $jet + \tilde{l} + \tilde{\chi}$. In the $F2$ case, the situation is quite similar, but the final selectron is replaced by a final squark. Since the existing limits on the squark masses are much higher than the slepton mass limits, $F1$ diagrams are favoured over $F2$ diagrams.

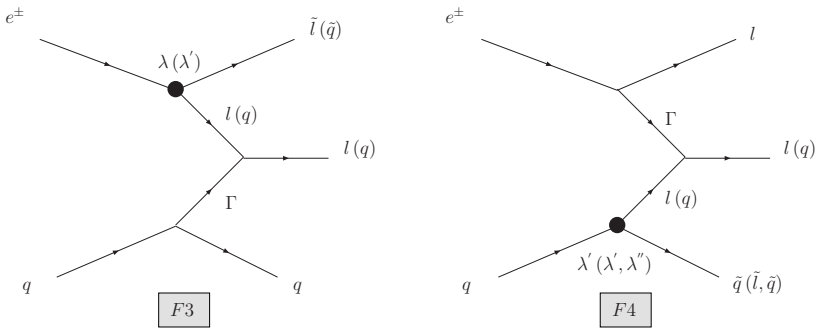

FIGURE 3.17: R_P-violating diagrams of type F with one $\not{R}_P$ vertex.

The diagrams with R_P-violating interactions can be subdivided by the number of $\not{R}_P$ vertices. Out of the three diagrams with one $\not{R}_P$ vertex only two exist (see Fig. 3.17). The diagram with the $\not{R}_P$ vertex in the middle would either represent a radiative correction to a C type diagram or include a lepton-quark vertex.

Diagrams with two R_P-violating vertices can be constructed with three possible distributions of the $\not{R}_P$ vertices. From these, four different SUSY-flow graphs can

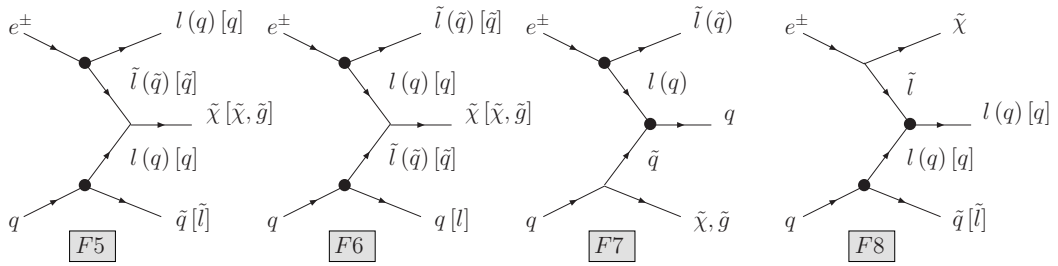

FIGURE 3.18: R_P-violating diagrams of type F with two $\not{R}_P$ vertices.

be derived which can be used to form abstract diagrams. They are shown in Figure 3.18. The abstract diagram with three R_P-violating vertices is not shown here.

Diagrams with one outgoing $W^{\pm}$ boson exist in 15 variations. The first seven ($F9$ to $F15$) correspond to the seven diagrams of type C with an additional $W^{\pm}$ radiated from the incoming electron. Similarly, there are seven diagrams where the $W^{\pm}$ is radiated from the incoming quark ($F16$ to $F22$). For the remaining case, where the $W^{\pm}$ sits in the middle of the type F topology, only one SUSY-flow graph is possible (the possibility of two subsequently radiated $W^{\pm}$ bosons is not considered) which has two $\not{R}_P$-vertices, only SM propagators and two outgoing SUSY particles ($F23$).

3.6 SUSY Processes at HERA

The two criteria which make a diagram interesting (*i.e.* increase their separation power with respect to SM processes) are a high cross section and a special final state. Factors which entail a high cross section are:

- A small number of SUSY propagators;
- a small number of outgoing SUSY particles;
- no squark propagators or produced squarks[2].

While special final states include:

[2]Here the underlying assumption is that squarks are heavy, since no evidence of them was found in former searches, as mentioned in the introduction.

- missing energy;
- isolated, high energy leptons or photons.

When the additional requirement of squarklessness is imposed, only 9 of the 55 diagram alternatives discussed above remain. Their final states are listed in Table 3.2. The full list for all diagrams is given in Appendix A (Tab. A).

TABLE 3.2: Overview of squark-less diagrams with two and three final state (s)particles. For diagrams with various alternatives the number of the alternative is added to the diagram name after a "-". Listed are also the number of sparticle propagators (N_{prop}^{SUSY}) and on-shell produced sparticles (N_{final}^{SUSY}).

Diagram	RPV	l	q	$W^{\pm}$	$\tilde{l}$	$\tilde{q}$	$\tilde{\chi}$	N_{prop}^{SUSY}	N_{final}^{SUSY}
C5	$\lambda^{'}$		1				1	1	1
C6-3	$\lambda\lambda^{'}$	1	1					1	0
D1			1		1		1	0	2
E5-1	$\lambda^{'}\lambda^{'}$		1		1		1	1	2
F1			1		1		1	1	2
F3-1	λ	1	1		1			0	1
F4-2	$\lambda^{'}$	1	1		1			0	1
F6-1	$\lambda\lambda^{'}$		1		1		1	1	2
F8-3	$\lambda^{'}\lambda^{'}$		1		1		1	1	2

The number of SUSY propagators and outgoing SUSY particles is determined already at the level of the SUSY-flow graph. The diagrams with one propagator and two produced (s)particles are separated from the diagrams with two propagators and three produced (s)particles by a horizontal line. Within this second group the most interesting diagrams are $F3$ and $F4$ since they have no SUSY propagators and only one sparticle (a slepton) is produced. The next interesting diagram is the $D1$ diagram with two produced sparticles. All others are disfavored since they include three SUSY particles.

3.6.1 Signatures

In order to identify the signatures which may result from the different diagrams the decay of the produced sparticles has to be considered. It depends strongly on the mass spectrum, and the branching ratios for different channels can vary

TABLE 3.3: Interesting SUSY signatures at HERA. Only diagrams without squarks are considered. The upper part of the table shows the final state decay products of the particles in the first column for different SUSY scenarios. The lepton l can be either an electron e, a muon μ, a tau τ or a neutrino ν with the signature of missing energy $\not\!\!E_T$. For the shown signatures the $\tilde{\chi}$ was taken to be a $\tilde{\chi}_1^0$. In case a $\tilde{\chi}_2^0$ or $\tilde{\chi}_1^\pm$ is produced an additional ff' pair has to be added to the given signatures. Additionally, cascade decays are possible which are not shown here.

Particle	RPC			RPV
	MSSM	GMSB		
	$\tilde{\chi}_1^0$ LSP	$\tilde{\chi}_1^0$ NLSP	$\tilde{\tau}_1$ NLSP	
$\tilde{\chi}_1^0$	stable	$\gamma\tilde{G}$	$\tilde{\tau}\tau \to \tau\tau\tilde{G}$	$l^\mp\tilde{l}^* \to l^\mp ff$
$\tilde{\chi}_1^\pm$	$\tilde{\chi}_1^0 ff'$	$\gamma\tilde{G}ff'$	$\tau\tau\tilde{G}ff'$	$\tilde{l}l \to ffl$
$\tilde{l}$	$\tilde{\chi}_1^0 l$	$l\tilde{G}$	$l\tilde{\chi}_1^0 \to l\gamma\tilde{G}$	ff
$\tilde{\chi}_2^0$	$\tilde{l}l \to \tilde{\chi}_1^0 ll$	$\gamma\tilde{G}ll$	$\tau\tau\tilde{G}ll$	$\tilde{l}l \to ffl$
Diagram	Signature			
C5	$j\not\!\!E_T$	$j\gamma\not\!\!E_T$	$j\tau\tau\not\!\!E_T$	$jjjl^\mp$
C6-3	jl	jl	jl	jl
D1	$jl\not\!\!E_T$	$jl\gamma\gamma\not\!\!E_T$	$j\tau\tau l\not\!\!E_T$	$jjjjjl^\mp$
E4-1	$jl\not\!\!E_T$	$jl\gamma\gamma\not\!\!E_T$	$j\tau\tau l\not\!\!E_T$	$jjjjjl$
F1	$jl\not\!\!E_T$	$jl\gamma\gamma\not\!\!E_T$	$j\tau\tau l\not\!\!E_T$	$jjjjjl$
F3-1	$jll\not\!\!E_T$	$jll\gamma\not\!\!E_T$	$jll\not\!\!E_T$	$jjjl$
F4-2	$lll\not\!\!E_T$	$lll\gamma\not\!\!E_T$	$lll\not\!\!E_T$	$jjl^\mp l$
F6-1	$jl\not\!\!E_T$	$jl\gamma\gamma\not\!\!E_T$	$j\tau\tau l\not\!\!E_T$	$jjjjjl^\mp$
F8-3	$jl\not\!\!E_T$	$jl\gamma\gamma\not\!\!E_T$	$j\tau\tau l\not\!\!E_T$	$jjjjjl^\mp$

largely for different regions in parameter space. Here, only the dominant decay channels shall be considered. These are the decays of $\tilde{\chi}_1^0$, $\tilde{\chi}_2^0$, $\tilde{\chi}_1^\pm$ and $\tilde{l}$ as presented in Sect. 2.4.6. Table 3.3 shows the resulting signatures in the MSSM and GMSB models for different NLSPs. It highlights the importance of the NLSP leading to characteristic signatures for different SUSY scenarios which are similar for all diagrams. The signatures include all kind of interesting final states:

- muons and taus
- electrons with sign opposite of the initial electron

- isolated photons
- missing energy
- possible reconstruction of the invariant mass of decaying particles

3.6.2 Conclusion

The list of SUSY signatures may serve as a reference to identify possible SUSY contributions to a given signature. In order to estimate the importance of the different channels, their cross section needs to be calculated. This represents a non-straightforward task for most of the given diagrams and the available generator programs. However, first calculations show that in some cases the cross sections are similar to the one investigated in this thesis, thus there are still potential SUSY discovery channels at HERA. The characteristic signatures for different scenarios on the other hand provide motivation for inclusive searches of *e.g.* $\tau + \not\!\!E_T$.

Chapter 4

Signal Processes and GMSB Phenomenology

In this chapter the signal processes investigated in this thesis are presented and their topologies are compared to possible SM background. This determines the analysis structure for this thesis which is shown in the following. In the next section the influence of GMSB parameters on the properties of the signal processes are discussed.

4.1 Signal Processes

For the investigation in this thesis the gaugino production in R_P-violating supersymmetry was chosen (diagram C5 from Chapter 3) with the subsequent decay in the GMSB model (see Figure 4.1). The reasons are: First, a cross section which can be expected to be high compared to the other diagrams discussed in the previous chapter. Second, a very characteristic decay signature for the GMSB decay $\tilde{\chi}^0 \to \tilde{G}\gamma$:

- Missing energy,
- an isolated, high energetic photon,
- and one jet.

Since R-parity is violated in the production process the gaugino can also decay in two R_P-violating decay channels with

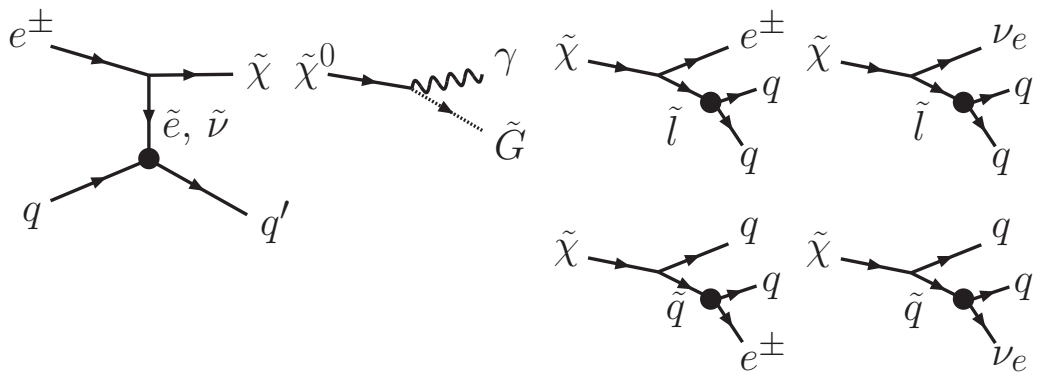

FIGURE 4.1: Feynman diagrams of the signal processes. Gaugino production in R_P-violating supersymmetry (left) and the three investigated decay channels: GMSB decay into the gravitino (second column), R_P-violating decay with electron final state (third column) and R_P-violating decay with neutrino final state (last column). The $\tilde{\chi}$ can either be a neutralino or a chargino leading to the same final states. For the decay into the gravitino only neutralinos contribute. The $\tilde{l}$ is either a selectron or a sneutrino depending on the charge of the $\tilde{\chi}$.

- an electron (or positron)
- and multiple jets,

if the final lepton is charged, or

- missing energy
- and multiple jets,

if the final lepton is a neutrino. The investigation of final states was restricted to first generation leptons, *i.e.* only couplings λ'_{1jk} were considered and the exchanged lepton thus has to be a selectron (for neutralino production) or a sneutrino (for chargino production). A complication results from the fact that due to the large momentum imbalance in the initial state, the produced gaugino (and thus its decay products), as well as the interacting quark will be boosted in the forward direction (the direction of the incoming proton), where reconstruction is more difficult (see Chapter 6).

Different λ'_{1jk} couplings lead to different cross sections since they pick different quarks from the proton. It turns out that only the processes with the couplings λ'_{111}, λ'_{121}, λ'_{112} and λ'_{113} have a cross section high enough to be observable within

TABLE 4.1: Gaugino production processes for different λ' couplings. Due to charge conservation, the Q term has to be a U term in neutralino production and a D term in chargino production. The relative cross sections of the processes which result from the different abundance of the initial quark in the proton[3]are indicated by font size. The coupling λ'_{131} is suppressed due to the high top mass.

$\lambda'_{ijk} L_i Q_j D_k$			
	$L = \tilde{e}_L^+, \tilde{e}_L^-$		$L = \tilde{\nu}_L, \bar{\tilde{\nu}}_L$
	$e^- U \to D\tilde{\chi}^0$	$e^+ D \to U\tilde{\chi}^0$	$e^\pm D \to D\tilde{\chi}^\pm$
λ'_{111}	$e^- u \to d\tilde{\chi}^0$ $e^- \bar{d} \to \bar{u}\tilde{\chi}^0$	$e^+ d \to u\tilde{\chi}^0$ $e^+ \bar{u} \to \bar{d}\tilde{\chi}^0$	$e^\pm d \to d\tilde{\chi}^\pm$ $e^\pm \bar{d} \to \bar{d}\tilde{\chi}^\pm$
λ'_{121}	$e^- \bar{d} \to \bar{c}\tilde{\chi}^0$ $e^- c \to d\tilde{\chi}^0$	$e^+ d \to c\tilde{\chi}^0$ $e^+ \bar{c} \to \bar{d}\tilde{\chi}^0$	$e^\pm d \to s\tilde{\chi}^\pm$ $e^\pm \bar{d} \to \bar{s}\tilde{\chi}^\pm$ $e^\pm s \to d\tilde{\chi}^\pm$ $e^\pm \bar{s} \to \bar{d}\tilde{\chi}^\pm$
λ'_{112}	$e^- u \to s\tilde{\chi}^0$ $e^- \bar{s} \to \bar{u}\tilde{\chi}^0$	$e^+ \bar{u} \to \bar{s}\tilde{\chi}^0$ $e^+ s \to u\tilde{\chi}^0$	$e^\pm d \to s\tilde{\chi}^\pm$ $e^\pm \bar{d} \to \bar{s}\tilde{\chi}^\pm$ $e^\pm s \to d\tilde{\chi}^\pm$ $e^\pm \bar{s} \to \bar{d}\tilde{\chi}^\pm$
λ'_{113}	$e^- u \to b\tilde{\chi}^0$ $e^- \bar{b} \to \bar{u}\tilde{\chi}^0$	$e^+ \bar{u} \to \bar{b}\tilde{\chi}^0$ $e^+ b \to u\tilde{\chi}^0$	$e^\pm d \to b\tilde{\chi}^\pm$ $e^\pm \bar{d} \to \bar{b}\tilde{\chi}^\pm$ $e^\pm b \to d\tilde{\chi}^\pm$ $e^\pm \bar{b} \to \bar{d}\tilde{\chi}^\pm$

the investigated HERA luminosity. The full list of production processes is given in Table 4.1[1]. For a comparison of the relative importance of the different λ' couplings the cross sections are given for an example parameter point in Table 4.2.

Also the number of expected events is given in Tab. 4.2 which makes it possible to rank the different couplings in terms of observability. For their calculation, the cross sections have to be weighted with the luminosities:

$$N_{\text{expected}} = \sigma_{e^-} \cdot L_{e^-} + \sigma_{e^+} \cdot L_{e^+} \tag{4.1}$$

[1]The list is obviously independent of the first index and holds also for the higher generation couplings obtained *via* $\lambda'_{1jk} \to \lambda'_{2jk}$ and $\lambda'_{1jk} \to \lambda'_{3jk}$.

[3]Additional differences result from different coupling strengths to the neutralino.

TABLE 4.2: Example cross sections for different λ' couplings. The cross sections are the sum of the quark and anti-quark contributions for $m_{\tilde{\chi}_1^0} = 73\,\text{GeV}$, $m_{\tilde{e}_L} = 75\,\text{GeV}$ and $\lambda'_{ijk} = 1$. The other GMSB parameters are $\sqrt{F} = 233\,\text{GeV}$, $M = 100\,\text{TeV}$, $\Lambda = 50\,\text{TeV}$, $\tan\beta = 2$ and $sign(\mu) = -1$. For λ'_{122} and λ'_{123} the numbers of expected events lie below 10 and 0.01, respectively; they are not investigated. For the calculation of N_{expected}, $\mathcal{L}_{e^+p} = 65\,\text{pb}^{-1}$ and $\mathcal{L}_{e^-p} = 17\,\text{pb}^{-1}$ were used.

Coupling	σ_{e^+} (pb)	σ_{e^-} (pb)	N expected
λ'_{111}	1.27	2.49	125
λ'_{121}	1.13	0.31	79
λ'_{112}	0.32	2.35	61
λ'_{113}	0.22	2.23	52

Hence, the ranking changes with the ratio of collected electron and positron luminosity. This can be observed also in Figure 4.2 which shows the number of expected events for the HERA I data set and the total data set used in this thesis as a function of the mass of the left-handed selectron. The plots shows that the chosen production process leads indeed to an observable signal, even for relatively high selectron masses. Due to the large amount of electron data collected in the HERA II period, the λ'_{11k} (k=2,3) couplings are now favoured against λ'_{121}. Except for λ'_{111} (where u and d quarks contribute) the number of expected events for a specific coupling is dominated either by the electron or the positron data. Hence, it would be possible to derive a common limit for the couplings λ'_{11k} (k=1,2,3) from the electron data and an other one for the λ'_{1j1} (j=1,2) from the positron data[4]. However, the best limits can only be derived when both channels are combined. Unfortunately, in this case the grouping observed for the separate cross sections in Tab. 4.2 breaks down for N_{expected} and the limits have to be given for all four λ' couplings separately.

4.1.1 Signal Topologies and Possible SM Background

For the development of a search strategy it is instructive to compare the topologies of signal and background events. Figure 4.3 and Figure 4.4 show simulated events for the gravitino and electron channel, respectively (see Chapter 7 for details on event simulation). As a general property, one observes that the activity is centered

[4]This strategy was followed by the H1 collaboration [60].

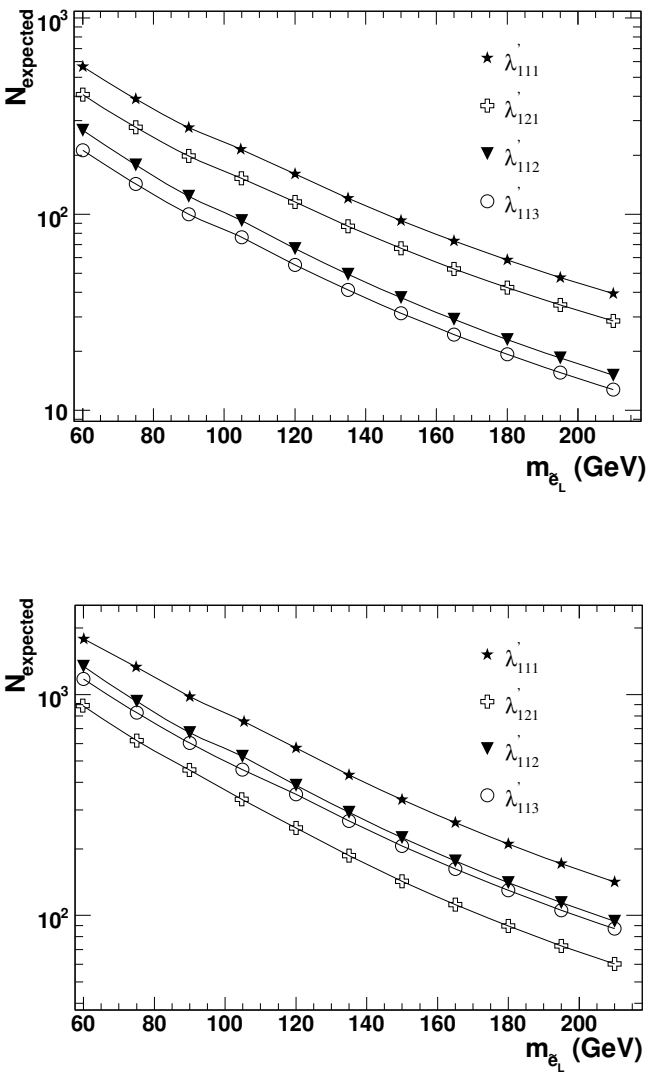

FIGURE 4.2: Number of expected events for different R_P-violating couplings for the HERA I data set (top, $\mathcal{L}_{e^+p} = 65\,\mathrm{pb}^{-1}$ and $\mathcal{L}_{e^-p} = 17\,\mathrm{pb}^{-1}$) and the combined HERA I and II data set (bottom, $\mathcal{L}_{e^+p} = 145\,\mathrm{pb}^{-1}$ and $\mathcal{L}_{e^-p} = 155\,\mathrm{pb}^{-1}$) (see Table 9.1) as a function of selectron mass. The neutralino mass was set to $m_{\tilde{\chi}_1^0} = 60\,\mathrm{GeV}$. The other GMSB parameters are $\sqrt{F} = 233\,\mathrm{GeV}$, $M = 80\,\mathrm{TeV}$, $\Lambda = 40\,\mathrm{TeV}$, $\tan\beta = 2$ and $sign(\mu) = -1$.

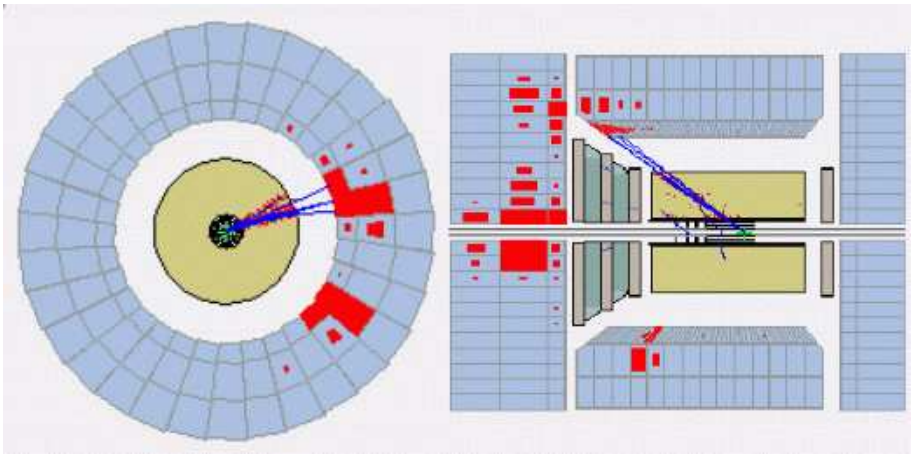

FIGURE 4.3: Event display of a generated MC event for the gravitino channel. Shown is the $r-\phi$ view (left) and the xz view (right).

in the forward direction as a result of the forward moving gauginos. In the $r-\phi$ view of the gravitino channel event, the imbalance due to the undetected gravitino is clearly visible. The R_P-violating decay channels are characterised by a much more isotropic distribution in $r-\phi$.

The properties of the signal processes can be mimicked by SM processes. Multi-jet topologies are expected in higher order (HO) events when additional high p_T gluons are emitted from the struck quark. A mismeasurement in the total energy (misMeasE) will result in a signature of missing energy. A fake photon candidate may be found or it may result from a jet (misId γ) or it may be confused with an electron if no track is found ($e^{\pm}$ as γ) or an additional photon may be emitted from the initial or final electron or quark (additional γ). A list of all conditions that have to be fulfilled for the different SM processes to contribute to one of the three signal processes is given in Table 4.3. In order to estimate the expected number of background events the SM processes were simulated by Monte Carlo generators (as described in Chapter 7).

The differences in $r-\phi$ topologies for signal and background processes, as illustrated in Figure 4.5, can be used for their separation. If the electron in NC events is misidentified as a photon it lies typically back-to-back with the jet, which is not the case for the photon in the gravitino channel. Thus, $\Delta\phi(jet,\gamma)$ can be used to discriminate these events. Similarly, neutrino and jet are typically back-to-back in CC events, which is not the case for gravitino and jet in the gravitino

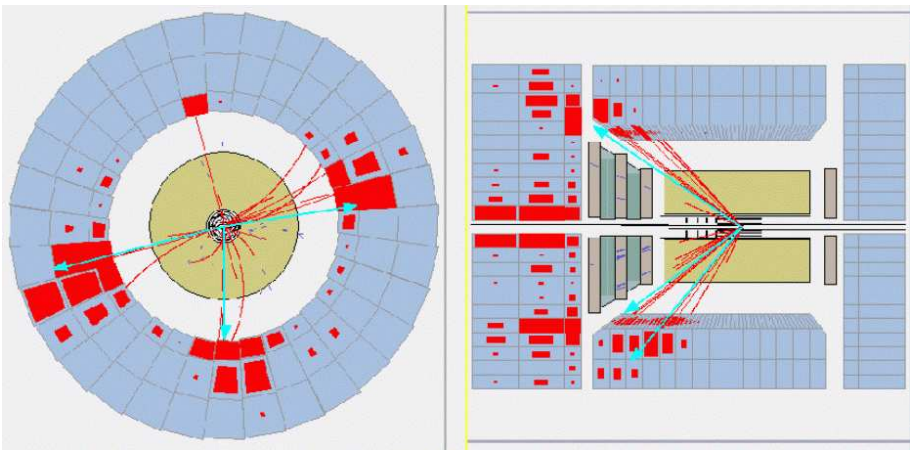

FIGURE 4.4: Event display of a generated MC event for the R_P-violating channel with electron in the final state. Shown is the $r-\phi$ view (left) and the xz view (right). The other R_P-violating decay channel has a similar topology but no electron, which is replaced by a invisible neutrino.

channel. Thus, $\Delta\phi(jet, \tilde{G})$ can be used to discriminate these events (see Sect. 6.7 for how the gravitino is reconstructed). Some unreduceable background events for the gravitino channel result from CC DIS processes where an additional photon is emitted from the quark. For the discrimination of the R_P-violating channels the circularity is used, which is 1 for an isotropic event topology and 0 if all activity lies in one direction (see Sect. 6.7 for how it is calculated).

TABLE 4.3: Conditions under which the different SM processes may contribute to the three different signal topologies. The signatures are given in parentesis; "mj" denotes multiple jets. Cases where three or more conditions would have to be fulfilled are not specified.

	Gravitino($\not\!\!E_T$, γ, $1j$)	Electron($e^{\pm}$, mj)	Neutrino($\not\!\!E_T$, mj)
PhP(1j)	misId γ+misMeasE	HO+misId $e^{\pm}$	HO+misMeasE
NC($e^{\pm}$, 1j)	$e^{\pm}$ as γ+misMeasE	HO	-
CC($\not\!\!E_T$, 1j)	additional γ	-	HO

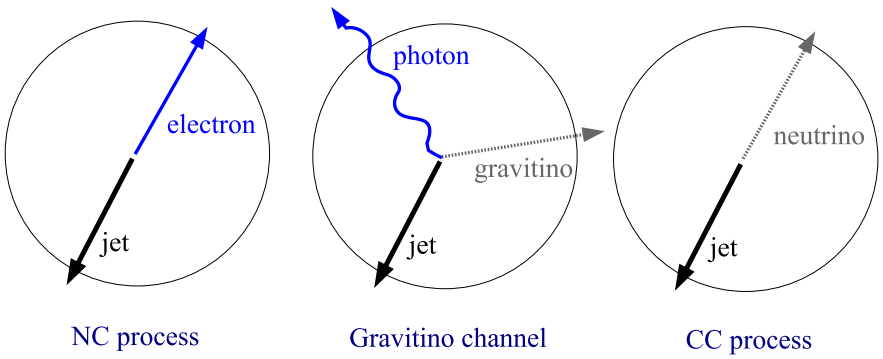

FIGURE 4.5: Comparison of signal and background topologies in the $r - \phi$ plane, for a neutral current process (left), the gravitino channel (middle) and a charged current process (right). All processes are shown in leading order.

4.1.2 Search Strategy and Analysis Structure

In order to interpret the data, control distributions are plotted for data events and their integral and shape is compared to distributions of MC generated events. The aim of the selection is to achieve a good signal-to-background separation (or purity) with the side condition of a high signal efficiency. Since these two aims are in opposition of each other they have to be optimized simultaneously. The general strategic approach, which is used for all three channels investigated in this thesis, is to separate the signal-to-background optimisation from the control selection step:

- First a loose preselection of the main SM background events is performed with the aim of maximising the signal efficiency;
- the signal-to-background ratio is then optimised with the help of a multivariate discriminant method (see Chapter 8) which takes into account all correlations between the chosen discriminating variables.

In the gravitino channel the dominant SM background comes from CC events. The main criteria to separate SM background and SUSY signal is the requirement of an additional photon which is explored in a second step.

In the case of the R_P-violating decay channels the background consists of NC events for the electron channel and CC events for the neutrino channel. The main separation criteria is the high total E_T and the high E_T jets in the signal, which

result from the high mass of the produced gauginos. Figure 4.6 gives an overview of the different analysis steps presented in this thesis[5]. Besides the three main selections, a separate electron control sample is used to study the electron/photon separation, needed for the gravitino channel. Different limits are derived in the $m_{\tilde{e}_L}$-$m_{\tilde{\chi}_1^0}$ plane by using the results from the gravitino channel only. To extend the limits toward higher $\sqrt{F}$ values, also the R_P-violating decay channels are needed.

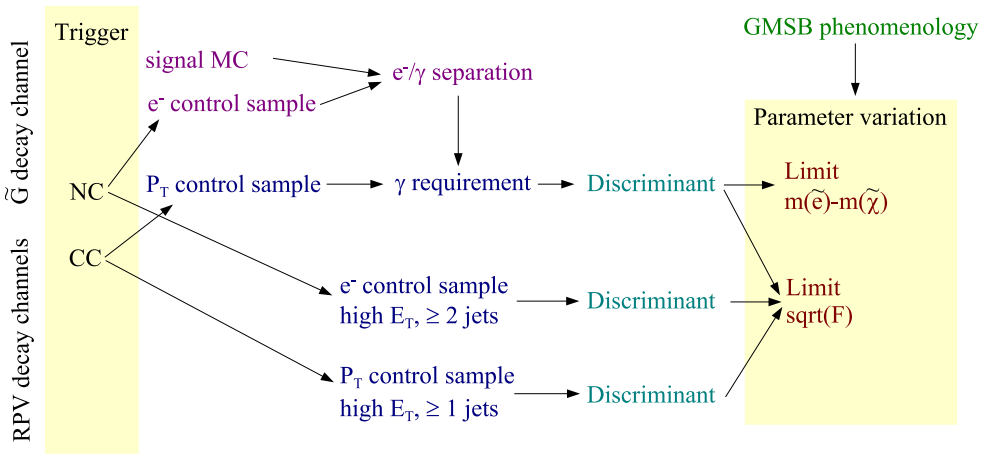

FIGURE 4.6: Overview of the analysis structure. The same selection steps are followed by data, SM background MC and signal MC events.

4.2 Effect of GMSB Parameters

For an interpretation of the results in the framework of the GMSB model, it has to be investigated how the observables of the different processes under study change for different regions of GMSB parameter space. The observables[6] which have to be known are:

- Cross sections,
- branching ratios,
- and selection efficiencies.

[5] A more detailed discussion of the steps performed to calculate the effect of the variation of model parameters is given in Section 10.3.

[6] The term "observable" is used here, in deviation from its usual meaning, for the three variables in the right column of Fig. 4.7

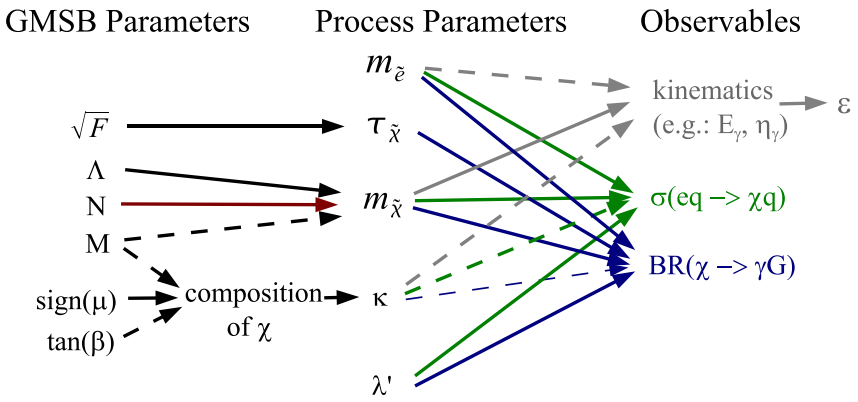

FIGURE 4.7: Influence of GMSB parameters (left) on observables (right) through the parameters which characterise the physical process (middle). κ denotes the $e\,\tilde{l}\,\tilde{\chi}$ coupling. Weak dependencies are shown as dashed lines. In this thesis the selectron mass is treated as a free parameter.

The relations between GMSB parameters and observables can be split into two parts by introducing a third set of parameters which are the physical parameters of the process under study as illustrated in Figure 4.7. They constitute an interface between the GMSB parameters they are determined from, and the observables. This is helpful since one observes for instance, that Λ, M and N have compensating effects on the gaugino mass. While Λ is the main sparticle mass parameter, M influences the masses through the RGEs. Also N effects the masses of the superpartners simply because for higher N more messenger particles contribute in the loop corrections. Therefore, for higher values of N, lower values of Λ have to be chosen to give the same gaugino mass. Fig. 4.7 also shows that, once the masses and $\sqrt{F}$ are fixed, the other GMSB parameters only have an influence through the variation of the gaugino composition, which is very small (see Sect. 4.2.2 below).

The separation into two classes of dependencies illustrated in Fig. 4.7 is used also for the organisation of the rest of this section. Since the investigation should focus on the parameter region with high observability the second column of arrows has to be discussed first.

4.2.1 Influence of Process Parameters on Observables

This section describes how the three observables of Fig. 4.7 depend on the masses and couplings of the particles in the signal processes. The relations discussed here are independent of the underlying SUSY model.

- **Selection efficiency**
  The probability that a signal event survives all cuts is called the efficiency ϵ:

$$\epsilon = \frac{N_{\text{after-cuts}}}{N_{\text{total}}} \tag{4.2}$$

  where $N_{\text{after-cuts}}$ denotes the number of events after all cuts and N_{total} denotes the total number of events before all cuts. It depends on the signal distributions in the cut-variables. For a given process it is completely determined by the kinematics, which are given by the mass of the produced gaugino and the mass of the exchanged slepton[7]. Since at HERA the initial state is only fixed partially (see Sect. 2.2) it depends also on the momentum fraction of the interacting quark x. A different efficiency may result for processes involving different quark flavours (with different x-distributions) resulting from different λ'_{ijk} couplings. To investigate the importance of this dependency, two samples were generated for the same parameter point (for λ'_{111}), one for electrons (with dominant u contribution) and one for positrons (with dominant d contribution, see Tab. 4.1). The difference in efficiency was below 5%.

- **Cross section**
  The cross section depends on the gaugino and slepton masses and the couplings [61]:

$$\frac{\mathrm{d}\sigma}{\mathrm{d}Q^2_{\tilde{e}}} \propto \kappa^2\, \lambda'^2 \frac{(Q^2_{\tilde{e}} + m^2_u)(Q^2_{\tilde{e}} + m^2_{\tilde{\chi}})}{(Q^2_{\tilde{e}} + m^2_{\tilde{e}})^2} \tag{4.3}$$

  Here, κ denotes the $e\,\tilde{l}\,\tilde{\chi}$ coupling which depends on the composition of the gaugino. For instance, a pure photino neutralino will not couple to neutral particles and a large higgsino component will lead to small couplings for light particles[8]. The production cross section for the lightest neutralino is shown in Figure 4.8 as a function of the two masses involved in the process, separately for an initial electron and positron. A steady increase toward lower masses

[7] It will be shown in Sect. 9.8 that the effect of the slepton mass is small.
[8] The gaugino composition is discussed in Sect. 4.2.2.

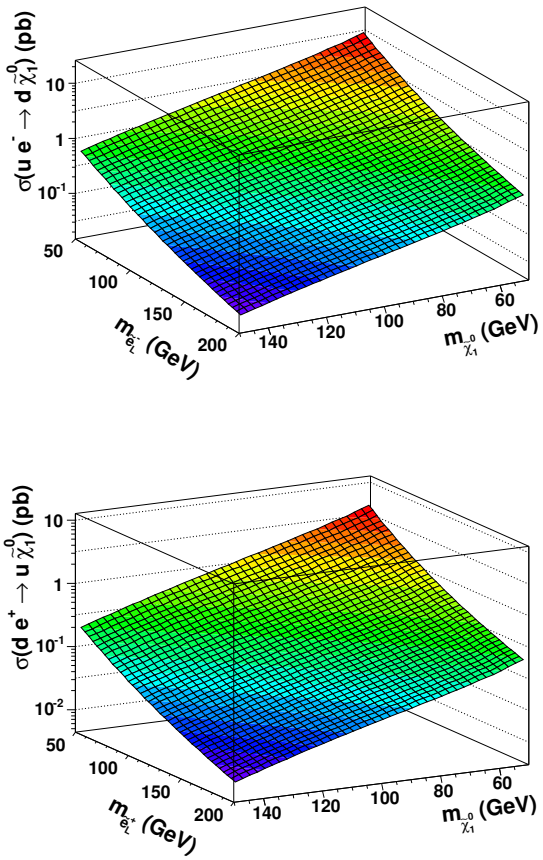

FIGURE 4.8: Production cross section of the lightest neutralino for a λ'_{111} coupling of strength 1 as a function of $m_{\tilde{e}_L}$ and $m_{\tilde{\chi}_1^0}$ with an initial electron (top) and positron (bottom).

is observed with over half of the mass plane lying above $\sigma \approx 10^{-1}$ for which a visible signal can be expected (for $\mathcal{L} = 300\,\mathrm{pb}^{-1}$).

- **Branching ratio**
  The branching ratio depends on all parameters entering in the different decay channels, for instance

$$\mathrm{BR}(\tilde{\chi}_1^0 \to \gamma\tilde{G}) = \frac{\Gamma(\tilde{\chi}_1^0 \to \gamma\tilde{G})}{\sum_f \Gamma_f}\,, \tag{4.4}$$

  where the different channels f that contribute to the decay of the lightest

TABLE 4.4: Decay modes of the lightest neutralino.

Decay	BR lower limit	BR upper limit
$\tilde{\chi}_1^0 \to \gamma\tilde{G}$	0% for high $\sqrt{F}$	100% for low $\sqrt{F}$
$\tilde{\chi}_1^0 \to lqq$	0% for $\lambda' = 0$	100% for high $\sqrt{F}$
$\tilde{\chi}_1^0 \to Z^0\tilde{G}$	0% mostly	2% for high $m_{\tilde{\chi}_1^0}$
$\tilde{\chi}_1^0 \to H^0\tilde{G}$	0% mostly	0.01% for high $\tan\beta$
$\tilde{\chi}_1^0 \to e^{\pm}\tilde{e}^{\mp}$	only if $m_{\tilde{e}_L} < m_{\tilde{\chi}_1^0}$	

neutralino are listed in Table 4.4. The neutralino and chargino decay rates were investigated elsewhere [62, 63] in the framework of RPV MSSM. In the GMSB model, the primary parameters which determine the branching ratios are $\sqrt{F}$ and $\lambda^{'}$ (see Sect. 4.2.2 below). The contributions from other than the investigated signal processes are observed to be small. Therefore, for a given value of $\sqrt{F}$ and λ', the BRs depend mainly on the selectron and neutralino masses, as shown for three different examples in Figure 4.9. One observes that for small values of $\sqrt{F}$ it is always close to 100% in the region where the $\tilde{\chi}_1^0$ is the NLSP, while it drops for values $m_{\tilde{e}_L} < m_{\tilde{\chi}_1^0}$ where the neutralino decay into the selectron becomes important[9]. The small bumps which are visible are caused by other decay channels. The dependence on the selectron mass which is observed for the two cases of higher $\sqrt{F}$ values results from the fact that the $\not{R}_P$ decay channel which proceeds through a virtual selectron is highly favored for selectron masses close to the neutralino mass.

4.2.2 Influence of GMSB Parameters on Process Parameters

The masses and couplings of the particles involved in the signal processes are determined from the six GMSB parameters (see Fig. 4.7). The formulas corresponding to the different arrows were already given in Section 2.4.4. However, in order to see what are the dominant signal processes it is necessary to ask some higher-level questions:

- Which of the gauginos are produced?
- What is the composition of the gauginos?

[9] In this region the branching ratio depends also on κ.

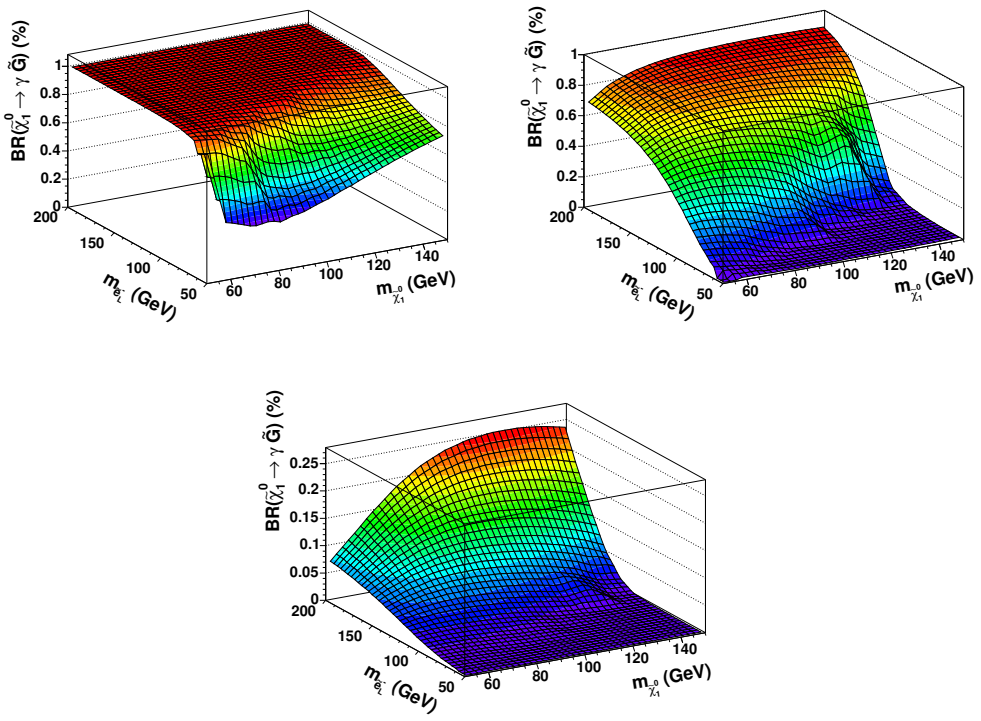

FIGURE 4.9: Branching ratio for the GMSB decay of the lightest neutralino as a function of $m_{\tilde{e}_L}$ and $m_{\tilde{\chi}_1^0}$ for $\sqrt{F} = 230\,\text{GeV}$ (top, left), $\sqrt{F} = 900\,\text{GeV}$ (top, right) and $\sqrt{F} = 2100\,\text{GeV}$ (bottom).

- Which sparticle is the NLSP?
- What is the contribution of the different decay channels?

The answers will in general be different for different regions in GMSB parameter space. To facilitate the understanding of the following paragrphes the last question will be answered first.

Contribution from different decay channels

The dominant variable for the determination of the decay channel is the SUSY breaking scale $\sqrt{F}$. In R_P-conserving models it determines the lifetime of the gauginos (see Eq. (2.52)). When also R_P-violating decays are allowed they will become important as the RPC-lifetime increases. Their relative importance will

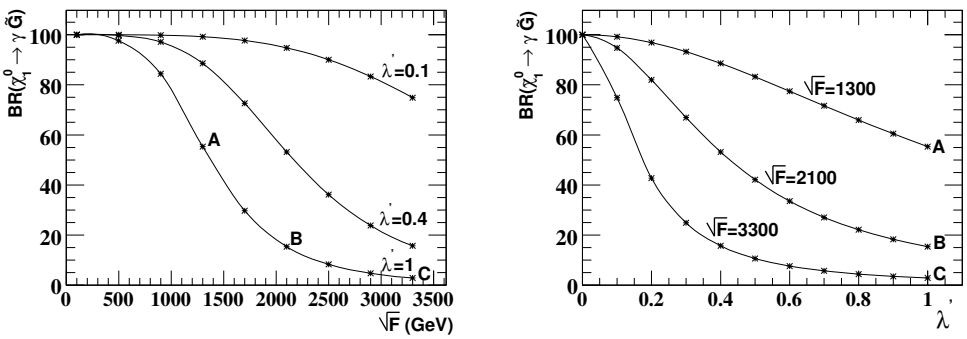

FIGURE 4.10: Influence of $\sqrt{F}$ and strength of $\lambda^{'}$ coupling on the branching ratio for an example of $m_{\tilde{\chi}_1^0} = 73\,\text{GeV}$ and $m_{\tilde{e}} = 190\,\text{GeV}$ (and $\tan\beta = 2$, $sign(\mu) = -1$). The points marked by A, B and C correspond to the same parameter points in the two graphs.

of course depend on the strength of the λ' coupling. The interplay of $\sqrt{F}$ and λ' is shown in Figure 4.10. The curves depend also on the masses of the neutralino (determined by Λ, M and N) and the selectron, while the dependence through the coupling, influenced mainly by the parameters $sign(\mu)$ and $\tan\beta$, has only a minor influence ($\lesssim 5\%$) on the branching ratio. For the lightest neutralino, the sum of the BRs for the decay into the gravitino and the $\not{R}_P$ decays adds up to almost 100%. Only at high values of $m_{\tilde{\chi}}$ the decay into the Z^0 receives some importance, but its contribution stays below $\sim 5\%$ in all the relevant parameter space.

For the heavier gauginos the situation is very different since they can decay into the particles which lie below them in the mass spectrum. Figure 4.11 shows the BR dependence on $\sqrt{F}$ for the GMSB and $\not{R}_P$ channels of the lightest chargino and the second lightest neutralino. Also here, the contribution of the GMSB decays decreases with increasing $\sqrt{F}$, while the $\not{R}_P$ decay contribution increases. In addition to the decays shown in Fig. 4.11, at high $\sqrt{F}$, the $\tilde{\chi}_1^+$ decays in over 30% of the cases into $\tilde{\tau}^+\nu_\tau$. The remaining are decays into the lightest neutralino (1%). The $\tilde{\chi}_2^0$ decays into $Z^0\tilde{G}$ (18%) for low $\sqrt{F}$ and into $\tilde{\tau}^\pm\tau^\mp$ (36%) and $\tilde{\mu}^\pm\mu^\mp$ (22%) for high $\sqrt{F}$ (all numbers are given for the parameters listed in Fig. 4.11).

Contribution from different gauginos

Another important question is which of the different gauginos have a high enough effective cross section ($\sigma_{\text{eff}} = \sigma \cdot BR$) to contribute significantly to the number of

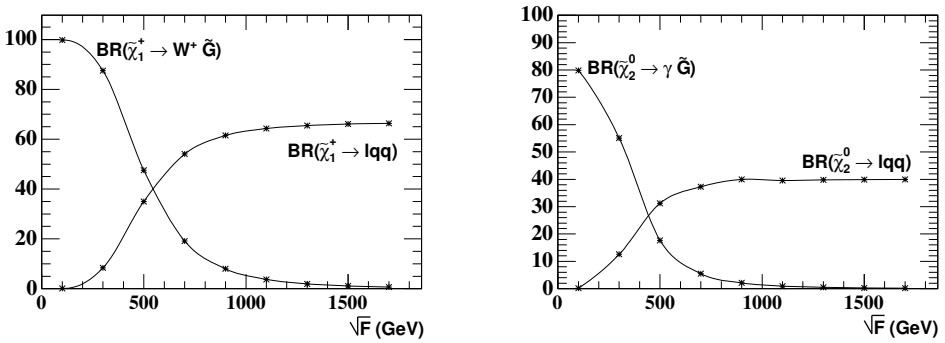

FIGURE 4.11: Branching ratios of $\tilde{\chi}_1^+$ and $\tilde{\chi}_2^0$ decay, as a function of $\sqrt{F}$. For $m_{\tilde{\chi}_1^+} = 126\,\text{GeV}$, $m_{\tilde{\chi}_2^0} = 127\,\text{GeV}$, $m_{\tilde{e}} = 190\,\text{GeV}$ and $\lambda' = 1$ ($sign(\mu) = -1$, $\tan\beta = 2$, $M\Lambda = 2$).

expected signal events. Figure 4.12 shows the number of expected events for the three lightest gauginos in the region of low $\sqrt{F}$, where the GMSB decays dominate. Since the shown behavior is mainly determined by the mass spectrum the effects of the other GMSB parameters is small. The $\tilde{\chi}_1^\pm$ decays into a different final state which is not investigated here. However, it is notable that it reaches similar effective cross sections as the lightest neutralino for high selectron masses. In the scan over $m_{\tilde{\chi}_1^0}$, the lines of the heavier gauginos are curved since their masses increase faster than $m_{\tilde{\chi}_1^0}$. The contribution from the second lightest neutralino lies below $\sim 10\%$. The situation changes for high values of $\sqrt{F}$ where the R_P-violating decay channels dominate, as shown in Figure 4.13. Since now the charged gauginos decay into the same final state the contribution from $\tilde{\chi}_1^\pm$ has to be taken into account. Also here the $\tilde{\chi}_2^0$ contribution is very small. The first increasing and then decreasing of the effective cross section, as visible for instance in the right plot of Fig. 4.13 for the second lightest neutralino $\tilde{\chi}_2^0$, is a branching ratio effect due to the transition of the $\not{R}_P$ decay from a decay through a real ($m_{\tilde{e}_L} < m_{\tilde{\chi}_2^0}$) to a virtual selectron ($m_{\tilde{e}_L} > m_{\tilde{\chi}_2^0}$). Toward small sectron masses the decay $\tilde{\chi}_2^0 \to e^\pm \tilde{e}_L^\mp \to e^\pm \tilde{\chi}_1^0 e^\mp$ is kinematically favoured.

Gaugino composition

The composition of the produced gaugino influences the cross section *via* the strength of the coupling between the initial lepton, the exchanged slepton and

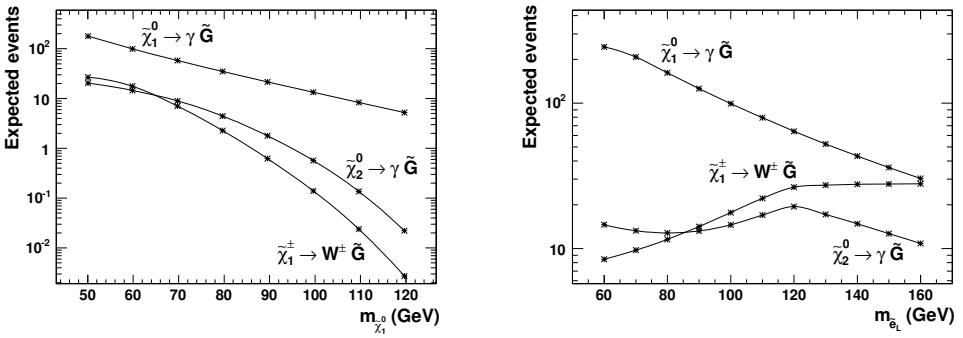

FIGURE 4.12: Number of expected events from the GMSB decays of the three lightest gauginos $\tilde{\chi}_1^0$, $\tilde{\chi}_1^\pm$ and $\tilde{\chi}_2^0$ as a function of neutralino mass (left) and selectron mass (right) for $\sqrt{F} = 230\,\text{GeV}$. For the left scan the selectron mass was increased with the neutralino mass according to $m_{\tilde{e}_L} - m_{\tilde{\chi}_1^0} = 40\,\text{GeV}$. In the right scan the other sparticle masses are $m_{\tilde{\chi}_1^0} = 60\,\text{GeV}$, $m_{\tilde{\chi}_1^+} = 127\,\text{GeV}$ and $m_{\tilde{\chi}_2^0} = 128\,\text{GeV}$. (The other GMSB parameters are $N = 1$, $M/\Lambda = 2$, $sign(\mu) = -1$ and $\tan\beta = 2$.)

the produced gaugino. It also effects the branching ratios of the different gaugino decay channels. Hence, for a high effective cross section ($\sigma_{\text{eff}} = \sigma \cdot BR$) in the GMSB channel two conditions have to be fulfilled:

1. For a high production cross section σ the higgsino component should be small since the higgsino coupling strength is proportional to the mass, and the electron is light.

2. For a high branching ratio the photino component should be large to enhance the decay into a photon.

For the $\not{R}_P$ decays only the first condition applies.

Since the charginos have only two components ($\tilde{H}^\pm$ and $\tilde{W}^\pm$) their composition can be displayed by one number. The lightest chargino is always $\sim 99\%$ wino (*i.e.* $\sim 1\%$ higgsino)[10] in the investigated GMSB parameter space.

In order to display the composition of the neutralinos a Dalitz-type plot may be used, as shown in Figure 4.14. It makes use of the geometrical property of equilateral triangles, that for each point inside the triangle, the sum of the distances

[10]Since not only the rows, but also the columns of the mixing matrix have to sum up to 100% it directly follows that the second chargino is $\sim 99\%$ higgsino and $\sim 1\%$ wino.

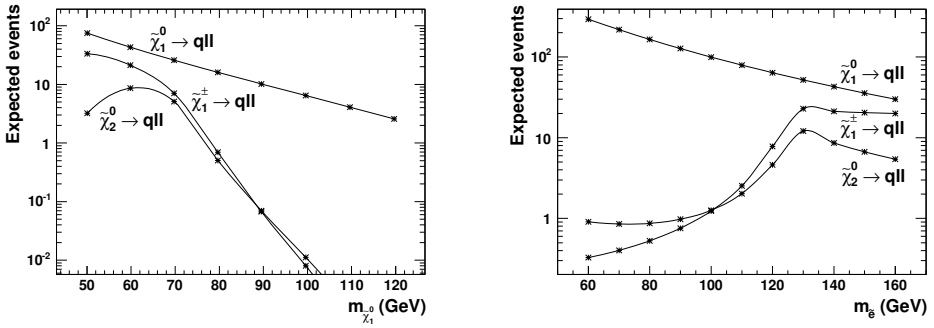

FIGURE 4.13: Number of events events from the R_P-violating decay channels of the three lightest gauginos $\tilde{\chi}_1^0$, $\tilde{\chi}_1^\pm$ and $\tilde{\chi}_2^0$ as a function of neutralino mass (left) and selectron mass (right) for $\sqrt{F} = 3300\,\text{GeV}$. For the left scan the selectron mass was increased with the neutralino mass according to $m_{\tilde{e}_L} - m_{\tilde{\chi}_1^0} = 80\,\text{GeV}$. In the right scan the other sparticle masses are $m_{\tilde{\chi}_1^0} = 60\,\text{GeV}$, $m_{\tilde{\chi}_1^+} = 127\,\text{GeV}$ and $m_{\tilde{\chi}_2^0} = 128\,\text{GeV}$. (The other GMSB parameters are $N = 1$, $M/\Lambda = 2$, $sign(\mu) = -1$ and $\tan\beta = 2$.)

to the three sides is always constant. In defining this constant to be 100% this plot enables to display the composition of the neutralino with one single point[11]. While in the MSSM all compositions are possible, in the more restricted GMSB model the composition is always similar for the investigated region in parameter space. All points lie in the photino-dominated region. Hence, the gaugino composition favoured by the GMSB model ensures a high value of the κ coupling in all the investigated parameter space.

Type of NLSP

The nature of the NLSP (see Tab. 2.8) influences the effective cross section ($\sigma \cdot BR$) of the signal processes. However, only the cases where the lightest stau is lighter than the lightest neutralino are problematic since the neutralino then decays *via* $\tilde{\chi}_1^0 \to \tilde{\tau}_1^\pm \tau^\mp$[12]. Due to the relation given in Eq. (2.51) this happens typically for higher values of N and lower values of M/Λ. Figure 4.15 shows the region where the lightest stau is the NLSP in the case of $N = 1$. Since the sparticle

[11] The two higgsino components $\tilde{H}_u^0$ and $\tilde{H}_d^0$ are not displayed separately, but only the total higgsino fraction.

[12] This does not mean that this region has to be excluded from investigation *a priori* since the BR may drop rather slowly in the transition region (see *e.g.* Fig. 4.9).

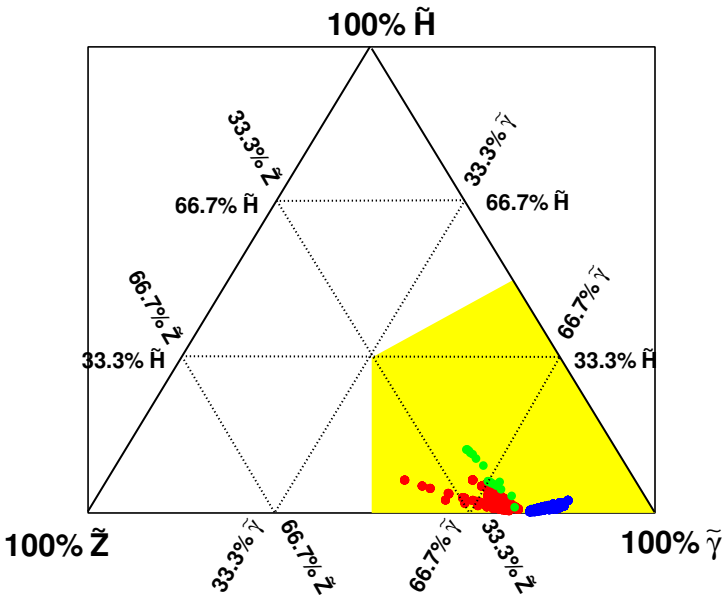

FIGURE 4.14: Dalitz-like neutralino composition plot. Here shown for the example of the lightest neutralino $\tilde{\chi}_1^0$. The points result from scans over the investigated GMSB parameter space. The shaded area denotes neutralinos which are predominantly photino-like.

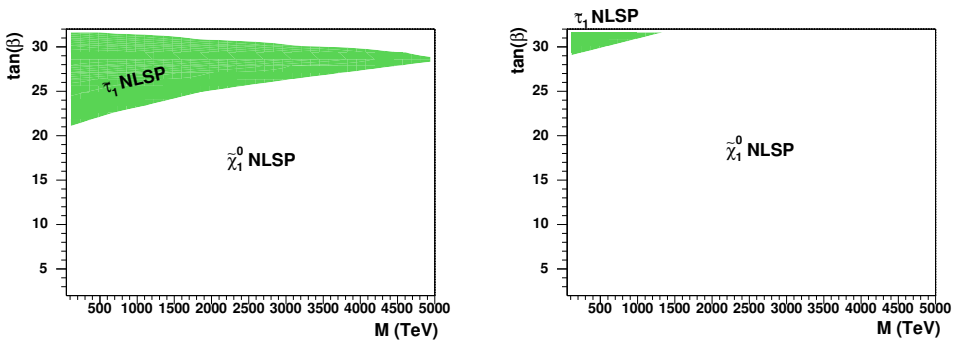

FIGURE 4.15: Parameter region where $\tilde{\tau}_1^{\pm}$ is the NLSP for $N = 1$. It is independent of $\sqrt{F}$ and Λ. The scan was made with $\Lambda = 50\,\text{TeV}$ so that M/Λ varies between 1 and 100. The results are shown separately for negative μ (left) and positive μ (right).

masses are proportional to Λ the hyperplane where $m_{\tilde{\chi}_1^0} - m_{\tilde{\tau}_1} = 0$ is independent of Λ. In the region where M/Λ lies between 1 and 1.1 the $\tilde{\tau}_1^{\pm}$ is the NLSP for all $\tan\beta$. For higher N rather high values of M are necessary to ensure a neutralino NLSP.

4.3 Limits of GMSB Parameter Space

Very few experimental constraints on GMSB parameters exist. A lower limit of $\sqrt{F} > 221\,\text{GeV}$ has been derived by the CDF collaboration from searches for the $\gamma \not{E}_T$ signal [64], translating into a lower limit for the gravitino mass of $m_{\tilde{G}} > 1.17 \times 10^{-5}\,\text{eV}$. The LEP experiments derived a lower limit for the mass of the lightest neutralino of $m_{\tilde{\chi}_1^0} \gtrsim 45\,\text{GeV}$ [65, 66, 67, 68]. They also investigated the GMSB process $e^+e^- \to \tilde{\chi}_1^0\tilde{\chi}_1^0 \to \tilde{G}\tilde{G}\gamma\gamma$ and derived a limit in the $m_{\tilde{\chi}_1^0} - m_{\tilde{e}_R}$ plane with a 95%CL limit on the neutralino mass of $m_{\tilde{\chi}_1^0} > 99.5\,\text{GeV}$ [69, 70, 71]. The CDF and D0 experiments have derived a combined limit for the GMSB decay of neutralinos and charginos of $m_{\tilde{\chi}_1^0} > 114\,\text{GeV}$ and $m_{\tilde{\chi}^{\pm}} > 209\,\text{GeV}$ for the parameter point $M/\Lambda = 2$, $N = 1$, $\tan\beta = 15$, $\mu > 0$ [72]. The parameter $\sqrt{F}$ was assumed to be small enough to ensure that the neutralino decays inside the detector [73].

Table 4.5 lists the existing lower and upper bounds for the GMSB parameters[13]. To summarise the effects discussed in this section it also shows the correlation between the GMSB parameters and the cross section and the branching ratio for the decay into the gravitino.

4.3.1 Standard Parameters

In order to check the possible reach of the analysis, the parameter point with the highest number of expected events has to be identified. Following the discussion above the following GMSB parameters were chosen:

$$\sqrt{F} = 233\,\text{GeV},\ N = 1,\ M/\Lambda = 1.1,\ |\mu| < 0,\ tan\beta = 2 \tag{4.5}$$

The number of expected events then depends only on the neutralino mass (determined by Λ) and the selectron mass. It should be noticed that the optimal set of parameters changes slightly for different points in the $m_{\tilde{\chi}_1^0} - m_{\tilde{e}_L}$ mass plane. The parameters were optimised for high neutralino masses. For the mass point

[13] For the theoretical limits see Sect. 2.4.4.

TABLE 4.5: Allowed regions of GMSB parameters, where superscripts t and e indicate theoretical and experimental bounds, respectively. The last two columns indicate whether cross section and branching ratio are positively or negatively correlated with the given parameter. The effects are given for constant $m_{\tilde{e}_L}$ and $m_{\tilde{\chi}_1^0}$ which requires Λ to be adjusted accordingly.

Lower Bound		Parameters		Upper Bound	σ	BR
-1	$\leq$	$sign(\mu)$	$\leq$	$+1$	-	-
2 $^{(t)}$	$\leq$	$\tan\beta$	$\leq$	50 $^{(t)}$	$-sign(\mu)$	-
1	$\leq$	M/Λ	$\leq$	10^4 $^{(e)}$	$sign(\mu)$	$+$
1	$\leq$	N	$\leq$	5 $^{(t)}$	not	-
$221\,\text{GeV}$ $^{(e)}$	$\leq$	$\sqrt{F}$	$\leq$	$10^7\,\text{GeV}$ $^{(t)}$	not	-

$(m_{\tilde{\chi}_1^0}, m_{\tilde{e}_L}) = (100\,\text{GeV}, 100\,\text{GeV})$ for instance 158 events are expected in the analysed HERA I and II data.

Chapter 5

HERA and ZEUS

The sacred marriage of HERA and ZEUS
was solemnly celebrated on Olympus,
in the presence of all gods.

Greek Mythology

This chapter introduces the experimental setup, mainly the electron-proton collider HERA and the general purpose detector ZEUS which provided the data investigated in this thesis. During the shutdown in 2000/2001 both HERA and ZEUS underwent a substantial upgrade[1]. The important changes are pointed out whenever appropriate. Special emphasis is placed on detector components with particular importance for the presented analyses.

5.1 HERA Accelerator

The primary discovery tools in particle physics during the last decades have been particle accelerators. HERA [74] which stands for "Hadron-Elektron-Ring-Anlage" is the main accelerator facility at DESY[2] (see Fig. 5.1) and, at the time of writing, the only electron-proton collider in the world. It is situated in a tunnel 15 m - 25 m underground in north-west Hamburg, Germany. Built between 1984 and 1990, the HERA collider started operation in 1992. Positrons can be accelerated instead of electrons by flipping the magnetic fields.

[1] The two phases of data taking before and after the upgrade are referred to as HERA I and HERA II.

[2] Deutsches Elektronen-Synchrotron

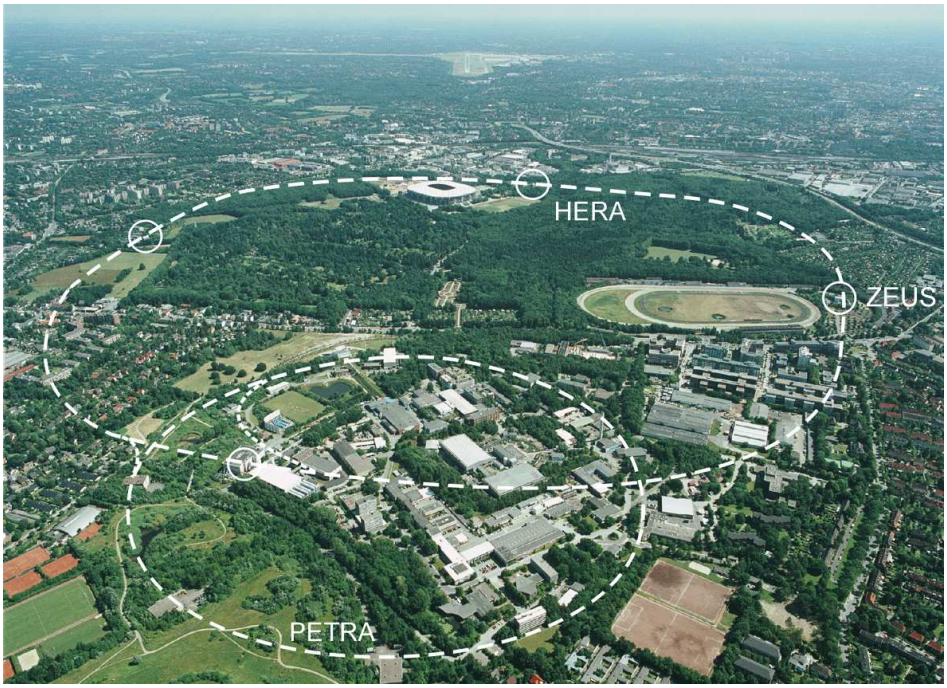

FIGURE 5.1: Aerial view of the DESY laboratory in Hamburg, Germany. The dashed lines mark the course of the beamlines for HERA and its pre-accelerator PETRA which encloses the main DESY site. The ZEUS detector is situated off of the main DESY campus at the south side of HERA.

The layout of the different accelerators at DESY is shown in Figure 5.2. The HERA ring consists of four straight segments with a length of 360 m each and four circular arcs with radii of 739 m. Leptons and protons are stored in two separate rings.

The HERA design parameters are summarized in Table 5.1. A center of mass energy of 318 GeV results in a maximal reachable Q^2 of 10^5 GeV^2 which exceeds the value of previous fixed-target experiments by two orders of magnitude. To estimate the number of background events originating mainly from beam-gas interactions, cosmics and halo-muons, non-colliding bunches (when either the lepton or proton bunch is empty) as well as "pilot bunches" (when both are empty) are used, so that only 180 of the 210 possible bunches are filled. A charged particle accelerated in a circle loses energy due to synchrotron radiation according to:

$$\Delta E \propto \frac{E^4}{m^4 r} \tag{5.1}$$

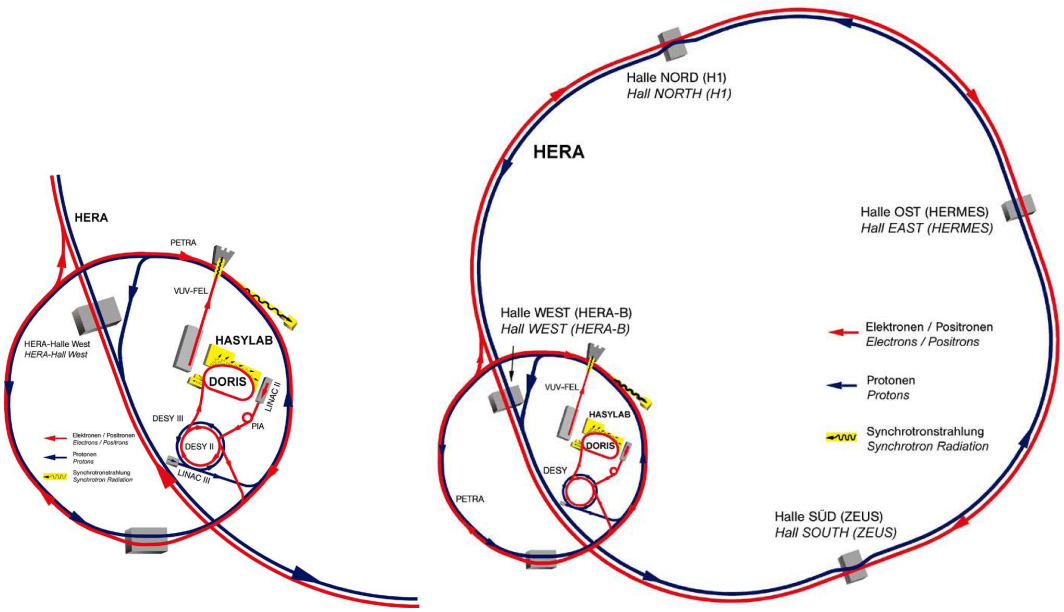

FIGURE 5.2: Schematic view of HERA and the pre-accelerator system.

This gives the main restriction for the reachable lepton beam energy. As it is proportional to the fourth power in energy, intense endeavors have to be made for a further increase in energy. For this reason, superconducting cavities are used for the lepton ring while the proton beam is accelerated in normal cavities. It is also obvious from the formula that an enlargement of the circle would lead only to a minor increase in lepton energy. Because of their higher mass, the energy loss through synchrotron radiation for the protons is 13 orders of magnitude smaller than for electrons and the strength of the bending magnets becomes the energy-limiting factor. Consequently, superconducting magnets providing a magnetic field of 5.3 T are used for deflecting the protons whereas normal conducting magnets of a field strength of 0.3 T bend the leptons. Before being injected into HERA leptons and protons pass through several pre-acceleration steps as follows:

Electrons and Positrons: Electrons are emitted from a hot cathode which is situated inside an electric field. In the linear accelerator LINAC II they are accelerated to an energy of 450 MeV. At the end of LINAC II, positrons can be produced by directing the initial electron beam onto a tungsten plate. The electrons are decelerated by emitting bremsstrahlung which induces pair production processes. As the number of positrons produced in this way is three orders of magnitude lower

TABLE 5.1: HERA parameters for different running periods *:since 1998 [75]; †:since 2003 [76]

Parameter	Value	
Circumference	6336 m	
Center of Mass Energy	314 GeV / 318 GeV*	
Beam Crossing Time	96 ns	
Luminosity	1.6×10^{31} cm^{-2}s^{-1} / 7.0×10^{31} cm^{-2}s^{-1}†	
	Proton Beam	Lepton Beam
Nominal Energy	820 GeV / 920 GeV*	27.5 GeV
Current	163 mA / 140 mA†	58 mA
Particles per Bunch	1.0×10^{11}	3.65×10^{10} / 4.18×10^{10}†
Max. Number of Bunches	210 / 180†	210/180†
Bunch Length	11 cm	0.8 cm
Beam Width (σ_x)	0.280 mm / 0.118 mm†	0.286 mm / 0.118 mm†
Beam Height (σ_y)	0.058 mm / 0.032 mm†	0.060 mm / 0.032 mm†

than the number of initial electrons they are collected in the storage ring PIA until the required number of particles per bunch has been reached. Subsequently, they are injected into DESY II and than into PETRA II[3] where they reach an energy of 12 GeV before they are finally transfered into HERA. The positron-beam lifetime for its final energy of 27.5 GeV is about eight hours. For electrons the lifetime is reduced due to interactions with positive charged dust particles.

Protons: A bottle of hydrogen serves as the source for protons. First, H^- ions are produced which are accelerated up to an energy of 50 MeV in the LINAC III accelerator. The negative ions are shot through a stripper foil where their two electrons are stripped of. Afterwards, the produced protons are accelerated in DESY III and PETRA up to 40 GeV, before being transfered into HERA. The procedure is repeated until HERA is filled with 180 bunches. The proton-beam lifetime is of the order of several days.

In both HERA I and HERA II running periods the lepton beam energy was

[3]The "Positronen-Elektronen Tandem Ring Anlage" PETRA was originally used for e^+e^- colliding beam experiments. At the time of writing it is used as a pre-accelerator for both electrons and protons.

27.5 GeV. The proton beam energy was changed from 820 GeV in 1994 – 1997 to 920 GeV since 1998, resulting in center of mass energies of 300 GeV and 318 GeV, respectively. The event rate N for a specific process a and its cross section σ_a are proportional:

$$N_a = \mathcal{L}\sigma_a \tag{5.2}$$

where the factor $\mathcal{L}$ is called luminosity. It depends on the number of particles in the two bunches, n_l and n_p, the collision frequency f and the beam profile described by σ_x and σ_y:

$$\mathcal{L} = f\frac{n_l n_p}{4\pi\sigma_x\sigma_y} \tag{5.3}$$

The increase of the total integrated luminosities as a function of operating time is shown in Figure 5.3 for HERA I and in Figure 5.4 for HERA II. The ratio of luminosity gated by ZEUS and delivered by HERA varies between 54% and 77% in the different running periods.

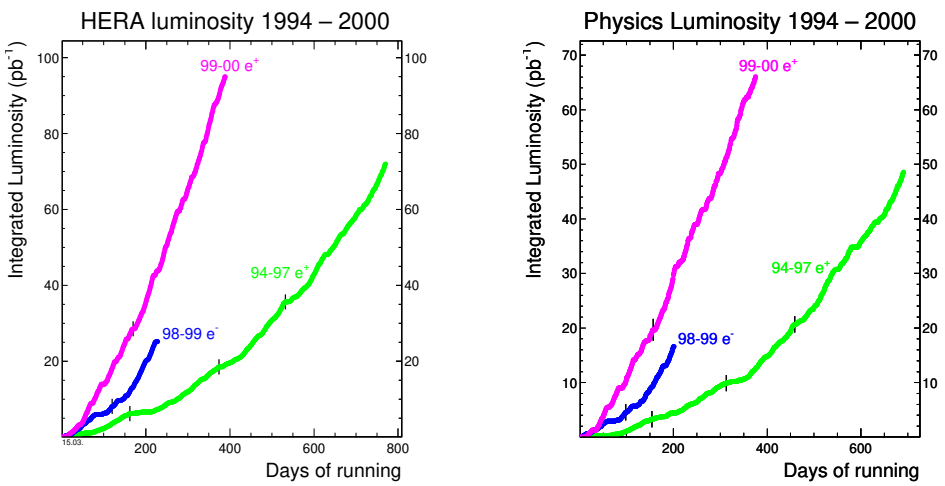

FIGURE 5.3: Integrated luminosities delivered by HERA (left) and luminosity recored by the ZEUS detector (right), for the HEAR I period 1994 – 2000.

The two beams are brought into collision under a crossing angle of zero degrees in the north and south experimental areas, where the two collider experiments H1 and ZEUS are located. The other two HERA experiments, HERMES in the east and HERA-B in the west, were designed to use only one of the two beams. The fixed target experiment HERMES investigates the spin structure of the nucleons of an internally polarized gas target. For this purpose it uses the lepton beam

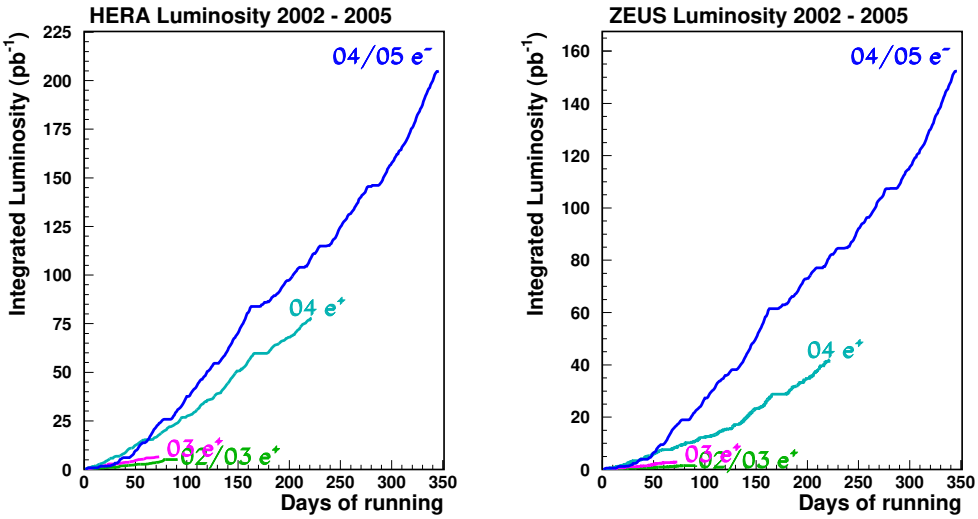

FIGURE 5.4: Integrated luminosities delivered by HERA (left) and luminosity recored by the ZEUS detector (right), for the HERA II period $2002-2005$.

which is longitudinally polarized in that area. HERA-B was designed to measure CP-violation in the $B^0\bar{B}^0$-system, where the B-mesons are produced by collisions of the proton beam halo with a wire target. It was in operation until 2003. The upgrade to the HERA accelerator in the years 2000 and 2001 was performed to increase the specific luminosity in the interaction points by a factor of 4 to 5. Additionally, spin rotators were installed in front of ZEUS and H1 to provide a longitudinally polarized lepton beam, as illustrated in Figure 5.5.

5.1.1 Polarisation Measurement

Particles circulating in a storage ring emit synchrotron radiation which induces a transverse polarisation $P_\perp$ *via* the *Sokolov-Ternov* effect [77]. It increases with time according to:

$$P_\perp(t) = -P_{max}(1 - e^{-t/\tau}) \tag{5.4}$$

where τ is the build up time. For the lepton beam at HERA (the energy dependence is $\tau \propto 1/E_e^5$) it has a value of $\tau \sim 40$min. Average values of P_{max} achieved at HERA are 35%[4]. Transverse magnetic fields can be used to convert the transverse into a longitudinal polarisation (so called *spin rotators* [78, 79], see Fig. 5.5). The transverse and longitudinal polarasation are measured by TPOL and LPOL,

[4]The theoretical limit is $P_{max} = 8/(5\sqrt{3}) \simeq 92.4\%$

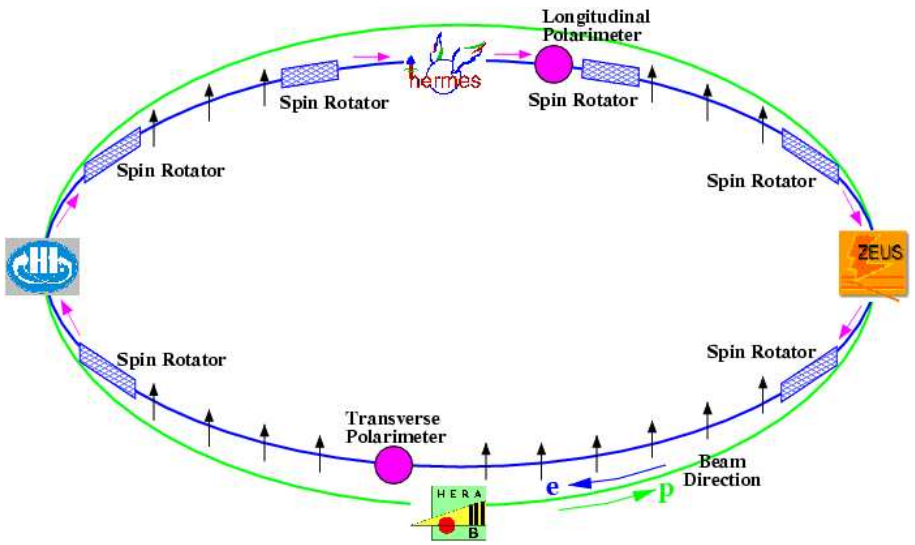

FIGURE 5.5: Schematic view of HERA showing the positions of the spin rotators and polarimeters for the lepton beam. Vertical arrows indicate transverse polarisation and arrows along the beam direction indicate longitudinal polarisation.

respectively. Circular polarised intense pulsed laser beams are used in order to explore the polarisation dependence of Compton scattering for the polarisation measurement. While LPOL measures the energy asymmetry of backscattered photons from left- and right-handed polarised laser beams, TPOL measures the angular asymmetry. For the HERA II upgrade, both polarimeters have been equipped to provide also single bunch polarisation measurements to deal with the polarisation difference between colliding and non-colliding bunches. The statistical uncertainty of the TPOL measurement is 0.5%, compared to 1% for the LPOL. The systematic uncertainties for TPOL and LPOL are 3.4% and 1.6%, respectively.

5.2 ZEUS Experiment

The ZEUS [80] detector [81] is a general purpose detector for the study of lepton-proton scattering. Its layout is adjusted to the event topologies produced at HERA. In CC DIS processes a hermetic detector is required in order to reconstruct the missing transverse momentum carried by the outgoing neutrino. For NC DIS processes the primary task is the identification of the scattered lepton, which requires precise measurements over a wide momentum range. For low-momentum

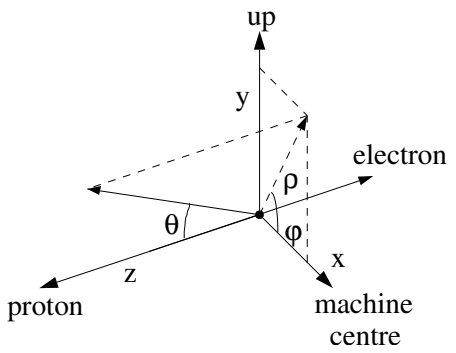

FIGURE 5.6: The ZEUS coordinate system.

particles tracking in a magnetic field is used (see Sect. 5.2.1) while high energy particles are well measured by a calorimeter system (see Sect. 5.2.3). Energies from a few MeV to hundreds of GeV can be measured in the forward region, where most of the final state particles are found due to the large momentum imbalance between the lepton and the proton beam. Consequently, another characteristic of the detector layout is a large forward-backward asymmetry to accommodate the boost of the center-of-mass in the proton beam direction. On the other hand, the symmetry around ϕ is reflected in a coaxial arrangement of the ZEUS sub-detectors around the beam line. The ZEUS coordinate system is shown in Figure 5.6. It is a right-handed, orthogonal system, with the origin at the nominal interaction point. The direction of the z-axis, pointing in the proton direction, is referred to as *forward* direction. The x-axis is pointing toward the center of HERA and the y-axis is pointing upwards. The polar angle θ and the azimuthal angle ϕ are measured relative to the z and x axes, respectively.

A cross section of the ZEUS detector is shown in Figure 5.7 and Figure 5.8. The main detector is approximately $20\,m$ long, $12\,m$ wide and $11\,m$ high, and weights 3600 tons. The innermost part of the ZEUS detector was the vertex detector (VXD), which was removed in the 1995/1996 shutdown. In 2001 a silicon vertex detector (MVD) was installed in its place. It is surrounded by the central tracking detector (CTD), which is enclosed by a superconducting solenoid providing a magnetic field of 1.43 T for the determination of charge and momentum of the particles. The CTD is supplemented by the forward tracking detector (FTD [82]) with interleaved transition radiation detectors (TRD) and the rear tracking detectors (RTD) to complete the tracking system. In 2001 the TRD system was replaced by

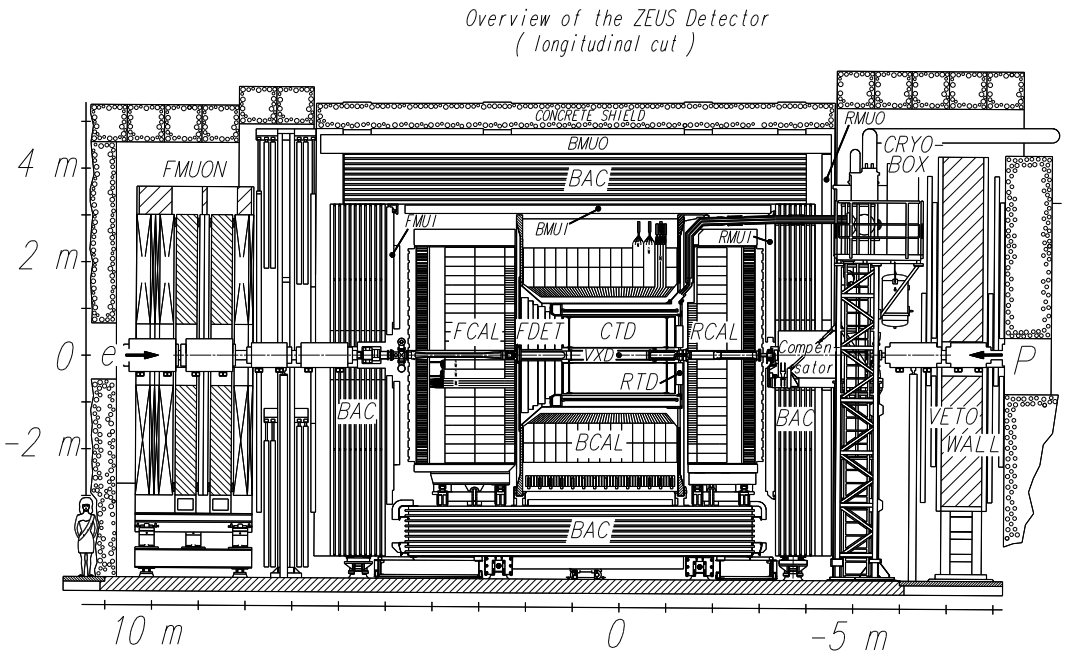

FIGURE 5.7: Cross section of the ZEUS detector along the beam axis.

a Straw Tube Tracker (STT) consisting of two modules built of straw tube layers filling the gaps between the three FTD chambers. Outside the solenoid a high-resolution uranium-scintillator calorimeter (CAL) is located. It is divided into three parts: the barrel (BCAL), forward (FCAL) and rear calorimeter (RCAL). An iron yoke encloses the CAL, providing a return path for the solenoid's magnetic field flux. It also serves as absorber for the backing calorimeter (BAC), which measures energy that escapes detection from the main calorimeter. Muon detectors are located inside (FMUI, BMUI, and RMUI) and outside (FMUO, BMUO and RMUO) the iron yoke. A detector composed of iron and scintillator (VETO wall), used to reject beam related background, is located outside the main detector in the rear direction. Several additional detectors are installed close to the beam-line to measure particles scattered at low polar angles. In the forward direction, the lead-scintillator strip detectors forming the proton-remnant tagger (PRT) are located. It is followed by the leading proton spectrometer (LSP) which allows a measurement of the momentum of protons scattered at very small angles in elastic reactions. Although the ZEUS detector has been in operation since 1992,

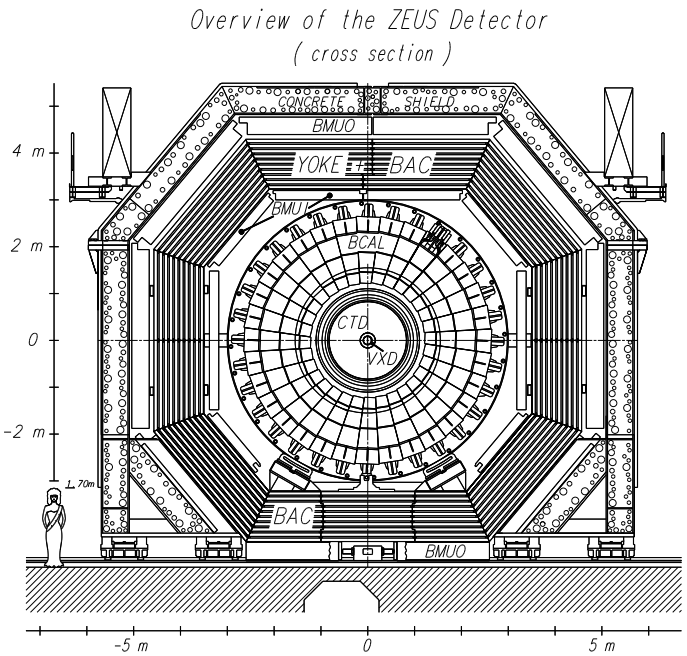

FIGURE 5.8: Cross section of the ZEUS detector in the xy plane.

new detector components were added continuously to incorporate the technical understanding gained during previous running periods and to take into account new physics goals. The most important components are discussed in detail in the following.

5.2.1 Central Tracking Detector (CTD)

The CTD [83, 84, 85] is a cylindrical wire chamber used to measure the direction, charge and transverse momentum of charged particles. Additionally, it provides information on the energy loss dE/dx for particle identification. The inner radius of the chamber is 18.2 cm and the outer radius is 79.4 cm. Its active region covers the longitudinal interval from $z = -100$ cm to $z = 103$ cm, resulting in a polar angle coverage of $15° < \theta < 164°$. The CTD is filled with a mixture of argon (Ar), carbon dioxide (CO_2) and ethane (C_2H_6) with ratios $85 : 5 : 1$. 72 radial layers of signal wires are organized in 9 *superlayers* (SL), each SL consisting of 8 wire layers (see Fig. 5.9). A group of eight radial signal wires with associated field wires in one SL makes up a *cell*. In total 4608 signal wires and 19584 field wires are contained in the CTD. The SLs 1, 3, 5, 7, 9 are mounted parallel to the beam axis (axial SL),

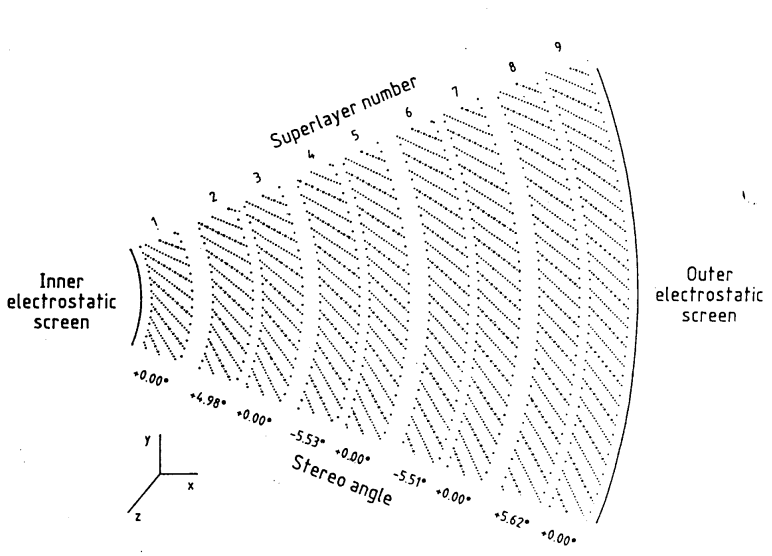

FIGURE 5.9: Cross section view of a CTD octant. Wires (dots) are arranged in 9 superlayers with different stereo angles.

whereas the SLs 2, 4, 6, 8 are inclined with a stereo angle of $\pm 5^\circ$ (stereo SL) to obtain a better determination of the z position. In order to improve the momentum measurement, the CTD was designed to operate inside a magnetic field inducing a Lorentz angle of 45° relative to the radial direction. Therefore, the signal wires are tilted to compensate for the Lorentz angle. The achieved resolution is $100-120\,\mu$m in the $r-\phi$ plane and 1.4 mm in the z coordinate. A charged particle crossing the CTD ionizes the gas along its path. The electrons produced in this way drift toward the positively charged signal wires while the positively charged ions drift toward the negative field wires. The drift velocity of the electrons is approximately constant at 50 mm/ns, but close to the wire an avalanche effect occures, giving an amplification factor of 10^4 on the number of electrons so that a measurable pulse is induced on the signal wire. For trigger purposes, the three inner axial SLs (1, 3, 5) are equipped with a z-by-timing system. The arriving time of the particle is used to determine the z-position, yielding a resolution of 4 cm. The relative transverse momentum resolution for tracks with $p_T > 150\,\text{MeV}$ fitted to the interaction vertex and passing at least three CTD SLs is given by:

$$\frac{\sigma(p_T)}{p_T} = 0.0056 \cdot p_T \oplus 0.0065 \oplus \frac{0.0014}{p_T} \tag{5.5}$$

where the symbol $\oplus$ indicates the quadratic sum and p_T is measured in GeV. The first term gives the contribution from the position resolution of the hits, while the other two terms are due to multiple scattering before and inside the CTD, respectively. The transverse momentum resolution changed with the installation of the MVD in 2001. While multiple scattering increases with the additional material, the hit resolution improves due to the inclusion of MVD hits. Integrating the MVD in the global track reconstruction yields a relative transverse momentum resolution of:

$$\frac{\sigma(p_T)}{p_T} = 0.0026 \cdot p_T \oplus 0.0104 \oplus \frac{0.0019}{p_T} \tag{5.6}$$

5.2.2 Micro Vertex Detector (MVD)

The MVD [86, 87, 88, 89] is a silicon-strip vertex detector which was installed in the upgrade shutdown in 2001 to improve tracking capabilities and increase the acceptance for high-mass and high-Q^2 physics. It is used to tag heavy flavour particles by the reconstruction of primary and secondary vertices. The layout reflects the given physics requirements as well as the restricted available space in the middle of the CTD (see Table 5.2). The MVD is divided into a barrel

Table 5.2: MVD design parameters.

Parameter	Value
Radial Extension	≤ 32.4 cm
Polar angle coverage	$10^\circ < \phi < 150^\circ$
Number of Points per Track	≥ 2
Hit Resolution for Nominal Incident Tracks	$\leq 20\mu$m
Two tracks separation	200μm
Hit Efficiency	$\geq 95\%$
Noise Occupancy	$\leq 10^{-3}$

region (BMVD) and a forward region (FMVD). Constrained by the extension of the longitudinal interaction region, which is determined mainly by the proton bunch length (20 cm), the barrel region is 64 cm long. The BMVD consists of three double layers of silicon strip sensors arranged in concentric planes around the interaction point with a polar coverage of $30^\circ < \phi < 150^\circ$. Due to the oval shaped beam pipe, which is not centered around the interaction point (see Fig. 5.10), the

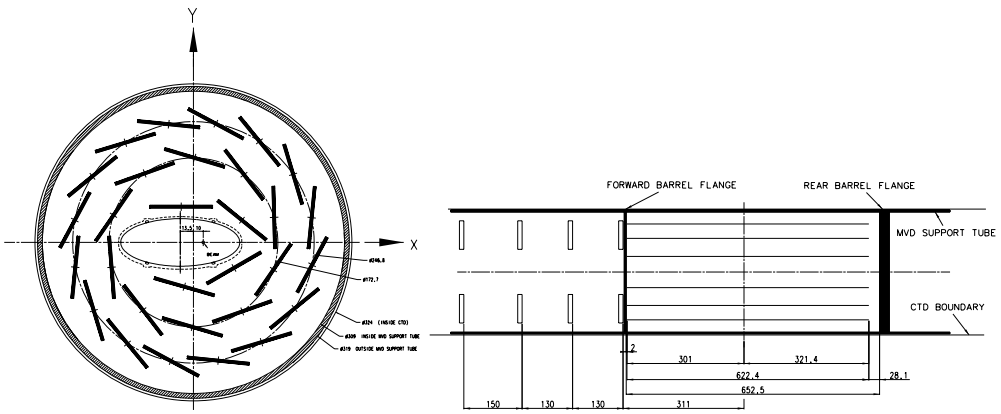

FIGURE 5.10: Schematic layout of the MVD, along the beamline (left) and perpendicular to the beamline (right). Support structures are omitted.

inner layer of the BMVD is incomplete. The silicon sensors used are 64.2 mm × 64.2 mm in size with a thickness of 320 μm. They are covered with 3082 stripes with a pitch of 20 μm. As only every sixth stripe is read out, the effective pitch is 120 μm. The position is determined through capacitive charge division between two readout stripes. The single hit resolution, determined in test beam measurements, is 7.5 μm. A *half module* is formed by two sensors put together along a thin side with perpendicular read out strips on the same side. Their read out strips are connected. Two half modules are glued together back to back to form a module providing two coordinates for each particle traversing it. The ambiguity due to the connected sensors of the half module is resolved at reconstruction level. The FMVD extends the coverage in pseudorapidity to $\eta = 2.6$ and provides additional forward tracking capabilities in a region which was only poorly covered before. It consists of four planes (wheels) mounted perpendicular to the beam axis. Each wheel is made of two back to back layers of 14 silicon sensors each. The number of readout strips per sensor is 480 for forward sensors. They are tilted by $180°/14$ to provide two coordinates for a particle traversing a wheel.

5.2.3 Calorimeter (CAL)

The ZEUS calorimeter [90, 91, 92, 93] is a high resolution compensating calorimeter consisting of alternating layers of uranium and scintillator material. It completely surrounds the tracking devices and the solenoid and covers 99.7% of the 4π solid

angle. The aborber layers are made of $3.3\,mm$ thick depleted uranium plates ($98.1\%\,U^{238}$, $1.7\%\,Nb$, $0.2\%\,U^{235}$). Due to the high density, traversing particles loose energy resulting in a shower development. Their energy is measured in the active material, made of organic scintillators (SCSN-38 polystyrene). Shower particles excite electrons in the scintillator which emit photons when passing to lower energy bands. The photon signal is converted to an electrical signal with the help of photomultiplier tubes (PMT) mounted at both ends of each calorimeter cell. The thickness of the absorber and of the active material was chosen in order to give the same response for an electron and a hadron of the same energy ($e/h = 1.00 \pm 0.02$). This mechanism, called *compensation* allows for good resolution in both electromagnetic and hadronic energy. The energy resolution of the ZEUS CAL was determined in test beam measurements to:

$$\frac{\sigma_{el}}{E} = \frac{18\%}{\sqrt{E}} \oplus 2\% \quad \text{and} \quad \frac{\sigma_{\mathrm{hac}}}{\mathrm{E}} = \frac{35\%}{\sqrt{\mathrm{E}}} \oplus 1\% \tag{5.7}$$

with E in GeV. The CAL is divided into three parts: the forward (FCAL), barrel (BCAL) and rear (RCAL) calorimeter (see Fig. 5.11). Since most of the final state particles produced in a lepton-proton interaction at HERA are boosted in the forward (proton) direction, the three parts are of different thickness, the thickest being the FCAL ($7\,\lambda$), then the BCAL ($5\,\lambda$) and finally the RCAL ($4\,\lambda$), where λ is the interaction length. Each part is subdivided into 23 *modules*, an example of an FCAL module is shown in Figure 5.12. FCAL and RCAL modules are rectangular whereas the BCAL modules, surrounding the CTD, are wedge-shaped (each covering 11.25° in azimuth). Each module consists of so called *towers* which are subdivided longitudinally into electromagnetic and hadronic *sections*. The sections are made up of *cells* whose size depends on the type (EMC or HAC) and position (FCAL, BCAL or RCAL), as reported in Table 5.3. Also listed are the interaction depth for the different CAL parts, separately for the electromagnetic and hadronic sections. The depth of the towers ensure that at least 90% of the jets, with energies corresponding to the kinematically allowed maximum energy, deposit at least 95% of their energy in the CAL.

The good time resolution of $< 1\,\mathrm{ns}$ (for energy deposits > 4.5 GeV) of the CAL is used to reject non-*ep* background. The CAL is calibrated on a daily basis using the natural radioactivity of U^{238} which produces a constant signal in the PMTs. Additionally, laser, LED and test pulses are used for the calibration. The achieved accuracy it better than 1%.

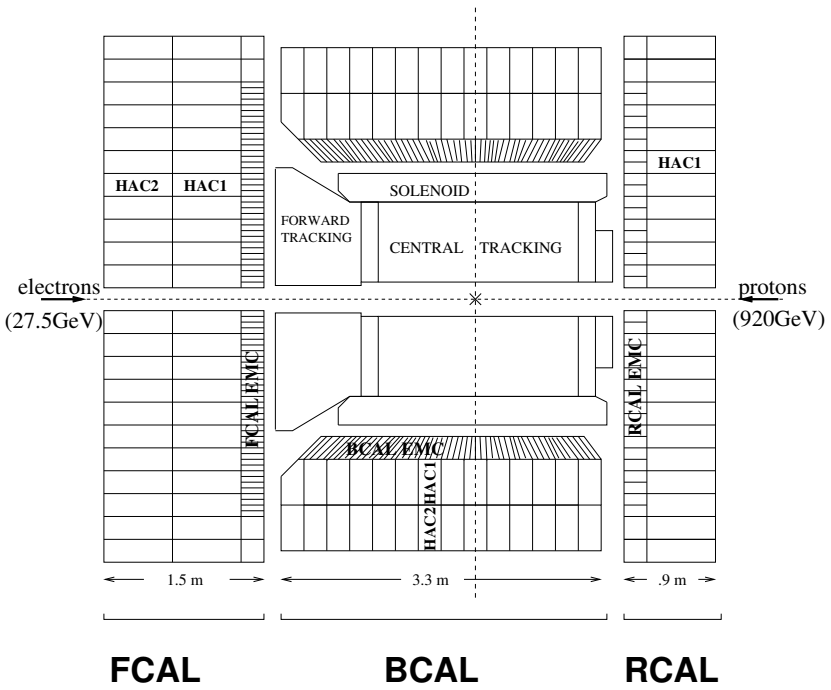

FIGURE 5.11: Schematic view of the ZEUS calorimeter along the beam axis.

5.2.4 Trigger and Data Acquisition System (DAQ)

The bunch crossing time at HERA of 96 ns corresponds to a potential rate of interesting events of about 10 MHz. Highest rates for physics events occur for soft photoproduction events (around 250 Hz) while DIS events with $Q^2 > 100\,\mathrm{GeV}^2$ have rates of less than 0.1 Hz. On the other hand, non physics events mainly from beam gas interactions have rates several orders of magnitude higher (typically 10 kHz). Other sources of background are muons which can cross the whole detector. They originate either from cosmic rays or from decaying hadrons which are produced in interactions of protons from the beam halo with the collimators. The separation of physics events from the background is the main task of the ZEUS trigger [94, 95]. As the rate to tape is limited to 1.5 MB/s and the total data size per event is 150 kB, additionally, a significant reduction of the data rate is needed to be achieved. Events are selected online by a three level trigger system as illustrated in Figure 5.13. As the throughput rate is reduced at each level, the complexity of the decision making algorithms can increase towards higher levels. The three levels are:

TABLE 5.3: Parts of the CAL with angular ranges and dimensions of the cells. Each tower has only one EMC section and each HAC section consists of only one cell.

CAL Part	Angular range (°)	Angular range (eta)	HAC sections per tower	Cells per EMC section
FCAL	$2.5° - 39.9°$	$1.0 - 3.8$	2	4
BCAL	$36.7° - 129.2°$	$-0.74 - 1.1$	2	4
RCAL	$128.1° - 178.4°$	$-4.2 - -0.72$	1	2
CAL Part	EMC cell	HAC cell	Depth of EMC section	Depth of HAC section
FCAL	$20 \times 5\,cm^2$	$20 \times 20\,cm^2$	$26\,X_0$	$3.1\,\lambda$
BCAL	$20 \times 5\,cm^2$	$20 \times 20\,cm^2$	$21\,X_0$	$2.0\,\lambda$
RCAL	$20 \times 10\,cm^2$	$20 \times 20\,cm^2$	$26\,X_0$	$3.1\,\lambda$

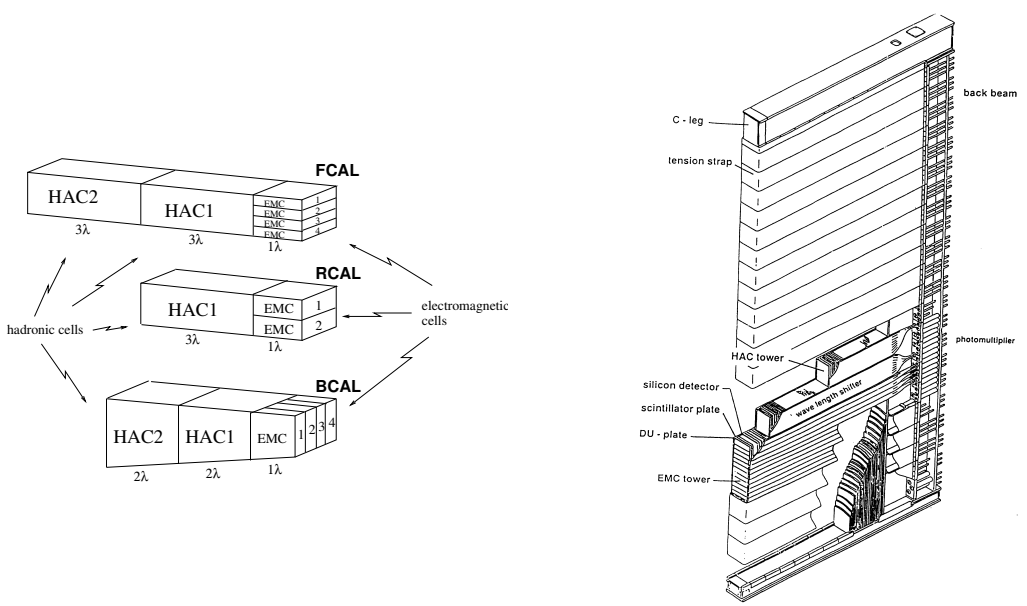

FIGURE 5.12: Schematic view of FCAL, RCAL and BCAL towers (left) and a FCAL module (right).

- **First Level Trigger (FLT):** At the lowest level, trigger algorithms are hard-wired to each component separately. Component specific quantities like energy sums or thresholds are computed and send to the global first level trigger (GFLT) which combines the information from different trigger slots. It decides within $4.4\,\mu s$ (*i.e.* 46 crossings) whether to send the event on to the next trigger stage. During this time, the event information is stored in logical pipelines. The FLT output rate is 1 KHz.

- **Second Level Trigger (SLT):** The SLT is implemented in a transputer network. At this level, a large fraction of the full data of the event is available so that event quantities can be recalculated with higher precision. As the analysis of the event is done in parallel the processing time is much larger than for the FLT. CAL timing information, which is available at this stage, is used to reject beam gas background. The information from all SLT branches is collected by the global second level trigger (GSLT), which delivers a decision after 7 ms, reducting the event rate to $50 - 100$ Hz. In 2001, the global tracking trigger (GTT [96]) was implemented in hard- and software to combine the information of the main tracking devices (CTD, MVD and STT) to benefit from the enhanced tracking capabilities.

- **Third Level Trigger (TLT):** For accepted events the event builder collects the information from all components and stores them in an ADAMO [97] database record. These are read by the TLT, which uses a computer farm and has access to the full event information to calculate kinematic variables and run electron finding algorithms, etc. The final output rate is $5 - 10$ Hz with event sizes of approximately 150 kB.

Once events have passed all trigger requirements they are sent to the DESY computing center and written to tape. During the following offline reconstruction, they are pre-classified according to physics quantities in order to facilitate following steps of data analysis.

5.2.5 Luminosity Measurement

To determine the luminosity available for physics processes inside the ZEUS detector, the bremsstrahlung process $ep \to ep\gamma$ is used. Its cross section is given by

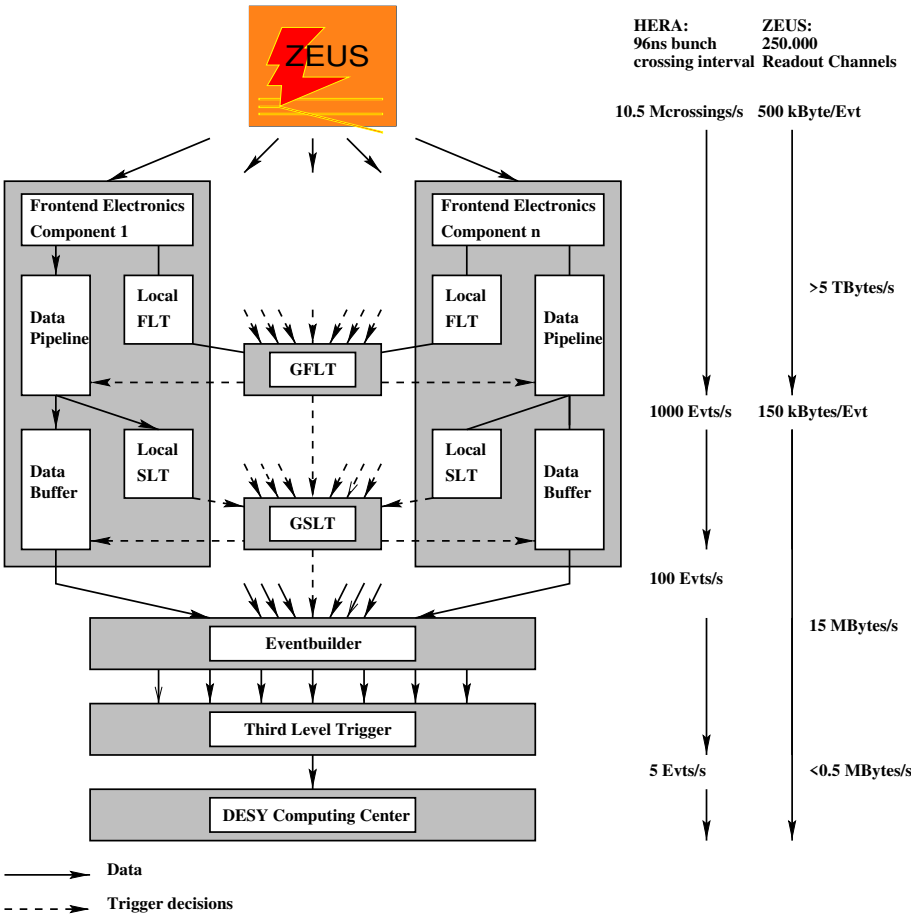

FIGURE 5.13: Overview of the ZEUS trigger and data acquisition system.

the Bethe-Heitler formula

$$\frac{d\sigma}{dk} = 4\alpha r_e^2 \frac{E}{kE}\left(\frac{E}{E'} + \frac{E'}{E} - \frac{2}{3}\right)\left(ln\frac{4E_pEE'}{m_em_pk} - \frac{1}{2}\right) \tag{5.8}$$

where k, E and E' are the energies of the photon, the incoming and the outgoing electron, respectively. The large cross sections of ($\sigma_{BH} \geq 20\,mb$) together with the fact that its theoretical prediction is known with an accuracy of $\simeq 0.5\%$ allows for a precise determination of the ep luminosity by measuring the rate and energy of the bremsstrahlung photons. The setup of the luminosity monitor system [98, 99, 100] is illustrated in Figure 5.14. Its main constituents are the two calorimeters for photons (LUMIG) and leptons (LUMIE), situated at $z = -106$ m and $z = -35\,m$, respectively. The collected photons originate from

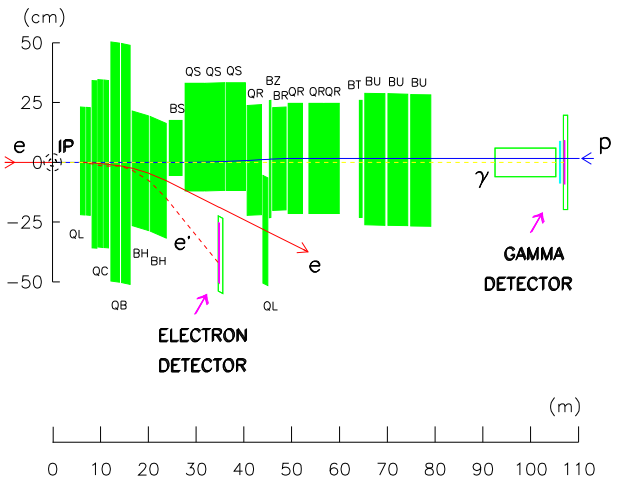

FIGURE 5.14: Schematic view of the ZEUS LUMI monitor system.

bremsstrahlung processes with $\theta_\gamma < 0.5\,\text{mrad}$ which can leave the beam pipe through a Cu-Be window at $z = -92.5$ m. To protect the photon calorimeter against synchrotron radiation it is shielded by a carbon-lead filter. The resulting resolution is $\sigma(E)/E = 23\%$. The bremsstrahlung event rate is determined by counting the number of photons above a fixed energy threshold. The luminosity is then calculated by dividing the evaluated rate by the bremsstrahlung cross section, corrected for the detector acceptance. The dominant background processes emerge from bremsstrahlung of leptons on the residual gas in the beam pipe. The rate of these events can be measured by using *pilot* bunches (where the proton bunch is empty). Statistical uncertainties are negligible due to the large rate of recorded Bethe-Heitler events. Contributions to the systematic uncertainties come from background subtraction, pile-up effects, energy calibration and the acceptance of the photon calorimeter. The achieved precision on the luminosity measurement is of the order of $2\% - 3.5\%$.

Chapter 6

Event Reconstruction

The basic entities measured in the detector are electrons, photons and jets, all of which are present in the signal processes. Although, the gravitino escapes undetected it can be fully reconstructed by measuring the missing energy in the calorimeter. In order to identify the high energy photon an electron finder is used while requiring that no track should be associated to the found energy deposition in the calorimeter. For the jet reconstruction track and energy information are combined into energy flow objects (EFOs) which are then used by the jet algorithm.

6.1 Kinematic Variables

The kinematics of a DIS event (see Sect. 2.2) is defined by two independent variables for fixed energies E_e and E_p of the incoming lepton and proton. They can be calculated fromt the physical quantities measured in the detector, namely the energy E'_e and the polar angle θ'_e of the scattered lepton (or alternatively E_ν and θ_ν of the reconstructed neutrino) and the four-momentum of the hadronic system p_{had}. The three most commonly used methods for the determination of the DIS kinematic variables Q^2, x and y are described briefly in the following and their main advantages and disadvantages are emphasized.

6.1.1 Electron Method

This method relies only on the reconstruction of the scattered lepton (namely E'_e and θ'_e). The kinematic variables are then given by

$$Q^2_{el} = 2E_e E'_e(1+\cos\theta'_e) \tag{6.1}$$

$$x_{el} = \frac{E_e}{E_p}\frac{E'_e(1+\cos\theta_e)}{2E_e - E'_e(1-\cos\theta'_e)} \tag{6.2}$$

$$y_{el} = 1 - \frac{E'_e}{2E_e}(1-\cos\theta'_e) \tag{6.3}$$

where s is the center-of-mass energy squared. The resolution of the kinematic variables in terms of E'_e and θ'_e can be calculated via error propagation:

$$\frac{dQ^2_{el}}{Q^2_{el}} = \frac{dE'_e}{E'_e} - \tan(\theta'_e/2)d\theta'_e \tag{6.4}$$

$$\frac{dx_{el}}{x_{el}} = \frac{1}{y_{el}}\frac{dE'_e}{E'_e} + \tan(\theta'_e/2)\left(x_{el}\frac{E_p}{E_e} - 1\right)d\theta'_e \tag{6.5}$$

$$\frac{dy_{el}}{y_{el}} = (1-\frac{1}{y_{el}})\frac{dE'_e}{E'_e} + (\frac{1}{y_{el}} - 1)\cot(\theta'_e/2)d\theta'_e \tag{6.6}$$

The lepton angle can be measured more precisely (see Sect. 6.4) than its energy due to the considerable amount of inactive material in the inner part of the detector. While being precise for high y_{el}, the relative error for x_{el} and y_{el} diverges for $y_{el} \to 0$. The resolution for x_{el} and Q^2_{el} has a similar problem for small lepton scattering angles ($\theta'_e \simeq \pi$). The accuracy of this method is affected by initial state radiation (ISR) as the emitted photon is not taken into account[1].

Advantage: Independent of the measurement of the hadronic system.

Disadvantage: Can only be used for NC DIS events; bad resolution for low y_{el} and $\theta'_e \simeq \pi$.

6.1.2 Jacquet-Blondel Method

The variables exploited in this method are the energies and angles of the particles belonging to the hadronic final state. With the definition of $\delta_{\text{had}} = \Sigma_i(E_i - p_{i,z})$ and $p_{T,\text{had}} = \sqrt{(\Sigma_i p_{i,x})^2 + (\Sigma_i p_{i,y})^2}$ (where i runs over all observed final state

[1]The effect of final state radiation (FSR) can be neglected, since in this case the emitted photon is in most cases combined into the electromagnetic cluster of the electron candidate.

hadrons) the kinematic variables can be expressed as:

$$Q^2_{jb} = \frac{p_{T,\mathrm{had}}}{1-y_{jb}} \tag{6.7}$$

$$x_{jb} = \frac{Q^2_{bj}}{s\, y_{bj}} \tag{6.8}$$

$$y_{jb} = \frac{\delta_{\mathrm{had}}}{2E_e} \tag{6.9}$$

The relative errors of the kinematic variables are:

$$\frac{dQ^2_{jb}}{Q^2_{jb}} = 2\frac{dp_{T,\mathrm{had}}}{p_{T,\mathrm{had}}} + \frac{1}{2E_e}\frac{d\delta_{\mathrm{had}}}{1-y_{jb}} \tag{6.10}$$

$$\frac{dx_{jb}}{x_{jb}} = \left(\frac{1}{2E_e(1-y_{jb})} - \frac{1}{2E_e y_{jb}}\right) d\delta_{\mathrm{had}} + \frac{2}{p_{T,\mathrm{had}}}\, dp_{T,\mathrm{had}} \tag{6.11}$$

$$\frac{dy_{jb}}{y_{jb}} = \frac{1}{2E_e y_{jb}}\, d\delta_{\mathrm{had}} \tag{6.12}$$

Divergent errors arise in Q^2_{jb} and x_{jb} for $y_{jb} \to 1$ and in y for $y \to 0$. Since only information from the hadronic system is used this method is not affected by ISR.
Advantage: Independent of electron reconstruction (and ISR).
Disadvantage: Highly sensitive to calorimetric energy uncertainties.

6.1.3 Double Angle Method

In this method only the polar angles of the scattered electron and the hadronic final state are used, with the kinematic variables given by:

$$Q^2_{da} = 4E_e^2 \frac{\sin\gamma_{\mathrm{had}}(1+\cos\theta'_e)}{\sin\gamma_{\mathrm{had}} + \sin\theta'_e - \sin(\theta'_e+\gamma_{\mathrm{had}})} \tag{6.13}$$

$$x_{da} = \frac{E_e}{E_p}\frac{\sin\gamma_{\mathrm{had}} + \sin\theta'_e + \sin(\theta'_e+\gamma_{\mathrm{had}})}{\sin\gamma_{\mathrm{had}} + \sin\theta'_e - \sin(\theta'_e+\gamma_{\mathrm{had}})} \tag{6.14}$$

$$y_{jb} = \frac{\sin\theta'_e(1-\cos\gamma_{\mathrm{had}})}{\sin\gamma_{\mathrm{had}} + \sin\theta'_e - \sin(\theta'_e+\gamma_{\mathrm{had}})} \tag{6.15}$$

where the inclusive angle γ_{had} is defined as:

$$\gamma_{\mathrm{had}} = \frac{\delta_{\mathrm{had}}}{p_{T,\mathrm{had}}} \tag{6.16}$$

The uncertainties of the energy scale are canceled by the ratio. Considering only the uncertainty due to the lepton angle, the relative errors are:

$$\frac{dQ^2_{da}}{Q^2_{da}} = -\frac{2}{\sin\theta'_e}d\theta'_e, \quad \frac{dx_{da}}{x_{da}} = -\frac{1+y_{da}}{\sin\theta'_e}d\theta'_e, \quad \frac{dy_{da}}{y_{da}} = -\frac{1-y_{da}}{\sin\theta'_e}d\theta'_e \tag{6.17}$$

Thus, the double angle method can be used to calibrate the calorimeter through the calculation of the energy of the scattered lepton:

$$E'_e = 2E_e \sin\gamma_{\text{had}} / (\sin\gamma_{\text{had}} + \sin\theta'_e - \sin(\gamma_{\text{had}} + \theta'_e)) \tag{6.18}$$

Advantage: Independent of calibration of the energy scale.
Disadvantage: Bad resolution for small Q^2_{da}.

6.2 Track and Vertex Reconstruction

Tracks were reconstructed using the CTD and after the upgrade in 2001 also the MVD. In order to be able to determine the original particle trajectory with high precision the magnetic field, multiple scattering effects due to dead material and the errors on the hit measurements are taken into account. Tracks can be reconstructed in three ways, only from the CTD, from the combination of CTD and MVD hits or only from the MVD. In all cases, tracks are fitted by a helix parametrisation designed to describe particle tracks in a toroidal magnetic field parallel to the beam axis. The track information was used to reconstruct the event vertex. For this analysis, only CTD tracks originating from the primary event vertex with a transverse momentum of $p_T^{trk} > 200\,\text{MeV}$ were considered.

6.3 Calorimetric Variables

The total energy and momentum deposited in the CAL, E_{tot} and $\vec{P}$, are defined as:

$$E_{tot} = \sum_i E_i \tag{6.19}$$

$$\vec{P} = \sum_i E_i \, \vec{r}_i \tag{6.20}$$

where i runs over all CAL cells and $\vec{r}_i$ is a unit vector along the line from the reconstructed vertex to the center of the cell i. P_X, P_Y and P_Z are the components of the vector $\vec{P}$. Then the imbalance of the detected transverse moment is given by:

$$P_{T,miss} = \sqrt{P_X^2 + P_Y^2} \tag{6.21}$$

Another useful variable is $E - P_Z$ defined as:

$$E - P_Z = E_{tot} - P_Z = \sum_i E_i(1 - cos\,\theta_i) \tag{6.22}$$

where θ_i is the polar angle of the i-th CAL cell. It is a substitute for P_Z with characteristic distributions for NC and CC events. Due to the unknown fraction of energy from the proton remnant leaving the detector through the beam pipe in forward direction, P_Z alone does not describe the missing Z-momentum of undetected particles. This problem is circumvented by using $E-P_Z$ where particles moving in the forward direction give zero contribution. Thus, for NC events $E-P_Z$ is given by twice the energy of the incident lepton beam, 55 GeV.

The values obtained in this way were corrected for detector effects. Noisy cells were excluded with the help of calibration lists which were generated offline for each year. To further suppress noise related effects, isolated cells with an energy content of less than 80 MeV in the electromagnetic part and 140 MeV in the hadronic part were excluded.

Energy correction factors for data events were derived by comparing the measured energies with the results obtained from MC simulations, as listed in Table 6.1. The remaining uncertainty is ±1% for the FCAL and BCAL, and ±2% for

TABLE 6.1: Energy correction factors for the different CAL regions for the running periods 1996-1997 and 1998-2005 [101].

CAL Region	Cell Type	Correction 1996-1997	Correction 1998-2005
FCAL	emc	+4.0%	+2.4%
	hac	-5.0%	-5.9%
BCAL	emc	+4.0%	+5.3%
	hac	+8.2%	+9.6%
RCAL	emc	+2.2%	+2.2%
	hac	+2.2%	+2.2%

the RCAL [102]. Further energy corrections were applied to specific event variables as described in the following sections.

6.4 Electron Identification

Electrons and photons produce electromagnetic showers in the calorimeter, predominantly in the electromagnetic part. Showers are produced by a sequence of pair creation, photo effect and bremsstrahlung reactions. A shower stops when electron energies pass a certain minimum after which the electrons lose their remaining energy through ionisation.

For electron identification the electron finder EM [103] was used which combines CAL and tracking information to calculate characteristic electron variables. These variables were studied using a sample of electrons found by other algorithms. It is optimised separately for the FCAL, BCAL and RCAL regions.

The EM algorithm starts by identifying CAL cells with a local energy maximum and groups them into clusters together with the surrounding cells which have an energy above the noise. The center of the cluster is obtained from a logarithmic weighting function of the energy deposit.

Tracks with a maximal distance of 2 cm from the beam line are extrapolated to the surface of the calorimeter. If the distance of closest approach (DCA) is less than 50 cm and $p_T^{TRK} > 0.1\,\mathrm{GeV}$, cluster and track are matched to form an electron candidate.

The seven characteristic electron variables used by EM are:

- The energy which is not associated to the electron candidate inside a cone of $R = 0.8$ around the cluster[2];
- the fraction of electromagnetic energy outside the highest energy cell;
- the energy fraction of the two hadronic sections HAC1 and HAC2;
- the energy fraction in the highest CAL module pair;
- $\delta\phi = |\phi_{TRK} - \phi_{CAL}|$;
- $\delta\theta = |\theta_{TRK} - \theta_{CAL}|$;
- $\delta_p = |1/p_{TRK} - 1/E|$.

For each of these variables first a subprobability is calculated. Only candidates which fulfill the following requirements are accepted:

[2]The cone radius is defined by $R = \sqrt{(\Delta\phi)^2 + (\Delta\theta)^2}$.

- $E > 4\,\mathrm{GeV}$;
- the total CAL probability $\mathcal{P}_{CAL}$ exceeds 10^{-5};
- the total track probability $\mathcal{P}_{TRK}(\delta\phi, \delta\theta, \delta_p)$ exceeds 10^{-3}.

All information is then used to calculate the overall likelihood according to:

$$\mathcal{Q} = \mathcal{P}_k \sum_{k=0}^{N-1} \frac{(-log\mathcal{P}_k)^k}{k!} \tag{6.23}$$

If the electron candidate has no associated track only the calorimetric variables are taken into account.

The energy of the electrons is calculated from their energy depositions in the CAL and corrected for energy losses in inactive material. The polar and azimuthal angles are determined form the associated track or, in absence of it, from the position of the calorimeter cluster.

Figure 6.1 shows the efficiency of the EM finder as a function of electron energy, electron angle and Q^2 [104]. In comparison, the results obtained by the electron finder SIRA5 [104, 105] which is based on an artificial neural network is shown. The EM finder shows a slightly better performance for high electron energies and in the forward region.

6.4.1 Photon Identification

The differences in shower shapes between electrons and photons are very small. Therefore, the EM finder is used also for photon finding and the electron-photon separation relies only on the tracking information.

The EM finder can be reconfigured in order to be optimised for photon finding. In this case no cluster-track matching is required for a photon candidate and the overall likelihood is calculated only from the calorimetric variables. The track information is evaluated by EM and represented in the following variables:

- nTrkNeighbour
- EtTrkNeighbour

which give the number of tracks and the summed transverse momenta of the tracks within a cone centered on the photon candidate. Up to four different cones with different radii can be specified in the EM initialisation routine. The default are two cones with radii $R = 0.2$ and $R = 0.4$.

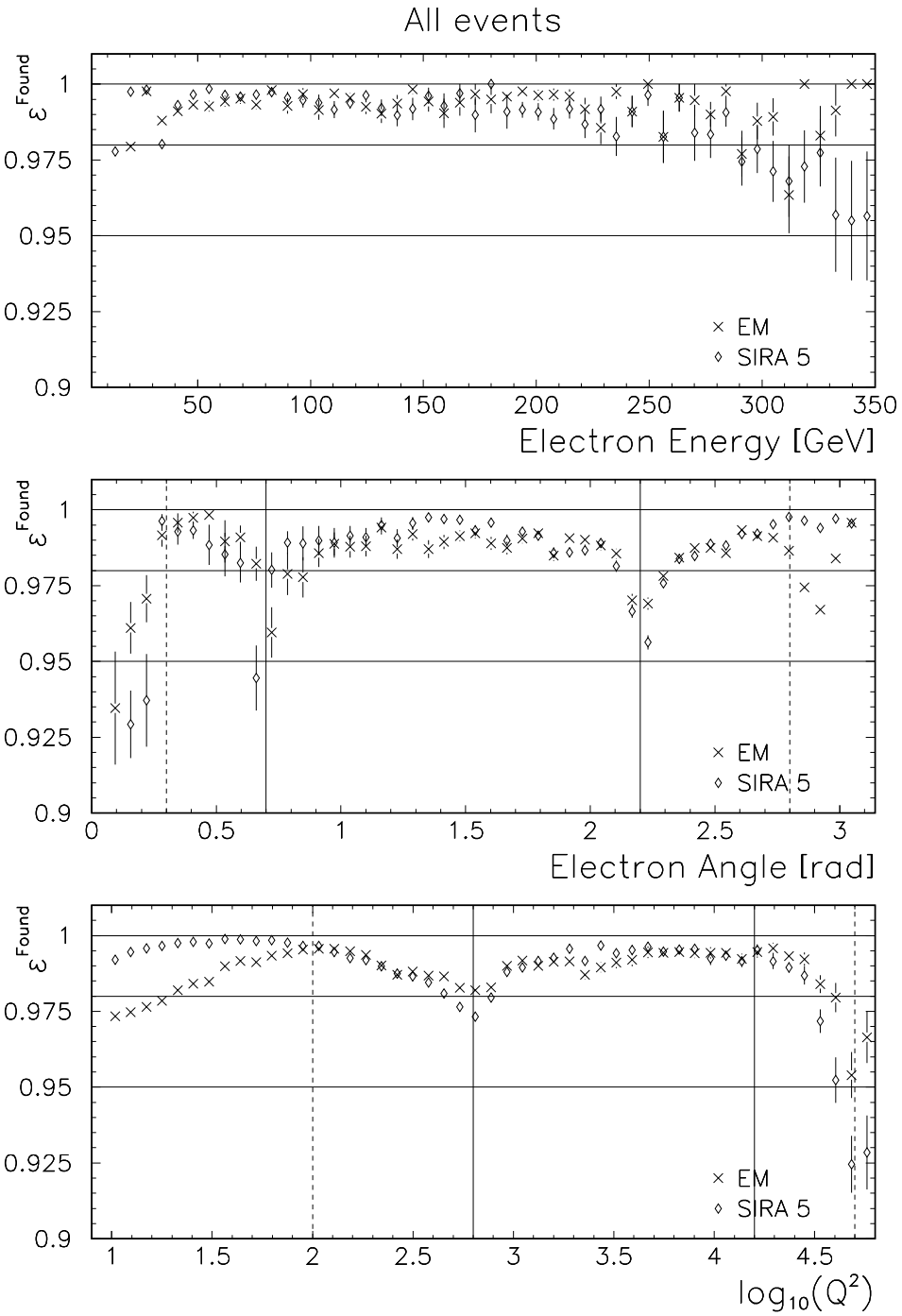

FIGURE 6.1: Efficiency of the electron finder as a function of electron energy (top), electron angle (middle) and Q^2 (bottom). The vertical lines denote the transition regions between different CAL parts (full line) and the end of the CTD (dashed line).

6.5 Energy Flow Objects

The energy resolution of the CAL improves for higher particle energies whereas the track reconstruction (see Sect. 5.2.1) gives a better energy resolution for low particle energies, as shown in Figure 6.2 [106].

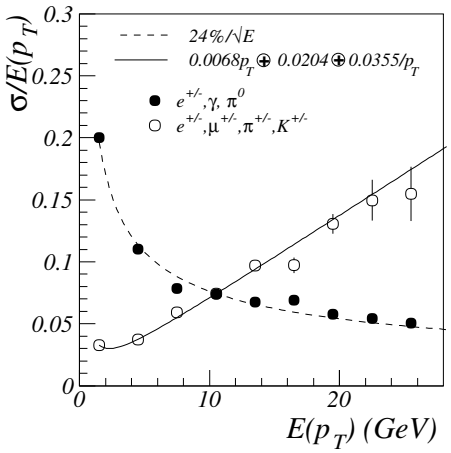

FIGURE 6.2: Confrontation of energy resolution obtained from MC simulations of $e^{\pm}$, $\mu^{\pm}$, $\pi^{\pm}$ and $K^{\pm}$ for the CTD (empty circles) and of electromagnetic showers from $e^{\pm}$, γ, and π^0 in the CAL (filled circles) and .

To benefit from the most accurate energy determination in both energy ranges, track reconstruction and CAL energy measurement are combined into *energy flow objects* (EFOs). They are used for the reconstruction of the hadronic system. The reconstruction of EFOs proceeds in five steps, as follows:

1. The CAL cells associated to the scattered electron are removed.

2. Clustering of CAL cells into *cell islands*: Each cell with sufficient energy is considered a candidate to be connected with one of its neighbours. The connection is made with the highest energy neighbour or with the highest energy cell next to the neighbour resulting in a unique assignment of each cell to a cell island. This clustering is performed separately for the three sections of the CAL (FCAL, BCAL and RCAL).

3. Clustering of cell islands into *cone islands*: Cell islands belonging to a shower of a single particle or a jet of particles are grouped together. The matching starts from the outermost islands and proceeds inwards by calculating the

angular separation to neighbouring islands in polar and azimuthal angles, ϕ and θ. The separation is transformed into a matching probability derived from a single pion MC simulation. All cell islands above a threshold are grouped into a cone island.

4. Computation of the *distance-of-closest-approach* (DCA): Each track is first extrapolated to the calorimeter surface and then further into the calorimeter, assuming a linear trajectory. The DCA is then computed as the shortest distance between the track trajectory and the center of the cone island, which is calculated as the energy weighted mean of all associated cell centers. The energy weight is determined logarithmically rather than linearly to cope with the observed systematic bias due to the varying cell projectivity resulting from the CAL geometry.

5. Matching of tracks and cone islands. Tracks and cone islands are matched together to EFOs if they fulfill the condition:

$$DCA \leq \max(r_{\text{island}}, r_{\text{min}}) \tag{6.24}$$

where r_{island} is the radius of the cone island and $r_{\text{min}} = 20\,cm$ is a parameter extracted from MC simulations by maximizing the track-island matching efficiency for single particles. In addition to the clean matches of one track

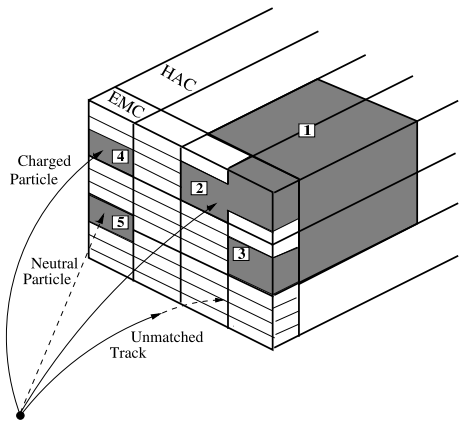

FIGURE 6.3: Schematic representation of the reconstruction of an EFO. First cells 1, 2 and 3 are clustered into a cone island. In a second step, cone islands and tracks are matched together. Shown are the three different match categories corresponding to a charged particle, a neutral particle and a unmatched track.

and one cone island, the following EFO categories are distinguished (see Fig. 6.3):

- charged tracks without an associated cone island are considered as pions. Their energy is calculated from the CTD measurement and the known pion mass;
- cone islands without a track are treated as neutral particles;
- cone islands with more than three associated tracks are treated as a jet, and the CAL information is used.

In some cases the track information is used instead of the CAL measurement for the determination of the four-momentum of the particle. This is the case if the relative momentum uncertainty is lower than the uncertainty from the energy measurement

$$\frac{\sigma(p)}{p} < \frac{\sigma(E_{cal})}{E_{cal}} \tag{6.25}$$

and the CAL energy exceeds the track momentum, but lies within the resolution of the E_{cal}/p ratio ($\sigma(E_{cal}/p)$):

$$E_{cal}/p < 1.0 + 1.2\,\sigma(E_{cal}/p) \tag{6.26}$$

6.6 Jet Reconstruction

In order to ensure a universal definition of a jet, standards for jet algorithms have been defined. A jet finder suited for *ep* collisions has to meet the following requirements:

- *collinear safety*: the resulting jets should be independent of one parton splitting into two collinear partons;
- *infrared safety*: the resulting jets should be independent of the emission of very low energy particles;
- treatment of beam remnants;
- independence from longitudinal Lorentz transformations.

A separation of soft and hard processes can be achieved with a cut on the transverse jet energy. The jets taken into account in this analysis were preselected by requiring a transverse energy of $E_T^{jet} > 4\,\mathrm{GeV}$.

6.6.1 Jet Finding Algorithm

The algorithm used in this analysis is the *longitudinally invariant k_t clustering algorithm*. It fulfills all requirements given above. Starting with an initial list of EFOs (see Sect. 6.5), an iterative clustering procedure is applied to group them into jets, as follows:

1. Hard scattering scales d_i and distances d_{ij} are calculated from:

$$d_i = E_{T,i}^2 \qquad d_{ij} = min(E_{T,i}, E_{T,j})[(\eta_i - \eta_j)^2 + (\phi_i - \phi_j)^2] \tag{6.27}$$

2. To decide whether two objects should be merged together, the smallest value of d_i and d_{ij} for all i and j is labeled d_{min}. Two cases are distinguished:

   - If $d_{\min}$ belongs to the set of d_{ij} the objects i and j are merged to a new object k with:

$$E_{T,k} = E_{T,i} + E_{T,j}, \qquad \eta_k = \frac{E_{T,i}\,\eta_i + E_{T,j}\,\eta_j}{E_{T,k}}, \qquad \phi_k = \frac{E_{T,i}\,\phi_i + E_{T,j}\,\phi_j}{E_{T,k}} \tag{6.28}$$

   - If d_{min} in one of the d_i the object i is removed from the list of objects and identified as a separate jet.

This procedure continues until the list of objects is empty.

6.7 Additional Event Variables

To reconstruct characteristic properties of signal events the following quantities are used:

- *Gravitino four-vector*
  The undetected gravitino leaves a signature of both missing transverse and longitudinal momentum if no other particle escapes undetected. While the missing transverse momentum is directly given by the total P_x and P_y in the calorimeter, the missing P_z can be obtained from:

$$(E - P_z)_{in} = 55\,\mathrm{GeV} = (E - P_z)_{out} = (E - P_z)_{DET} + (E_{\tilde{G}} - p_{z,\tilde{G}}) \tag{6.29}$$

  Since for a not too heavy gravitino $E^2 = p_{T,\tilde{G}}^2 + p_{z,\tilde{G}}^2$, then $p_{z,\tilde{G}}$ can be calculated from:

$$p_{z,\tilde{G}} = \frac{p_{T,\tilde{G}}^2}{2[55 - (E - P_z)_{DET}]} - \frac{1}{2}[55 - (E - P_z)_{DET}] \tag{6.30}$$

- *Invariant mass of photon and gravitino*
  The sum of the four-vectors of the photon and the gravitino gives the four-vector of the neutralino. The mass of the neutralino is then given by the invariant mass of photon and gravitino:

$$m^2_{\chi^0_1} = (p_\gamma + p_{\tilde{G}})^2 = (E_\gamma + E_{\tilde{G}})^2 - (\vec{p}_\gamma + \vec{p}_{\tilde{G}})^2 \simeq 2E_\gamma E_{\tilde{G}}(1 - cos\theta) \quad (6.31)$$

  where θ is the angle between $\vec{p}_\gamma$ and $\vec{p}_{\tilde{G}}$.

- *Selectron momentum transfer*
  The momentum transfered by the exchanged selectron can be calculated from the difference in the four-vector of the initial lepton[3] $p_e = (E_e, 0, 0, -E_e,)$ and the four-vector of the neutralino:

$$Q^2_{\tilde{e}} = (p_e - p_{\tilde{\chi}})^2 = E_e\,(E_{\tilde{\chi}} - p_{z,\tilde{\chi}}) \quad (6.32)$$

- *Circularity*
  The circularity measures the event distribution in the $r - \phi$ plane perpendicular to the beamline. It is defined as:

$$\text{circ} = 2(1 - \max(\lambda_1, \lambda_2))\,, \quad (6.33)$$

  where λ_1 and λ_2 are the eigenvalues of the matrix 2×2 matrix

$$M_{ij} = \frac{\sum_k p_{i,k} p_{j,k}}{\sum_k (p^2_{1,k} + p^2_{2,k})} \quad (6.34)$$

  with $p_{1,k}$ and $p_{2,k}$ being the x and y momentum components of the k^{th} object, respectively, and the sum runs over all jets and either the electron, in the case of the R_P-violating decay channel with an electron in the final state, or the missing P_T vector, in the case of the R_P-violating decay channel with a neutrino final state.

[3]For a high energy electron in the ZEUS coordinate system.

Chapter 7

Monte Carlo Simulation

An essential task for all scientific research is the choice of an appropriate interface which allows to compare theoretical predictions and experimental results. Since in elementary particle physics the fundamental parameters of the theory can not be measured directly the theoretical picture has to be extended down to the experimental observables. A further complication results from the intrinsically statistic nature of the investigated quantum properties which opens an immense phase space of possible experimental outcomes. Therefore, statistical methods, so called *Monte Carlo* programs, which perform a random sampling of this probability space, are used to predict the average expected outcome as well as statistical fluctuations. MC methods may be used for different purposes. The three most typical applications are:

- Test of theoretical predictions;
- modulation of detector properties (as resolution, acceptance, *etc.*);
- development of selection criteria for new types of events.

The simulation process, from a Feynman diagram to the response of the detector, proceeds in several steps as described in the following sections.

7.1 Hard Process

The hard process is described by the Feynman diagram where the initial particles are the lepton and a parton (quark or gluon) from the proton, which carries a momentum $q = xp$ (see Sect. 2.2 for a description of DIS kinematic variables).

The hard cross section $\hat{\sigma}$ depends on the available center-of-mass energy in the hard process $\hat{s} = xs$ and the transfered momentum $t = (q' - q)^2$. The total cross section can then be derived by folding the hard cross section with the parton densities $q_f(x, Q^2)$:

$$\sigma = \int \mathrm{d}t \int_{x_{min}}^{1} \mathrm{d}x \sum_f q_f(x, -t) \frac{\mathrm{d}\hat{\sigma}(\hat{s}, t)}{\mathrm{d}t} \tag{7.1}$$

For the production of heavy particles high values of x are necessary:

$$x_{min}\, s = \Big(\sum_i m_i \Big)^2 \tag{7.2}$$

In the case of the production of gauginos with $m_{\tilde{\chi}} = 100\,\mathrm{GeV}$ one finds $x_{min} \approx 0.1$. The cross section of the hard process is calculated up to a specific order in perturbation theory. In the used MC generators (see below) only LO calculations are performed. Additional effects are then added in subsequent steps as described in the following.

7.2 Higher Order and Non-Perturbative Effects

In QED, photons can be radiated from the initial (ISR) or final lepton (FSR). Also prompt photons from a quark can occur, for which however, the cross section is very small. These effects are included in the MC generator programs. QCD effects are more difficult to calculate due to the self interaction of the gluons.

7.2.1 QCD Radiation

A typical higher order QCD process is the radiation of hard gluons which leads to the production of additional jets. To date, simulations for two- and three-jet production in DIS can be calculated to next to leading order (NLO) at the parton level. In order to describe multi-jet production at the hadron level two different approaches are commonly used:

- *Color Dipole Model (CDM)*
  In the CDM [107], QCD radiation is describes as parton showers evolving from gluons radiating quark-antiquark pairs, which form color dipoles. The first dipole is spanned by the quark struck by the exchanged boson on the one hand, and the remaining quarks from the proton remnant on the other

hand. Radiated gluons can form further colour dipoles ($g \to q\bar{q}$) resulting in a cascade of gluon emission until a minimal cut off energy is reached.

- *Matrix Element and Parton Shower Model (MEPS)*
  In the MEPS model the parton shower is generated using the *Altarelli-Parisi* splitting functions [108] which determine the energy fractions in each branch. They are derived in summing up higher orders of perturbation theory to all orders by using the DGLAP leading-log approximation [109, 110]. Quarks and gluons evolve by successive branchings until all partons reach a minimum cut off energy.

7.2.2 Fragmentation and Hadronisation

The produced colored partons finally merge together to from stable colorless hadrons. This process can not be described perturbatively, therefore phenomenological models are used:

- *Lund Model*
  In the Lund string fragmentation model [111, 112, 113] the color field between a quark and an antiquark is treated as a string of constant energy density by taking into account the self-interactions of the gluons. With growing $q\bar{q}$ distance the string energy increases linearly until it is large enough to create a new $q\bar{q}$ pair from the vacuum. Thus, the string splits consecutively into smaller parts until the energy of the initial $q\bar{q}$ pair is exhausted.

- *Cluster Hadronisation*
  The cluster hadronisation model [114, 115] assumes color preconfinement [116] of the quarks in the parton shower. The remaining gluons are split non-perturbatively into $q\bar{q}$ pairs, so that in the next step all neighbouring quarks and antiquarks can be combined to low mass color singlet clusters, which decay isotropically into hadrons by momentum exchange with the neighbouring clusters taking into account the available phase space.

7.3 Simulation of Background

Following the reasoning given in the introduction of this chapter, MC generators which apply the discussed models, were used to simulate the SM background. This was done separately for the dominant topologies at HERA (see Sect. 2.2), *i.e.* for

TABLE 7.1: Used generator programs and the models they apply. The event generator DJANGOH [117] interfaces LEPTO [118] which simulates *ep* interactions to HERACLES [119] which models first order QED radiation. The JETSET program is an implementation of the Lund string model. For resolved PhP the GRV-G LO parametrisation for the structure of the photon was used.

Process	Generator	QCD Rad.	Hadronisation	PDF
NC DIS	DJANGOH/ARIADNE	CDM	JETSET	CTEQ5D
CC DIS	DJANGOH/ARIADNE	CDM	JETSET	CTEQ5D
CC DIS	DJANGOH/MEPS	MEPS	JETSET	CTEQ5D
PhP	HERWIG	MEPS	clustering	CTEQ4L
PhP	PYTHIA	MEPS	string	CTEQ4L
SUSY	SUSYGEN	MEPS	JETSET	CTEQ5M
SUSY	CompHep	MEPS	string	MRST

PhP as well as NC and CC DIS events. The approaches used by the different generators are listed in Table 7.1 together with the used PDFs, CTEQ [120, 121] or MRST [128, 129]. In photoproduction both direct and resolved events were simulated. To investigate the influence of the QCD-radiation model on the background expectation, additional sets of CC DIS MC samples were generated by using MEPS instead of ARIADNE. The generated samples of PhP (Tab. C.1), NC DIS (Tab. C.4) and CC DIS (Tab. C.3) are listed in Appendix C with their minimal Q^2 cuts and generated luminosities. For the production of the search tree used in the discriminant method (see Chapter 8) further CC DIS samples were prepared, with a total of 650K events.

7.4 Simulation of Signal

The event generator SUSYGEN [122, 123, 124] was used to simulate the signal events. It allows to simulate any two-to-two SUSY production process for electron-quark interactions in R_P-violating MSSM. To derive the mass spectrum of the GMSB model it is interfaced to the SUSPECT [125] program. All sparticle decays in two and three body processes can be simulated. Matrix elements are calculated in LO by taking into account the s, t, and u-channel contributions. Initial-state

radiation from the beam electron is implemented using the Weizsäcker-Williams approximation [126]. More information is given in Table 7.1. To simulate also QCD effects for the signal processes investigated in this thesis, SUSYGEN was interfaced to PYTHIA [111] (where the gravitino was treated as a neutrino).The structure functions were evaluated at the scale $\sqrt{\hat{s}}$.

The SUSYGEN program can be run in two different modes:

- *Generate*: An eventlist is produced in the HEPevt format which is than read into PYTHIA.
- *Scan*: Cross sections and branching ratios are calculated while varying one or more of the input parameters (*e.g.* the selectron mass or any GMSB parameter).

Some small changes were made to the SUSYGEN code in order to perform all scans presented in this thesis.

In order to confirm the results obtained by SUSGEN, the generator program CompHEP [127] was used (see Tab. 7.1). Here, the parton density functions of the proton in the MRST parametrisation were used. Initial-state radiation is not included. Table C.2 (in Appendix C) lists the generated signal MC files for different selectron and neutralino masses.

7.5 Detector Simulation

To enable a detector-level comparison between data and MC events, the events generated by the above programs were passed through a complete detector simulation.

For the simulation of the ZEUS detector the simulation package MOZART is used which internally relies on GEANT [130] for the simulation of particle interactions in the detector. GEANT is a general tool for the description of detector geometry and the distribution of inactive material. MOZART further generates the detector responds which is then passed to the trigger simulation program CZAR. The events which pass the trigger are send to the reconstruction package ZEPHYR which is the common root of the offline analysis software used also for all data events.

Chapter 8

Discriminant Method

An important aim of the event selection is to enrich the data sample with signal events, especially in searches for new phenomena where the expected number of produced signal events is very small. In this thesis a multivariate discriminant method is used to optimize the signal-to-background ratio. Technically, it stores the event positions in multi-variable binary trees (one for the signal and one for the background) and makes use of a range-searching algorithm to calculate the discriminant.

8.1 Introduction

The selection of the physical process is a multidimensional problem which can be described by different sets of variables. For a given set of variables, signal and background are typically not equally distributed. Thus, the question arises: What is the best set of cuts to separate them?[1]

Different approaches are used to sample this phase space. By making only one-dimensional cuts the signal-to-background ratio can normally (if correlations between the cut-variables exist) not be maximized. This is illustrated in Figure 8.1. Another method which is often applied for classification problems are artificial neural networks (ANNs). While they show excellent results in tasks of pattern recognition, they also require extensive training and interpolate over empty phase space.

[1] Here "best" needs to be defined by a quality function which depends on the signal efficiency and the signal-to-background ratio.

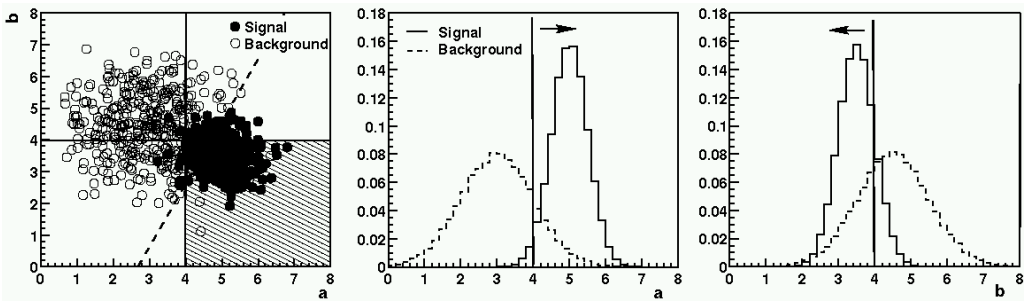

FIGURE 8.1: Example distributions for signal and background in two variables a and b. The two one-dimensional cuts indicated in the middle and right plots increase the signal-to-background ration by a factor of $S = 17.7$ while a cut along the dashed line leads to an improvement of $S = 22.4$ (for the same signal efficiency). Figure taken from [131].

The most obvious approach is to cut away all regions of parameter space where the probability to find a signal event lies below a certain threshold. In the discriminant method this probability is calculated from:

$$D = \frac{S}{S+B} \tag{8.1}$$

where S and B are the number of signal and background MC events found within a multi-dimensional region around the event which is to be classified[2]. In the used implementation of the discriminant method, this region is taken to be a *dim*-dimensional box, where *dim* is the number of used variables. An independent box is used for each to be classified event, which is centered around the event position. In the standard approach the box size is the same for all events. The discriminant value D is only identical to the probability that the event is a signal event in the limit where the box size goes to zero and S and B are the signal and background densities at this point. Hence, the smaller the used boxes, the more accurate is the description of the investigated phase space. This is of course only true if D can be calculated with high accuracy, *i.e.* its error

$$\Delta D = \frac{1}{(S+B)^2}\sqrt{(B \times \Delta S)^2 + (S \times \Delta B)^2} \tag{8.2}$$

is small, which is the case if $S+B$ is large. Therefore, a huge amount of MC events is needed. It was shown that, if this condition is fulfilled, the performance of the

[2]The to be classified events are in general not part of the signal or background MC samples, like *e.g.* data events.

discriminant technique is compatible with the results obtained by ANNs [132]. Technically, the requirement of an individual box for each to be classified event makes it necessary that the position of all MC events is kept in memory simultaneously. If a large number of events are to be classified, efficient search algorithms need to be applied to identify the MC events lying in each box. The reason why this method was not applied very often in the past is the large amount of MC events needed to sample the multidimensional signal and background densities and the resulting increased need of computing power and memory.

Computation time and memory are two resources which are interchangeable to some extent. For instance, information which is needed at different points in the program may be saved instead of being recalculated. The minimal information which needs to be saved for each point is its position in all dim dimensions[3] where dim is the number of chosen discriminant variables[4].

The best search algorithms known today have a performance of $O(log\, n!)$ in time for n search points [133]. In the discriminant implementation used here the MC events are stored in binary trees with one event at each node. During the built up of the tree, events are filled in an ordered way so that range searching techniques can be used to identify the events which lie inside a given box (details on this procedure can be found elsewhere [131]). In the case of binary trees the number of remaining points that have to be searched is halved after each decision, thus giving a search time of $O(log_2\, n!) \approx O(n\, log_2\, n)$. The price one has to pay for this in terms of memory is two extra numbers (the pointers to the two lower level nodes in the tree) for each node.

8.2 Dynamic Discriminant Method

The dynamic discriminant method is based on the insight that, while on the one hand, the range search algorithm does not allow a variation of the box size during calculation (since it has to be fixed before the first decision is taken), on the other

[3] It would be possible to introduce a quantised position space and merge all points within one quantum together which could reduce the needed memory immensely but would also lead to a lose of accuracy.

[4] In case the set of variables factorizes into two groups of variables which are uncorrelated, many resources can be saved (or may be used to achieve a higher accuracy) by using two independent discriminants for the two groups. (The method could even be nested by using the two discriminants as input into a meta-discriminant.)

hand, due to the high dimensionality of the problem, using several small boxes is still much faster than one large box. Therefore, the dynamic approach starts with a small box size enlarging it in several steps. In order to have a starting point for the box size variation the program calculates the approximate box sizes from

$$d_i^0 = \text{range}_i / \left(\frac{N_{evts}}{N_{min}}\right)^{1/\text{dim}} \tag{8.3}$$

where N_{evts} is the total number of available MC events (signal+background), N_{min} is the required number of events per box and $range_i$ is the range in which the variable i would normally be plotted, which has to be given by the user (it is needed for the relative scaling of the different dimensions). It is possible to use such an approximation since the optimisation is done automatically by the dynamic box-size adjustment process.

The variation of the box size proceeds as follows: First the number of signal and background events within a starting box of length d_i is counted (usually $d_i = 0.2 \times d_i^0$ is used). If the total number of counted events $N_{total} = S + B$ is below the required statistic minimum N_{min}, the box size is multiplied by a factor which is calculated from the ratio

$$f_1 = \frac{N_{min}}{N_{total}}\,. \tag{8.4}$$

This would be the proper factor if the density would be constant. Since this is normally not the case, smaller steps are made (too large steps are very expensive):

$$f_2 = a(f_1 - 1) + 1 \tag{8.5}$$

where a is the parameter[5] which determines how fast the box size is changed[6]. The factor f_2 is then used to scale the box length d_i of each variable by

$$d_i' = d_i \times \sqrt[dim]{f_2} \tag{8.6}$$

For the trees used in this analysis the optimum value of a was determined by plotting the average number of events that need to be counted for the classification of one event $\hat{n}$ (where the sum goes over all iterations of the above procedure) as a function of a. The plotted function has a minimum at $a = 0.35$ where $\hat{n}$ has a value of 1029 and the average number of iteration steps is 6.7.

Figure 8.2 shows the distribution of the final factor $\sqrt[dim]{f_2}$ which leads to a box with $N_{total} \geq N_{min}$. A box of length d_i^0 corresponds to a factor of 1 in Fig. 8.2

[5]Since $f_1 > 1$ a value of $0 < a < 1$ ensures that $0 < f_2 < f_1$.

[6]Also higher order functions may be chosen for $f_2(f_1)$.

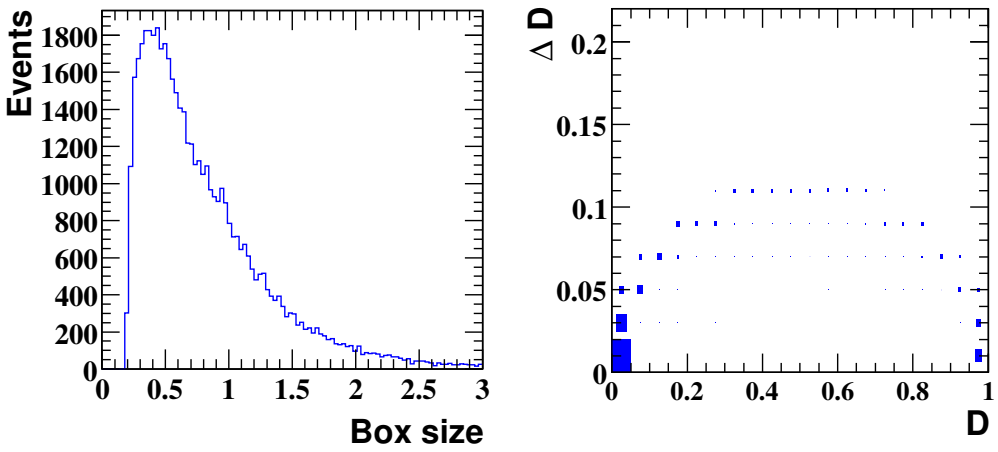

FIGURE 8.2: Control distributions for box size factor (left) and discriminant uncertainty as a function of discriminant value (right). The used sample contains 50000 events.

(d_i^0 is only a rough approximation for the box length in fix-box-size approaches). The exact box length used in fix-box-size approaches would be ~ 2 since all boxes with $N_{total} < N_{min}$ (which correspond in this case to all events with box length factors > 2) will not get classified and the percentage of such events should not be larger than $\approx 5\%$, since the tails of the distributions are important. Thus, in using fixed box sizes the accuracy is limited by the 5% of events which require a high box size. Fig. 8.2 shows that the number of events which need to be counted for the required statistics is for most boxes much smaller[7] in the variable-box-size method.

Another advantage of the dynamic method is the small number of free parameters. In principle the only parameter which has to be adjusted is the minimal number of events in a box which are required for the classification of an event, N_{min}[8]. Its influence can be seen in Figure 8.3. While for small N_{min} rather chaotic discriminant distributions are observed, the quality increases with increasing N_{min}. Finally between $N_{min} = 10$ and $N_{min} = 20$ no further improvement

[7] If the relative factor difference is r and the density is constant, then the number of counted events which need to be counted is smaller by a factor r^{dim} !

[8] In the case where different MC samples with different kinematic cuts and thus different weights contribute, N_{min} is the minimum sum of weights of all events in a box.

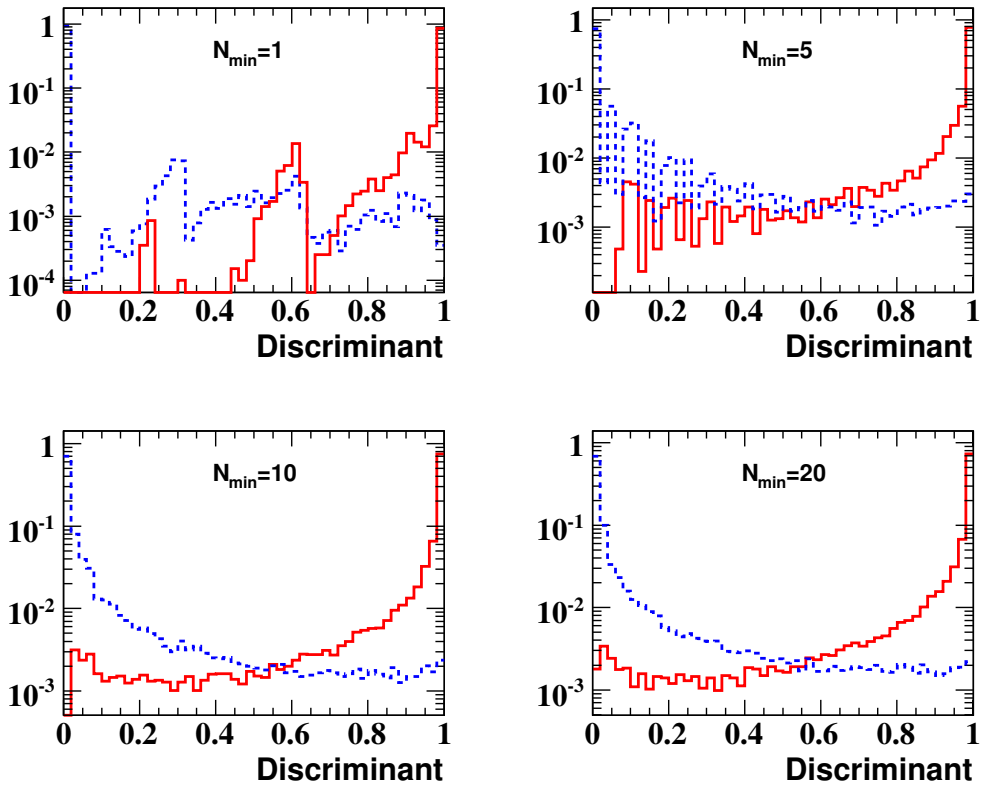

FIGURE 8.3: Discriminant distributions for signal (solid red line) and background (dashed blue line) for different values of N_{min}.

is observed; the optimum separation power of the algorithm for the given signal and background distributions has been found. The value used for the analyses presented in this thesis is $N_{min} = 20$.

The program calculates automatically the appropriate weight factors for signal and background events in applying simultaneously the following adjustments:

- Events from different background samples are weighted according to the luminosity they represent;
- signal and background weights are normalised to the same integral;
- the maximal background weight is set to one.

This procedure assures that the appropriate value of N_{min} is always approximately the same and has to be changed only for fine tuning purposes[9].

On the right side of Fig. 8.2 also the error on the discriminant calculated for 50000 signal and background events according to Eq. (8.2) is shown as a function of the discriminant value. It decreases toward the edges of the discriminant distribution. The result of this inaccuracy is that the distribution gets flatter since more events from the higher bins are falsely reconstructed in lower bins than *vice versa*. With an error of less than 0.05 in the last bin and bin sizes not smaller than that, the last bin will be calculated approximately 10% to low, which is acceptable.

In conclusion, the dynamic discriminant method has the following advantages:

- Less parameters have to be set by hand;
- more events get classified;
- less MC statistics is necessary;
- calculation is faster;
- results are more accurate since smaller pieces of phase space are investigated.

Details on the implementation are given in Appendix E.

[9]Practically it is an important advantage that the parameters are adjusted automatically since finding the right combination of weight factors, box sizes and N_{min} "by hand" may represent a tedious task.

Chapter 9

Event Selection

In this chapter the data set used and the selection cuts applied are presented. In the first step the concrete search strategy is derived from generator level studies of the signal processes. In the following the investigation of the main GMSB decay channel is described in detail. The R_P-violating decay channels, which only contribute for higher SUSY breaking scales, are described shortly. The selection for the gravitino channel is done in two steps according to the two main characteristics of the signal: The *preselection* represents a minimal set of cuts to select signal like events by exploring the characteristic of missing transverse energy resulting from the undetected gravitino. In the second step, the *final selection*, the subset of events which also possess the second characteristic, an isolated photon, is investigated. It is important to cease from any apparently obvious cut which aims for a signal-to-background separation within the preselection and final selection as each one-dimensional cut will lower the final signal-to-background ratio achieved by the *discriminant method* (see Chapter 8).

9.1 Data Set

The data events used in this analysis were recorded with the ZEUS detector in the years 1996 to 2005. They include events with both, electrons and positrons in the initial state and two different proton energies (for details on HERA operation see Sect. 5.1). Table 9.1 lists the different periods and corresponding luminosities of the analysed data. The total luminosity is $\mathcal{L} = 300.3 \pm 7.0\,\mathrm{pb}^{-1}$. Events with a shifted vertex were excluded.

A polarisation dependence of the coupling (and hence the cross section) may

TABLE 9.1: Data sets for different periods of HERA running. The error on the luminosity measurement is 2.5% for the HERA I period and 3.5% [134] for the considered HERA II period. The polarisation can be determined with an average uncertainty of 3% [135].

Year	CMS Energy	Lepton	Polarisation	Luminosity
1996-1997	300 GeV	e^+	0	$38.65\,\mathrm{pb}^{-1}$
1998-1999	318 GeV	e^-	0	$16.68\,\mathrm{pb}^{-1}$
1999-2000	318 GeV	e^+	0	$65.07\,\mathrm{pb}^{-1}$
2002-2003	318 GeV	e^+	0	$0.98\,\mathrm{pb}^{-1}$
2003	318 GeV	e^+	+ 0.33	$2.08\,\mathrm{pb}^{-1}$
2004	318 GeV	e^+	0	$0.47\,\mathrm{pb}^{-1}$
2004	318 GeV	e^+	+ 0.33	$7.90\,\mathrm{pb}^{-1}$
2004	318 GeV	e^+	− 0.39	$17.52\,\mathrm{pb}^{-1}$
2004	318 GeV	e^+	+ 0.36	$12.80\,\mathrm{pb}^{-1}$
2004-2005	318 GeV	e^-	+ 0.27	$8.32\,\mathrm{pb}^{-1}$
2004-2005	318 GeV	e^-	− 0.26	$46.91\,\mathrm{pb}^{-1}$
2004-2005	318 GeV	e^-	+ 0.35	$42.53\,\mathrm{pb}^{-1}$
2004-2005	318 GeV	e^-	− 0.28	$40.34\,\mathrm{pb}^{-1}$
Sum	318 GeV	e^-	− 0.04	$154.78\,\mathrm{pb}^{-1}$
Sum	318 GeV	e^+	+ 0.01	$106.82\,\mathrm{pb}^{-1}$
Total Sum	300 GeV & 318 GeV	e^- & e^+	− 0.02	$300.25\,\mathrm{pb}^{-1}$

result from the fact that only either right-handed or left-handed particles interact. It is therefore clear that the dependence on the polarisation will be linear. In the case of the signal process this is relevant at the R_P-conserving e-$\tilde{l}$-$\tilde{\chi}$ vertex. The other vertex allows only for left-handed selectrons. However, as Table 9.1 shows, the average polarisation for all three different running conditions are compatible with zero within the errors. Therefore, all used cross sections in this thesis are derived assuming an unpolarised lepton beam.

9.2 Generator Studies

In order to derive a quantitative description of the characteristics of the signal processes (see Chapter 4) events were generated with the MC generator program SUSYGEN (see Sect. 7.4). For the plots in this section no detector effects are

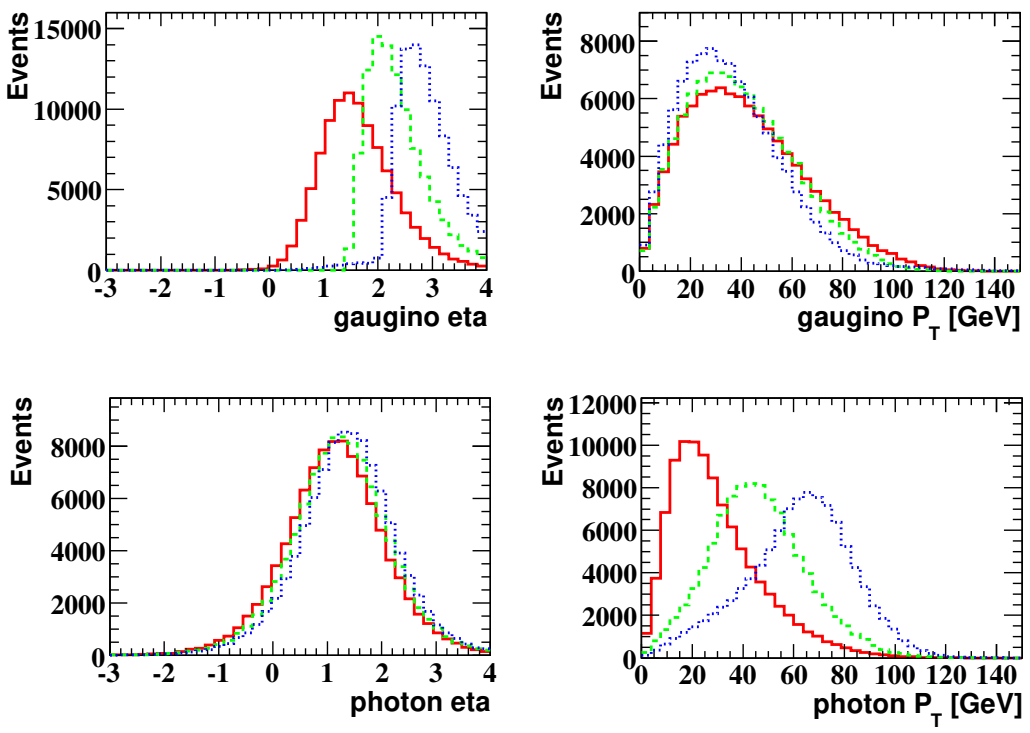

FIGURE 9.1: Generator level distributions for the produced gaugino (η and p_T) and the final photon (also η and p_T) for neutralino masses $m_{\tilde{\chi}_1^0} = 50\,\text{GeV}$ (red line), $m_{\tilde{\chi}_1^0} = 100\,\text{GeV}$ (green, dashed line) and $m_{\tilde{\chi}_1^0} = 150\,\text{GeV}$ (blue, dotted line). The slepton mass was kept constant at $m_{\tilde{e}_L} = 200\,\text{GeV}$. Each of the samples contains 100.000 events.

included. Figure 9.1 shows the η and p_T distributions of the produced gaugino for three different gaugino masses. The gauginos are boosted in the forward direction, especially for high masses, while no big mass effect is visible in the p_T distribution. The lower row in Figure 9.1 shows the corresponding distributions for the photon resulting from the neutralino decay. As a result of the neutralino boost towards the forward direction also the photon is emitted relatively forward. This fact complicates the photon identification, since the efficiency drops in the forward region (see Fig. 6.1). However, the dependence on the neutralino mass is small and with a peak around 1.2, which is the transition region from BCAL to FCAL (see Fig. 5.11), still a large fraction of signal photons are expected in the barrel region. In contrast to this, a large dependence on the neutralino mass is observed

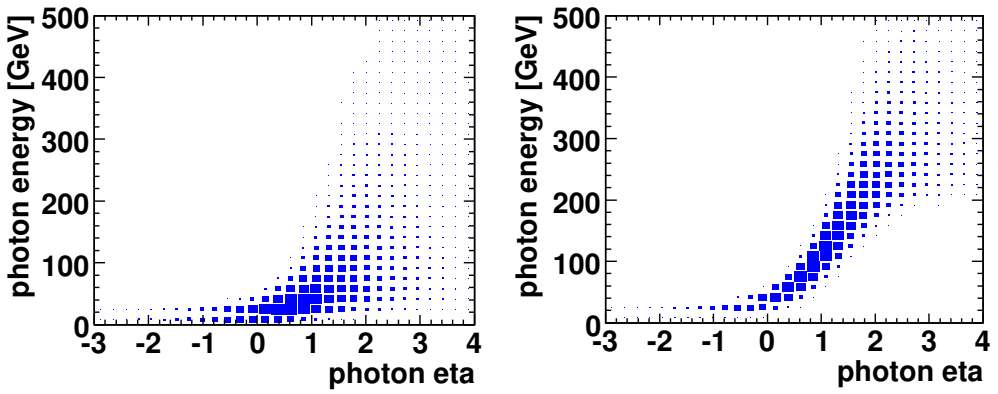

FIGURE 9.2: Correlation of photon energy and theta for $(m_{\tilde{\chi}_1^0}, m_{\tilde{e}_L}) = (50\,\text{GeV}, 200\,\text{GeV})$ (left) and $(m_{\tilde{\chi}_1^0}, m_{\tilde{e}_L}) = (150\,\text{GeV}, 200\,\text{GeV})$ (right).

in the p_T distribution, which represents a Jacobian peak, smeared out due to the Lorentz transformation into the laboratory system. The peak position, lying at half the neutralino mass, is moving towards higher p_T values proportional to $m_{\tilde{\chi}_1^0}$.

Figure 9.2 shows the correlation of photon energy and theta for different neutralino masses. The average angle of the emitted photon relative to the neutralino direction depends on the energy like:

$$\theta \propto \frac{1}{\gamma} = \frac{m_{\tilde{\chi}}}{E_{\tilde{\chi}}} \tag{9.1}$$

This correlation becomes more visible for higher neutralino masses where the variation of the neutralino direction becomes smaller due to the smaller available phase space. Hence, the difficulty to measure at small angles is partly eased by higher photon energies.

The effect of different slepton masses is shown in Figure 9.3. The cross section dependence on the momentum transfered by the slepton ($Q_{\tilde{l}}^2$) is given by the propagator term

$$\sigma \propto \frac{1}{(m_{\tilde{l}}^2 + Q_{\tilde{l}}^2)^2}\,. \tag{9.2}$$

For heavy propagator masses ($m_{\tilde{l}} = O(100\,\text{GeV})$) the cross section is dominated by the mass and the Q^2 distribution that contributes. The Q^2 distributions depends only marginally on the gaugino mass and gets only slightly shifted by variations

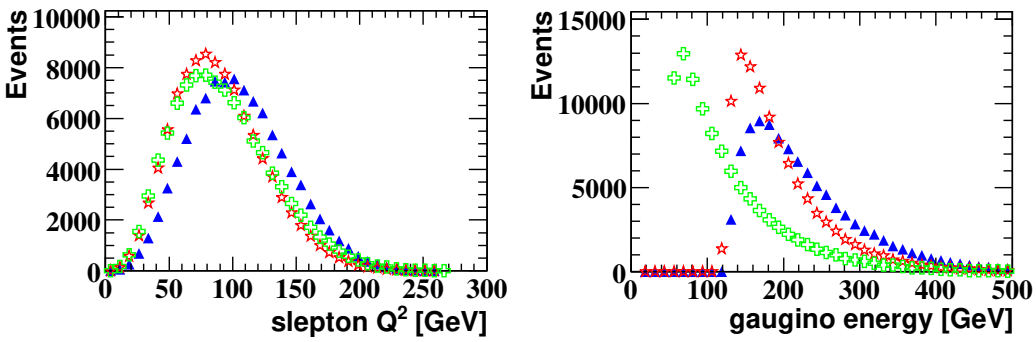

FIGURE 9.3: Slepton four-momentum transfer and gaugino energy for different slepton and gaugino masses, $(m_{\tilde{\chi}_1^0}, m_{\tilde{e}_L}) = (100\,\text{GeV}, 100\,\text{GeV})$ (blue triangles), $(m_{\tilde{\chi}_1^0}, m_{\tilde{e}_L}) = (100\,\text{GeV}, 250\,\text{GeV})$ (red stars) and $(m_{\tilde{\chi}_1^0}, m_{\tilde{e}_L}) = (50\,\text{GeV}, 250\,\text{GeV})$ (green crosses).

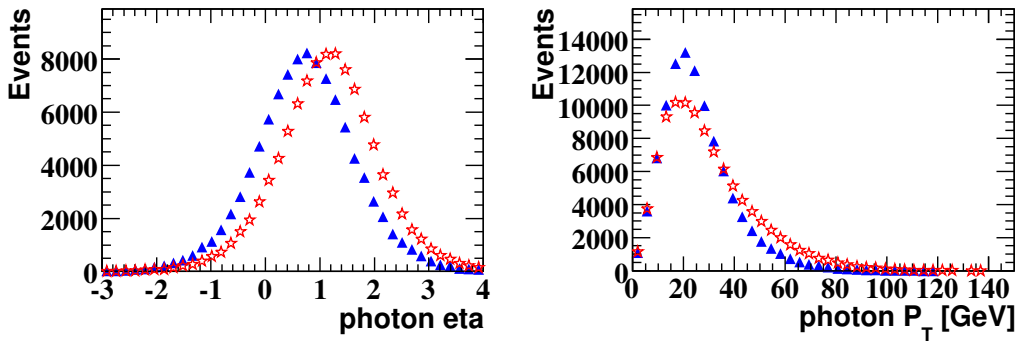

FIGURE 9.4: Effect of different slepton masses on gamma eta and gamma p_T, $(m_{\tilde{\chi}_1^0}, m_{\tilde{e}_L}) = (50\,\text{GeV}, 50\,\text{GeV})$ (blue triangles) and $(m_{\tilde{\chi}_1^0}, m_{\tilde{e}_L}) = (50\,\text{GeV}, 250\,\text{GeV})$ (red stars).

of the slepton mass. It is nearly the same for all investigated SUSY parameter points.

As a consequence, all kinematic variables have only a small dependence on the slepton mass and are mainly determined by the gaugino mass, as for example seen in the energy distribution of the produced gauginos (Fig. 9.3). Other examples are the energy, p_T and η distributions of the decay products which are only slightly effected by the slepton mass. The maximal difference is shown in Figure 9.4 for

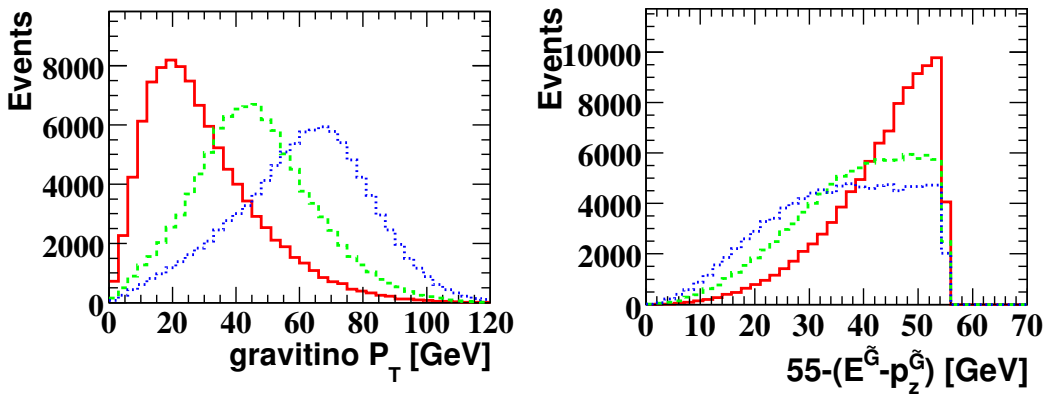

FIGURE 9.5: Gravitino distributions (p_T, and $E - p_z$) at generator level for neutralino masses $m_{\tilde{\chi}_1^0} = 50\,\text{GeV}$ (red line), $m_{\tilde{\chi}_1^0} = 100\,\text{GeV}$ (green, dashed line) and $m_{\tilde{\chi}_1^0} = 150\,\text{GeV}$ (blue, dotted line). Each of the samples contains 100.000 events.

selectron masses of 50 GeV and 250 GeV.

After what has been said it is easy to predict the distributions for the gravitino (compare with Figure 9.5). The same effect as for the photon p_T is visible in the p_T distribution of the gravitino, which represents the total missing transverse momentum that is expected in the calorimeter. Similar to the missing P_T also the missing P_z will increase with $m_{\tilde{\chi}_1^0}$. The expected distribution of visible $E - P_z$ (see Eq. (6.29)) is shown in Figure 9.5. It is significantly different from the main background of CC DIS events.

9.3 Selection of Electron Sample

In order to study the performance of the electron finder which is used as the basis of the photon identification, NC DIS events were selected, representing the typical source of electrons at HERA. The selected sample also serves as a basis for further studies (see Sect. 9.5 below). To check the selection in the signal-like high electron-p_T region the following cuts were applied:

- DST trigger bit 32
- $-40\,\text{cm} < Z_{vtx} < 40\,\text{cm}$
- $45\,\text{GeV} < E - P_z < 62\,\text{GeV}$

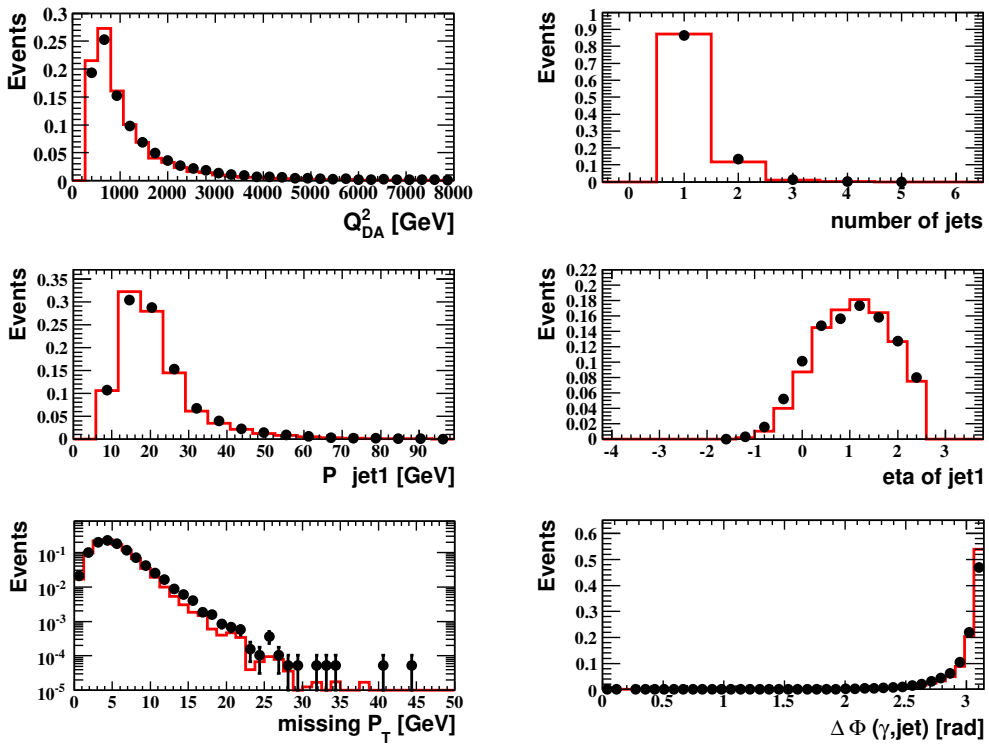

FIGURE 9.6: Control distributions for electron sample. Both distributions are normalised to 1.

- $Q^2_{DA} > 400\,\mathrm{GeV}^2$
- at least one jet with $p_T^{jet} > 6\,\mathrm{GeV}$ and $-1.5 < \eta^{jet} < 2.5$
- EM electron with $prob > 0.001$ and $-1.2 < \eta^e < 2.8$ and $p_T^e > 15\,\mathrm{GeV}$

For this study the positron data recorded in 1999-2000 was used (see Tab. 9.1). After the cuts 19277 events remain while the MC predicts 19029. Some control distributions are shown in Figure 9.6.

The electron distributions show an excellent agreement between data and MC. This proves that the electron finder works fine. As expected, the $\Delta\phi$-distribution between electron and first jet has a strong peak at 180°.The observed width results mainly from multi-jet contributions. A cut at $\Delta\phi < 3.0$ *rad* will thus cut away most of the NC events.

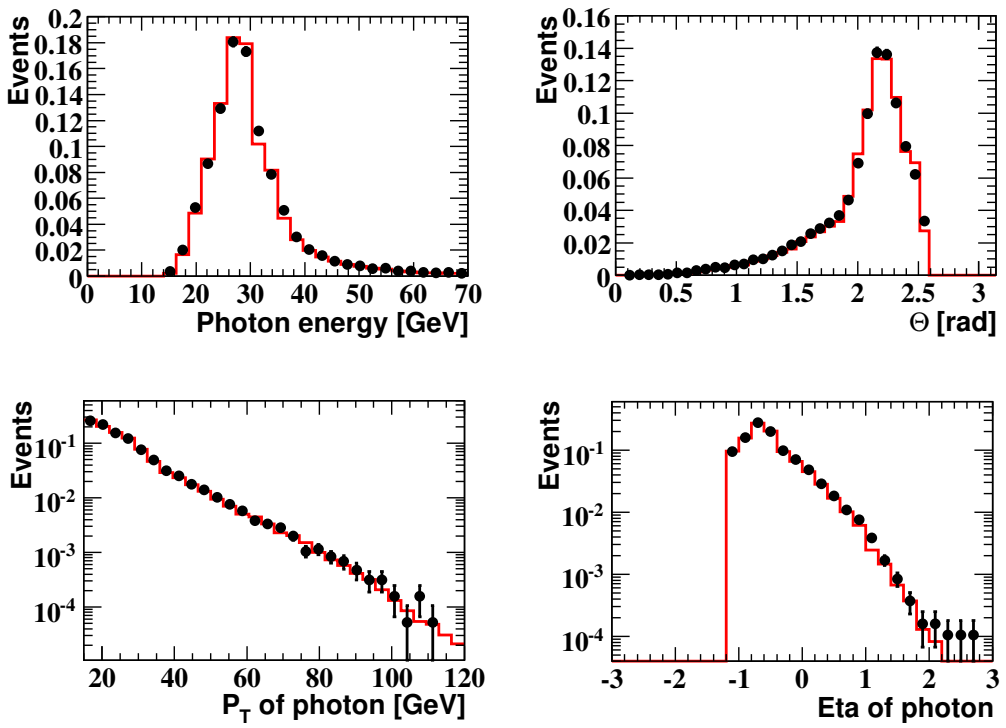

FIGURE 9.7: Distributions of electron variables for electron sample. Both distributions are normalised to 1.

Looking at the P_T-miss distribution one observes that the MC describes the data well only for $P_T < 11\,\text{GeV}$; for higher values of P_T the MC predictions tend to be too low. After a cut of P_T-miss $> 22\,\text{GeV}$ very few NC events survive. Instead (after releasing the $E - P_z$ cut) CC events will become dominant, as described in the next section.

9.4 Control Selection for Gravitino Channel

In order to control the gravitino selection the first selection step explores only the signature of missing transverse energy in the signal. As a consequence, the selected standard model data events are mainly charged current events. Neutral current and photoproduction events may contribute due to mismeasurements of the energy in the calorimeter. The cuts are:

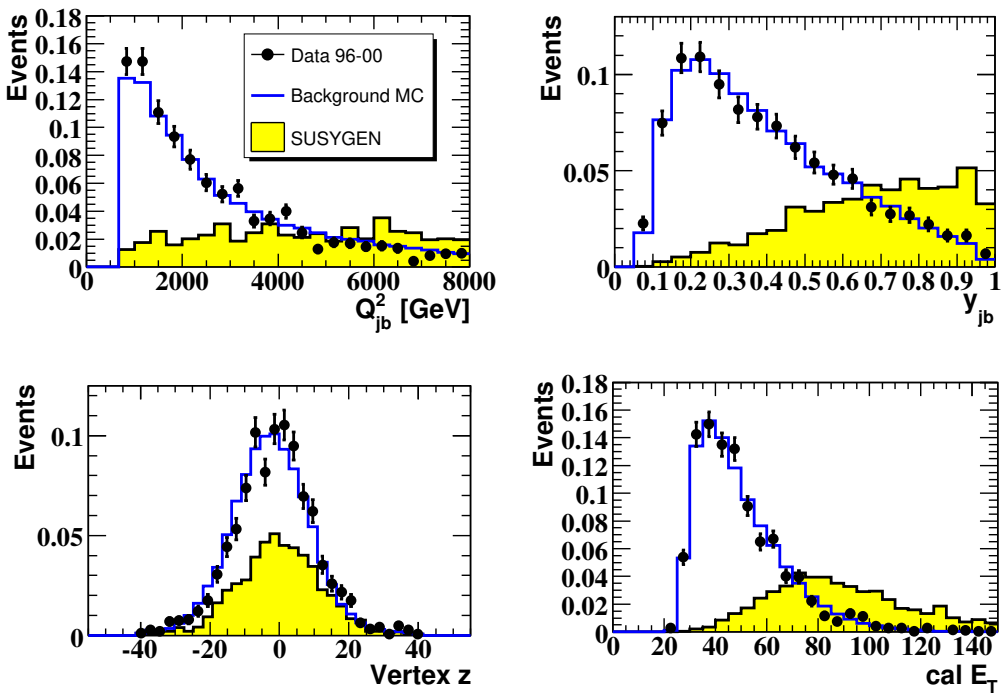

FIGURE 9.8: Control distributions for gravitino channel of Q^2_{JB}, y_{JB}, Z_{vtx} and E_T for the HERA I data set. Data and background distributions are normalised to 1, the signal to 1/2.

- *Trigger selection:* The CC trigger bit DST 34 was used to pre-filter the events. In addition the following chain of trigger bits was required:[1]

$$FLT60 \quad \&\& \quad ExoSLT04 \quad \&\& \quad (ExoTLT02 \quad || \quad ExoTLT06)$$

- *Vertex position:*

$$|Z_{vtx}| < 40\,\text{cm}$$

- *Kinematic restriction:*

$$Q^2_{JB} > 700\,\text{GeV}^2$$

- *Rejection of missmeasured events:*

$$E - P_z < 65\,\text{GeV} \tag{9.3}$$

[1]See Appendix B for a description of the trigger bits.

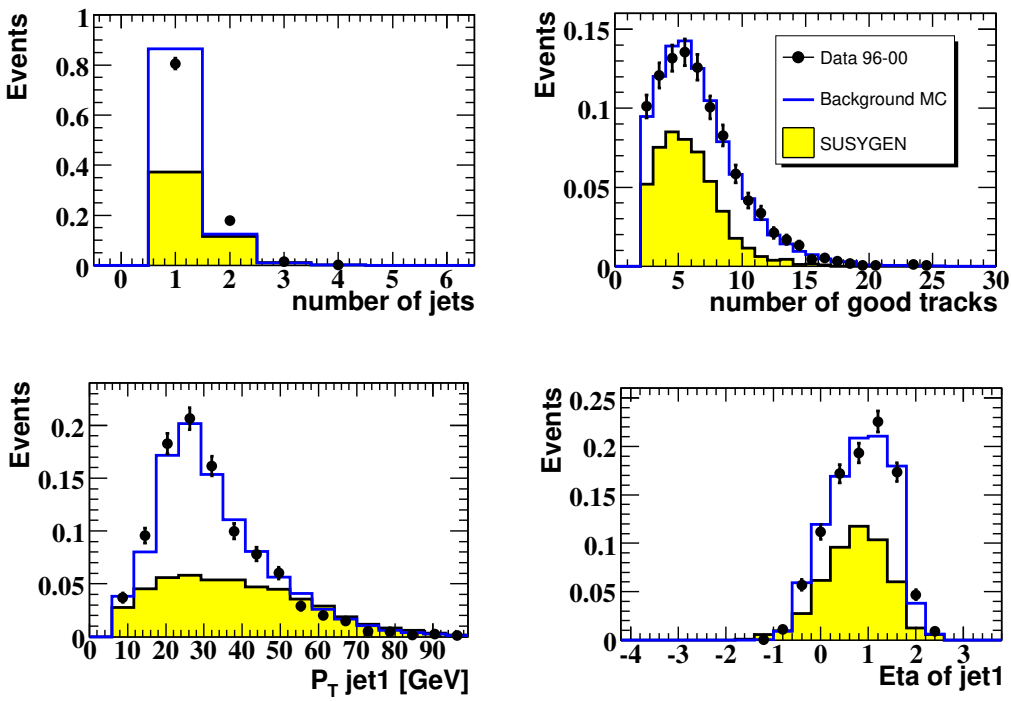

FIGURE 9.9: Control distributions for gravitino channel of number of jets, number of good tracks, p_T of the first jet and eta of the first jet for the HERA I data set. Data and background distributions are normalised to 1, the signal to 1/2.

- *Jet requirements:* At least one jet is required with the following properties:

$$p_T^{jet} > 6\,\text{GeV} \qquad -1.5 < \eta^{jet} < 2.5$$

- *Rejection of photoproduction events:* Since these events are balanced in p_T and since signal events posses a large value of missing momentum, they can be rejected by:

$$P_T > 22\,\text{GeV}$$

- *Rejection of neutral current events:* Also these events are rejected by the P_T cut. Due to their higher transverse momentum compared to photoproduction events the effect of missmeasuremets is larger. Therefore, an additional cut is applied which makes use of differences in topology. While in LO neutral current events electron and jet are back-to-back this is not the case for signal

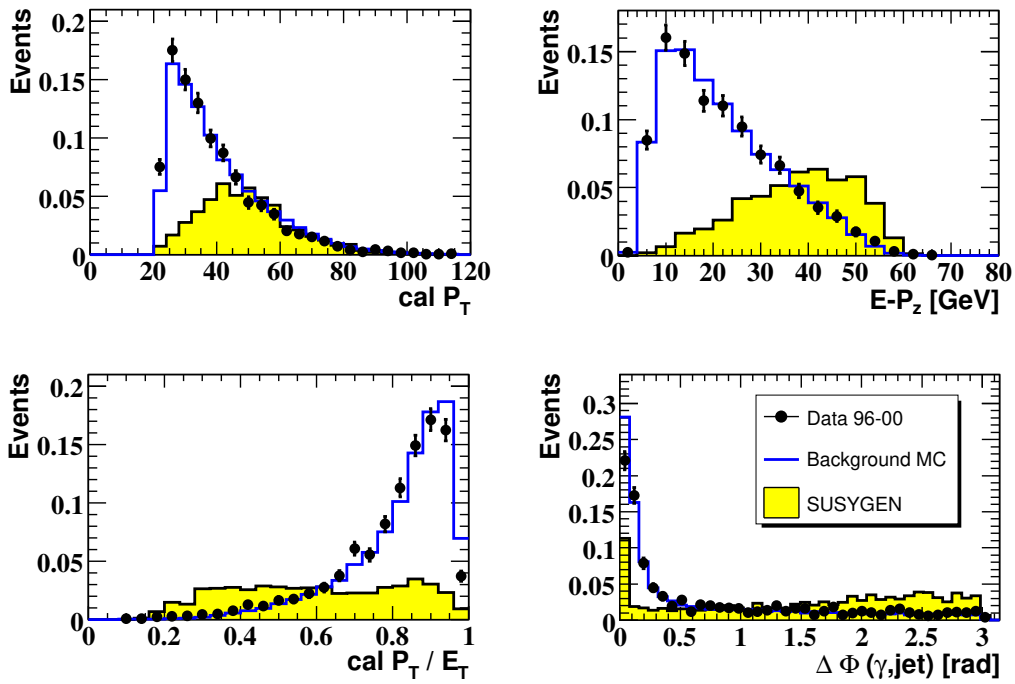

FIGURE 9.10: Control distributions for gravitino channel of P_T, $E - P_z$, P_T/E_T and $\Delta\Phi(\gamma, jet)$ for the HERA I data set. Data and background distributions are normalised to 1, the signal to 1/2.

events, due to the additional gravitino. It was found that using the angle in the $r - \phi$ plane gives a better separation than the three-dimensional angle. Therefore, the cut used is:

$$\Delta\phi(jet, \gamma) < 3.0\,\text{rad}$$

This cut was only used for events for which a photon candidate was found.

- $N_{Trk}^{Good} \geq 2$*;* at least two good tracks are required, where good tracks are primary vertex tracks with $p_T^{Trk} > 200\,\text{MeV}$.

- *Beam gas rejection:* Events resulting from proton-beam-gas interactions typically have a large number of low-energy tracks not originating from the primary vertex. They can be rejected by requiring:

$$(N_{Trk} - 20)/N_{Trk}^{Good} < 4$$

- *Cosmic muon rejection:* High energetic muons resulting from cosmic rays may traverse the detector and deposit energy in the calorimeter. If they survived the selection cuts and attributed a high discriminant value they were removed by a visual scan.

- *Beam muon rejection:* A prominent background for charged current events are muons originating from the proton beam which traverse the detector horizontally. Three different halo muon finders were used to reject such events. In addition an upper cut was applied to the fraction of electromagnetic and hadronic energy in the BCAL:

$$E^{emc}_{BCAL}/E^{hac}_{BCAL} < 0.85$$

  A lower cut was not applied because of the presence of signal in this region.

- *CAL timing:* Events resulting from proton-beam gas interactions may be suppressed by using the calorimeter timing information, which is calibrated to be zero for relativistic particles.

$$\begin{aligned} |t_b| < 5\text{ns} \quad & \text{if} \quad E_{BCAL} > 4\,\text{GeV} \\ |t_f| < 5\text{ns} \quad & \text{if} \quad E_{FCAL} > 4\,\text{GeV} \\ |t_r| < 5\text{ns} \quad & \text{if} \quad E_{RCAL} > 4\,\text{GeV} \\ |t_f - t_r| < 6\text{ns} \quad & \text{if} \quad E_{CAL} > 5\,\text{GeV} \end{aligned}$$

  Here, t_f, t_b and t_r denote the detection times in ns in the FCAL, BCAL and RCAL, respectively, and the total energy in the CAL is $E_{CAL} = E_{FCAL} + E_{BCAL} + E_{RCAL}$.

After these cuts 1951 data events remain from the HERA I data set while 1938.2 ± 3.8 are expected from SM MC simulations. MC samples for NC DIS, CC DIS and PhP events were used. The contribution from NC DIS to the SM expectation is 10.4 ± 0.1 events. No event from the PhP MC sample survived the selection. For the evaluation of the signal efficiency the reference sample with $m_{\tilde{\chi}^0_1} = 100\,\text{GeV}$ and $m_{\tilde{e}_L} = 140\,\text{GeV}$ is used giving $\epsilon_S = 73\%$ after the preselection. The control distributions are shown in Figure 9.8, Figure 9.9 and Figure 9.10 together with the SUSY signal. One observes a good agreement between data and MC. The signal distribution shows that it is not possible to apply the usual P_T/E_T-cut for non-ep background and PhP reduction. Also upper cuts on y_{JB} that are usually used

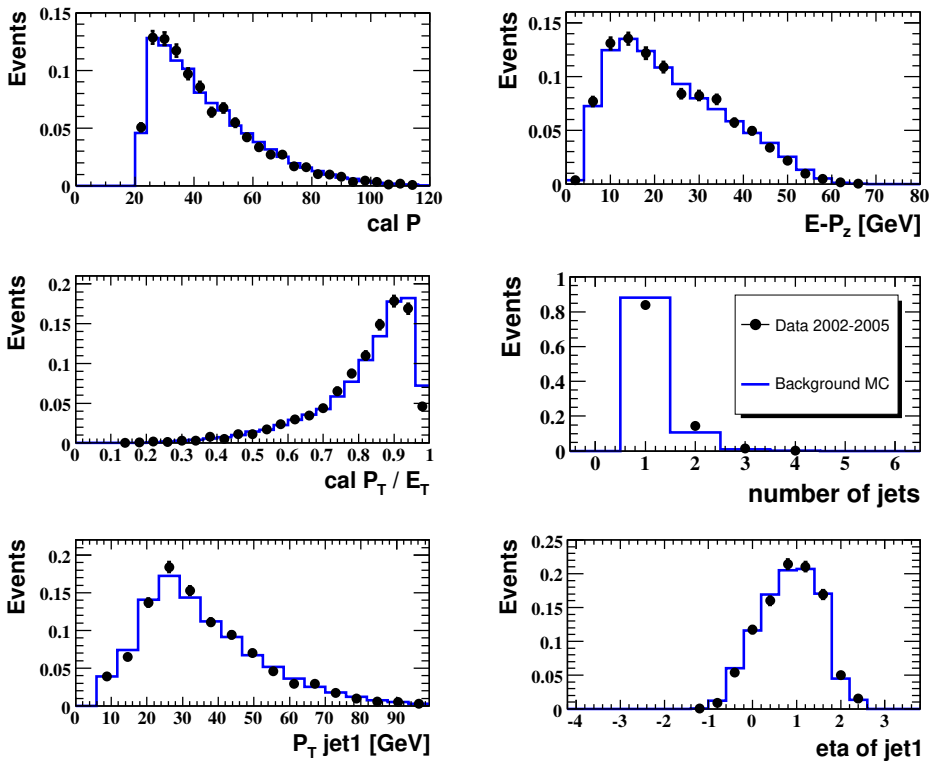

FIGURE 9.11: Control distributions for the gravitino channel of P_T, $E - P_z$, P_T/E_T, number of jets, p_T of the first jet and eta of the first jet for the HERA II data set. All distributions are normalised to 1.

to reject photoproduction events can not be applied. A good agreement between data and MC is observed in all variables.

9.4.1 Selection of HERA II Data

Due to the changed trigger configuration in the HERA II period the trigger chain used in the HERA I selection could not be used. Instead the corresponding cuts were applied offline. After this, still an excess of background events remained which could be removed by slightly tightening the Good-Track-fraction cut:

$$(N_{trk} - 20)/N_{Gtrk} < 2 \tag{9.4}$$

In the HERA II data, 4801 events are observed, compared to a SM MC prediction of 5030.1 ± 19.8 events. The control distributions are shown in Figure 9.11 and Figure 9.12. Also here, the data is well described by the SM MC.

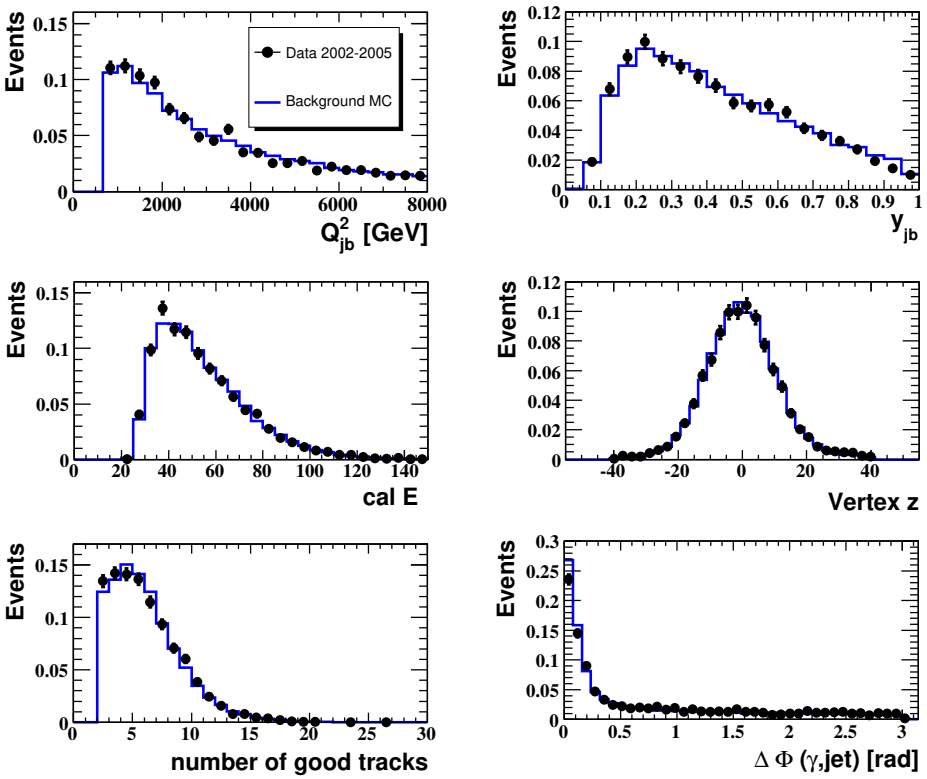

FIGURE 9.12: Control distributions for the gravitino channel of Q^2_{JB}, y_{JB}, E_T, Z_{vtx}, number of good tracks and $\Delta\Phi(\gamma, jet)$ for the HERA II data set. Distributions are normalised to 1.

9.5 Studies of Photon Properties

The optimisation of the photon selection has two conflicting aims, which have to be balanced. On the one hand, the efficiency for signal photons should be as high as possible, but and on the other hand, the acceptance for any type of background particles should be minimized.

The first aim deals with the difficulty that a signal event my be rejected because:

- the photon is not found;
- it converts into an electron-positron pair and therefore produces a track;
- it stays a photon but a neighboring track is wrongly associated to it.

To address the first point the efficiency of the electron finder was investigated with the help of the electron sample as presented in Sect. 9.3. In the next step, the electron finder was configured for photon finding (see Sect. 6.4) and the efficiency for photon identification was studied. The distribution of the photon probability is shown in Figure 9.13. It is generally well described. The signal MC was used to

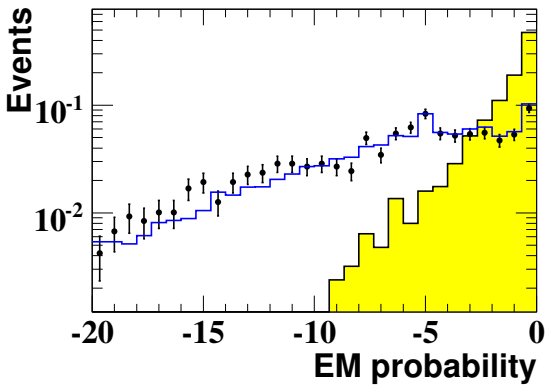

FIGURE 9.13: EM probability distribution. The x-axis shows $\log_{10}(P)$. All distributions are normalised to 1.

determine in how many cases the right photon was found by comparing the found photon with the generator information. Without applying any cuts 98% of the found and generated photons matched within $R < 1$ ($R = \sqrt{\Delta\phi^2 + \Delta\eta^2}$).

Since the conversion of the photon happens in a late part of the simulation it is not written in the FMCKIN table[2]. Therefore, instead the effect of a track cut on the signal efficiency was studied with the signal MC which gives the combined effect of the last two points. The track finding efficiency was determined from the electron sample of Sect. 9.3. It was found that in 96.3% of the cases a track could be associated to the electron candidate. On the other hand, in only 18% of the signal events a track was found in the neighborhood of the photon candidate. Thus, a tracking cut provides a good tool to separate background electrons and signal photons.

Two possible track cuts were investigated as listed in Table 9.2. The first requires that no track should be associated to the photon candidate. The second allows an associated track if it is at least 30 cm away from the cluster in the

[2]The MC table which holds the information of the generated events.

TABLE 9.2: Effect of different track cuts on signal and background MC. For the signal MC the full set of SUSY MC for different parameter points was used. The distributions are normalised to one.

Cuts	SUSY MC	CC DIS MC	S/B
Before Track Cut	65%	26.1%	2.5
No Track	53%	4.7%	11.3
$DCA > 30\,\text{cm}$	59%	7.4%	8.0

calorimeter. The signal and background distributions for the distance of the closest track are confronted in Figure 9.14. Since the background distribution falls toward

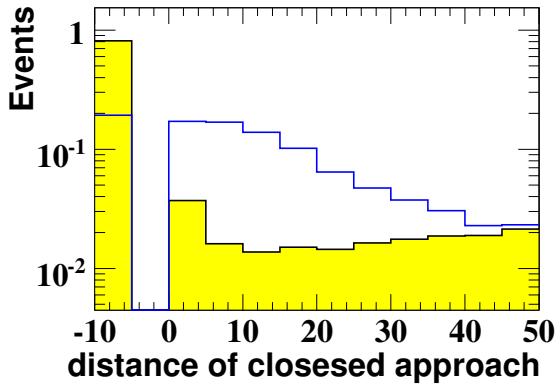

FIGURE 9.14: Distance of closed approaching track to the energy cluster in the calorimeter identified by the EM finder, for the signal MC (filled histogram) and the background CC DIS MC (blue line). The bin at -10 shows the events where no associated track was found ($DCA > 50\,\text{cm}$). Both distributions are normalised to 1.

higher DCA values while the signal distribution rises, no big difference is observed at high DCA values. Hence, the second cut was applied as it leads to higher signal efficiencies which can be used in the discriminant method to achieve higher signal-to-background ratios.

The second aim mentioned in the beginning of this chapter deals wit the difficulty that the following particles may fake a signal photon:

- A η, π^0 or photon resulting from a jet;

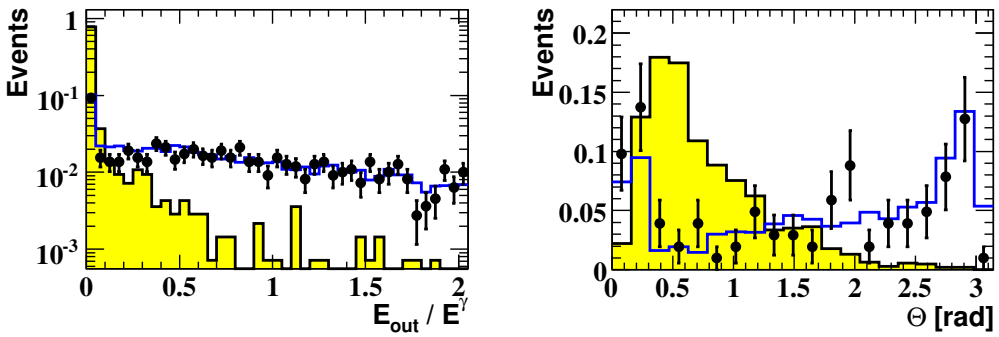

FIGURE 9.15: Fraction of photon energy in an outer cone with $0.7 < R < 1.2$ (E_{out}) and an inner cone with $R < 0.7$ (E^{γ}), shown on the left. On the right: photon theta after a cut of $E_{out}/E^{\gamma} < 0.05$. All distributions are normalised to 1.

- an electron where the track has not been found;
- a photon radiated from the initial electron (ISR).

The first point can be addressed by an isolation cut of the photon to the surrounding jets. It was found that an isolation requirement of $\Delta R \geq 1$ can increase the signal-to-background ratio by a factor 1.3, but it also lowers the signal efficiency by 15%.

A better method is to compare the photon energy of all cells inside an inner cone with the energy of the neighboring cells outside this cone (contained within a second larger cone). Different cone sizes were studied and the best results were obtained for an inner and outer cone of 0.7 and 1.2, respectively. The distribution of the cone-energy fraction is shown in Figure 9.15. The resulting theta distribution after a cut of $E_{out}/E^{\gamma} < 0.05$ is also shown. One observes that now the contribution from initial state radiation becomes visible at high theta values. In the forward region the number is still higher due to the increased activity in this region. However, the results obtained in multidimensional cuts by the discriminant method (see Chapter 8) can not be improved with this additional cut, since it mainly cuts events at low discriminant values. Moreover, a further decrease in statistics as input for the limit calculation would make it more sensitive to statistical fluctuations. Finally, an indirect isolation requirement is already included in the EM probability (see Sect. 6.4).

9.6 Final Selection for Gravitino Channel

Here, the data set is further reduced by making the additionally requirement of a photon in the final state. The cuts are:

- At least one photon candidate with the following properties:
- $E^{\gamma} > 4\,\mathrm{GeV}$
- $-2.8 < \eta^{\gamma} < 2.8$
- $Prob > 10^{-4}$
- DCA $> 30\,\mathrm{cm}$

Loose cuts are applied to the photon in order to maximize the input efficiency for the discriminant. Of the HERA I data events 337 are selected, while 325 ± 0.7 are predicted from SM MC. At this stage, the contribution from NC DIS events

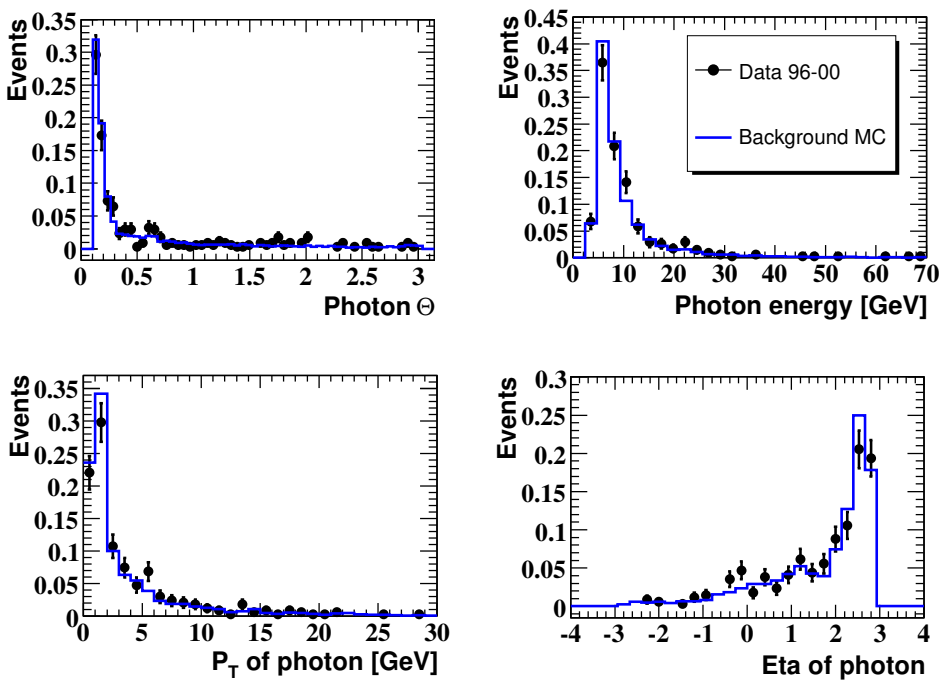

FIGURE 9.16: Distributions of photon variables for gravitino channel after final selection cuts for HERA I data set. Distributions are normalised to 1.

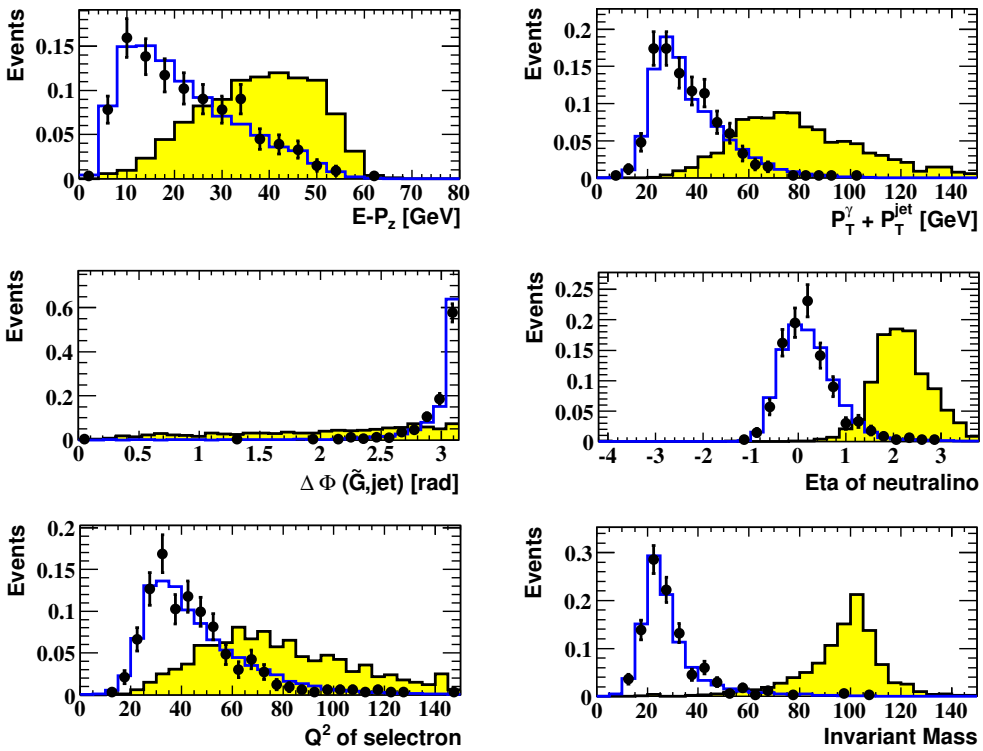

FIGURE 9.17: Distributions of discriminant variables for gravitino channel after final selection for HERA I data set. All distributions are normalised to 1.

of less than one event is negligible. The signal efficiency after all cuts is still 63%. Figure 9.16 shows the photon variables E^γ, p_T^γ and η^γ after these cuts. Given the loose selection of a rather complicated final state the MC ability to describe the data is remarkable.

The distributions of six additional event variables are shown in Figure 9.17. They all show a prominent difference in the distributions for signal and background:

- $E - P_z$ in the calorimeter, since the gravitino is traveling more forward than the neutrino in CC events, its p_z is higher for the same energy (see Eq. (6.29));
- $p_T^\gamma + p_T^{jet}$, since both photon and jet have a high momentum the difference gets even more pronounced when taking the sum;
- $\Delta\phi(\tilde{G}, jet)$, while in CC DIS events neutrino and jet are back-to-back this is

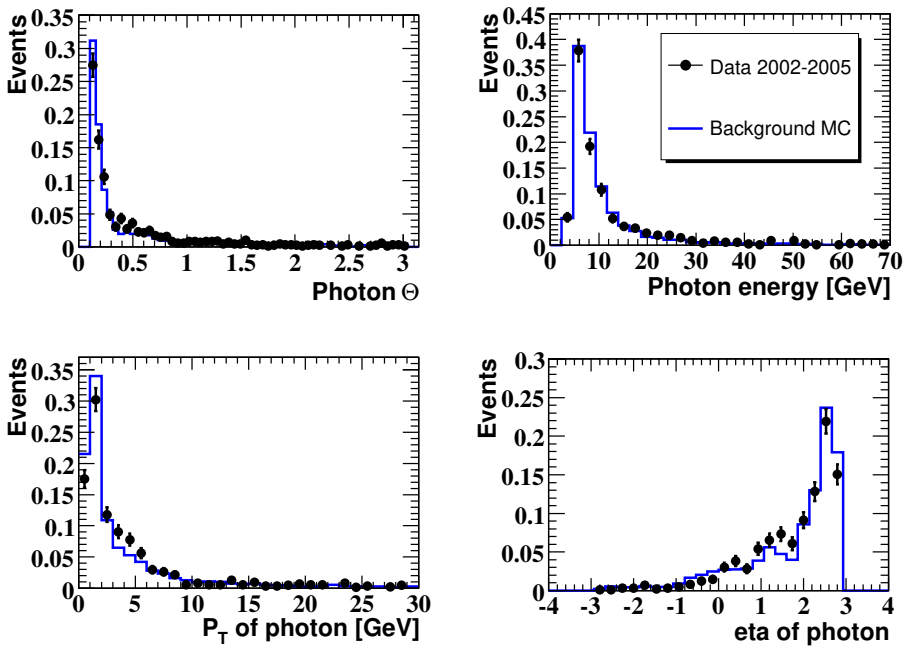

FIGURE 9.18: Distributions of photon variables for gravitino channel after final selection cuts for HERA II data set. Distributions are normalised to 1.

not the case for the gravitino due to the additional photon;

- η of the neutralino, which is traveling very forward in the signal, while the reconstruction out of CC DIS events is nearly symmetric;
- the momentum transfered by the selectron (see Eq. (6.32));
- the invariant mass of photon and reconstructed gravitino.

These variables are used for the discriminant method.

9.6.1 Selection of HERA II Data

The control distributions for the final selection of HERA II data are shown in Figure 9.18 for the photon variables and Figure 9.19 for the discriminant variables. 942 datat events remain and 912 ± 3.6 are predicted from SM MC. Also here, the agreement is satisfactory.

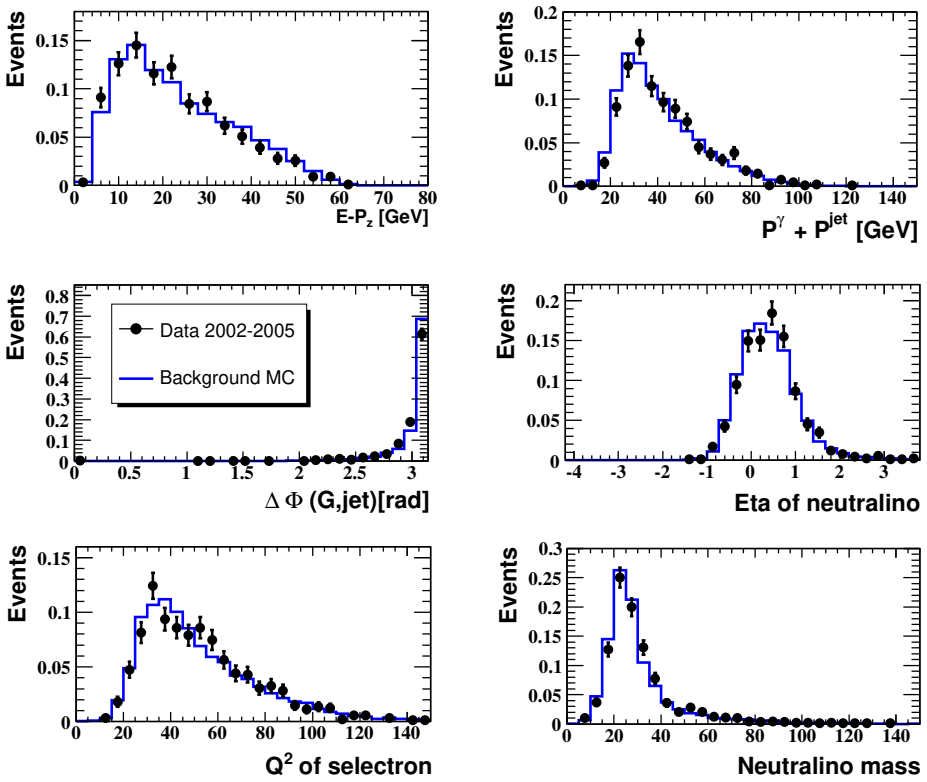

FIGURE 9.19: Distributions of discriminant variables for gravitino channel after final selection for HERA II data set.

9.7 Cut Performance Studies

An important question is the performance of the different cuts. In order to reach high signal efficiencies it has to be studied how critical they are and what is their potential. A linear listing of the number of events cut by the different cuts in sequence is not adequate since it depends on the sequence in which the cuts are applied. Here, the total number of cut events (N inclusive) and the number of events which are cut by no other cut (N exclusive) are used[3]. They are listed in Table 9.3 for signal and CC background MC[4]. The number of exclusive and

[3]This idea could be extended to multidimensional correlation matrices, but this was not followed up here.

[4]Since the background MC samples consist of various files with different Q^2 cuts, the sum of the weights of the cut events is used to computed the percentage of cut events, since otherwise the effect of cuts on variables correlated to Q^2 would be underestimated.

TABLE 9.3: Effect of the most important cuts before (N^{inc}) and after (N^{exc}) all other cuts of the final selection are applied, for the SUSY signal and CC background MC. The signal values are for $m_{\tilde{\chi}_1^0} = 100\,\text{GeV}$.

Cut	N^{inc}_{SUSY}	N^{inc}_{CC}	N^{exc}_{SUSY}	N^{exc}_{CC}
DST 34	1.0%	5.5%	0%	0%
Number of Jets	3.1%	13.7%	1.9%	0.9%
$Q^2_{JB} > 700$	4.0%	35.1%	0.1%	1.0%
P_T	9.8%	38.1%	2.5%	1.8%
Number of good tracks	10.0%	22.3%	5.9%	4.6%
EM candidate	0.6%	33.9%	0.2%	12.2%
Track cut ($DCA > 30\,\text{cm}$)	8.1%	20.2%	8.0%	18.3%
$\Delta\phi(\gamma, jet1)$	6.8%	0.9%	3.5%	0.2%

inclusive events represent the minimal and maximal efficiency that can be gained by varying only the considered cut, or all cuts. Although the P_T cut rejects a large total number of signal events, releasing it would only lead to a small increase in signal efficiency.

If the exclusive number of cut events are zero this means that the cut is unnecessary. Apparently a minimal set of cuts has been found. Since all trigger cuts are repeated offline, the exclusive number of events cut by $DST34$ is zero, as it should be. The Q^2-cut is obviously not very important in the presence of the P_T-cut. A high number of exclusively cut signal events indicates a potential for signal efficiency improvements. An obvious candidate is the cut on the number of good tracks. However, it was found to be important for a good data/MC agreement. On the other hand, a high number of exclusively cut background events indicates effective cuts. A good example is the track cut. Most events it rejects would pass all other cuts.

It is interesting to see how the performance changes for different signal points. Figure 9.20 shows the number of exclusively cut events for different neutralino masses. While the P_T cut is critical for low neutralino masses, where the forward boost of the neutralino is smaller, at high neutralino masses the cut on the number of good tracks dominates, since the tracks from the jet are less well measured in the forward direction. Overall Fig. 9.20 shows that a good set of cuts has been found.

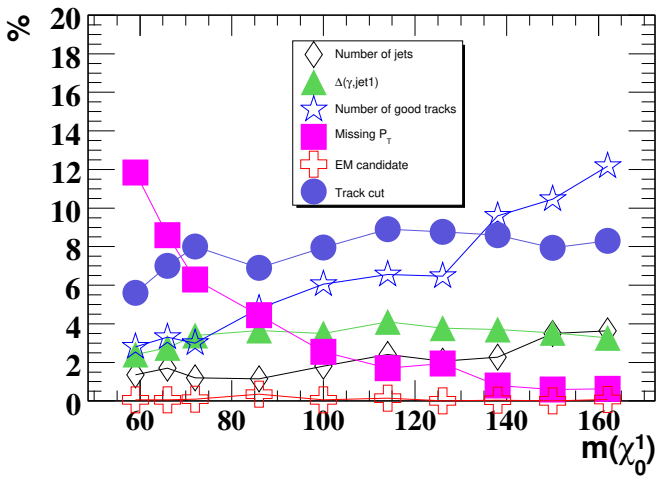

FIGURE 9.20: Percentage of signal events cut exclusively by one cut (N^{exc}_{SUSY}), for different neutralino masses.

After all these cuts the background is reduced to 5.3% of its expectation before-cuts (considering the integral). The total selection efficiency for the signal is shown in Figure 9.21 as a function of neutralino mass. With values between 52% and 62% this a satisfactory result. After the final selection, the signal-to-background ratio is enhanced by a factor 11. An overview of the number of found data and MC events is given in Table 9.4.

9.8 Effect of Slepton Mass on Selection Efficiency

In principle, the selection efficiency depends also on the mass of the exchanged slepton. However, after the discussion in Section 9.2 the dependence is expected to be small since

- the shift in the eta distribution is small, and
- the energy and p_t distributions remain unshifted.

In order to study the effect on the efficiency, for each neutralino mass-point below 120 GeV three samples with different selectron masses were generated, each sample containing 2000 events, as listed in Table C.2. The result is shown in Figure 9.22.

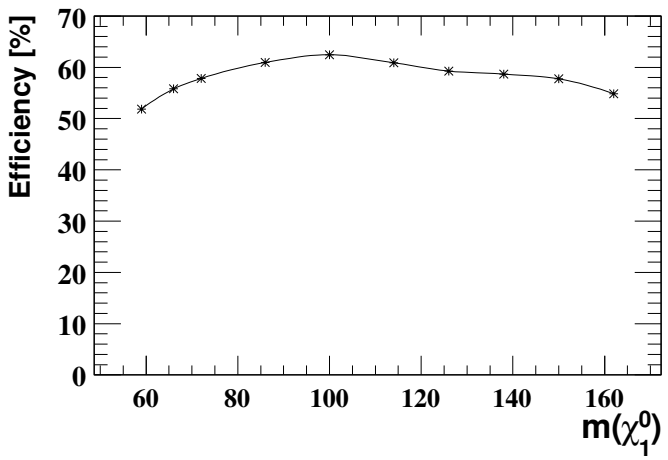

FIGURE 9.21: Total signal selection efficiency after final cuts for varying neutralino mass.

TABLE 9.4: Number of observed and expected events in the gravitino channel after preselection and final selection, separately for the HERA I (I) and HERA II (II) data sets and total (I+II). For the signal the sample with $m_{\tilde{\chi}_1^0} = 100\,\text{GeV}$ and $m_{\tilde{e}_L} = 140\,\text{GeV}$ was used.

	Observed	Expected		Signal
	data	SM	GMSB	efficiency
Preselection I	1951	1938	8.7	73%
Preselection II	4801	5030	13.1	73%
Preselection I+II	6752	6968	21.8	73%
Final selection I	337	325	7.6	63%
Final selection II	942	912	11.4	63%
Final selection I+II	1279	1237	19.0	63%

All points belonging to either the smallest, the middle or the highest value of $m_{\tilde{e}_L}$ are connected by a line. No systematic order in efficiency is observed. The variation lies within the expected range of statistical fluctuations of $\sim 3\%$.

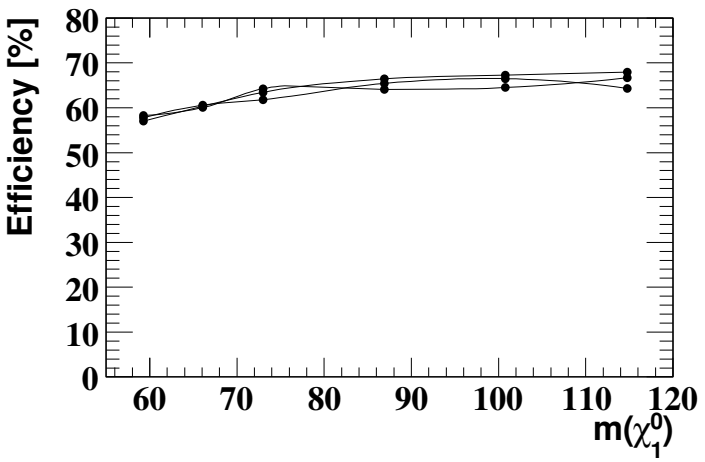

FIGURE 9.22: Total signal selection efficiency after final cuts for varying neutralino mass.

9.9 Signal-to-Background Optimisation

The final step consists in optimising the signal-to-background ratio with the help of the discriminant method as described in Chapter 8. Therefore, two questions have to be answered: How many variables should be used and which variables should that be?

Obviously, using more variables will in principle result in higher separation power. Practically however, the number of dimensions that can be used is limited by the amount of available MC events, which increases exponentially with the number of dimensions. Using more dimensions which are statistically not well described will result in worse results than using less variables with the same number of MC events. Furthermore, the separation power can not be arbitrarily increased by using more dimensions but is limited by the dimensionality of the physical process (the signal process has dimensionality six). This is true as long as the "right" variables are chosen.

This brings us to the second question. The variables used should be uncorrelated. Using two totally correlated variables would represent a waste of MC statistics and CPU time. As a criteria for the selection of a variable the separation power that it has already on its own (in the one-dimensional projection of the problem) was used. While this is not a sufficient criteria (the variable with the

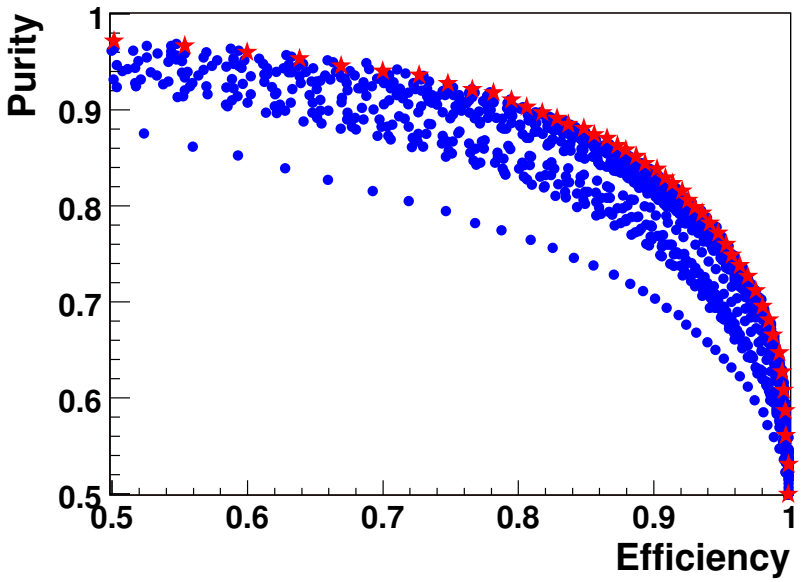

FIGURE 9.23: Purity against efficiency after cuts on the discriminant for different six-dimensional sets of discriminant variables. Points forming a line correspond to different cuts on the same discriminant. The total integral of signal and background discriminant distributions was set to one.

highest separation power does not have to belong to the set of variables with the highest separation power) but it is a necessary criteria (adding a variable with no separation power at all will not improve the result).

Consequently, in a first step the variables with a high separation power were considered and the best 12 of them were selected to form the ground set for further investigations. These variables are: $\Delta\phi(\gamma, jet)$, $\Delta\phi(\tilde{G}, jet)$, η^{χ}, p_T^{χ}, $\Delta\eta(\gamma, jet)$, $\Delta R(\gamma, \tilde{G})$, $E - P_z$, E^{γ}, E_{out}/E^{γ}, $p_T^{\gamma} + p_T^{jet}$, Q_{sel}^2 and $M(\gamma, \tilde{G})$[5]. Then the set was reduced to eight variables by computing all possible two-dimensional correlation plots. In order to select the best set of variables for the discriminant method, then all possible subsets of six variables where used (there are $\begin{pmatrix} 6 \\ 8 \end{pmatrix} = 28$ such subsets) and the discriminants were calculated[6]. Figure 9.23 shows purity against

[5]In principle, it would be possible to use also any linear (or non-linear) combination of these variables, but this would cloud the physical motivation.

[6]The automatic calculation of all possible subsets was implemented in the discriminant code,

efficiency for varying cuts on the discriminant for the different subsets. While some sets are obviously worse than the others, several subsets give similarly good results. The final set of selected discriminant variables (red stars in Fig. 9.23) are $E - P_z$, $p_T^{\gamma} + p_T^{jet}$, $\Delta\phi(\tilde{G}, jet)$, η^{χ}, Q^2_{sel} and $M(\gamma, \tilde{G})$.

The calculated discriminant distributions for signal, background and data events are shown in Figure 9.24. It includes all analysed data from the HERA I and HERA II running periods. The dependence of the signal efficiency and signal-to-background ratio on the discriminant cut are shown in Fig. 9.25 for an example SUSYGEN sample. While even for very high discriminant cuts the loss in signal efficiency is small, considerable improvements in the signal-to-background ratio can be achieved.

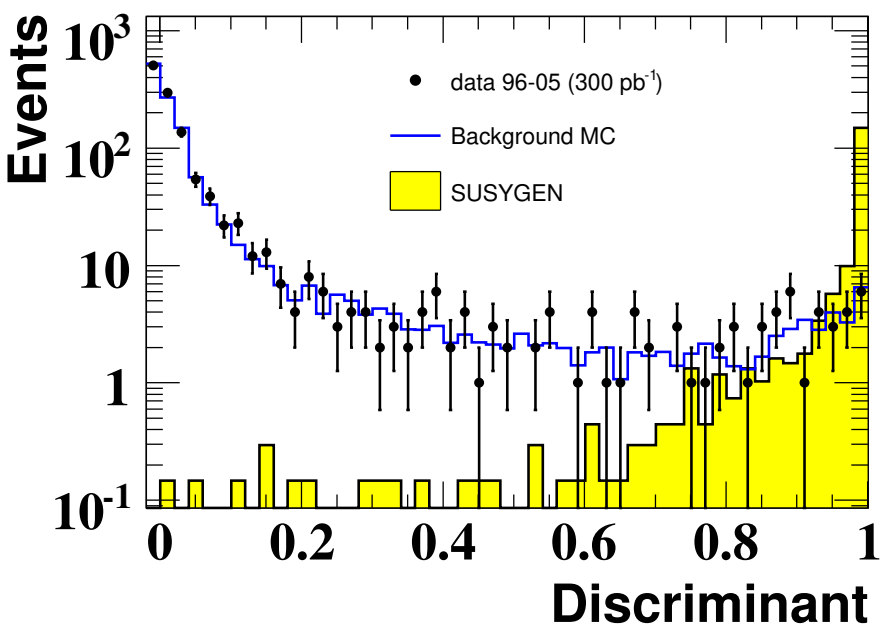

FIGURE 9.24: Discriminant distribution for gravitino channel. For the signal the reference point with $m_{\tilde{\chi}_1^0} = 100\,\text{GeV}$ and $m_{\tilde{e}_L} = 140\,\text{GeV}$ was used.

Figure 9.24 is the essence of this analysis since it provides a condensed view of the signal region (at high discriminant values). One observes that:

see Appendix E.

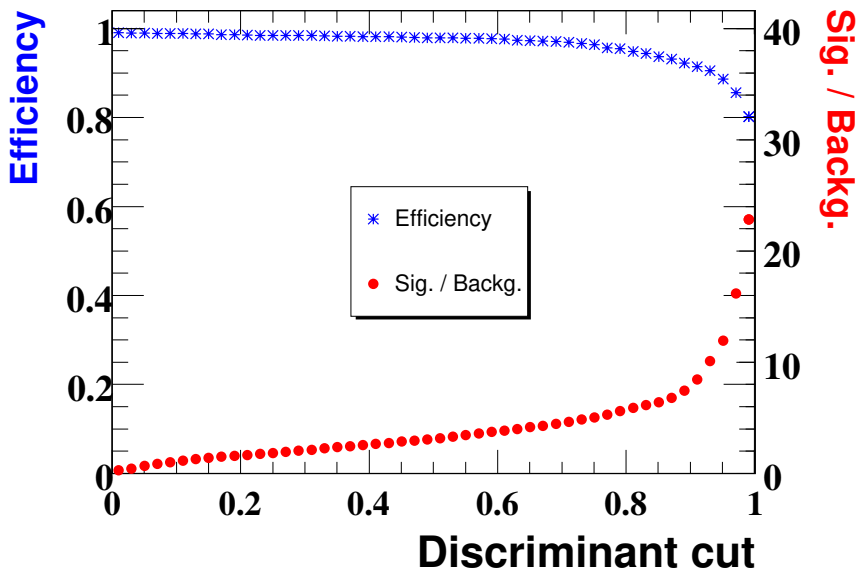

FIGURE 9.25: Efficiency and signal-to-background ratio for gravitino channel as a function of discriminant cut for the reference point with $m_{\tilde{\chi}_1^0} = 100\,\text{GeV}$ and $m_{\tilde{e}_L} = 140\,\text{GeV}$. The preselection efficiency was defined as 1 for this plot.

1. A very good separation of signal and background is achieved;
2. the data agrees well with the SM expectation also in the signal region, *i.e.*
3. no excess of SUSY events is visible in the data.

The non-observation of a kinematic excess seen in the control distributions is confirmed also in the discriminant distribution. The data agrees with the SM MC both in normalisation and shape. This agreement is remarkable considering that it is achieved in complete six dimensional parameter space. As expected, fluctuations are visible toward higher discriminant values where only a small number of events per bin are found.

The last bin shows the power of the discriminant method to increase the signal-to-background ratio. If all distributions are normalised to 1 (corresponding to a situation with S=B) it lies at 0.810 while the SM MC bin lies at 0.005. Hence, the discriminant method increases the signal-to-background ratio by a factor 147 in addition to what was achieved in the preselection if a cut at $D > 0.955$ is applied.

9.10 R_P-violating Decay Channels

As illustrated in Section 4.1 the two main R_P-violating decay channels lead to multiple-jet final states including either an electron or a neutrino. These channels were already analysed elsewhere [7] and the results were interpreted in the MSSM. In the course of this thesis an independent controll analysis was performed. Here the selection criteria are discussed rather briefly.

9.10.1 R_P-violating Decay Channel with Electron Final State

The main background for the electron channel are NC DIS events. To enrich the sample with signal events the multi-jet characteristic of the signal is exploited. Cuts which were already explained for the gravitino channel are only noted shortly here. The selection cuts applied for the electron channel are:

- DST bit 32
- $E_T > 60\,\text{GeV}$: This cut exploits the high E_T character of the signal events

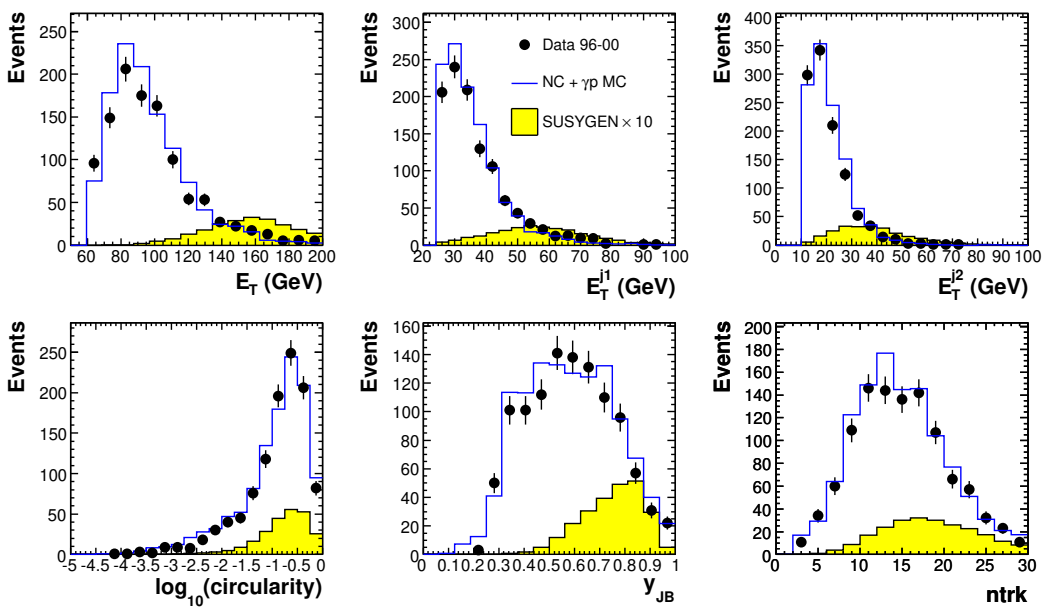

FIGURE 9.26: Control distributions for R_P-violating channel with electron final state. Shown are the total E_T in the event, the E_Ts of the first and second jet, circularity, y_{jb}, and number of tracks. The example SUSYGEN sample was scaled by 10.

compared to the background;

- $44 < E - P_z < 64\,\text{GeV}$: The NC DIS region is selected; while the lower cut rejects PhP events, the upper one removes non-ep background;
- $y_{DA} > 0.3$: PhP events are removed by this cut;
- $P_T < 20\,\text{GeV}$: This cut removes CC DIS events;
- an electron candidate with $prob > 10^{-3}$, $E^e > 10\,\text{GeV}$, $p_T^e > 6\,\text{GeV}$ and $\theta^e < 115°$ is required;
- at least two jets with $-0.5 < \eta^{jet} < 2.7$ and $E_T^{jet1} > 25\,\text{GeV}$ and $E_T^{jet2} > 12\,\text{GeV}$ are required;
- at least one good track with $p_T^{Trk} > 200\,\text{MeV}$, $-1.8 < \eta^{Trk} < 1.8$, fitted to a primary or secondary vertex, is required;
- $(N_{Trk} - 20)/N_{Trk}^{Good} < 4$
- $E_{BCAL}^{emc}/E_{BCAL}^{hac} < 0.9$

The control distributions for total E_T in the event, the E_Ts of the first and second jet, circularity, y_{jb}, and the number of tracks are shown in Figure 9.26. A good agreement between data and MC events is observed. While 1098 data events are selected, 1163.3 ± 34.1 SM events are expected from MC simulations. The set of six variables shown in Fig. 9.26 was found to possess the best separation power and was used as input for the discriminant method. It is instructive that, although the circularity distribution has nearly no separation power on its own, it leads to a significant improvement in separation power in the full multidimensional description of the process exploited by the discriminant method. The discriminant distribution is shown in Figure 9.27. The data and MC distributions agree well, besides in the first bin, which however corresponds to a region in parameter space where no signal is expected. Also in this channel no excess of data events can be observed in the signal region.

9.10.2 R_P-violating Decay Channel with Neutrino Final State

The dominant background in the neutrino channel are CC DIS events. As main characteristic the high total E_T is used to enrich the sample with signal events. In

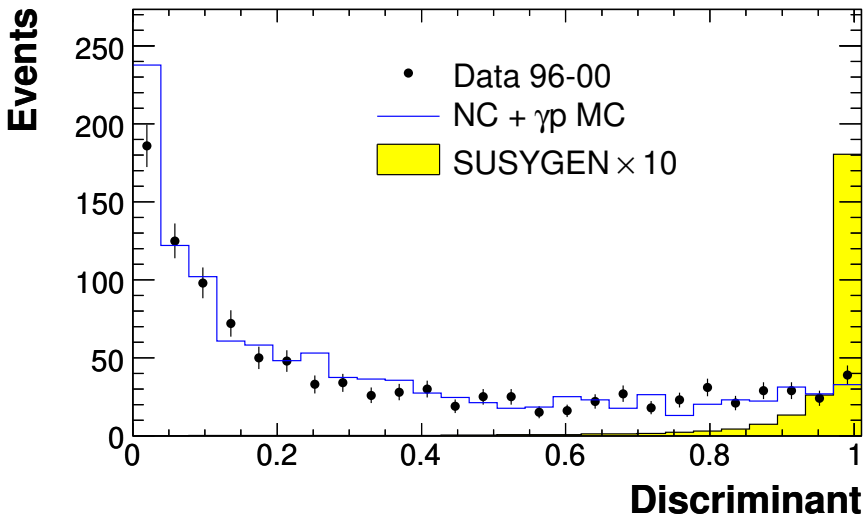

FIGURE 9.27: Discriminant distribution for the R_P-violating channel with electron final state.

order to derive an exclusive sample, which is independent from the other two channels, events where an electron candidate is found were rejected. For the selection of events in the neutrino channel the cuts used are:

- DST bit 34
- $|Z_{vtx}| < 40\,\text{cm}$
- $E_T > 50\,\text{GeV}$
- $0.3 < y_{JB} < 0.98$
- $P_T > 20\,\text{GeV}$ and $P_T^{exIR} > 18\,\text{GeV}$
- events with a electron candidate which fulfills $prob > 10^{-3}$, $p_T^e > 6\,\text{GeV}$ and $\theta^e < 180°$ are rejected;
- at least one jets with $-0.5 < \eta^{jet} < 2.7$ and $E_T^{jet} > 10\,\text{GeV}$ is required;
- at least three good track with $p_T^{Trk} > 200\,\text{MeV}$, $-1.8 < \eta^{Trk} < 1.8$ and fitted to a primary or secondary vertex are required;

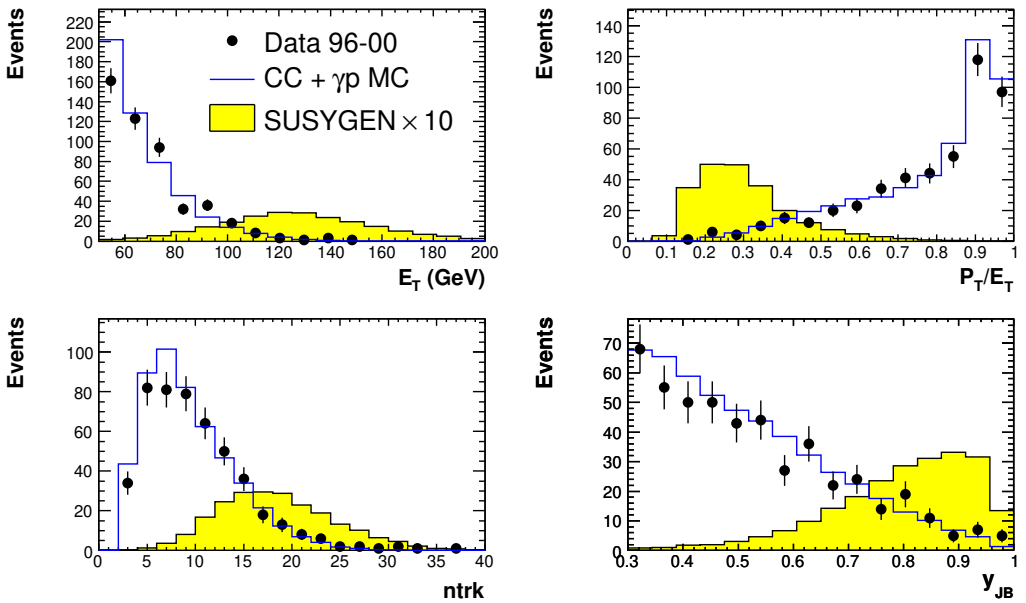

FIGURE 9.28: Control distributions for R_P-violating channel with neutrino final state. Shown are the total E_T in the event, P_T/E_T, number of tracks and y_{jb}. The example SUSYGEN sample was scaled by 10.

- $(N_{Trk} - 20)/N_{Trk}^{Good} < 4$
- $E_{BCAL}^{emc}/E_{BCAL}^{hac} < 0.9$ and $E_{RCAL}^{emc}/E_{RCAL}^{hac} < 0.9$

In addition cleaning cuts where applied as discussed for the gravitino channel to reject cosmic events, events from beam-gas interactions and halo muons. The number of found and expected events are listed in Table 9.5. The control distributions for the total E_T in the event, the ratio of the vectorial and scalar sum of transverse energy P_T/E_T, the number of tracks and y_{jb} are shown in Figure 9.26. This set of four variables was selected to be used as input for the discriminant method. The data/MC agreement is satisfactory also here. The discriminant distribution is shown in Figure 9.29. As one observes, a good separation of signal and background could be achieved, however the data is in agreement with the SM prediction also in the signal region. In conclusion, no evidence of signal events could be observed in any of the three investigated channels. Therefore, the results were used to calculate limits on the SUSY parameters, as described in the following chapters.

TABLE 9.5: Number of observed and expected events in the R_P-violating decay channels. For the signal the sample with $m_{\tilde{\chi}_1^0} = 100\,\text{GeV}$ was used.

	Observed	Expected		Signal
	data	SM	GMSB	efficiency $\times BR$
Electron channel	1098	1163.3 ± 34.1	21.9	35%
Neutrino channel	480	508.5 ± 22.5	22.7	33%

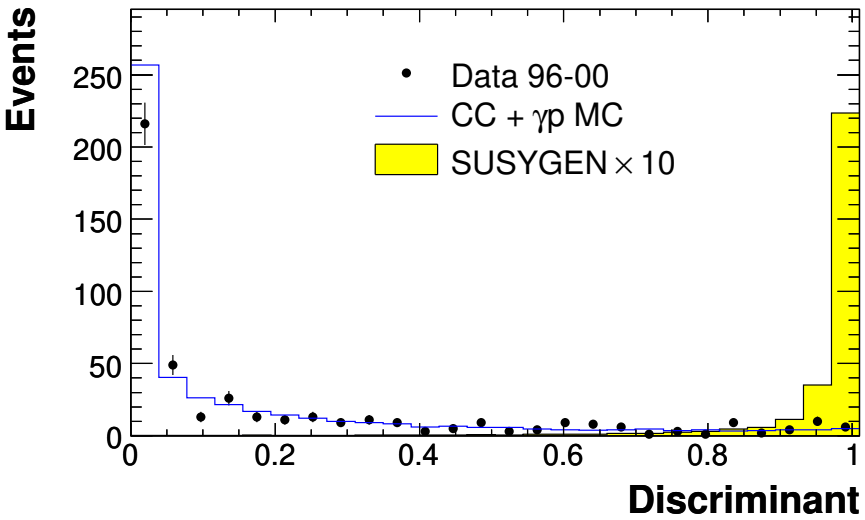

FIGURE 9.29: Discriminant distribution for the R_P-violating channel with neutrino final state.

Chapter 10

Limit Calculation

The limit θ_{lim} for some parameter θ which determines the number of events expected in some experiment $\mu = b + s(\theta)$ (where b and s are the contributions from background and signal, respectively) can be given with a confidence level CL [136] if

$$\sum_{r=0}^{d} \mathcal{P}(r, \mu) = \mathrm{CL}\,, \tag{10.1}$$

where d is the number of observed data events and $\mathcal{P}$ is the probability[1] to observe r events when μ are expected[2]. For small μ, $\mathcal{P}$ is given by the Poisson distribution:

$$\mathcal{P}(r, \mu) = \frac{e^{-\mu}\mu^r}{r!}\,. \tag{10.2}$$

Thus, it is straight forward to determine θ_{lim} by varying θ (and therefore μ) until Eq. (10.1) is fulfilled. However, the complexity of the calculation is highly increased by the necessity

- to integrate systematic uncertainties and
- to combine different search channels.

Therefore, these two aspects will be discussed in more detail in the following.

10.1 Systematic Uncertainties

Different sources of systematic errors were considered, both theoretical and experimental. These are:

[1] Viewed as a function of μ for fixed r, this is generally called the *Likelihood* function.
[2] This is the classical "frequentist" CL definition.

- *CAL energy scale*
  The energy of the calorimeter cells were varied by ±1.5% for the electromagnetic CAL and by ±2% (±3%) in the hadronic FCAL (BCAL). The difference in the number of events after the final selection cuts (see Chapter 9) was below 2.5% for the background and 0.6% for the signal.

- *Luminosity measurement*
  The uncertainty on the luminosity measurement is estimated as 2.25%.

- *QCD radiation model*
  For the background the LEPTO MEPS MC model was used instead of the ARIADNE CDM MC model resulting in a difference of 1.7%.

- *Signal Cross Section*
  Since no NLO generator programs are available for the signal process it is not possible to determine the difference between NLO and LO calculations directly. Other analyses, were NLO calculations were available, typically obtained values of 10%. If COMPHEP was used instead of SUSYGEN a difference of 5% was found. Furthermore, SUSYGEN offers the possibility to evaluate the PDFs at different energy scales ($\sqrt{\hat{s}}$, $\sqrt{Q^2}$ and $\sqrt{\hat{p}_T^2}$). The results differ by less than 10%. Consequently, a systematic error of 10% was assigned to the signal cross section.

- *Parton Density Function*
  The uncertainty on the up and down quark PDF is estimated as 3% and 7%, respectively.

- *Interpolation*
  The systematic effect due to interpolations required in the limit setting procedure is estimated as 10%.

In addition to these uncertainties, the effects of cut variations were studied in order to check for threshold effects.

- *Z_{vtx} cut variation*
  The $|Z_{vtx}| < 40\,\text{cm}$ cut was shifted by $\pm 10\,\text{cm}$. The observed differences were below 1.9% for the background and 2% for the signal.

- Q^2_{JB} *cut variation*
  The $Q^2_{JB} > 700\,\mathrm{GeV}^2$ cut was varied by $\pm 100\,\mathrm{GeV}^2$ resulting in a difference of less than 1.9% for the background and 0.4% for the signal.

- P_T *cut variation*
  The $P_T > 22\,\mathrm{GeV}$ cut was varied by $\pm 4\,\mathrm{GeV}$ resulting in a difference of less than 5.6% for the background and 2.5% for the signal.

- y_{JB} *cut variation*
  The $y_{JB} > 0.1$ cut was varied by ± 0.02 resulting in a difference of less than 2.3% for the background and 0.1% for the signal.

- $\Delta\phi(jet, \gamma)$ *cut variation*
  The $\Delta\phi(jet, \gamma)$ cut was varied by $\pm 2^\circ$ resulting in a difference of less than 0.5% for the background and 1.4% for the signal.

The effects of the considered systematic uncertainties are summarized in Table 10.1. Due to the low statistics of the data the resulting systematics was obtained from shifts to the MC samples where appropriate, as described in the next section.

TABLE 10.1: List of considered systematic uncertainties for background and signal MC.

Uncertainty on	Background	Signal
Energy Scale	2.5%	0.6%
Luminosity	2.25%	2.25%
QCD radiation model	1.7%	–
Signal cross section	–	10%
PDF	7%	7%
Interpolation	–	10%
Z_{vtx}	1.9%	2%
Q^2_{JB}	1.9%	0.4%
P_T	5.6%	2.5%
y_{JB}	2.3%	0.1%
$\Delta\phi(jet, \gamma)$	0.5%	1.4%
Σ	10.4%	13.2%

10.2 Confidence Level Calculation

For the calculation of confidence levels in this thesis a modified version of the basic method presented in the beginning of this chapter is used, as proposed by T. Junk [137][3]. For a given number of signal (s), background (b) and observed data events (d), an estimator function X is defined as the likelihood ratio:

$$X(d) = \frac{e^{-(s+b)}(s+b)^d}{e^{-b} \cdot b^d} \tag{10.3}$$

In this equation the situations with and without signal are compared for a given number of observed events. The probability to find d or less events in the data when $s+b$ are expected is then given by:

$$\mathcal{P}_{s+b} = \sum_{X(r) \leq X(d)} \frac{e^{-(s+b)}(s+b)^r}{r!}, \tag{10.4}$$

where the sum runs over all possible numbers of observed events r which have an estimator X less than or equal to the observed one. Finally, the confidence level for a configuration (s,b,d) can be calculated from:

$$\mathrm{CL} = 1 - \frac{\mathcal{P}_{s+b}}{\mathcal{P}_b} \tag{10.5}$$

where $\mathcal{P}_b$ is the probability for the background only hypothesis. This is analogous to Eq. (10.3). From this relation it becomes clear that the presented method is especially suitable for searches with a small number of events in the signal region since statistical fluctuations for which also $\mathcal{P}_b$ becomes small are treated more accurately.

Systematic uncertainties are taken into account by varying s and b according to a Gaussian distribution (where the widths are given by the different sources of systematic uncertainties). For the numerical implementation a Monte Carlo sampling technique is used in order to explore the resulting $s \times b$ phase space.

Following the proposal of A. Favara and M. Pieri [138] the method can be used in a multi-bin approach by defining a joint estimator for n bins:

$$X_{tot} = \prod_{i=1}^{n} X_i \tag{10.6}$$

[3]This method has been implemented in the ROOT class *TLimit*.

where the X_i are likelihood ratios as defined in Equation (10.3). In this case the probability in Eq. (10.4) becomes the product of the probabilities for the single bins.

Since the discriminant distribution represents a condensed description of the signal region it provides an ideal interface between event selection and limit calculation. Therefore, the bins of the discriminant distributions of the SM background, the SUSY signal and the data are used as input for b, s and d, respectively. It is important to notice that, unlike in former analyses which made a cut on the discriminant and compared the integrated number of events after the cut to derive limits in a similar way as discussed in the beginning of this chapter, in the approach used here also the *shape* of the discriminant is used, resulting in better limits.

Futhermore, since each bin can be interpreted as a different channel this method also provides the basis for limit calculations with several contributing search channels, which is the topic of the next section.

10.3 Limits on Model Parameters

The analysis process as discussed so far is summarized in Figure 10.1. Here the limit θ_{lim} on some parameter θ is determined for a given set of constant parameters θ_c (consisting of all parameters besides θ). For instance, limits in the MSSM parameter plane $\mu - M_2$ might be derived by doing the iteration over μ for a fixed M_2 and to repeat it for different values of M_2, with a final interpolation of the limit along M_2. The bottlenecks[4] of this cycle are the CL calculation (CPU-time intensive) and the generation of events for hundreds of different parameter points (working-time intensive). The aim of this section is to show how to avoid them.

The key to the following discussion is the fact that the problem factorises into two parts, as was already presented in Figure 4.7, *i.e.* :

$$\theta_i^m \;\leftrightarrow\; \theta_j^p \;\leftrightarrow\; \theta_{lim}\,, \tag{10.7}$$

where θ_i^m are model parameters (*e.g.* the parameters of the GMSB model) and θ_j^p are process parameters (*e.g.* the masses in the signal process). This can also be expressed in a functional description, as $\theta^p(\theta^m)$ and $\theta_{lim}(\theta^p)$. Therefore, instead

[4]The reasons for this are the big improvements that could be made in the processing (see Appendix D) and in the discriminant calculation (see Chapter 8).

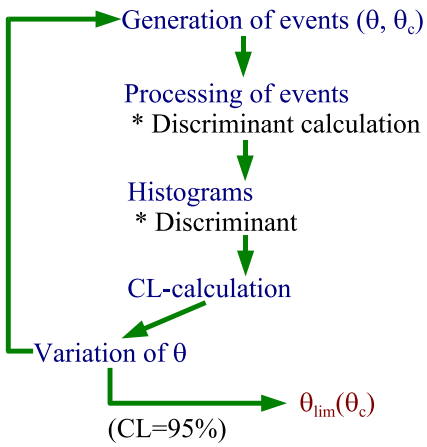

FIGURE 10.1: Standard analysis cycle.

of using parameters θ^m in the above cycle one might as well use θ^p (resulting in θ^p_{lim}) and then determine θ^m_{lim} by variation of θ^m[5]. This new procedure is surely favorable, if

$$N_i \gg N_j \qquad \text{with } i = 1 \ldots N_i,\ j = 1 \ldots N_j \tag{10.8}$$

In fact, this condition is probably fulfilled for most searches, if the number of model parameters N_i is high, since the number of relevant process parameters N_j is often smaller than one might think. Furthermore, the procedure has some other advantages, which are listed below.

Since the relations $\theta^p(\theta^m)$ have been investigated already in Section 4.2 the focus here will lie on the $\theta_{lim}(\theta^p)$ dependence. The variables used as the interface between the physical process and the theoretical model should fulfill the following two conditions:

- They should form a minimal set, and
- be easily accessible from both sides (*i.e.* they should, on the one hand, be calculated in a scan over the model parameter space and on the other hand determine the selection efficiency).

As stated in Sect. 10.2 the limits depend on the number of events, as well as the shapes of the discriminant distributions (D) for the background, the data and

[5]The reversed relation $\theta^m(\theta^p)$ is normally not available, but $\theta^p(\theta^m)$ is smooth.

the signal:

$$\theta_{lim}(b, d, s, D_b, D_d, D_s) \tag{10.9}$$

The number of expected signal events after all cuts is given by:

$$s = \sum_p \sum_{ch(p)} \sum_r \sigma_{p,r} \cdot \mathcal{L}_r \cdot \mathrm{BR}_{p,ch} \cdot \epsilon_{p,ch} \tag{10.10}$$

where r denotes different run conditions $r = \{e^-/e^+, E_{CMS}\}$, p denotes different production processes of different particles and ch denote different decay channels (which may differ for each p)[6]. For each channel a separate discriminant is calculated whose bins contribute in the sum of Eq. (10.6). Here, another important advantage of the use of the discriminant method becomes obvious, which is that it is not necessarily required to adjust the selection cuts for different model parameters, since the method automatically focuses on the signal region (if the used variables are "good" in the sense of Sect. 9.9). As a consequence b, D_b, d and D_d are independent of θ^m, and θ_{lim} will only be a function of s and D_s. On the other hand, it is important to notice that different channels have to be treated in a consistent way in the CL calculation and their discriminants can not be added beforehand. For n different channels we now have:

$$\theta_{lim}(s_1, D_1, .., s_n, D_n) \tag{10.11}$$

and

$$s_{ch} = \sum_p \sum_r \sigma_{p,r} \cdot \mathcal{L}_r \cdot \mathrm{BR}_{p,ch} \cdot \epsilon_{p,ch} \tag{10.12}$$

As a concrete example, first the case of the GMSB model at low values of $\sqrt{F}$ shall be considered where only the gravitino channel contributes. The relations between the relevant parameters are illustrated in Figure 10.2. As shown, cross section and branching ratios depend on the masses m_i involved in the process as well as on the couplings κ_j. For a given process *i.e.* where the *types* of couplings are fixed (which depend on the spins of the particles involved) the angular distribution of the events in the detector does only depend on the kinematic properties (*i.e.* the m_i). The *strength* of the couplings only influence (together with the BR) the number of expected events. Therefore, the efficiency is only a function of the m_i.

The parameters of Fig. 10.2 can be divided into two groups: On the one hand σ and BR which are determined by the theoretical model, and ϵ on the other

[6]Thus, in the following the term *channel* refers to different final states with different selection criteria.

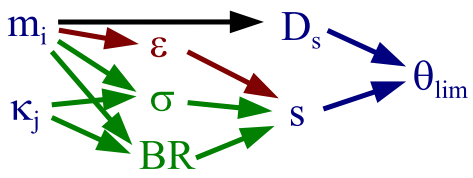

FIGURE 10.2: Relations between process parameters: masses m_i, couplings κ_j, efficiency ϵ, cross section σ, branching ratio BR, shape of the signal discriminant D_s and number of signal events s.

hand, which has to be determined experimentally. Consequently, the different cross sections and branching ratios may be combined into $N_{exp} = \sum_r \sigma_r \cdot \mathcal{L}_r \cdot \mathrm{BR}$ and then be compared with the minimal number of events which have to be expected before cuts are applied so that the given parameter point can be excluded with 95% CL: N_{lim}, which depends on the efficiency. As shown in Sect. 9.8, for the production process under study the m_i are dominantly given by the neutralino mass $m_{\tilde{\chi}_1^0}$. The modified analysis process is illustrated in Figure 10.3. There are two important differences with respect to Fig. 10.1. The first is that now the discriminants are calculated for different process parameters instead of different model parameters ($D_s(\theta^m) \rightarrow D_s(\theta^p)$). And the second is that the theoretical and experimental parts have been separated (θ appears only on the right side in Fig. 10.3), so that once N_{lim} has been calculated limits for all model parameters can be derived just by scans over the model parameter space (*i.e.* by only investigating the $\theta_i^m \leftrightarrow \theta_j^p$ relation of Eq. (10.7)). Thus, the necessary work is highly reduced. Another advantage is that one can now interpolate over N_{lim} and in this way produce smooth limits. This procedure was used to derive all limits at low SUSY breaking scales (see Chapter 11). However, the situation gets more complicated for cases in which:

- more than one produced particle contributes for a given parameter point
- different channels contribute (*e.g.* if the particles can decay in different ways, depending on the model parameters)

Two examples for such cases which have been investigated in the course of this thesis are:

- Limits in the MSSM, where $m_i = \{m_{\tilde{\chi}_1^0}, m_{\tilde{\chi}_2^0}, m_{\tilde{\chi}_1^\pm}\}$ and $ch = \{NC, CC\}$;

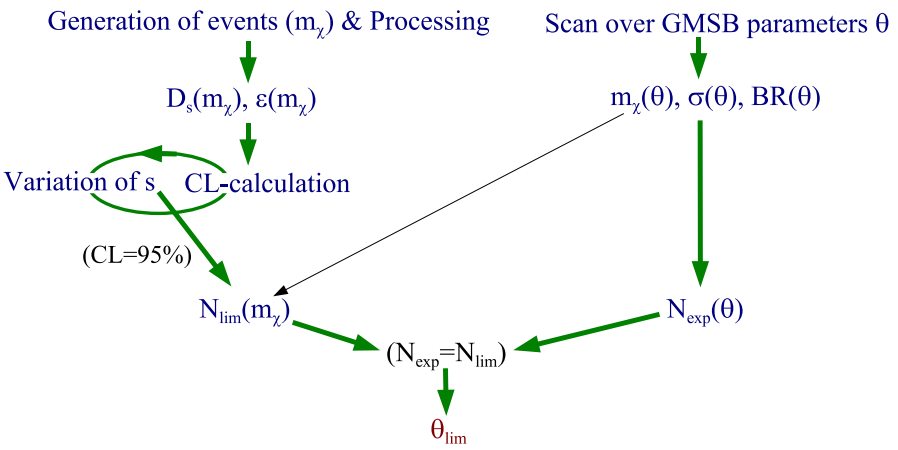

FIGURE 10.3: Improved analysis cycle for one particle and one decay channel.

- limit over the GMSB parameter $\sqrt{F}$, where $m_i = \{m_{\tilde{\chi}_1^0}, m_{\tilde{\chi}_1^\pm}\}$ and $ch = \{\text{Gravitino}, NC, CC\}$.

This will have consequences for the efficiency. Concerning the first point, we make the assumption that the efficiency does only depend on the final state independent of the initially produced particle[7], *i.e.* $\epsilon_{p,ch} \rightarrow \epsilon_{ch}$. Then, coming to the second point, the total efficiency is a weighted sum of the channel efficiencies[8]:

$$\epsilon = \frac{\sum_{ch} \text{BR}_{ch} \cdot \epsilon_{ch}}{\sum_{ch} \text{BR}_{ch}} \tag{10.13}$$

which has the unwanted consequence that through the BRs, the efficiency now also depends on the couplings! Furthermore, such a summation is not possible for N_{lim} (one would hope *e.g.* that by including an additional channel, N_{lim} would stay constant), but it will now also depend on the BRs (for n produced particles and m decay channels):

$$N_{lim}(m_{p1}, .., m_{pn}, \text{BR}^{p1}_{ch1}, .., \text{BR}^{p1}_{chm}, , , , \text{BR}^{pn}_{ch1}, .., \text{BR}^{pn}_{chm}) \tag{10.14}$$

A multi-dimensional function like this is difficult to handle (and to compare the results). However, a solution is still possible. The mentioned issues lead to two important conclusions:

[7] If there are differences, they should be treated as different channels.

[8] Here the sum goes only over the *analysed* channels for which the BRs in general do not add up to 100%.

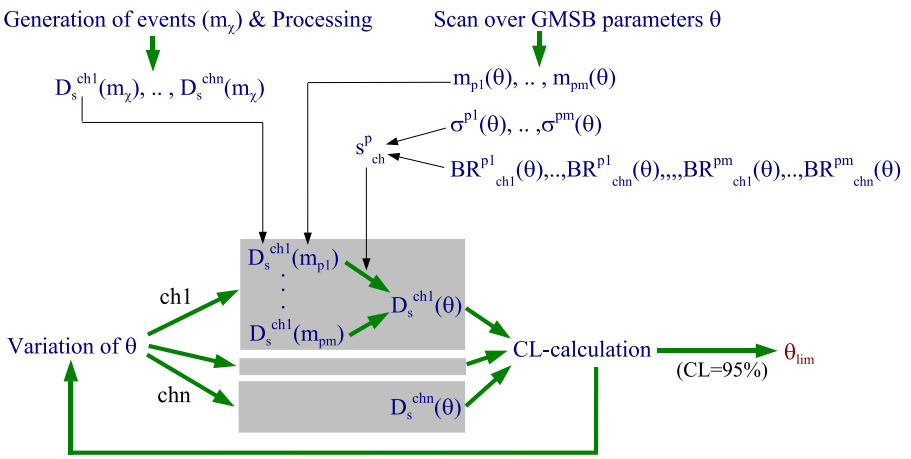

FIGURE 10.4: Analysis cycle for m different produced particles decaying into n different decay channels.

1. N_{lim} does not provide a suitable interface between experimental results and theoretical interpretation anymore;

2. instead the ϵ_{ch} should be used.

In practice, it is sufficient to calculate the discriminant distributions D_s which contain both the shape and efficiency information (as the integral of events after cuts). The resulting analysis process is illustrated in Figure 10.4. Each channel discriminant is calculated by adding up the discriminants which correspond to the masses of the different produced particles (since the additional events resulting from the decay of an additionally produced particle p will contribute to the total channel discriminant D^{ch} just like described by $D^{ch}(m_p)$). In this way the advantage of having to generate less points is kept (*e.g.* for two channels and ten mass points per channel, only 20 points have to be generated) but the drawback is that now the CL calculation has to be done many times for each limit calculation (it appears together with θ now). However, in this method which may be used to derive limits for an arbitrary number of produced particles which decay in an arbitrary number of decay channels the advantages prevail:

- In the analysis process a clearer separation of the physical relevant variables is achieved;

- less points have to be generated;

- it is easier to compare the results between two analysis (using D_s or N_{lim} instead of the limits themselves);
- limits can be produced for a very large phase space of model parameters.

Chapter 11

Results

Since no excess of data events could be observed in the signal region, the results are used to compute exclusion limits by using the methods discussed in the previous chapter. The aim of this chapter therefore is to display the multi-dimensional space spanned by all the parameters which have an influence on the number of expected signal events. This can be achieved only approximately for hyperplanes where most parameters are kept constant. The limits shown in this chapter use the full data set presented in Sect. 9.1. For the publication [139] limits were derived for the HERA I data set. They are shown in Appendix F. The strategy used for the representation of the limits consists of two main points:

1. limits are computed in the mass plane of the process particles;
2. the influence of all model parameters on these limits are studied.

This will be discussed in detail in the following.

11.1 Limits on Sparticle Masses

The first decision that has to be made is between limits on SUSY parameters on the one hand, or process parameters on the other hand. SUSY parameters are abstract, often interchangeable (as *e.g.* N, Λ and M) or have only a small influence on the number of expected events and the kinematics (*e.g.* $\tan\beta$). The masses $m_{\tilde{e}_L}$ and $m_{\tilde{\chi}_1^0}$, on the other hand, are the central physical quantities which determine the kinematics of the signal process; all other parameters only change the rate at which the events are produced. Therefore, the decision for the masses

seems obvious and other effects (on couplings and mass spectrum) are considered as variations.

11.1.1 Limit for Standard Parameters

The limit which can be derived for the standard parameters presented in Sect. 4.3.1 are shown in Figure 11.1. The parameters were chosen to give the highest limit on the neutralino mass. For a λ'_{111}-coupling of strength one, electron masses of up to $m_{\tilde{e}_L} = 360\,\text{GeV}$ and neutralino masses of up to $m_{\tilde{\chi}^0_1} = 200\,\text{GeV}$ can be excluded at 95% C.L. For the performed scan, Λ which directly determines the neutralino mass (see Eq. (2.45)) was varied between 33 TeV and 173 TeV. The relation between $m_{\tilde{\chi}^0_1}$ and Λ is illustrated at the side of Fig. 11.1.

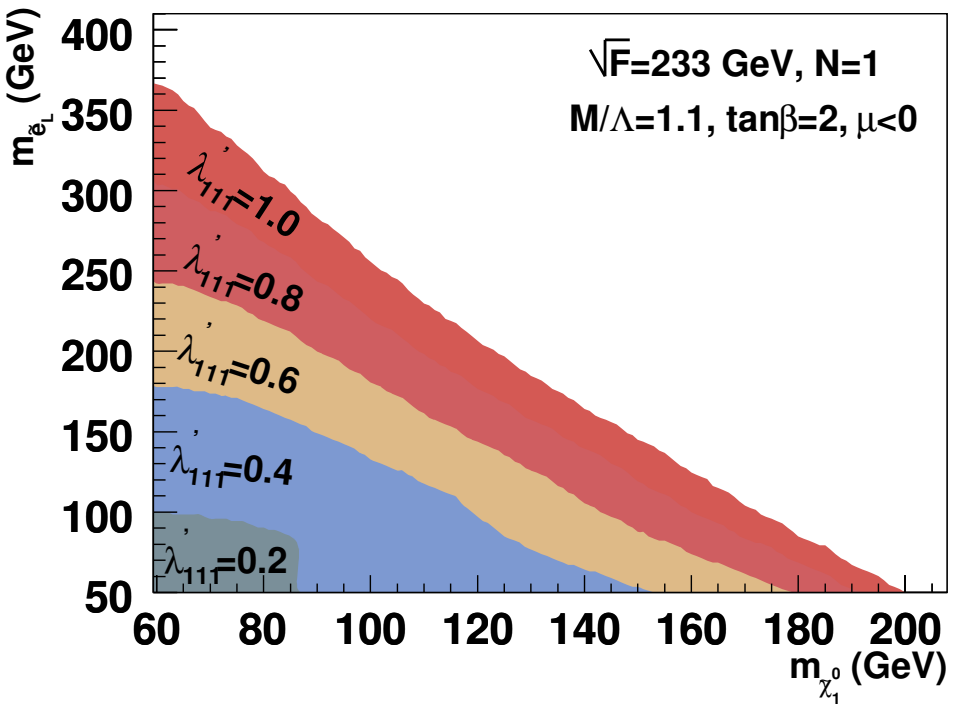

FIGURE 11.1: Limits in the mass plane of the left-handed selectron and the lightest neutralino for the standard GMSB parameters defined in Sect. 4.3.1. The different contours correspond to different strength of the R_P-violating coupling λ'_{111}.

11.1.2 Influence of Strength of R_P-violating Coupling

The next question is how the strength of the $\lambda^{'}$-coupling affects the limits given. As shown in Eq. (4.3) the cross section is proportional to the square of the Yukawa coupling. However, in order to incorporate also the effects on the branching ratio, independent scans have been performed in equidistant steps of $\lambda^{'}_{111} = \{0.2, 0.4, 0.6, 0.8, 1.0\}$. The results are the different colored areas in Figure 11.1. In order to compare to the strength of the SM gauge couplings the Yukawa couplings fulfill the relation:

$$\alpha = \frac{\lambda^{'2}}{4\pi} \tag{11.1}$$

Thus, Yukawa couplings of $\lambda^{'} \approx 0.3$ have electromagnetic strength ($\alpha_{em}(Q^2 = 10^4\,\mathrm{GeV}^2) = 1/137$). The limits for $\lambda'_{111} = 0.2$ shows the effect of the decreasing branching ratio in the $m_{\tilde{e}_L} < m_{\tilde{\chi}^0_1}$ region while for higher neutralino masses the effect of the increasing cross section toward smaller selectron masses is dominant.

11.1.3 Limit for Different λ'_{ijk} Couplings

In the case of the gravitino channel where the λ'-coupling only enters in the production cross section, the difference in the limits for different types of λ'_{ijk} couplings will be the one displayed in Figure 4.2 if the following two conditions are fulfilled:

1. The signal efficiency and the shape of the discriminant distribution are independent of the selectron mass[1];

2. The branching ratio is the same for the two compared selectron masses.

In this case Figure 4.2 can be used to translate a given limit for one coupling into the corresponding limit for any other of the four couplings. To do so, at a fixed neutralino mass one reads off the limit on $m_{\tilde{e}_L}$ *e.g.* for λ'_{111}, then in Fig. 4.2 one finds the value of N_{lim} at this point by going upward at the given $m_{\tilde{e}_L}$ until one crosses the λ'_{111} line. At this N_{lim} value on can now go vertically to any other λ' line and read off the limit on $m_{\tilde{e}_L}$ for this λ' by going downward again. Fig. 4.2 can be used for any neutralino mass since varying it would only induce a shift of the lines in Fig. 4.2 along the y direction while the slope stays the same (this can be seen in Fig. 4.8). In order to check the above procedure, the limits for the

[1] This was shown in Sect. 9.8.

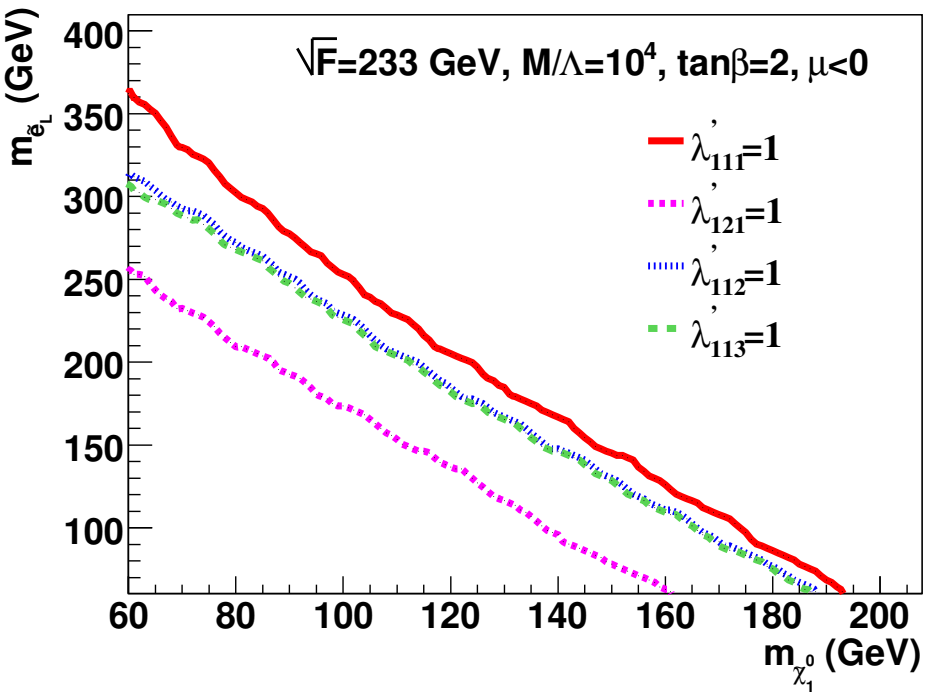

FIGURE 11.2: Mass limits for different λ'-couplings.

couplings λ'_{111}, λ'_{121}, λ'_{112} and λ'_{113} have been determined by individual scans as shown in Figure 11.2. They are in a good agreement with what is expected from the application of the procedure. Therefore, in the following sections all limits will be given only for λ'_{111}.

11.2 Limit Dependence on GMSB Parameters

For the following studies, GMSB parameters were varied in the complete range of their possible values (as far as not jet excluded by theory or experiment) as listed in Table 4.5 (in Sect. 4.3). As discussed in Sect. 4.2.2 for small values of SUSY breaking scale $\sqrt{F}$, the neutralino decays exclusively into a photon and a gravitino. Therefore, the following discussion will focus on this region by setting $\sqrt{F} = 233\,\text{GeV}$ and the situation for high values of $\sqrt{F}$ will be discussed separately at the end of this chapter. Furthermore, the easiest GMSB scenario with one messenger field ($N = 1$) will be considered first.

TABLE 11.1: Special scenarios

Scenario	M/Λ	$sign(\mu)$	$tan(\beta)$
Best limits	10^4	-1	2
Worst limits	2	$+1$	50

11.2.1 Influence of Messenger Scale, tanβ and sign(μ)

In order to explore the remaining GMSB parameter space a scan was performed over $m_{\tilde{e}_L}$, Λ (*i.e.* $m_{\tilde{\chi}_1^0}$), M/Λ and sign(μ) within the limits of Tab. 4.5. A technical difficulty results from the fact that by varying M and $sign(\mu)$ also the $m_{\tilde{\chi}_1^0}(\Lambda)$ relation changes. The scan was done for $tan\beta = 2$ and $tan\beta = 50$ as shown in Figures 11.3 and 11.4. The two scenarios which gave the best and worst limits of all cases are listed in Table 11.1. The main difference between the best and worst

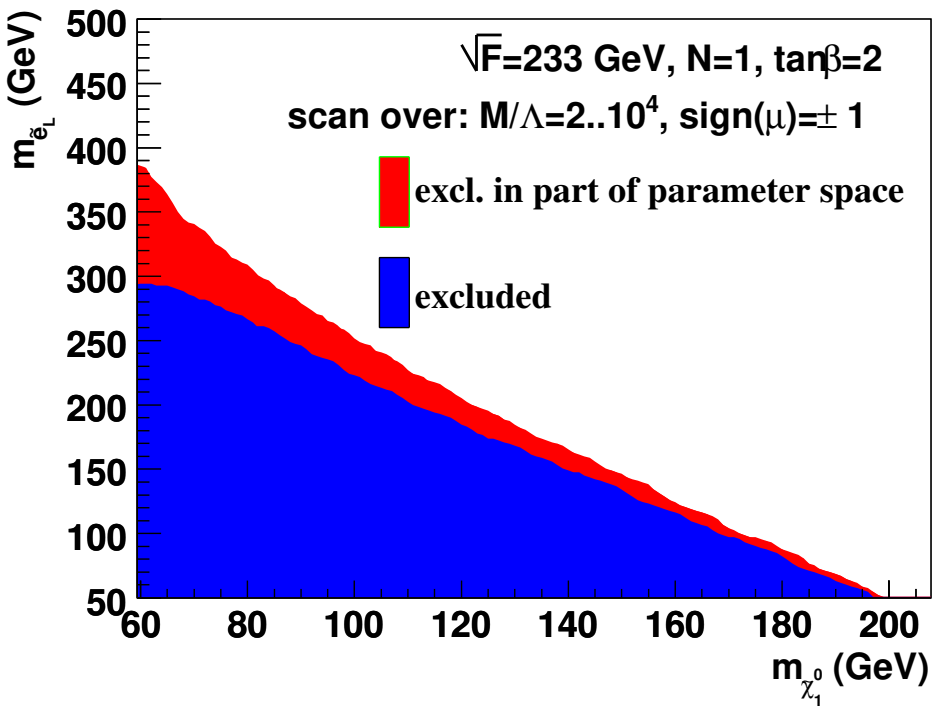

FIGURE 11.3: Mass limit dependence on messenger scale and $sign(\mu)$ for $tan\beta = 2$.

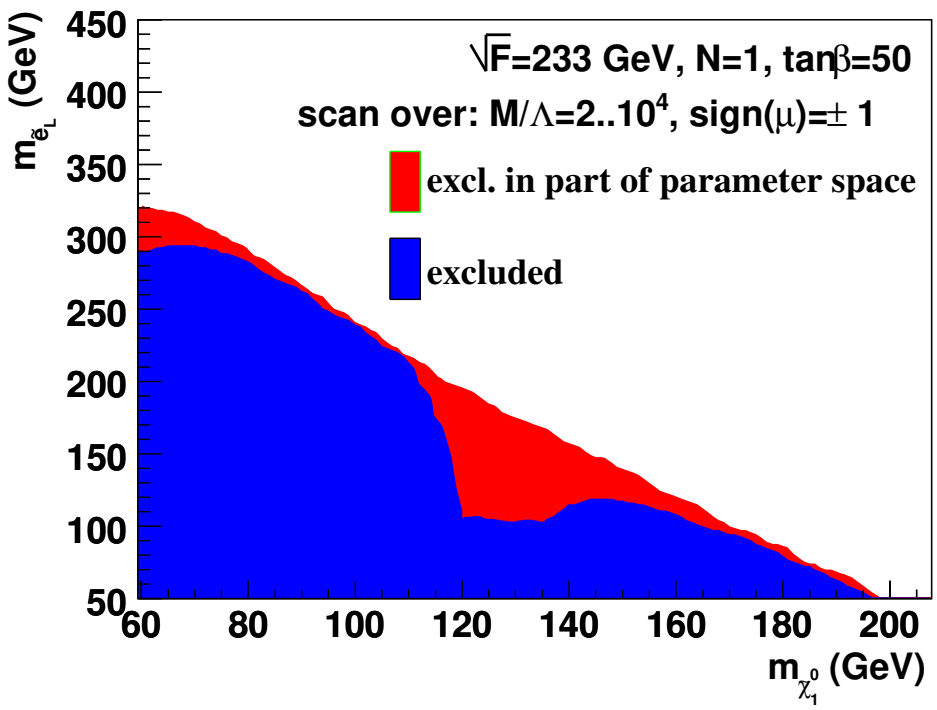

FIGURE 11.4: Mass limit dependence on messenger scale and $sign(\mu)$ for $tan\beta = 50$.

limits result from the two different $sign(\mu)$ values, while the effect due to M/Λ is less than 10%.

The dip observed in Fig. 11.4 occurs for the parameter region of $sign(\mu) = +1$. In the dip region the lightest stau is the NLSP (thus $\Gamma(\tilde{\chi}_1^0 \to \gamma\tilde{G})/\Gamma(\tilde{\chi}_1^0 \to \tilde{\tau}^{\pm}\tau^{\mp})$ becomes small). Its left border corresponds to the transition line where $m_{\tilde{\tau}_1^{\pm}} = m_{\tilde{\chi}_1^0}$ and the curved contours are a result of the additional variation of M. The lower border results from the increase in cross section towards smaller $m_{\tilde{e}_L}$. It can thus be concluded that the limits on $m_{\tilde{e}_L}$ and $m_{\tilde{\chi}_1^0}$ are similarly valid in a large part of GMSB parameter space.

11.2.2 Influence of Number of Messenger Fields

As discussed in Sect. 2.4.4, in scenarios with higher N the lightest stau tends to be lighter than the neutralino with the consequence that the branching ratio of the gravitino decay is rapidly reduced to zero. However, this effect can be counteracted

by choosing high values of M/Λ. While at values of $M/\Lambda = 10^4$ the cross sections are somewhat lower, the branching ratio of the gravitino channel can be kept near to 100%. Figure 11.5 shows results of scans for varying $N = 1 \ldots 5$ where the other parameters were set to the standard values of Sect. 4.3.1. In fact, one observes that for $N \leq 3$ the branching ratio effect of N is totally annihilated, and even for N=4 and N=5 a large part of the mass plane can still be excluded. Since $m_{\tilde{\chi}_1^0}$ depends also on N, different Λ-regions can be excluded for different N.

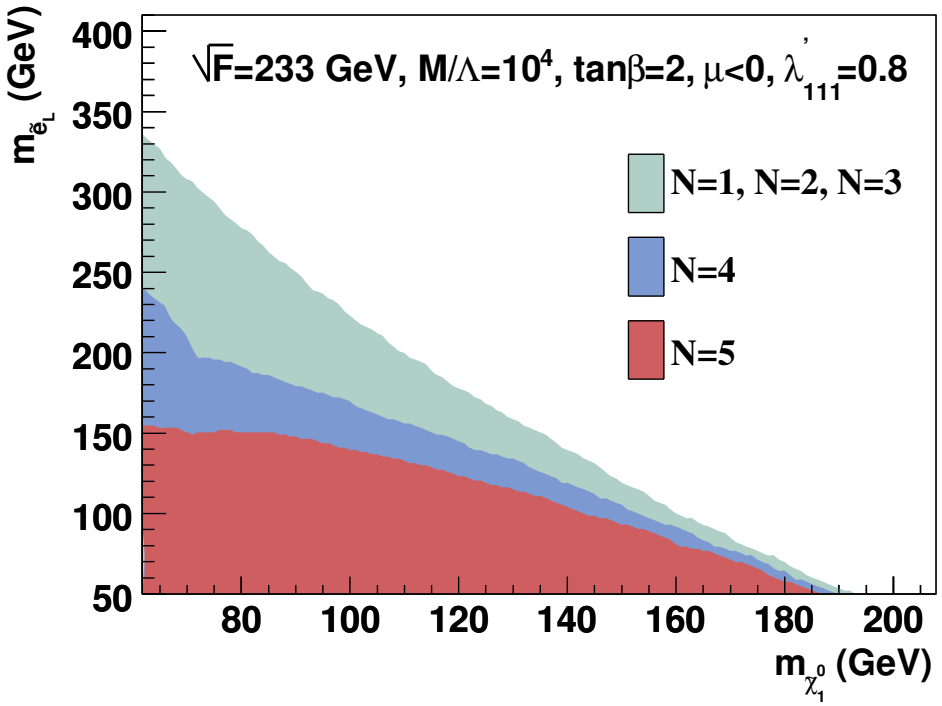

FIGURE 11.5: Mass limits for different number of messenger fields.

11.2.3 Influence of SUSY Breaking Scale

In order to explore also regions of higher $\sqrt{F}$ values, additional decay channels have to be taken into account. As seen in Sect. 4.2.2 the branching ratio of the gravitino channel goes down with increasing $\sqrt{F}$ and instead the neutralino decays through the R_P-violating channels. Therefore, for the limit calculation, now the third method presented in Sect. 10.3 has to be used. Since only the HERA I data

was analysed for the R_P-violating channels, also for the gravitino channel only the smaller data set was used. For all values of $\sqrt{F}$ the branching ratios of the three investigated decay channels add up to nearly 100%. Figure 11.6 shown how the limit on the selectron mass changes as a function of $\sqrt{F}$. Here, the selectron mass is used on the y-axis since the branching ratio changes with the neutralino mass, while the selectron mass is treated as a free parameter. The decrease of the limit toward higher $\sqrt{F}$ values is due to the different sensitivities in the three channels, as can be seen by comparing the discriminant distributions Fig. 9.24, Fig. 9.27 and Fig. 9.29. Scans were performed for a neutralino mass of $m_{\tilde{\chi}_1^0} = 50\,\text{GeV}$, as shown in Fig. 11.6. This result has an interesting interpretation. As discussed in

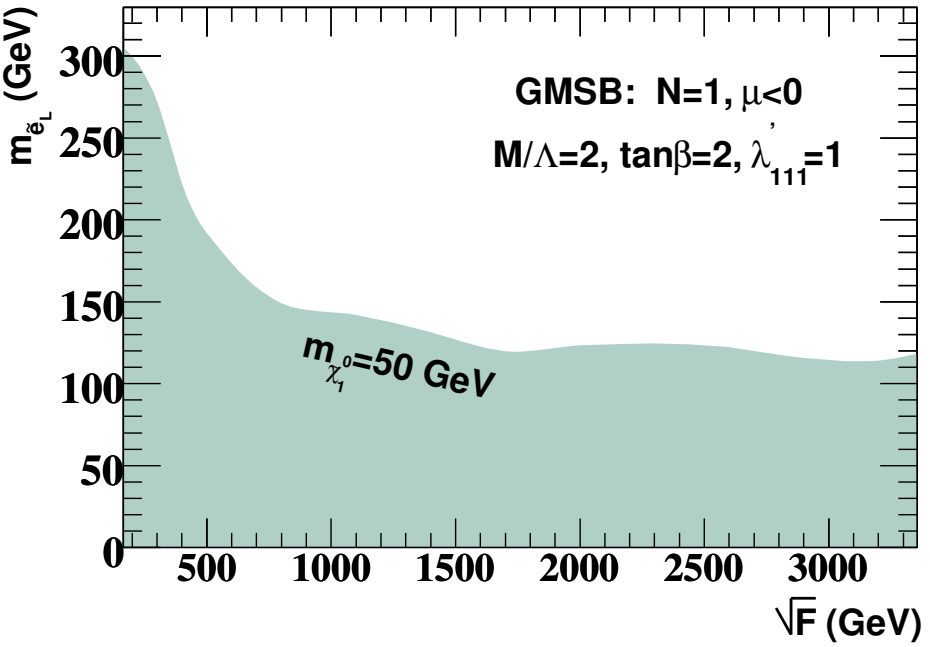

FIGURE 11.6: Dependence of the selectron mass limit on the SUSY breaking scale.

Sect. 2.4.4 the difference in the GMSB model compared to mSUGRA models is the introduction of an additional messenger sector with the consequence of a lower SUSY breaking scale and the appearance of the gravitino channel. In going to higher values of $\sqrt{F}$ the gravitino channel disappears and the situation resembles

the one expected in mSUGRA models. Hence, the variation of $\sqrt{F}$ simulates a continuous change between the two models. The investigation of the GMSB parameter space is thus completed.

Chapter 12

Conclusions and Outlook

There are two possible outcomes: If the result confirms the hypothesis, then you've made a measurement. If the result is contrary to the hypothesis, then you've made a discovery.

Enrico Fermi

12.1 Summary

A classification scheme for SUSY processes at HERA was developed and a complete list of interesting SUSY production processes was derived. For the diagrams without squarks, the signatures for the dominant decays in the MSSM and GMSB models were derived, both for the R_P-conserving and R_P-violating case.

Focusing on the diagram with the highest cross section, this thesis then presented a search for gravitinos which are expected in the framework of Gauge Mediated Supersymmetry Breaking. The data set used, corresponding to an integrated luminosity of $300\,\mathrm{pb}^{-1}$, was recorded by the ZEUS detector at HERA in e^-p and e^+p collisions at center of mass energies of 300 GeV and 318 GeV in the years 1996-2005. It is the first ZEUS thesis which investigated such a large amount of luminosity.

The processes $eq \to q'\gamma\tilde{G}$, $eq \to q'\nu qq$ and $eq \to q'e^{\pm}qq$ were searched for. In the channels with a gravitino or a neutrino in the final state the dominant SM background consists of CC DIS events, while it is NC DIS for the electron channel. The signal-to-background ratio achieved after preselection could be further increased by a factor of 147 with the help of a dynamic discriminant method.

Since the data was observed to be well described by the expected SM processes and no evidence for signal events was found, exclusion limits on the masses of the left-handed selectron and the lightest neutralino were derived for the Yukawa couplings λ'_{111}, λ'_{112}, λ'_{121} and λ'_{113}. In order to study the relevance of these limits, the entire GMSB parameter space has been investigated. For some parameter regions, selectron masses of up to 360 GeV and neutralino masses of up to 190 GeV could be excluded at 95% CL. Similar limits were found to hold for many combinations of the parameters M, $sign(\mu)$, $\tan\beta$ and N. Finally, also the influence of the SUSY breaking scale $\sqrt{F}$ could be investigated by including the results from the R_P-violating decay channels of the produced gauginos.

The derived limits are the best existing in the framework of RPV GMSB. They considerably extend the onces derived by the H1 Collaboration in a similar analysis using a smaller data set [60]. The investigation of λ'-couplings at the Tevatron is difficult (and not published) since the dominant slepton s-channel process (resulting in two jets) has a huge background. The slepton and gaugino mass limits from LEP which are around 100 GeV for both R_P-conserving and R_P-violating cases can be extended for large λ' couplings.

The results presented here are being published by ZEUS. Due to the ZEUS policy of two independent analysis for each publication, the publication will include only HERA I data. The results corresponding to the publication are therefore shown in Appendix E.

12.2 Prospects at HERA

Due to its unique initial state HERA stays the best place to search for λ'-couplings[1]. With an aimed luminosity of 700 pb^{-1} to be collected until 2007 at HERA the reachable SUSY phase space will be further increased. It could further be extended by combining H1 and ZEUS results for the same channel.

The study presented in Chapter 3 also showed that still some channels with potential for SUSY discovery at HERA exist. Inclusive studies could be performed to search for events with τ's in the final state. These are expected in GMSB models where the lightest stau is the NLSP. Such searches are complementary to the analysis presented here and could investigate the GMSB parameter space for high N.

[1] See the discussion in Sect. 2.4.5

Another interesting channel results from diagram $F4-2$ where a single slepton can be produced through an R_P-violating coupling λ'_{ijk}. The highest cross section results from events with a soft photon emitted from the electron. It was calculated with the SUSY generator program COMPHEP to $0.1\,\mathrm{pb}^{-1}$ for slepton masses of 100 GeV [140]. Since the electron and one of the quarks escape through the beam pipe, the detected signal will only result from the produced slepton. Many different Yukawa couplings could be investigated, leading to the production of $\tilde{e}$s, $\tilde{\mu}$s and $\tilde{\tau}$s with characteristic signatures. Especially interesting are GMSB decays into a lepton and a gravitino resulting in signatures of isolated leptons and missing energy. An excess of such events was observed by the H1 collaboration in the e and μ channel [141] but not by ZEUS [142]. Contrarily, in the τ channel, ZEUS has seen an excess [143]. Note however, that such a process should also have a high cross section at the Tevatron.

12.3 Prospects at LHC and ILC

The Large Hadron Collider (LHC) at CERN, which will start its operation in 2007, was conceived to be a decisive tool for SUSY discovery. Due to its high center of mass energy of 14 TeV it has a high potential to discover SUSY particles within several months of data taking at nominal luminosity. If the mass threshold is passed (see Fig. 2.4) sparticles could be produced with similar rates as SM particles. This would open a new era of particle physics.

The next step after SUSY discovery would consist in the precise measurement of the parameters of the underlying SUSY model. Here, the 106-dimensional parameter space of the MSSM opens a wide range of exploration. Additional assumptions that are made in more predictive models, such as relations between sparticle masses at the GUT scale and their connection to the masses at the electro-weak scale, the mechanism of electro-weak symmetry breaking and the source of supersymmetry breaking, all have to be studied concisely. The International Linear Collider (ILC), thanks to its clean initial state of electrons and positrons, will be able to measure many SUSY parameters with high precision.

Appendix A

List of SUSY Production Diagrams at HERA

The table given below lists all diagrams discussed in Chapter 2 and the on-shell produced (s)particles which decay subsequently into final states characteristic for the different SUSY models.

TABLE A.1: List of SUSY production diagrams and produced (s)particles possible at HERA within the restrictions of Sect. 3.5.

Diagram	RPV	leptons	quarks	$W^{\pm}$	sleptons	squarks	gauginos
A1	λ'		1				1
A2-1	$\lambda'\lambda'$	1	1				
A2-2	$\lambda'\lambda''$		2				
B1-1	$\lambda'\lambda'$		1		1		1
B1-2	$\lambda'\lambda''$		1			1	1
B1-3	$\lambda'\lambda'$	1				1	1
B2-1	$\lambda'\lambda'$		1		1		1
B2-2	$\lambda'\lambda''$	1				1	1
B2-3	$\lambda'\lambda''$		1			1	1
C1					1	1	
C2	λ'		1				1
C3	λ'		1				1
C4-1	$\lambda'\lambda'$	1	1				

Diagram	RPV	leptons	quarks	$W^{\pm}$	sleptons	squarks	gauginos
C4-2	$\lambda'\lambda''$		2				
C4-3	$\lambda\lambda''$	1	1				
D1			1		1		1
D2	λ'					1	2
D3-1	$\lambda'\lambda'$		1		1		1
D3-2	$\lambda'\lambda'$	1				1	1
D3-3	$\lambda'\lambda''$		1			1	1
D4-1	λ'	1	1		1		
D4-2	λ'		2			1	
D4-3	λ'			1			1
D5-1	$\lambda'\lambda'$	1			1		1
D5-2	$\lambda''\lambda'$		1		1		1
D5-3	$\lambda'\lambda$		1			1	1
E1		1				1	1
E2-1	λ'	2			1		
E2-2	λ'	1	1			1	
E2-3	λ'	1		1			1
E3	λ'					1	2
E4-1	$\lambda'\lambda'$		1		1		1
E4-2	$\lambda'\lambda'$	1				1	1
E4-3	$\lambda'\lambda''$		1			1	1
E5-1	$\lambda\lambda'$	1				1	1
E5-2	$\lambda'\lambda'$		1		1		1
E5-3	$\lambda'\lambda''$		1			1	1
F1			1		1		1
F2		1				1	1
F3-1	λ	1	1		1		
F3-2	λ'		2			1	
F4-1	λ'	2			1		
F4-2	λ'	2				1	
F4-3	λ''	1	1			1	
F5-1	$\lambda\lambda'$	1				1	1
F5-2	$\lambda'\lambda''$		1			1	1

Diagram	RPV	leptons	quarks	$W^{\pm}$	sleptons	squarks	gauginos
F5-3	$\lambda^{'}\lambda^{'}$		1		1		1
F6-1	$\lambda\lambda^{'}$		1		1		1
F6-2	$\lambda^{'}\lambda^{''}$		1			1	1
F6-3	$\lambda^{'}\lambda^{'}$	1				1	1
F7-1	$\lambda\lambda^{'}$		1		1		1
F7-2	$\lambda^{'}\lambda^{''}$		1			1	1
F8-1	$\lambda\lambda^{'}$	1				1	1
F8-2	$\lambda^{'}\lambda^{''}$		1			1	1
F8-3	$\lambda^{'}\lambda^{'}$		1		1		1

Appendix B

Trigger Definitions

The recorded ZEUS events are stored in data summary tapes (DST) and pre-classified into different DST bits to enable a faster processing for the subsequent analysis. The definitions of the DST bits relay on ExoSLT and ExoTLT definitions which will be given first.

ExoSLT 3

- $(E - P_z)^{SLT} > 34\,\text{GeV}$ [1]
- $(E_T^{\text{ex1ir}})^{SLT} > 16\,\text{GeV}$ [2]

ExoSLT 4

- $|t_g| < 7\,\text{ns}$ [3]
- $P_T^{SLT} > 6\,\text{GeV}$
- $(E_T^{\text{ex2ir}})^{SLT} > 6\,\text{GeV}$
- $(N_{Trk}^{Good})^{FLT} \geq 1$ or $\left(P_T^{SLT} > 9\,\text{GeV} \text{ and } (E_T^{\text{ex1ir}})^{SLT} > 8\,\text{GeV}\right)$
- $E_{FCAL}^{SLT} > 20\,\text{GeV}$

[1] The superscripts FLT, SLT and TLT indicate whether a variable is reconstructed at the first, second or third trigger level.

[2] The superscripts ex1ir and ex2ir denote that the innermost or two innermost rings of the FCAL were excluded from calculation.

[3] t_g, t_u and t_d are the timings measured in the global, upper and lower calorimeter relative to the interaction time.

ExoTLT 2

- $P_T^{FLT} > 6\,\text{GeV}$
- $(N_{Trk}^{Good})^{TLT} \geq 1$
  with $(p_{T,Trk}^{Good})^{TLT} > 0.5\,\text{GeV}$ and $DCA < 1.5\,\text{cm}$ and $|Z_{vtx}^{TLT}| < 60$ cm
- $|t_u - t_d| < 8\,\text{ns}$

ExoTLT 5

- $(E_T^{\text{ex1ir}})^{TLT} > 15\,\text{GeV}$
- $(E - P_z)^{TLT} > 32\,\text{GeV}$
- $E^{TLT}(\theta > 150^\circ) < 5\,\text{GeV}$
- $|t_u - t_d| < 8\,\text{ns}$

ExoTLT 6

- ExoSLT4
- $|t_u - t_d| < 8\,\text{ns}$
- $P_T^{TLT} > 6\,\text{GeV}$
- $(N_{Trk}^{Good})^{FLT} \geq 1$ or $E_{FCAL}^{TLT} > 10\,\text{GeV}$

ExoTLT 7

- $(E - P_z)^{VC} > 32\,\text{GeV}$
- not BeamGasVertex
- ≥ 1 electron candidate
- $(X_{vtx}^{e,TLT} + Y_{vtx}^{e,TLT})^2 < 30\ \text{cm}^2$
- $E_e^{TLT} > 10\,\text{GeV}$
- $\max((Q_{DA}^2)^{TLT}, (Q_{EL}^2)^{TLT}) > 200\,\text{GeV}^2$

DST 32

- ExoTLT4 or ExoTLT5 or ExoTLT7 or MuTrig[4]
- $(E - P_z)^{TLT} > 32\,\mathrm{GeV}$
- $E_e^{TLT} > 4\,\mathrm{GeV}$
- $(Q^2_{EL})^{TLT} > 160\,\mathrm{GeV}^2$ or $(Q^2_{DA})^{TLT} > 160\,\mathrm{GeV}^2$
- $(p_T^e)^{TLT} > 2\,\mathrm{GeV}$

DST 34

- ExoTLT2 or ExoTLT6 or $P_T^{\mathrm{ex1ir},TLT} > 6\,\mathrm{GeV}$
- $P_T^{TLT} > 6\,\mathrm{GeV}$
- Events which fulfill all of the following conditions are vetoed:
  - not ExoTLT2
  - $(P_T^{\mathrm{ex1ir}})^{TLT} < 10\,\mathrm{GeV}$
  - $P_T^{TLT} < 25\,\mathrm{GeV}$
  - $P_T^{TLT}/E_T^{TLT} < 0.7$
  - $(E - P_z)^{TLT} < 10\,\mathrm{GeV}$
  - $P_T^{TLT}/P_z^{TLT} < 0.08$
  - $P_x^{TLT} < 0\,\mathrm{GeV}$
  - $|P_y^{TLT}| < 4\,\mathrm{GeV}$

[4] MuTrig is a cosmic and halo muon rejection trigger.

Appendix C

Generated MC Samples

The following tables list the MC samples which were generated to simulate the signal and background processes relevant for the processes under study.

TABLE C.1: PhP MC samples. Since the studies for the HERA I data set resulted in no sizable contribution of PhP events no separate samples were generated for the HERA II period.

Period	Generator	minimal E_T cut	σ (pb)	Events	$\mathcal{L}$ (pb^{-1})
Direct					
99-00	HERWIG	$18\,\mathrm{GeV}^2$	$21.7 \cdot 10^3$	100000	4.61
e^+p		$20\,\mathrm{GeV}^2$	$15.6 \cdot 10^3$	560000	35.9
318 GeV		$40\,\mathrm{GeV}^2$	283	100000	352
Resolved					
99-00	HERWIG	$18\,\mathrm{GeV}^2$	$115 \cdot 10^3$	350000	3.03
		$40\,\mathrm{GeV}^2$	598	100000	167

TABLE C.2: Generated signal MC samples for the processes $e^{\pm}q \rightarrow q(\tilde{\chi}_1^0 \rightarrow \gamma\tilde{G})$ and $e^{\pm}q \rightarrow q(\tilde{\chi}_1^0 \rightarrow lqq)$ with $l = e^{\pm}, \nu$.

Generator	$\sqrt{F}$	Neutralino Mass	Selectron Mass	Events
SUSYGEN	230	59 GeV	69 GeV/109 GeV/169 GeV	3×2000
SUSYGEN	230	66 GeV	76 GeV/116 GeV/156 GeV	3×2000
SUSYGEN	230	72 GeV	82 GeV/122 GeV/162 GeV	3×2000
SUSYGEN	230	86 GeV	96 GeV/116 GeV/156 GeV	3×2000
SUSYGEN	230	100 GeV	120 GeV/140 GeV/200 GeV	3×2000
SUSYGEN	230	114 GeV	119 GeV/124 GeV/129 GeV	3×2000
SUSYGEN	230	126 GeV	190 GeV	3000
SUSYGEN	230	138 GeV	190 GeV	3000
SUSYGEN	230	150 GeV	190 GeV	3000
SUSYGEN	230	162 GeV	190 GeV	3000
SUSYGEN	230	174 GeV	190 GeV	3000
SUSYGEN	230	186 GeV	190 GeV	3000
SUSYGEN	230	198 GeV	190 GeV	3000
SUSYGEN	230	210 GeV	190 GeV	3000
CompHEP	230	60 GeV	100 GeV	5000
CompHEP	230	85 GeV	100 GeV	25000
CompHEP	230	85 GeV	150 GeV	25000
SUSYGEN	3300	50 GeV	190 GeV	5000
SUSYGEN	3300	60 GeV	190 GeV	5000
SUSYGEN	3300	70 GeV	190 GeV	5000
SUSYGEN	3300	80 GeV	190 GeV	5000
SUSYGEN	3300	90 GeV	190 GeV	5000
SUSYGEN	3300	100 GeV	190 GeV	5000
SUSYGEN	3300	110 GeV	190 GeV	5000
SUSYGEN	3300	120 GeV	190 GeV	5000
SUSYGEN	3300	130 GeV	190 GeV	5000
SUSYGEN	3300	140 GeV	190 GeV	5000
SUSYGEN	3300	150 GeV	190 GeV	5000
SUSYGEN	3300	160 GeV	190 GeV	5000

TABLE C.3: CC DIS MC samples.

Period	Generator	minimal Q^2 cut	σ (pb)	Events	$\mathcal{L}$ (pb^{-1})
96-97	ARIADNE	$10\,\mathrm{GeV}^2$	41.5	10000	241
e^+p	CDM	$5000\,\mathrm{GeV}^2$	2.54	5000	$1.97 \cdot 10^3$
300 GeV		$10000\,\mathrm{GeV}^2$	0.480	5000	$10.4 \cdot 10^3$
98-99	ARIADNE	$10\,\mathrm{GeV}^2$	79.4	25000	314
e^-p	CDM	$100\,\mathrm{GeV}^2$	73.4	25000	340
318 GeV		$5000\,\mathrm{GeV}^2$	14.8	15000	$1.01 \cdot 10^3$
		$10000\,\mathrm{GeV}^2$	5.57	5000	898
		$20000\,\mathrm{GeV}^2$	1.18	5000	$4.24 \cdot 10^3$
99-00	ARIADNE	$10\,\mathrm{GeV}^2$	45.2	24990	552
e^+p	CDM	$100\,\mathrm{GeV}^2$	39.8	25000	629
318 GeV		$5000\,\mathrm{GeV}^2$	3.20	15000	$4.69 \cdot 10^3$
		$10000\,\mathrm{GeV}^2$	0.683	4995	$7.32 \cdot 10^3$
		$20000\,\mathrm{GeV}^2$	0.0619	5000	$80.8 \cdot 10^3$
99-00	MEPS	$10\,\mathrm{GeV}^2$	45.2	25000	553
e^+p		$100\,\mathrm{GeV}^2$	39.8	25000	628
318 GeV		$5000\,\mathrm{GeV}^2$	3.20	14768	$4.61 \cdot 10^3$
		$10000\,\mathrm{GeV}^2$	0.683	9960	$14.6 \cdot 10^3$
		$20000\,\mathrm{GeV}^2$	0.0619	9996	$161 \cdot 10^3$
2004	ARIADNE	$100\,\mathrm{GeV}^2$	39.6	50000	$1.26 \cdot 10^3$
e^+p	CDM	$5000\,\mathrm{GeV}^2$	3.29	15000	$4.57 \cdot 10^3$
318 GeV		$10000\,\mathrm{GeV}^2$	0.706	5000	$7.08 \cdot 10^3$
		$20000\,\mathrm{GeV}^2$	0.0643	5000	$77.8 \cdot 10^3$
2005	ARIADNE	$100\,\mathrm{GeV}^2$	73.4	50000	681
e^-p	CDM	$5000\,\mathrm{GeV}^2$	14.9	15000	$1.01 \cdot 10^3$
318 GeV		$10000\,\mathrm{GeV}^2$	5.57	5000	898
		$20000\,\mathrm{GeV}^2$	1.18	5000	$4.24 \cdot 10^3$

TABLE C.4: NC DIS MC samples.

Period	Generator	minimal Q^2 cut	σ (pb)	Events	$\mathcal{L}$ (pb^{-1})
99-00	ARIADNE	$100\,\mathrm{GeV}^2$	$8.12 \cdot 10^3$	136000	16.74
e^+p	CDM	$400\,\mathrm{GeV}^2$	$1.17 \cdot 10^3$	60000	51.38
318 GeV		$1250\,\mathrm{GeV}^2$	198	25000	126.56
		$2500\,\mathrm{GeV}^2$	58.9	12000	203.68
		$5000\,\mathrm{GeV}^2$	14.8	12000	808.30
		$10000\,\mathrm{GeV}^2$	2.79	12000	4295.53
		$20000\,\mathrm{GeV}^2$	0.310	12000	38722.17
		$30000\,\mathrm{GeV}^2$	0.0544	6000	110294.12
		$50000\,\mathrm{GeV}^2$	0.0021	6000	2857142.86
02-05	ARIADNE	$25\,\mathrm{GeV}^2$	$46.3 \cdot 10^3$	100000	2
e^+p	CDM	$400\,\mathrm{GeV}^2$	$1.17 \cdot 10^3$	120000	103
318 GeV		$1250\,\mathrm{GeV}^2$	197	50000	253
		$2500\,\mathrm{GeV}^2$	58.9	24000	407
		$5000\,\mathrm{GeV}^2$	14.8	24000	$1.62 \cdot 10^3$
		$10000\,\mathrm{GeV}^2$	2.8	24000	$8.59 \cdot 10^3$
		$20000\,\mathrm{GeV}^2$	0.3	24000	$77.4 \cdot 10^3$
		$30000\,\mathrm{GeV}^2$	0.05	12000	$220 \cdot 10^3$
		$50000\,\mathrm{GeV}^2$	0.002	12000	$5.66 \cdot 10^6$

Appendix D

Analysis Framework

For the technical realisation of the data analyses presented in this thesis a generic analysis framework was developed which may be used for all types of analyses involving a large number of different variables. Based on the object oriented and pattern oriented programming paradigms it uses original C++ [144] as well as ROOT[1] classes. The construction followed the principles of

- *Generality:* It should be usable for a wide range of different analyses;
- *Flexibility:* Changes and extensions should be easy to integrate;
- *Efficiency:* Each formula should be implemented only once at a specific place and calculation time should be minimized.

A necessary technique for the implementation of these principles is the ability to handle not only pointers to data members but also to functions as available in C++ *via* abstract classes and RTTI (Run Time Type Information)[2].

A clear code structure is achieved by using a separate class for each variable. Figure D.1 shows for instance the definition of the variable SELQ2 which represents the four-momentum transfered by the selectron in the signal process. A characteristic is the use of *abstract labels* instead of direct ntuple variables. This allows to define the meaning of *e.g.* SELQ2 independent of the names of the variables it depends on in the ntuple and whether or not these variables themselves are calculated from other more fundamental variables. In this example the variable

[1] A class library for high-energy physics analysis.

[2] Since this technique is not available in older programming languages the construction of such a generic analysis tool was not possible before.

vars is a pointer to a map between abstract variables and pointers to classes of variables (which all derive from a common mother class), thus providing direct access to all other variables that have been integrated in the program.

```
#include "CVar_Higher.h"

class CVar_SELQ2 : public CVar_Higher {
 public:
  CVar_SELQ2() {};
  CVar_SELQ2(map<Axis,CVar_Mother*> *vs) :CVar_Higher(vs) {};
  ~CVar_SELQ2() {};
  void NeededVars(VarList_t &varlist) {
    varlist[vecNEUTRALINO]=true;
  };
  Float_t Calculate() {
    TLorentzVector * neutralino = (*vars)[vecNEUTRALINO]->GetVec();
    if(neutralino==NULL) return value = DONTFILL;

    TLorentzVector electronInVec(0.,0.,-27.5,27.5);
    TLorentzVector selectronVec(electronInVec - *neutralino);
    return value = TMath::Abs(selectronVec.M());
  };
 private:
};
```

FIGURE D.1: Example class for the variable SELQ2.

To create a new variable this structure can be copy-and-pasted and only the functions *Calculate()* and *NeededVars()* have to be changed. At the next start of the program the class will be automatically compiled and is then available for all analyses which are using the same main program.

The consequence of this program design is that a large number of different analyses sharing a common set of variables can use the same analysis framework by keeping their own mapping between ntuple variables and abstract labels in separate directories. All this is possible because (while all variables are in principle available) for a given run of the program only the necessary variables are read from the ntuple and only the necessary *Calculate()* functions are called (without needing to check a list of if-conditions). Consequently, the processing time is immensely reduced which allows for a more efficient analysis.

Probably the most important advantage is that all this works without the need of recompilation once the necessary set of variables is implemented. Compared to approaches which need to modify the code for each run (because of different

cuts, histogram booking or used variables) the number of possible errors is highly reduced[3].

The program is divided into three different running modes:

- *Script mode*
  The ROOT interpreter CINT is used to set all needed information in:
  - *setGeneral()*
  - *setCuts()*
  - *setHistos()*
  - *LoadNtupleFiles()*

  This has the advantage that no input file parser has to be written (which would need to be modified for each new variable) and the input syntax is automatically checked before the program is run. The information is saved in ROOT files.

- *Run mode*
  The information is read from ROOT files and histograms are produced by looping over the given ntuples and applying the given cuts.

- *Display mode*
  Various histograms of selected variables and different types (DATA, NC, SUSY, *etc.*) are displayed together.

An overview of the main class structure is shown in Figure D.2. Many additional features were implemented, like the possibility to produce event lists and write out ntuples with selected variables (also calculated ones). In conclusion, the program provides a generic organisational structure for physics analysis which may be used also for analysis at future colliders. Documentation and code is available at *www-zeus.desy.de/∼horn/AnalysisFramework.html*.

[3]To some approximation the number of potential errors will be proportional to the number of times the program needs to be changed.

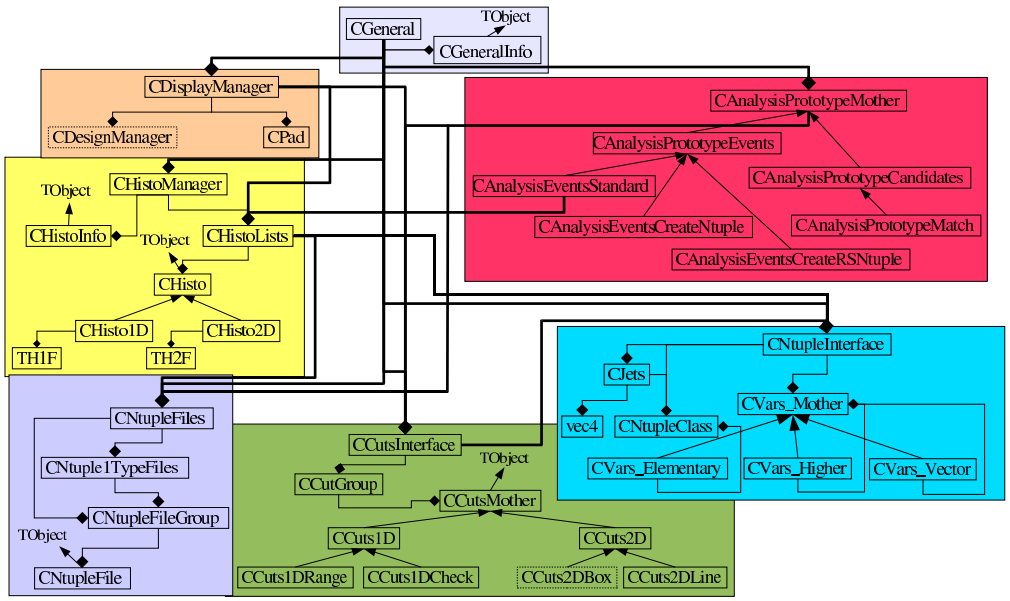

FIGURE D.2: Overview of the main class structure of the used analysis framework. The arrows indicate inheritance and the squares a "is a member of" relation.

Appendix E

Implementation of Discriminant Method

The method was implemented in a C++ class package which consists of the following classes:

- *BinaryRangeSearcher* Holds the basic range search algorithm as described elsewhere [131].
- *CDriverRS* Responsible for the steering of the discriminant calculation and the variation of the box size.
- *CMetaDriverRS* Performs the calculation of discriminant distributions for all possible combinations of n variables out of a set of m given ones and thus can be used to identify the best set of discriminant variables.
- *CDocuRS* A documentation class which provides control histograms for the number of points per box, the used factor distributions, the discriminants, *etc.*

More information and the source files together with a small example script can be found at *www-zeus.desy.de/∼horn/Discriminant.html*.

Appendix F

Publication Plots

For the publication [139][1] only the HERA I data set (1996-2000) was used corresponding to an integrated luminosity of 121 pb^{-1}. Control distributions for this sample are shown in Figure F.1. Further plots used are listed in the following.

[1] Preliminary results were shown at several conferences [145, 146, 147, 148].

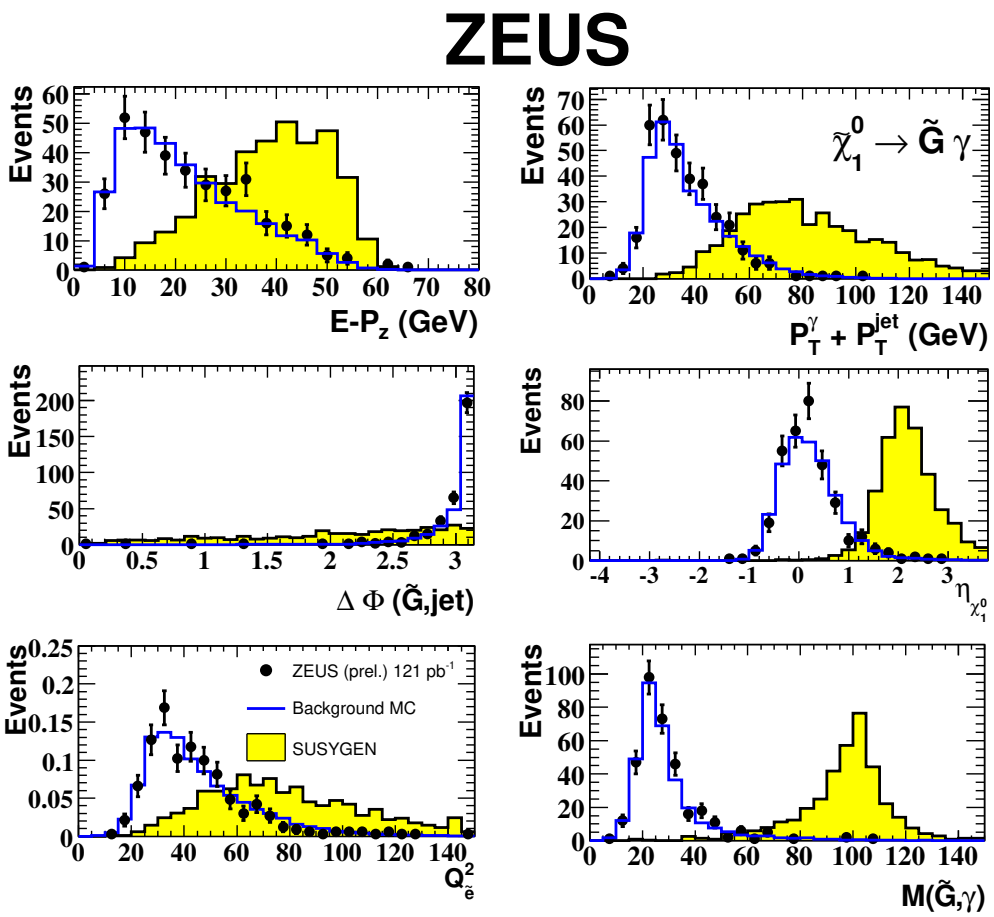

FIGURE F.1: Control distributions of discriminant variables.

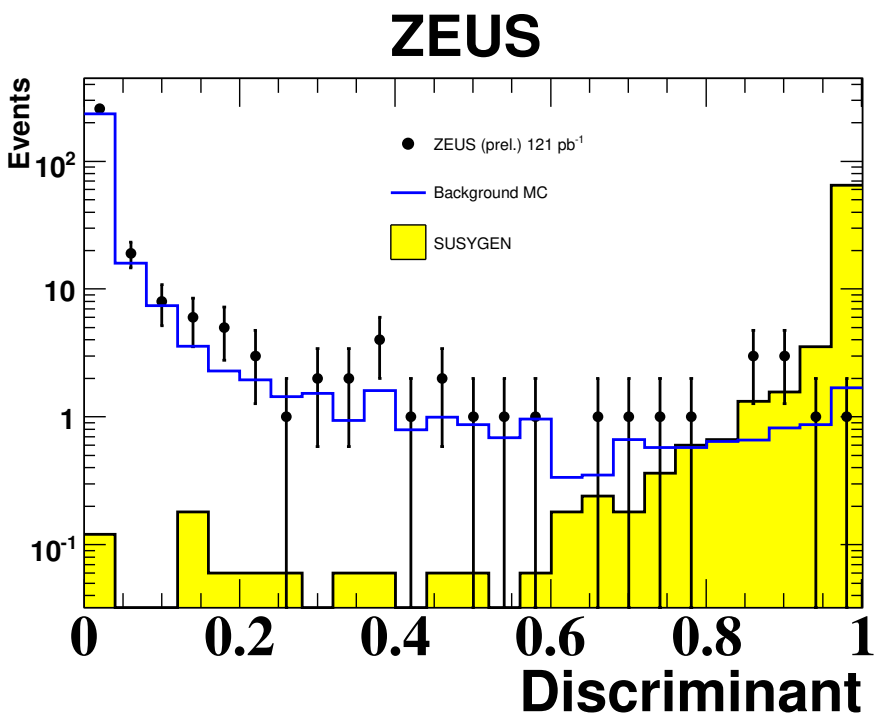

FIGURE F.2: Discriminant distribution.

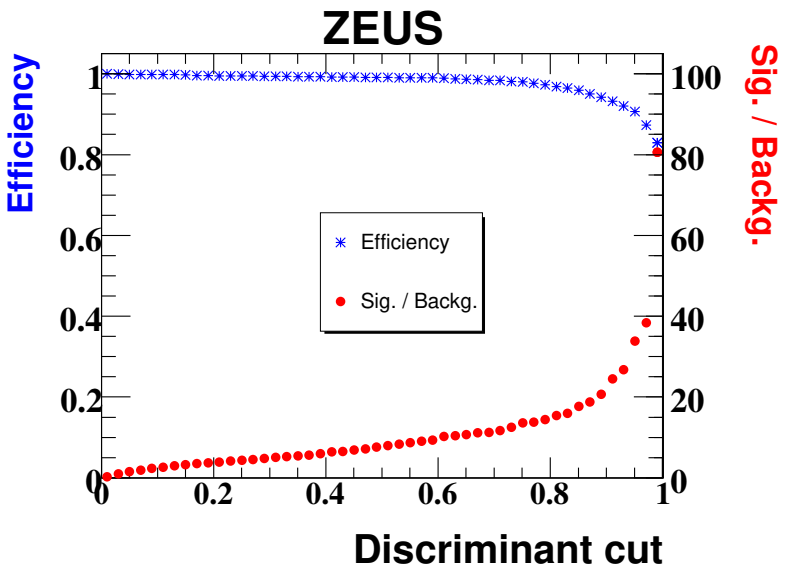

FIGURE F.3: Efficiency and purity as a function of discriminant cut.

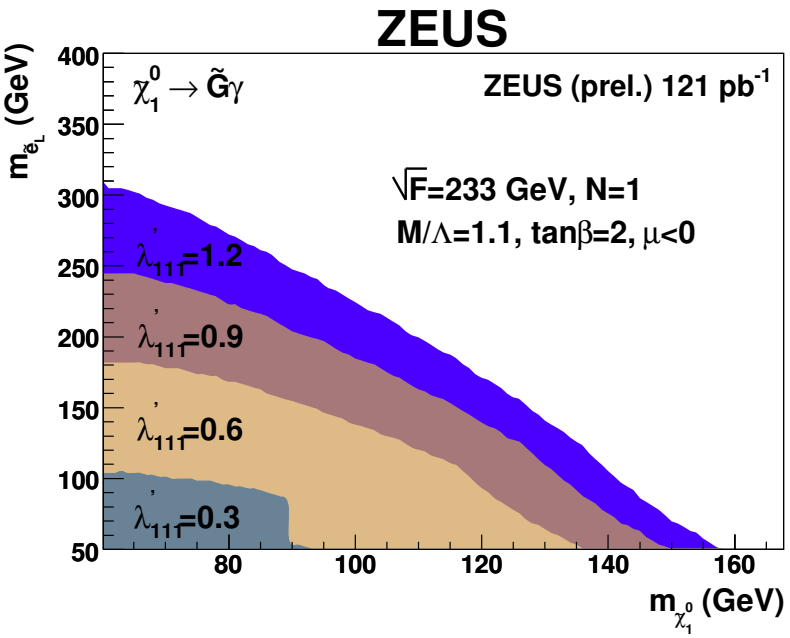

FIGURE F.4: Limits for varying strength of R_P-violating coupling.

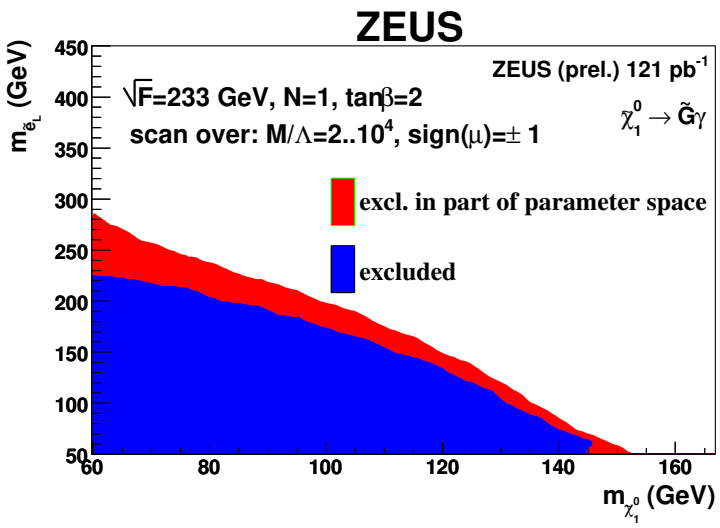

FIGURE F.5: Mass limit dependence on messenger scale and $sign(\mu)$ at $\tan\beta = 2$.

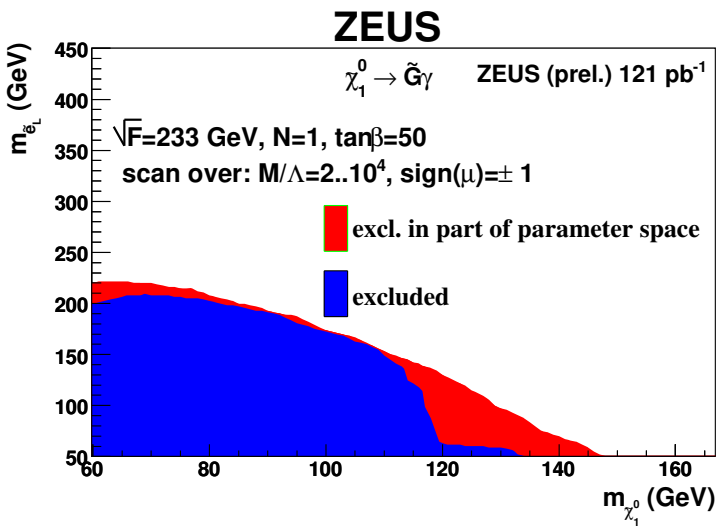

FIGURE F.6: Mass limit dependence on messenger scale and $sign(\mu)$ at $\tan\beta = 50$.

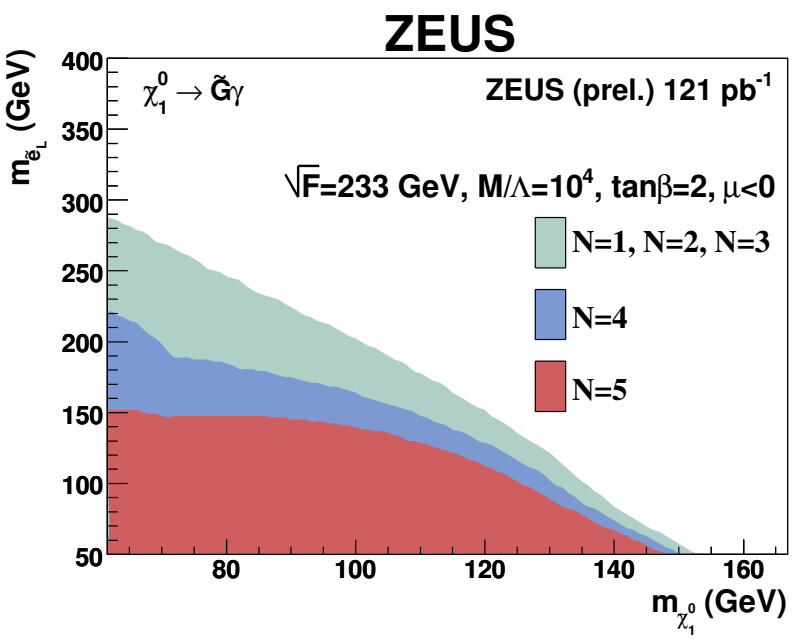

FIGURE F.7: Mass limit for different number of messenger fields N.

Bibliography

If I have seen further it is by standing
on the shoulders of giants.

Sir Isaac Newton

[1] H.P. Nilles. *Phys. Rep.*, **110**, 1 (1984).

[2] H.E. Haber and G.L. Kane. *Phys. Rep.*, **117**, 75 (1985).

[3] CDF Coll., D. Acosta et al. *Phys. Rev.*, **D 66** (2002); hep-ex/0110015.

[4] H1 Coll., A. Aktas et al. *Eur. Phys. J.*, **C 36**, 425 (2004).

[5] H1 Coll., A. Aktas et al. *Phys. Lett.*, **B 599**, 159 (2004).

[6] H1 Coll., A. Aktas. et al. *Phys. Lett.*, **B 599**, 159 (2004).

[7] C. Nhan Nguyen. *Search for Gaugino Production in R-Parity violating Supersymmetry with the ZEUS Detector at HERA*. PhD thesis, Universität Hamburg (2005). DESY-THESIS-2005-043.

[8] C. Berger. *Elementarteilchenphysik*. Springer (2002).

[9] Particle Data Group. pdg.lbl.gov (2006).

[10] Tevatron Electroweak Working Group. *Combined CDF and D0 results on the mass of the top quark* (2006); hep-ex/0603039.

[11] D.H. Perkins. *Introduction to High Energy Physics*. Addison-Wesley (1987).

[12] F. Halzen and A.D. Martin. *Quarks and Leptons.* John Wiley & Sons, Inc. (1984).

[13] D. Griffiths. *Introduction to elementary particles.* John Wiley & Sons, Inc. (1987).

[14] C. Qigg. *Gauge theories of the strong, weak and electromagnetic interaction.* B. Cummings (ed.), Frontiers on Physics, Menlo Park, California (1983).

[15] T.P. Cheng and L.F. Li. *Gauge Theory of Elementary Particle Physics.* Clarendom Press (Oxford Science Publication), Oxford, UK (1984).

[16] I.J.R. Aitchison. *Gauge Theories in Particle Physics.* IOP publishing, Bristol and Philadelphia (1984).

[17] J.D. Bjorken and S.D. Drell. *Relativistic Quantum Mechanics.* McGraw-Hill (1965).

[18] M.E. Peskin and D.V. Schroeder. *Quantum Field Theory.* Addison-Wesley (1995).

[19] P. Schmüser. *Feynman-Graphen und Eichtheorieen für Experimentalphysiker.* Springer (1995).

[20] S.L. Glashow. *Nucl.Phys.*, **22**, 579 (1961).

[21] A. Salam. *Phys.Rev.*, **127**, 331 (1962).

[22] S. Weinberg. *Phys. Rev. Lett.*, **19**, 1264 (1967).

[23] P.W. Higgs. *Phys. Rev. Lett.*, **13**, 508 (1964).

[24] P.W. Higgs. *Phys. Rev.*, **145**, 1156 (1966).

[25] A. Müller (ed.). *Perturbative QCD.* World Scientific (1989).

[26] W.J. Stirling, R.K. Ellis and B.R. Webber. *QCD and Collider Physics.* Cambridge University Press (1996).

[27] R. Devenish and A. Cooper-Sarkar. *Deep Inelastic Scattering.* Oxford University Press (2004).

[28] S. Dawson. *Introduction to electroweak symmetry breaking.* (1999); hep-ex/9901280.

[29] M. Drees. *An introduction to supersymmetry.* (1996); hep-ph/9611409.

[30] LEP EWWG, updates for the winter 2006 conferences. lepewwg.web.cern.ch/LEPEWWG/plots/winter2006 (2006).

[31] S. Hannestad. *Neutrino mass bounds from cosmology.* (2004); hep-ph/0412181.

[32] J.T. Lopuszanski R. Haag and M. Sohnius. *All possible generators of supersymmetries of the S matrix. Nucl. Phys.*, **B 88**, 257 (1975).

[33] J. Wess and B. Zumino *Phys. Lett.*, **B 49**, 52 (1974); S. Ferrara, J. Iliopoulos and B. Zumino *Nucl. Phys.*, **B 77**, 52 (1974).

[34] G. Kane. *Perspectives on Supersymmetry.* World Scientific (1988).

[35] LEP Electroweak Working Group. lepewwg.web.cern.ch.

[36] J. Ellis. *Beyond the standard model for hillwalkers* (1998); hep-ph/9812235.

[37] H. Pagels and J.R. Primack. *Phys. Rev. Lett.*, **48**, 223 (1982).

[38] W. Buchmuller, K. Hamaguchi, and J. Kersten. *Phys. Lett.*, **B 632**, 366–370 (2006); hep-ph/0506105.

[39] S.R. Coleman and J. Mandula. *All possible symmetries of the S matrix. Phys. Rev.*, **159**, 1251–1256 (1967).

[40] L. Giradello S. Ferrara and F. Palumbo. *Phys. Rev.*, **D 20**, 403 (1979).

[41] Particle Data Group. *Review of Particle Physics.* Elsevier (2004).

[42] G.F. Giudice and R. Rattazzi. *Theories with gauge-mediated supersymmetry breaking. Phys. Rept.*, **322**, 419–499 (1999).

[43] A. Masiero S. Borgani and M. Yamaguchi. *Phys. Lett.*, **B 386**, 189 (1996); hep-ph/9605222.

[44] F. Takayama and M. Yamaguchi. *Phys. Lett.*, **B 485**, 388 (2000); hep-ph/0005214.

[45] R. Godbole, M. Drees and P. Roy. *Theory and Phenomenology of Sparticles*. World Scientific (2004).

[46] LEPSUSYWG, DELPHI, L3, ALEPH and OPAL experiments. note LEPSUSYWG/01-03.1.

[47] LEPSUSYWG, DELPHI, L3, ALEPH and OPAL experiments. note LEPSUSYWG/04-02.1.

[48] S. Weinberg. *The Quantum Theory of Fields*, volume 3.

[49] G.F. Guidice, V. Barger and T. Han. *Phys. Rev.*, **D 40**, 2987 (1998).

[50] C. Qigg, B.W. Lee and H.B. Thacker. *Phys. Rev.*, **D 16**, 1519 (1977).

[51] A.Yu. Smirnov and F. Vissani. *Phys. Lett.*, **B 380**, 317 (1996).

[52] G. Bhattacharyya and P.B. Pal. *Phys. Rev.*, **D 59**.

[53] M. Bastero-Gill and B. Brahmachari. *Phys. Rev.*, **D 56**, 6912 (1997).

[54] B. Brahmachari and P. Roy. *Phys. Rev.*, **D 50**, 39 (1994).

[55] J.L. Goity and M. Sher. *Phys. Lett.*, **B 346**, 69 (1995).

[56] H.V. Klaptor-Kleingrothaus, G. Bhattacharyya and H. Päs. *Phys. Lett.*, **B 463**, 77 (1999); hep-ph/9907432.

[57] H.V. Klaptor-Kleingrothaus, M. Hirsch and S.G. Kovalenko. *Phys. Rev. Lett.*, **75**, 17 (1995).

[58] P. Roy, C.E. Carlson and M. Sher. *Phys. Lett.*, **B 357**, 99 (1995).

[59] M. Raidal, K. Huitu, J. Maalampi and A. Samtamaria. *Phys. Lett.*, **B 430**, 335 (1998).

[60] H1 Coll., A. Aktas et al. *Phys. Lett.*, **B 616**, 31–42 (2005); hep-ex/0501030.

[61] J. Butterworth and H. Dreiner. *Nucl.Phys.*, **B 397** (1993).

[62] H. Dreiner and P. Morawitz. *Signals for supersymmetry at HERA. Nucl. Phys.*, **B 428**, 31–60 (1994).

[63] S. Lola, H. Dreiner and P. Morawitz. *Phys. Lett.*, **B 389**, 62 (1996).

[64] CDF Coll., D. Acosta et al. *Phys. Rev. Lett.*, **89**, 281801 (2002); hep-ex/0205057.

[65] A. Heister et al. *Eur. Phys. J.*, **C 31**, 1 (2003).

[66] J. Abdallah et al. *Eur. Phys. J.*, **C 36**, 1 (2004).

[67] P. Achard et al. *Phys. Lett.*, **B 524**, 65 (2002).

[68] G. Abbiendi et al. *Eur. Phys. J.*, **C 11**, 619 (1999).

[69] L3 Coll., P. Achard et al. CERN-EP/2003-068.

[70] ALEPH Coll., A. Heister et al. *Eur. Phys. J.*, **C 28**, 1 (2003).

[71] DELPHI Coll. DELPHI/2003-040 CONF 660.

[72] CDF Coll. and D0 Coll., V. Buescher et al. (2005); hep-ex/0504004.

[73] M. Kim. *Search for Gauge-Mediated SUSY Breaking in Diphoton Events in $p\bar{p}$.* PhD thesis. Kyungpook National University (2005); FERMILAB-THESIS-2004-41

[74] G.A. Voss and B.H. Wiik. *Ann. Rev. Nucl. Part. Sci.*, **44**, 413 (1994).

[75] U. Schneekloth. (1998); hep-ex/9806010.

[76] U. Schneekloth (ed.). *The HERA luminosity upgrade.* (1998). DESY-HERA-98-05.

[77] A.A. Sokolov and I.M. Ternov. *Sov. Phys. Dokl.*, **8**, 1203 (1964).

[78] U. Schneekloth (ed.), (1998). HERA-98-05.

[79] M. Seidel. *The upgraded interaction region of HERA.* DESY-HERA-00-01.

[80] D.H. Saxon. Proc. HERA workshop, r.d. peccei (ed.), (1987).

[81] ZEUS Coll., U. Holm (ed.) *The ZEUS detector*, status report, (1993).

[82] B. Bock et al. *Design construction and test of the ZEUS forward tracking detector.* (1993). ZEUS-NOTE-93-110.

[83] D.G. Cussans et al. *Nucl. Inst. Meth.*, **A 315**, 397 (1992).

[84] B. Foster et al. *Nucl. Phys. Proc. Suppl.*, **B 32**, 181 (1993).

[85] B. Foster et al. *Nucl. Inst. Meth.*, **A 338**, 257 (1994).

[86] A. Grafagnini. *Nucl. Inst. Meth.*, **A 435**, 34 (1999).

[87] C. Coldewey. *Nucl. Inst. Meth.*, **A 447**, 44 (2000).

[88] C. Coldewey for the ZEUS MVD group. *Nucl. Inst. Meth.*, **A 453**, 149 (2000).

[89] E.N. Koffeman for the ZEUS MVD group. *Nucl. Inst. Meth.*, **A 453**, 89 (2000).

[90] M. Derrick et al. *Nucl. Inst. Meth.*, **A 309**, 77 (1991).

[91] A. Andresen et al. *Nucl. Inst. Meth.*, **A 309**, 101 (1991).

[92] A. Caldwell et al. *Nucl. Inst. Meth.*, **A 321**, 356 (1992).

[93] A. Bernstein et al. *Nucl. Inst. Meth.*, **A 336**, 23 (1993).

[94] ZEUS Coll., R. Carlin et al. *Nucl. Inst. Meth.*, **A 379**, 542 (1996).

[95] G.H. Health et al. *Nucl. Inst. Meth.*, **A 315**, 413 (1992).

[96] A. Polini. ECONF (2003). MOGT005.

[97] S.M. Fisher and P. Palazzi. *Adama programmers manual* - version 3.2. CERN ECP.

[98] D. Kisielewska et al. *Nukleonika*, **31**, 205 (1986). DESY-HERA-85-25.

[99] J. Andruszków et al. *Acta Phys. Pol.*, **B 32**, 2025 (2001).

[100] J. Andruszków et al. (1992). DESY-92-066.

[101] J. Repond. *ZEUS-Note 96-133* (1996).

[102] ZEUS Collab., S. Chekanov et al. *Phys. Lett.*, **B 539**, 197 (2002).

[103] B. Straub. *The EM electron finder.*, (1998); *www.desy.de/∼straub/doc/em.ps.*

[104] A. Lopez and S. Schlenstedt. ZEUS-Note-99-077 (1999).

[105] A. Caldwell H. Abramowicz and R. Sinkus. *Neural network based electron identification in the ZEUS calorimeter.* DESY 95-054 (1995); hep-ex/9505004.

[106] N. Tuning. *Zufos: Hadronic final state reconstruction with calorimeter, tracking and backsplash correction.* (2001). ZEUS-Note 01-21.

[107] L. Lönblad. *Compt. Phys. Commun.*, **71**, 15 (1992).

[108] G. Parisi and G. Alterelli. *Nucl. Phys.*, **B**, 298 (1977).

[109] V.N. Gribov and L.N. Lipatov. *Sov. J. Nucl. Phys.*, **15**, 438 (1972).

[110] Y.L. Dokshitzer. *Sov. Phys. JETP*, **46**, 641 (1977).

[111] M. Bengtsson and T. Sjöstrand. *Comp. Phys. Comm.*, **46**, 43 (1987).

[112] T. Sjöstrand and M. Bengtsson. *Comp. Phys. Comm.*, **43**, 367 (1987).

[113] T. Sjöstrand. *Comp. Phys. Comm.*, **39**, 347 (1986).

[114] G. Marchesini et al. *Compt. Phys. Commun.*, **67**, 465 (1992).

[115] G. Corcella et al. *J. of High Energy Phys.*, 01.

[116] D. Amati and G. Veneziano. *Preconfinement as a property of QCD. Phys. Lett.*, **B 83**, 87 (1979).

[117] G.A. Schuler K. Charchula and H. Spiesberger. *Comp. Phys. Comm.*, **81**, 381 (1994).

[118] A. Edin G. Ingelman and J. Rathsman. *Comp. Phys. Comm.*, **101**, 108 (1997).

[119] H. Spiesberger, A. Kwiatkowski and H.-J. Möhring. *Comp. Phys. Comm.*, **69**, 155 (1992); also in Proc. Workshop at HERA (1991), DESY, Hamburg.

[120] CTEQ Coll., H.L. Lai et al. *Eur. Phys. J.*, **C 12**, 375 (2000).

[121] H. L. Lai et al. *Phys. Rev.*, **D 55**, 1280–1296 (1997); hep-ph/9606399.

[122] Stavros Katsanevas and P. Morawitz. *Compt. Phys. Commun.*, **112**, 227 (1998).

[123] Nabil Ghodbane (1999); hep-ph/9909499.

[124] E. Perez. Proc. workshop on monte carlo generators of HERA physics. DESY, Hamburg, Germany (1999).

[125] J.L. Kneuer A. Djouadi and G. Moultaka. *Suspect: A fortran code for the supersymmetric and higgs particle spectrum in the MSSM* (2002); hep-ph/0211331.

[126] C. Berger and W. Wagner. *Phys. Rept.*, **146**, 1 (1987).

[127] A. Pukhov et al. *Preprint INP MSU*, p98–41/542 (1999); hep-ph/9908288.

[128] W.J. Stirling, A.D. Marti and R.G. Roberts. *Phys. Rev.*, **D 50**, 6734 (1994).

[129] A.D. Marti et al. *Eur. Phys. J.*, **C 14**, 133 (2000).

[130] M. Maire, A.C. McPherson, R. Brun, F. Bruyan and P. Zanarini. (1997). CERN-DD/EE/84-1.

[131] B. Koblitz. *Search for instanton-induced processes with the H1 detector in deep-inelastic electron-proton collisions at HERA.* PhD thesis, Universität Hamburg (2002). DESY-THESIS-2002-015.

[132] T. Carli and B. Koblitz. *Nucl. Inst. Meth.*, **A 501**, 576 (2003).

[133] R. Sedgewick. *Algorithms in C++.* Addison Wesley (1992).

[134] M. Helbich et al. *The spectrometer system for measuring ZEUS luminosity at HERA.* (2006). ZEUS-Note 06-002.

[135] O. Ota. *Measurement of lepton beam polarisation at HERA.* (2005). ZEUS-Note 05-012.

[136] R.J. Barlow. *A Guid to the Use of Statistical Methods in the Physical Sciences.* Wiley (1989).

[137] T. Junk. *Confidence level computation for combining searches with small statistics.*, (2002); hep-ex/9902006.

[138] A. Favara and M. Pieri. (1997); hep-ex/9706016.

[139] ZEUS Coll. *Search for gauginos and gravitinos in R-parity violating supersymmetry at HERA*. (2006). to be published.

[140] C. Blohm, private communication.

[141] H1 Coll., A. Aktas et al. *Phys. Lett.*, **B 561**, 241 (2003).

[142] ZEUS Coll., S. Chekanov et al. *Phys. Lett.*, **B 559**, 153 (2003).

[143] ZEUS Coll., S. Chekanov et al. *Phys. Lett.*, **B 583**, 1 (2004).

[144] B. Stroustrup. *The C++ Programming Language*. Addison Wesley (1999).

[145] C. Horn. *Searches for R-parity violating supersymmetry at ZEUS.* In W.H. Smith and S.R. Dasu (ed.), 13th International Workshop on Deep Inelastic Scattering, p603–606 (2005).

[146] C. Horn. *Searches for gravitinos in R-parity violating supersymmetry at ZEUS.* Paper submitted to Europhysics Conference on High Energy Physics (2005).

[147] C. Horn. *Searches for gravitinos in R-parity violating supersymmetry at ZEUS.* Paper submitted to XXII International Symposium: Lepton and Photon Interactions at High Energies (2005).

[148] C. Horn. *Searches for Supersymmetry at HERA.* 14^{th} International Conference on Supersymmetry and the Unification of Fundamental Interactions, June 12-17, Irvine, U.S.A. (2006).

Acknowledgements

There is a theory which states that if ever anybody discovers exactly what the Universe is for and why it is here, it will instantly disappear and be replaced by something even more bizarre and inexplicable. There is another theory which states that this has already happened.

Douglas Adams

I would like to thank my advisor Prof. Dr. Peter Schleper for giving me the opportunity to work on such a challenging and sophisticated research project. His good humored spirit and fascination for particle physics was always inspiring and provided the basis for an enjoyable working atmosphere in the group. I learned a great deal of physics from him. Many thanks also to Prof. Dr. Klanner for his continuous support. I admire his extraordinary insight in particle physics.

This thesis would not have been possible without the immense help from Dr. Thomas Schörner-Sadenius, especially during the beginning of my PhD. Dr. Georg Steinbrück shared with me the fun of leading exercise for physics students. I want to thank them both for check-reading my thesis.

Uwe Pein was the good heart of the University Hamburg group. I want to thank them all for their good company, namely Dr. Eckhart Fretwurst, Markus Stoye, Davis Contarato, Frank Hönniger, Thorben Theedt, Marcel Bleyl, Olaf Schulz, Jolanta Sztuk, Erik Butz, Alessio Bonato, Christian Blohm and all the others.

I am thankful to all people from the ZEUS collaboration for making this work possible. Many thanks to the other PhD students from the ZEUS group, for the nice time spend together, Oliver Gutsche, Volker Adler, Ingo Bloch, Benjamin Kahle, Raquel Santamarta, Elizabeth Nuncio-Quiroz, Amita Raval and especially Chi Nhan Nguyen as a close comrade in the quest for supersymmetry. The same holds for the members of the exotics group, and the coordinators, especially

Dr. Kunihiro Nagano and Dr. Alexander Tapper for their help with conference and paper questions. Umer Syed Noor is gratefully acknowledged for his assistance on stylistic problems of the English language.

In Bologna I was cordially welcomed by Dr. Lorenzo Bellagamba. In the following months I got to appreciate the Italian way of life. Special thanks to my office made Marco Garbini and the ZEUS students Stefano Antonelli, Lorenzo Rinaldi, Marcello Bindi, and the rest of the Bologna people for inviting me to so many exquisite espressos[2].

I would like to express my gratitude toward Prof. Masahiro Kuze for inviting me to Tokyo Institute of Technology and his concern for my well being during my stay. This was an exciting experience owed to the nice people I got to know, Natta-San, Kuniki-San, Takai-San, Maeda-San, Kuwahra-San, Funaki-San and Nao-San.

Further thanks go to Prof. Dr. Caren Hagner for reading my thesis and Prof. Dr. Joachim Mnich for his questions during the disputation.

The work for the DESY Public Relations office was a lot of fun, thanks to Veronika Werschner, Christian Mrotzek and the rest of the team. In summary, the time at DESY was an overwhelming experience. I enjoyed very much working with so many nice people from such a wide range of countries.

Last but not least, I want to take the opportunity to thank my parents and my sister for their great support on all the way until now.

[2]The DAAD is gratefully acknowledged for providing the funding for my stay in Italy.